AN ABSTRACT OF THE THESIS OF

Jochen Braunmiller for the degree of Doctor of Philosophy in Geophysics presented on October 23, 1998. Title: Seismotectonics of the Explorer Region and of the Blanco Transform Fault Zone.

Redacted for privacy

Abstract Approves: _____

John L. Nábelek

In this thesis, we present the first detailed, long-term seismotectonic studies of oceanic ridge-transform systems. The proximity of the Juan de Fuca plate to a network of broadband seismic stations in western North America provides a unique synergy of interesting tectonic targets, high seismicity, and recording capabilities. Our main tools are earthquake source parameters, determined by robust waveform modeling techniques, and precise earthquake locations, determined by joint epicenter relocation. Regional broadband data are used to invert for the source moment tensors of the frequent, moderate-sized ($M \geq 4$) earthquakes; this analysis began 1994. We include Harvard centroid moment-tensors available since 1976 for larger ($M \geq 5$) earthquakes.

Two studies comprise the main part of this thesis. In the first, we determine the current tectonics of Explorer region offshore western Canada. Earthquake slip vector azimuths along the Pacific-Explorer boundary require an independent Explorer plate. We determine its rotation pole and provide a tectonic model for the plate's history over the last 2 Ma. Plate motion changes caused distributed deformation in the plate's southeast corner and caused a small piece in the southwest corner to transfer to the Pacific plate. Capture of the plate fragment indicates that preserved fragments not necessary represent entire microplates.

In the second study, we investigate seismicity and source parameters along the Blanco Transform Fault Zone (BTFZ). The deformation style-- strike slip and normal faulting-- correlates well with observed changes in BTFZ's morphology. We infer that Blanco Ridge probably consists of two fault segments, that several parallel faults are active along BTFZ's

west part, and that Cascadia Depression possibly is a short spreading center. The slip distribution along the BTFZ is highly variable, although seismicity could account for the full plate motion rate along the entire BTFZ.

The final part is a short study where we locate an earthquake in the tectonically active Mendocino triple junction region offshore northern California using land and offshore data. The precise location may be useful as a master event for relocating other earthquakes.

Seismotectonics of the Explorer Region and of the Blanco Transform Fault Zone

by

Jochen Braunmiller

A THESIS

submitted to

Oregon State University

in partial fulfillment of
the requirements for the
degree of

Doctor of Philosophy

Presented October 23, 1998
Commencement June 1999

Doctor of Philosophy thesis of Jochen Braunmiller presented on October 23, 1998

APPROVED:

Redacted for privacy

Major Professor, representing Geophysics

Redacted for privacy

Dean of College of Oceanic & Atmospheric Sciences

Redacted for privacy

Dean of Graduate School

I understand that my thesis will become part of the permanent collection of Oregon State University libraries. My signature below authorizes release of my thesis to any reader upon request.

Redacted for privacy

Jochen Braunmiller, Author

TABLE OF CONTENTS

TABLE OF CONTENTS (Continued)

TABLE OF CONTENTS (Continued)

LIST OF FIGURES

LIST OF FIGURES (Continued)

LIST OF FIGURES (Continued)

LIST OF TABLES

Seismotectonics of the Explorer Region and of the Blanco Transform Fault Zone

1. INTRODUCTION

Earthquake source parameters (seismic moment tensor, seismic moment, and centroid depth) provide important seismotectonic and earthquake hazard related information. This study, which is primarily concerned with the seismotectonics of selected regions offshore western North America, is part of a larger effort to characterize the seismotectonics and the state of stress in the north-western United States and adjacent regions, and to provide rapid estimates of source parameters, particularly for larger, potentially damaging earthquakes.

1.1 OSU Regional Moment Tensor Analysis - an Overview

The newly-established broadband seismic network in the Pacific Northwest of the US and south-western Canada (Figure 1.1) allows the routine determination of source parameters for moderately sized earthquakes in the entire region as well as the adjacent offshore plate boundaries associated with the Juan de Fuca plate system. The method for the analysis, which solves for the source parameters by minimizing the least squares misfit between observed and synthetic three-component complete regional (event-station distance $\Delta < 1000$ km) seismograms, is described by Nábelek and Xia (*1995*), with an application to the 1993 Scotts Mills, Oregon earthquake. Analysis of 21 earthquakes of the 1993 Klamath Falls, Oregon earthquake sequence (*Braunmiller et al., 1995a*) helped to streamline data extraction from the seismic stations (which are operated by six different institutions, Figure 1.1) and data pre-processing (windowing, band-pass filtering, deconvolution of the seismograph instrument response to obtain true ground motion). Figure 1.2 shows an example of the analysis for an earthquake in the Puget Sound region of Washington on June 23, 1997. The azimuthal coverage by the broadband stations is very good; the three component waveforms vary considerably, but predictably, in

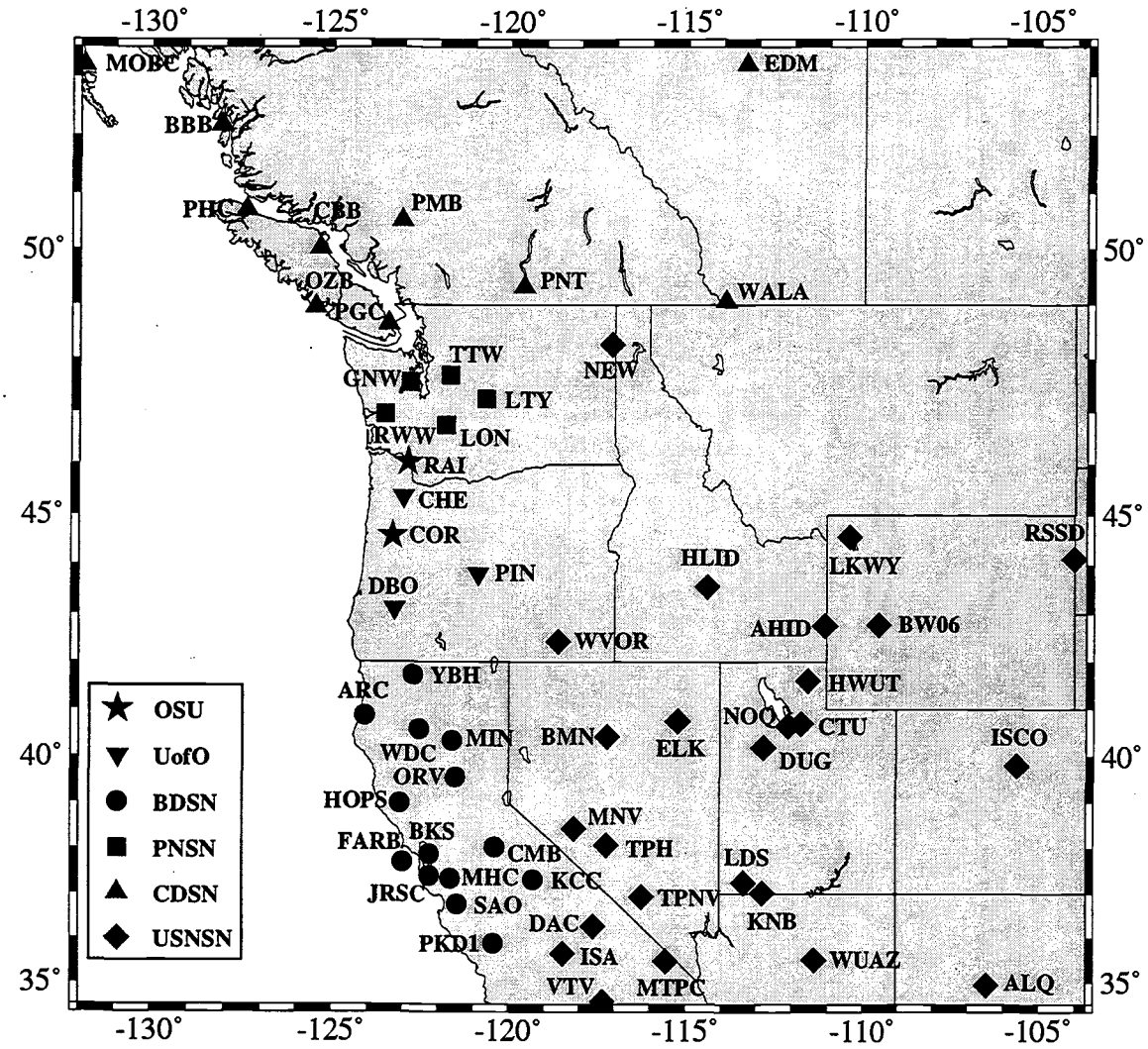

Figure 1.1. Broadband seismic stations used for regional moment-tensor analysis. The network abbreviations are OSU for Oregon State University (station COR is also part of the global digital seismic network GDSN), UofO for University of Oregon, BDSN for Berkeley Digital Seismic Network, PNSN for Pacific Northwest Seismic Network, CDSN for Canadian Digital Seismic Network, and USNSN for US National Seismic Network.

Figure 1.2. Example of the regional moment-tensor analysis. Shown is the Bremerton, Washington earthquake, which occurred on June, 23 1997. Analysis was performed in the 15-40 sec pass-band, and we obtained a 4 km shallow thrust source mechanism with east-west trending fault nodal planes and a M_w of 4.5. Top: Fit of observed (solid) and theoretical (dashed) seismograms. Azimuth and epicentral distance to each station are given under each station name. Z, R, and T are vertical, radial and transverse component. All seismogram amplitudes are normalized to 100 km epicentral distance assuming cylindrical geometrical spreading. The variance vs. centroid depth (lower left) shows the depth is well resolved and the mechanism is stable over a wide depth range; the first number beneath each fault plane solution is the seismic moment (in 10^{15} Nm), the second the double-couple component of the moment tensor (in %). The variance vs. deviation from best-fitting double-couple mechanism shows the mechanism is well resolved; the dashed line represents a 5% increase in variance.

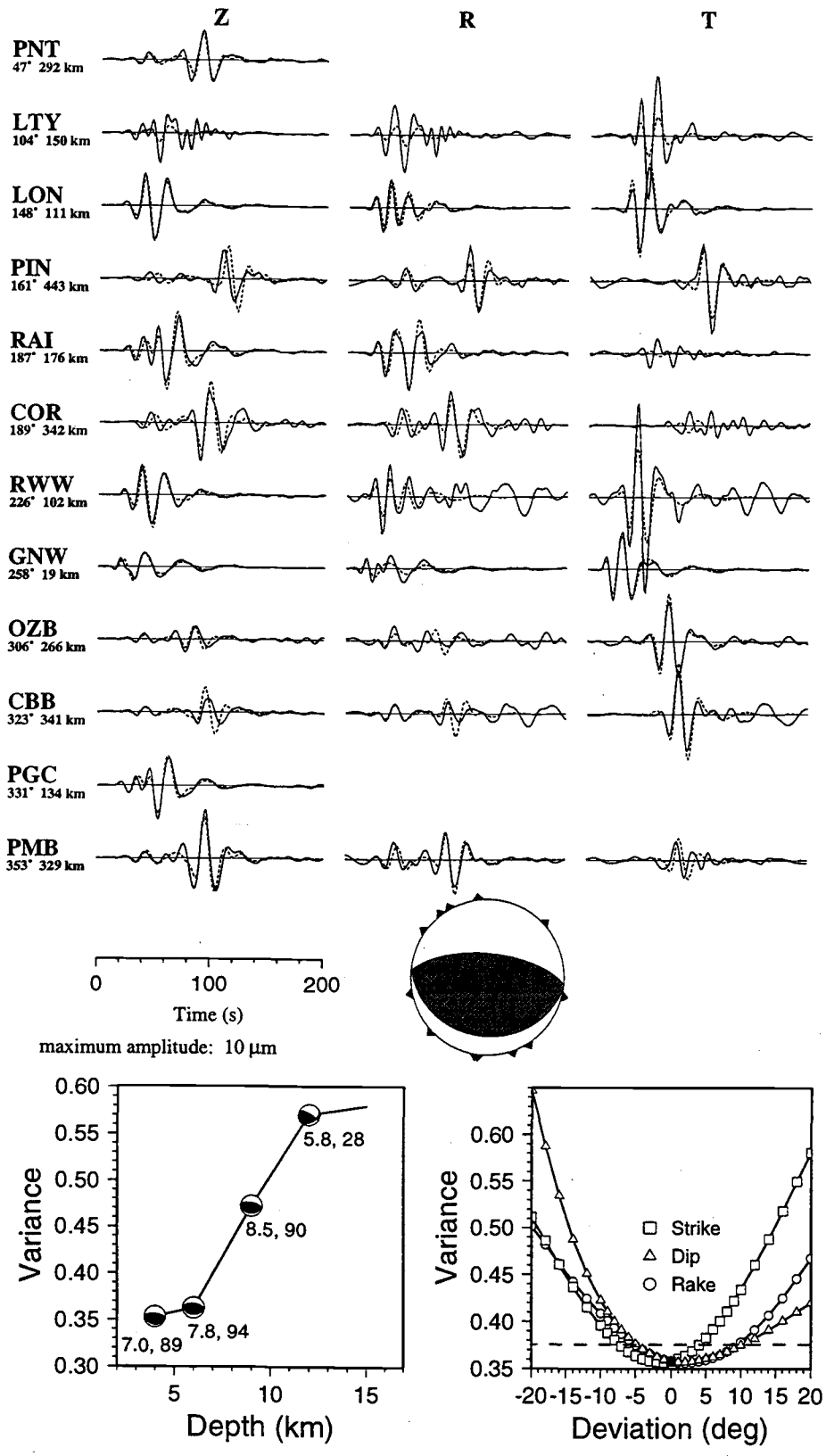
Bremerton, WA, 97/ 6/23 19:13:27 Mw=4.53 15-40s 4km
Z
R
T
PNT
47° 292 km
LTY
104° 150 km
LON
148° 111 km
PIN
161° 443 km
RAI
187° 176 km
COR
189° 342 km
RWW
226° 102 km
GNW
258° 19 km
OZB
306° 266 km
CBB
323° 341 km
PGC
331° 134 km
PMB
353° 329 km
0
100
200
Time (s)
maximum amplitude: 10 μm
Variance
0.60
0.55
0.50
0.45
0.40
0.35
0.30
5.8, 28
8.5, 90
7.8, 94
7.0, 89
5
10
15
Depth (km)
Variance
0.60
0.55
0.50
0.45
0.40
0.35
Strike
Dip
Rake
-20 -15 -10 -5 0 5 10 15 20
Deviation (deg)

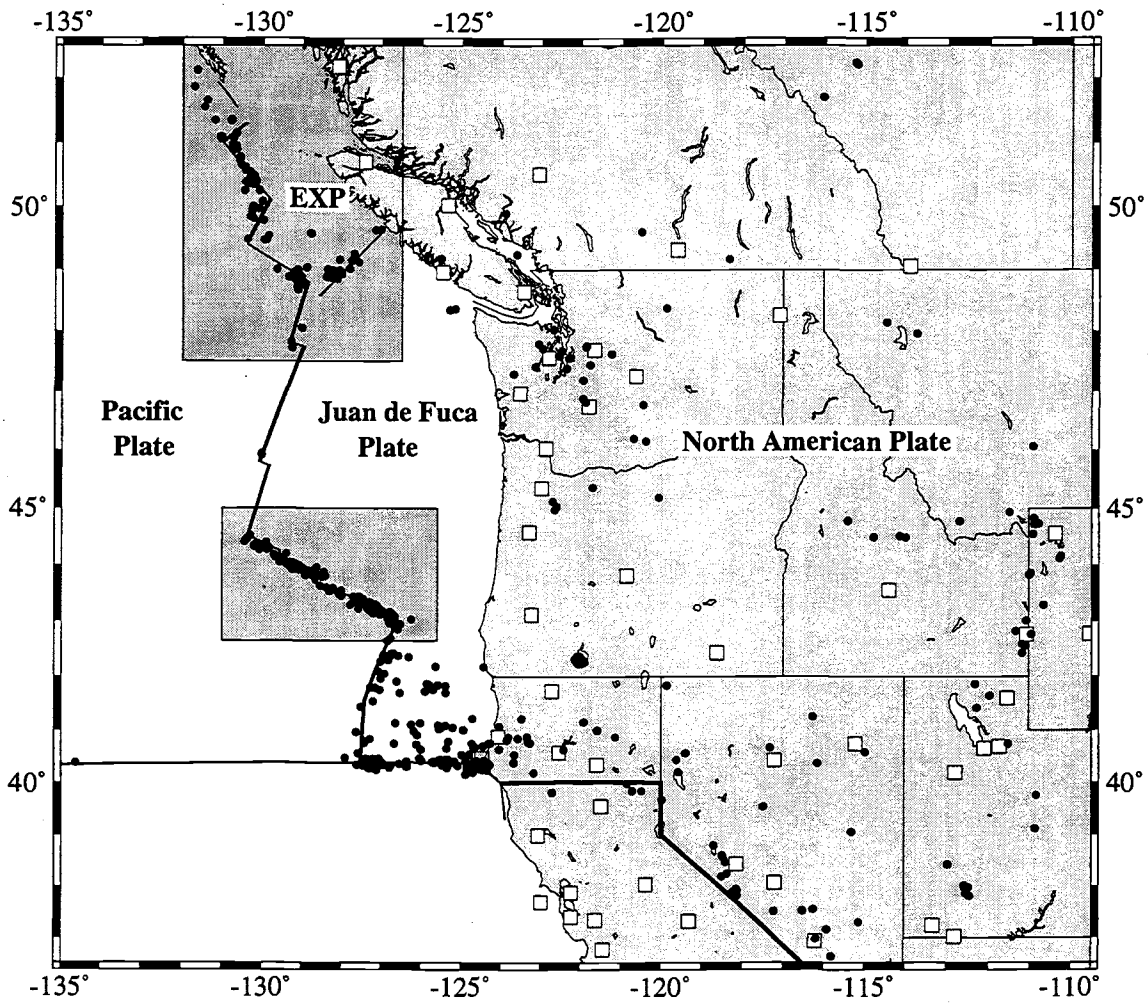

Figure 1.3. Location of the analyzed earthquakes (solid circles). Open squares are the locations of the broadband seismic stations. Highlighted are the areas covered in subsequent chapters of this thesis. EXP: Explorer plate. We do not attempt analysis of events in California south of the heavy line.

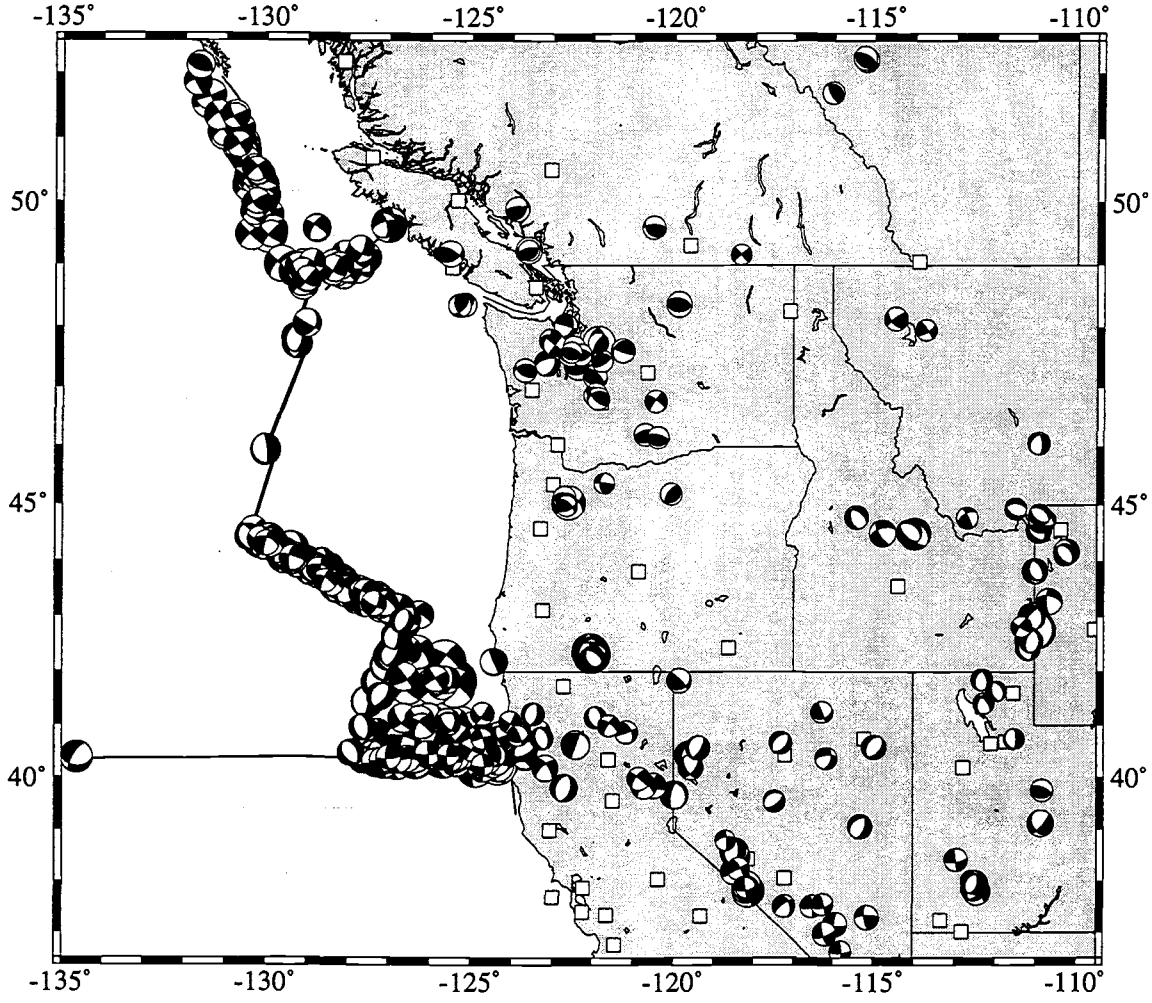

Figure 1.4. Fault plane solutions of the analyzed earthquakes. Size is proportional to M_W. Open squares are the locations of the broadband seismic stations.

amplitude and shape, thus providing a strong constraint on the source mechanism. Both the shallow source depth and the dip-slip mechanism are very well resolved.

In January 1994 we began routine operation. During the last five years, we determined more than 500 earthquake source mechanisms (Figures 1.3 and 1.4) ranging in size from moment magnitude M_W = 3.3 to 7.0. Automated data retrieval and streamlined data pre-processing allow complete analysis within a few hours after an earthquake occurred. We disseminate our solutions to interested clients (approximately 30, mainly researchers from universities and government institutions in the Pacific Northwest) and up-date a World Wide Web site (http://quakes.oce.orst.edu/moment-tensors) immediately after an earthquake is analyzed. Quick dissemination of the earthquake source parameters has helped seismometer deployment for an aftershock study (J. Zollweg, pers. comm. 1994), and, as part of the Pacific Northwest Seismic Network, provides rapid information to the public.

A detailed description and discussion of the analyzed earthquakes are beyond the scope of this dissertation. A cursory look at Figure 1.4, however, shows that we have sampled known seismically active areas fairly well; the mechanisms within various provinces are remarkably consistent with each other and reflect the tectonics of those provinces. Our catalog, in spite of the short recording period, is now by far the most comprehensive collection of earthquake source mechanisms available for the region. Many events actually occurred in relatively uninstrumented areas or-- as in the case for offshore events-- even outside of seismic networks; most of those events could not have been analyzed by conventional techniques (the exception being the larger, M > 5-5.5, earthquakes which can be analyzed with teleseimic data recorded several thousand kilometers from an earthquake's epicenter).

1.2 Seismotectonic Studies - Chapters of this Thesis

The body of this thesis is comprised of three parts. In Chapters 2 and 3, a subset of the analyzed earthquakes is used for detailed seismotectonic studies of two offshore regions: the Explorer region offshore Vancouver Island, and the Blanco Transform Fault zone offshore Oregon. For both studies, I augmented our data set with additional seismological data (catalog seismicity and Harvard CMT source mechanisms) and relocated larger earthquakes using a joint epicenter determination (JED) technique (*Douglas, 1967*). The

JED technique provides superior relative locations of an earthquake cluster compared to commonly used single-event locations. The improved locations show where the earthquakes happened; the source mechanisms indicate how the faults moved, and the catalog seismicity provides an estimate of the seismic energy release over several decades.

The primary objective in Chapter 2 is to deduce the current plate motions of the Explorer region offshore Vancouver Island. The region split from the Juan de Fuca plate about 4 million years (Ma) ago (*Riddihough, 1984*) and formed an independently moving micro-plate. Recently, Rohr and Furlong (*1995*) suggested the plate no longer moves independently; according to their model a transform fault separating the Pacific and North American plates cuts through and the micro-plate's remnants are now permanently attached to either side. The earthquake data in Chapter 2 provide direct information about the current tectonics not available to previous studies; they also provide some indications about the fate of small micro-plates caught between larger plates, a research topic which has only recently gained more recognition.

In Chapter 3, I am mainly interested in the style of deformation, the distribution of earthquakes, and the fault segmentation along the length of the Blanco Transform Fault Zone (BTFZ), a 350 km long transform fault system which forms the Pacific-Juan de Fuca plate boundary between the Juan de Fuca and Gorda ridges. The proximity of the BTFZ to the broadband seismograph network and the availability of high-quality earthquake locations (derived from hydrophone array data which only recently were made available to the research community by the US Navy) provide the framework for monitoring an oceanic transform fault system with unprecedented accuracy and detail. The JED-relocations also provide an important comparison to the locations derived with the hydrophone data, whose performance for earthquake studies has not been fully independently checked.

The location and source parameters of an earthquake offshore northern California--which occurred during the 1994 Mendocino triple junction experiment (*Tréhu et al., 1995*)--are presented in Chapter 4. The event was well recorded by ocean bottom hydrophones (OBH) and seismometers (OBS). Generally, offshore earthquake locations are hampered by a one-sided distribution of the land stations; adding the OBH/OBS data provided a good azimuthal station coverage. The precise location of the 1994 earthquake may be useful as a master event for relocating other events in this tectonically complicated region.

2. SEISMOTECTONICS OF THE EXPLORER REGION

2.1 Introduction

The Explorer region, offshore western Canada, is a small remnant of the Farallon plate which occupied large parts of the northeast Pacific basin in Cretaceous times. Two contradictory models exist for the region's current tectonics. According to the first, the region forms the independent Explorer plate (*Riddihough, 1977; 1984*) surrounded by the Pacific, North America and Juan de Fuca plates (Figure 2.1). The second model (Figure 2.2), in contrast, has the region cut by a transform fault forming the Pacific-North America plate boundary, with Explorer plate's remnants now permanently attached to either side (*Barr and Chase, 1974; Rohr and Furlong, 1995*). This controversy raised our interest, and we present new, previously unavailable, seismological data to constrain current regional plate motions.

Since the Tertiary, the Farallon plate and its successors have steadily decreased in size and experienced multiple stages of plate break-up (*Engebretson et al., 1985; Lonsdale, 1991; Stock and Lee, 1994*). The first major break-up, into the Juan de Fuca plate in the north and the Nazca-Cocos plate in the south, occurred about 55-50 Ma ago when the Farallon-Pacific spreading center approached the Farallon-North America subduction zone (*Stock and Molnar, 1988; Atwater, 1989*). Juan de Fuca plate's size has steadily decreased since its inception due to northward migration of its southern triple junction (*Atwater, 1989*) and additional plate fragmentation. For the last few Ma years, two fragments, the Gorda deformation zone (*Riddihough, 1980; Wilson, 1986; 1989*) in the south and the Explorer plate (*Barr and Chase, 1974; Riddihough, 1977; 1984; Botros and Johnson, 1988*) in the north, moved distinctly from the remainder of Juan de Fuca plate.

A difference between Explorer and Juan de Fuca ridge orientation, starting about 4 Ma ago, requires an independent Explorer plate at least since that time (*Riddihough, 1984; Botros and Johnson, 1988*). Riddihough (*1984*) determined mean instantaneous Pacific-Explorer rotation poles averaged over 1 Ma time intervals for the last 4 Ma from the spreading rates and directions at Explorer ridge. The most recent pole, assuming plate motions did not change during the last 1 Ma, thus describes current Explorer plate motions

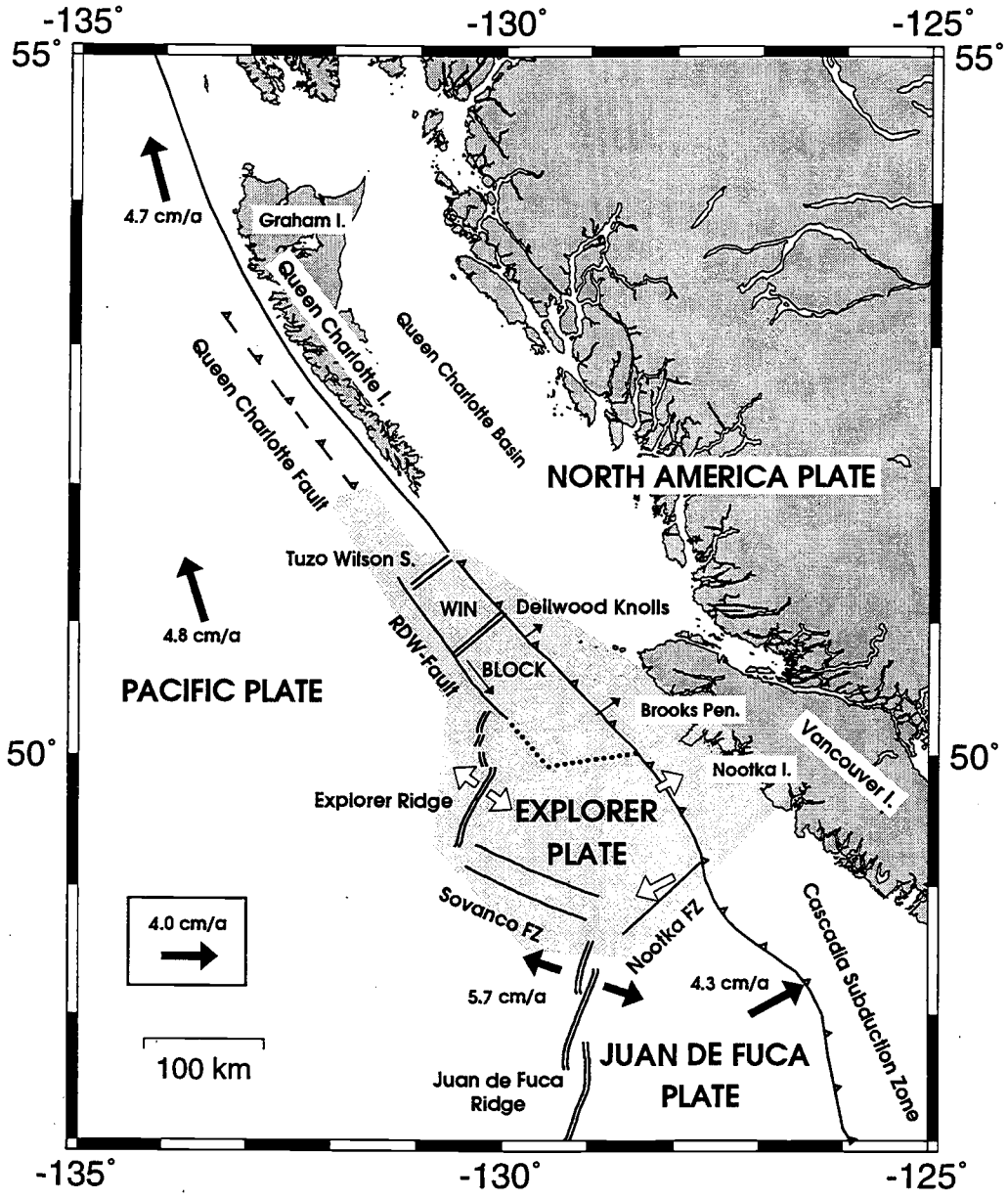

Figure 2.1. Map of Explorer region (lightly shaded) and surroundings. Plate boundaries are based on Riddihough's (*1984*) and Davis and Riddihough's (*1982*) tectonic models. Solid lines are active plate boundaries (single line: transform fault; double: spreading center; barbed: subduction zone, barbs in down-going plate direction). The wide double-line outlines the width of the Sovanco Fracture zone, and the dots sketch the Explorer -Winona boundary. Plate motion vectors (solid arrows) are from NUVEL-1A (*DeMets et al., 1994*) for Pacific-North America motion and from Wilson (*1993*) for Pacific-Juan de Fuca and Juan de Fuca-North America motion. Open arrows are Explorer relative plate motions (*Riddihough, 1984*). Winona block motions (thin arrows), described only qualitatively by Davis and Riddihough (*1982*), are not to scale. RDW: Revere-Dellwood-Wilson; Win: Winona; FZ: fault zone; I: island; S: seamount; Pen: peninsula.

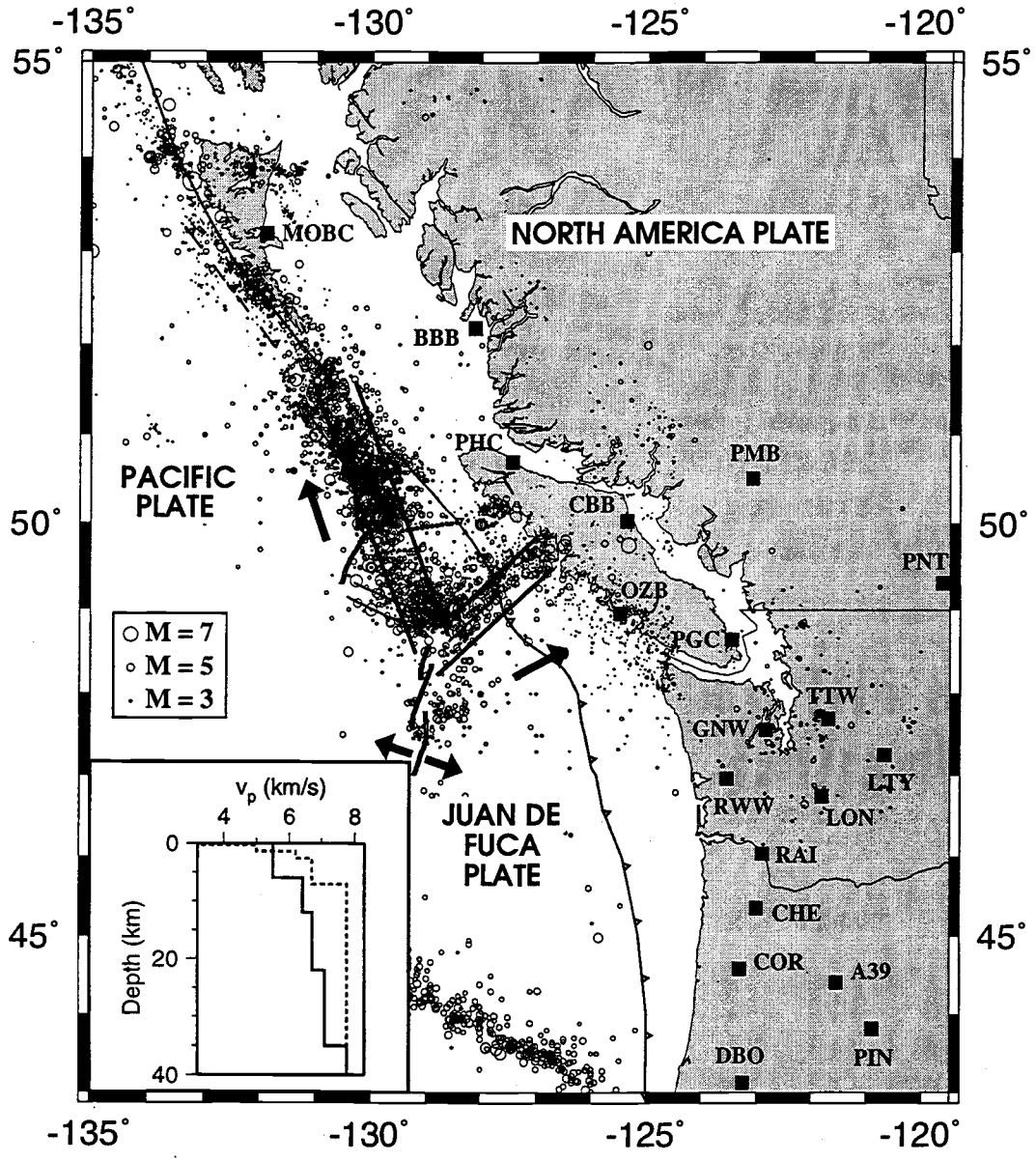

Figure 2.2. Map of broadband seismic stations (solid squares) and 1912-1997 seismicity (open circles; from the International Seismological Centre, Preliminary Determination of Epicenters, Earth Physics Branch and Decade of North American Geophysics catalogs). A northwest trending, broad epicenter band inside Explorer region parallels the predicted Pacific-North America motion direction (solid arrow); a northeast trending band marks Nootka fault zone, and activity along the Explorer-North America boundary is low. Not shown are stations NEW and WALA east and DLBC north of the map. The inset shows the P-wave velocity-depth model used for synthetic seismogram calculations. We applied an oceanic model (dashed line) for stations MOBC, BBB, PHC, and OZB, and a land model (solid line) for all other stations. The vp/vs ratio used is 1.78 except for the thin uppermost sediment layer in the oceanic model where the ratio was set to 1.91.

[subsequently, we mean this most recent rotation pole and its resulting plate motions when referring to "Riddihough's (*1984*) model"].

Explorer region's tectonics complicated further 1-2 Ma ago when spreading shifted from offshore Brooks peninsula to the vicinity of the Dellwood Knolls and Tuzo Wilson seamounts (*Riddihough et al., 1980*). Revere-Dellwood-Wilson transform fault's more northerly orientation compared to Explorer ridge's spreading direction suggests that the Winona block (Figure 2.1) is an independent plate fragment (*Davis and Riddihough, 1982*).

Figure 2.1 depicts the current plate boundaries and expected plate motions in the Explorer region following Riddihough (*1984*) and Davis and Riddihough (*1982*). The model includes two small, independent plates: Explorer plate and Winona block.

An entirely different model for Explorer region's current plate motions was presented by Barr and Chase (*1974*) and Rohr and Furlong (*1995*). They argue that seismicity, which appears to cut in a northwesterly direction through Explorer region (Figure 2.2), defines a new Pacific-North America transform plate boundary: Explorer plate and Winona block are no longer independent plates but part of the Pacific and North American plates.

This second model implies that independent motion of the small Explorer and Winona plate fragments ceased before they were entirely subducted beneath North America. Similar "plate capture" is well documented for several microplates in the seafloor magnetic anomaly record offshore California and Baja California (*Lonsdale, 1991*). Each of these preserved microplates fragmented off the southward retreating Cocos plate and moved as an independent plate for only a few Ma before becoming attached to the Pacific plate (*Atwater, 1989; Lonsdale, 1991; Stock and Lee, 1994*).

The purpose of our study is to determine the Explorer region's current tectonics. We use broadband data from the recently established network of three component seismograph stations in British Columbia and the Pacific Northwest of the United States (Figure 2.2) to obtain the first reliable earthquake source parameter estimates for the region's frequent, moderately-sized earthquakes. Combined with the Harvard centroid moment-tensor solutions (*Dziewonski et al., 1994*, and references therein), they represent the region's largest earthquake source parameter data set determined by robust waveform matching techniques. In addition, because of documented bias in routine locations (*Hyndman and Rogers, 1981*), we relocate larger earthquakes using the joint epicenter determination technique (*Douglas, 1967; Dewey, 1972*).

2.2 Methods and Results

2.2.1 Moment-Tensors

The new three-component, high-dynamic range, broadband seismic network in British Columbia and the Pacific Northwest (Figure 2.2) now allows seismological studies once impossible to perform with the classical short-period vertical seismometer network. In this study we employ robust waveform fitting techniques to determine source parameters of small-medium magnitude ($M \geq 4$) earthquakes in the offshore Explorer region. Source parameter estimates based on P-wave first-motion polarities from earlier short-period networks in western Canada and Washington are unreliable because the stations cover only a small azimuthal segment of the focal sphere.

The broadband network in the Pacific Northwest, which initiated in the late 1980's with the installation of the Corvallis, Oregon station (COR), currently consists of about 15 stations and is still growing (Figure 2.2). Routine earthquake source parameter analysis in the Explorer region became possible only after stations in western British Columbia opened during 1993 (PGC, BBB, PMB). Since the onset of our study in 1994, the network has evolved further, most significantly with the installation of sites on Vancouver Island (PHC, OZB, CBB) and on Moresby Island (MOBC) in 1996. These new stations, close to the Explorer region, lowered the magnitude threshold for analysis from about M = 4.5 to M = 4.0 and improved the source parameter resolution.

We invert for the earthquake source parameters (deviatoric seismic moment tensor and source time-function) by minimizing the least squares misfit between observed and synthetic seismograms. Strike, dip, rake, and seismic moment of the source follow directly from the moment tensor formulation (e.g., *Aki and Richards, 1980*). The centroid depth is found by observing the misfits for a set of trial depths; we usually start at 4 km depth with 3 km-increments for depths of 6 km and more. The inversion of the complete, three-component seismograms is performed at low frequencies using data from all available stations simultaneously. At low frequencies, the regional (event-station distance $\Delta \leq 1000$ km) seismograms are dominated by guided waves and surface waves which can be adequately modeled using a relatively simple 1-D velocity depth model (Figure 2.2 inset). Synthetic seismograms are calculated with Bouchon's (*1982*) wavenumber summation technique. For more details of the method, refer to Nábelek and Xia (*1995*), and Braunmiller et al. (*1995a*).

The actual frequency band used for inversion depends on earthquake size and station-event distances. We adjust the band such that the signal-to-noise ratio is good, and the prominent phases of synthetic and observed seismograms are in phase. In most instances, the passband is 0.02-0.05 Hz. For larger events, when we include more distant stations, the passband is shifted to lower frequencies, while for smaller events, when long-period noise buries the signal, the passband is changed to higher frequencies. On average, 20-25 waveforms from about 10 stations are used. We use three component data whenever possible; however, noisy traces are discarded.

Since 1994, we have determined source parameters of 79 earthquakes in the Explorer region (Table 2.1). Several examples of waveform fits and source parameter uncertainty estimates are shown in Appendix A. The average uncertainties in strike, dip, and rake of ±5°, ±15°, and ±20°, and centroid depth of ±3 km, were estimated by observing the variance increase relative to each event's best-fit model.

In addition to our regional moment tensor (RMT) solutions, we used source parameter estimates from the 33 Harvard centroid moment-tensor (CMT) solutions existing for the Explorer region from 1976 until 1998 (Table 2.2). For recent, larger earthquakes, both RMT and CMT solutions exist, and they generally agree very well (Appendix A).

The majority of the RMT and CMT solutions inside Explorer region (shaded region in Figure 2.3) has a strike-slip source mechanism. This implies that most earthquakes strong enough for moment tensor analysis ($M \geq 4$) occurred along transform faults or within the plates. Spreading segments are either aseismic, or earthquakes are too small for analysis.

Before our RMT analyses, hypocenter depths for only a few earthquakes in the Explorer region were well determined. For the small earthquakes, centroid and hypocenter depth are roughly equivalent; and the centroid depth distribution (Figure 2.4) indicates that the seismogenic fault width in the Explorer region is about 10 km. This agrees well with hypocenter depth estimates from ocean bottom seismometer studies (*Hyndman and Rogers, 1981*) and a shallow 4-5 km centroid depth estimate for the $M_w = 6.7$, 920406 earthquake on the Revere-Dellwood-Wilson fault (*Cassidy and Rogers, 1995*).

2.2.2 Slip Vectors

Earthquake slip vector azimuths describe relative plate motion directions and are a key to understanding the region's current tectonics. We derived the slip vectors from the fault

Table 2.1. Regional Moment-Tensor Solutions.

Date	Lat (°N)	Lon (°W)	S/D/R (°)	M_O Nm Ex	M_W	CD (km)	DC (%)	CO	SV (°)	SO
9401030126	49.583	127.042	254/40/332	2.83 17	5.6	20	68	28	95	9
9402120704	49.102	129.350	131/82/157	4.02 17	5.7	6	26	20	315	8
9404122114	50.302	130.190	324/84/211	9.43 15	4.6	10	47	17	320	5
9404270030	48.677	129.145 •	134/63/168	1.54 16	4.8	8	9	18	320	8
9407150502	50.472	130.065	136/86/165	1.50 16	4.8	10	72	14	317	4
9408211305	50.398	130.430 •	140/86/166	4.80 16	5.1	12	53	18	321	4
9411021352	50.515	130.286 •	141/84/166	2.89 15	4.3	12	91	14	323	4
9411200122	49.180	125.535 •	301/65/130	1.92 15	4.2	60	96	12		12
9501090650	51.045	130.737	335/63/187	1.20 16	4.7	4	87	14	332	3
9501160701	49.971	130.096 •	142/85/157	3.85 15	4.4	15	43	8	324	5
9501170813	50.026	130.120 •	148/62/168	6.76 15	4.5	6	43	13	334	5
9501171442	50.004	130.188 •	151/58/174	4.94 16	5.1	6	85	15	334	5
9503081630	50.503	129.965	139/84/167	1.53 16	4.8	12	76	14	320	4
9504230929	50.457	130.219 •	132/87/169	4.50 15	4.4	12	92	8	313	4
9505310338	50.931	130.683	146/79/168	5.89 16	5.2	12	41	17	328	3
9506212024	50.919	130.747	158/61/193	1.45 17	5.4	6	69	15	332	3
9509122244	51.143	131.200	333/86/216	7.92 16	5.2	9	53	14	330	3
9509130759	51.312	130.900	148/90/155	1.08 17	5.3	9	71	13	328	3
9509131119	51.092	131.034 •	148/87/151	1.50 16	4.8	9	62	13	330	3
9510150129	48.850	128.601 •	310/79/214	4.82 15	4.4	9	19	13	303	8
9510311940	50.617	130.456 •	146/83/165	5.04 15	4.4	12	72	13	328	4
9511121305	48.838	129.179 •	130/67/166	1.53 16	4.8	9	13	17	316	8
9512010329	50.363	130.038 •	135/77/156	4.14 15	4.4	9	78	18	321	4
9601031312	49.473	130.242	134/84/169	7.88 16	5.2	6	72	17	315	7
9601281130	48.945	129.276 •	135/80/161	7.72 15	4.6	6	21	18	318	8
9603102112	50.573	130.436 •	143/85/169	1.21 16	4.7	12	78	26	324	4
9603162318	50.690	129.880	324/86/194	6.86 16	5.2	12	91	28	323	4
9603180801	49.791	127.103	246/61/343	4.12 16	5.0	15	78	37	74	9
9604231516	48.983	128.233 •	215/62/0	3.88 15	4.4	9	48	22	35	9
9608160341	51.097	130.645	155/88/170	4.90 16	5.1	4	82	33	335	3
9608160954	51.150	130.670 •	158/83/176	1.37 16	4.7	4	85	28	338	3
9608202241	50.512	130.277 •	323/73/192	1.06 15	4.0	9	86	16	319	4
9608230913	47.727	129.261 *	10/62/270	1.66 16	4.8	9	68	39	100	11
9609092228	49.011	128.833 •	115/75/188	1.89 15	4.2	6	24	16	293	8
9610062013	48.965	128.208	41/86/335	2.40 18	6.2	4	81	30	43	9
9610062029	48.863	128.144 •	42/88/337	1.95 16	4.8	4	56	19	43	9
9610062043	48.792	128.250 •	227/80/12	1.75 16	4.8	4	62	29	45	9
9610070204	48.815	128.157 •	246/80/25	6.55 15	4.5	4	40	38	61	9
9610070737	48.831	128.324 •	23/88/341	5.90 15	4.5	4	53	25	24	9
9610071018	48.944	128.259 •	57/90/347	4.39 15	4.4	4	86	29	57	9
9610071836	48.920	128.113 •	189/68/349	2.07 16	4.8	6	96	33	19	9
9610090712	49.581	129.977	147/75/153	5.77 17	5.8	6	46	32	335	7
9610090952	49.546	129.920 •	128/73/168	3.38 15	4.3	9	82	20	312	7
9610131133	48.899	128.164 •	29/86/342	2.67 15	4.3	6	9	28	30	9
9610142304	48.841	128.203 •	31/83/332	5.82 15	4.5	4	29	24	35	9
9611060655	50.454	130.213 •	323/69/199	4.42 15	4.4	9	87	14	316	4
9611210124	49.579	128.786 •	316/88/203	5.19 15	4.4	6	61	27	315	10
9611210130	49.583	128.813 •	304/79/204	1.79 15	4.1	6	39	20	299	10

Table 2.1. Continued.

Date	Lat (°N)	Lon (°W)	S/D/R (°)	M_O Nm Ex	M_W	CD (km)	DC (%)	CO	SV (°)	SO
9612241240	51.867	131.715 •	157/79/159	5.78 15	4.5	15	43	13	341	2
9702051927	51.615	131.432	159/87/184	3.41 16	5.0	6	63	20	339	2
9702051929	51.543	131.474	159/87/182	8.69 16	5.3	6	87	20	339	2
9703290545	50.475	130.226 •	324/77/189	3.85 15	4.4	9	84	17	322	4
9703300650	50.485	130.221 •	322/84/207	3.61 15	4.3	6	72	19	319	4
9704132025	51.388	131.224	330/82/197	1.45 16	4.7	9	96	25	328	3
9707100649	49.231	127.881 •	20/75/334	3.47 15	4.3	6	47	22	27	9
9708160623	48.848	129.196 •	114/65/177	7.69 15	4.6	12	79	19	295	8
9709200439	50.892	130.298	56/76/282	8.79 16	5.3	4	69	37	325	3
9709200709	50.754	130.523	61/79/284	1.37 17	5.4	4	61	37	331	3
9710041515	48.057	129.022 *	120/87/232	5.53 15	4.5	4	60	27	115	11
9710210810	50.412	130.169 •	320/82/203	8.40 15	4.6	9	95	26	317	4
9712200422	50.447	130.342 •	141/89/164	9.48 15	4.6	9	95	15	321	4
9802081911	50.499	130.287 •	323/79/197	4.80 15	4.4	9	81	23	320	4
9802140545	50.845	130.505 •	156/66/199	4.49 15	4.4	4	52	22	328	3
9802140619	50.855	130.511 •	154/51/179	5.03 15	4.4	4	60	18	335	3
9802181846	49.543	129.858 •	131/80/160	1.02 16	4.6	12	57	21	315	7
9806122024	48.892	129.032 •	122/83/170	5.67 15	4.5	9	68	17	304	8
9806252251	50.085	130.269	144/81/160	1.21 17	5.4	9	35	27	328	5
9806271020	49.630	127.160 •	250/66/337	9.76 14	4.0	24	88	23	80	9
9807100305	50.548	130.328 •	146/83/199	1.14 15	4.0	9	82	20	324	4
9807140105	48.728	129.144 •	127/74/175	1.05 16	4.7	6	54	24	308	8
9807140149	48.773	129.009 •	128/59/179	1.04 15	4.0	6	41	18	309	8
9807140227	48.773	129.015 •	127/75/169	4.84 15	4.4	6	36	22	310	8
9807150030	47.821	129.285 *	5/57/261	1.17 16	4.7	6	72	33	103	11
9807310740	51.362	130.782 •	158/71/177	7.72 15	4.6	6	96	23	339	3
9807310818	51.341	130.798 •	153/79/178	1.30 15	4.0	6	63	22	333	3
9808060243	52.126	131.664 •	312/37/110	5.04 15	4.4	15	32	20	18	1
9808061811	48.789	129.223 •	116/70/172	8.03 15	4.6	12	72	20	299	8
9808061817	48.885	129.349 •	119/68/173	1.89 16	4.8	9	39	23	302	8
9808161925	50.009	130.245 •	144/61/170	2.14 15	4.2	9	71	21	329	5
9808190439	50.386	130.338 •	321/79/191	2.37 16	4.9	9	93	27	319	4
9808301133	50.969	130.658	160/50/181	1.92 18	6.2	4	61	34	339	3
9809010743	50.901	130.710 •	327/84/180	2.34 15	4.2	9	80	19	327	3
9809010919	49.143	127.775 •	49/78/323	3.92 15	4.4	6	32	31	58	9
9809011812	50.732	130.584 •	156/63/189	1.01 16	4.6	6	43	24	332	4

Date: year month day hour minute. Lat, Lon: relocated latitude and longitude (unless indicated by • or *). •: located by Pacific Geoscience Centre, Sidney, BC. *: located by NOAA-PMEL, Newport, OR. S/D/R: strike, dip and rake. M_O: seismic moment. M_W: moment magnitude. CD: centroid depth. DC: double couple percentage. DC = (1-2ε)x100 [%], ε = |smallest| / |largest| moment-tensor eigenvalue. CO: number of components (vertical, radial and transverse) used. SV: slip-vector azimuth. SO: source region. 1: Queen Charlotte Islands, 2: NW of TW seamounts, 3: TW seamounts to Dellwood knolls, 4: Dellwood knolls to Explorer rift, 5: Explorer rift, 6: Explorer deep, 7: north of western Sovanco, 8: eastern Sovanco, 9: Nootka transform, 10: inside Explorer plate, 11: Juan de Fuca ridge, 12: Juan de Fuca-North America subduction zone.

Table 2.2. Harvard Centroid Moment-Tensor Solutions.

Date	Lat (°N)	Lon (°W)	S/D/R (°)	M_O Nm Ex	M_W	CD (km)	DC (%)	SV (°)	SO	
7602231514	51.452	130.656	355/80/191	1.14 18	6.0	23	82	353	1	
7612202033	48.766	129.405	127/89/181	1.20 19	6.7	15*	90	307	8	
7806111455	49.156	129.691	315/90/180*	3.37 18	6.3	11	76	315	8	
7807110255	52.647	132.236	296/28/79	1.34 17	5.4	15*	98	26	1	
7903130951	49.770	130.177	330/90/180*	1.63 17	5.4	10	92	330	5	
7903131200	49.802	130.027	315/90/180*	3.94 17	5.7	10	98	315	5	
7906211703	51.107	130.973	323/88/171	2.23 17	5.5	15*	72	323	3	
8005162234	49.593	128.191	300/90/180*	1.24 17	5.4	15*	86	300	10	
8010020342	50.115	130.394	345/90/180*	2.23 17	5.5	15*	46	345	5	
8012171621	49.417	129.888	326/90/180*	1.40 19	6.7	10	80	326	7	
8205151848	50.178	130.438	331/90/180*	5.80 17	5.8	10	96	331	5	
8406242133	50.916	130.914	160/80/188	6.12 17	5.8	10	88	339	3	
8408120024	50.086	130.258	142/76/181	1.10 17	5.3	10	50	321	5	
8805261901	48.886	128.765	116/88/178	7.59 16	5.2	15*	52	296	8	
8807191054	50.391	130.234	167/87/175	2.98 17	5.6	15*	66	347	4	
8811270036	50.614	130.470	319/41/178	3.24 17	5.6	15*	26	321	4	
9002030954	50.834	130.542	338/90/180*	2.01 17	5.5	15*	52	388	3	
9002161328	49.033	127.972	208/85/12	1.41 17	5.4	15*	98	27	9	
9107170712	50.692	130.636	329/80/176	2.19 17	5.5	15*	72	330	4	
9201021640	48.602	129.610	315/90/174	1.30 18	6.0	23	76	315	8	
9201130608	49.060	129.212	306/75/203	1.28 17	5.4	15*	64	300	8	
9204061354	50.55	130.46	331/73/191	1.19 19	6.7	15*	90	328	4	
9204061516	50.490	130.318	166/76/181	1.02 18	6.0	15*	72	346	4	
9204070042	50.663	131.116	354/90/180*	8.24 16	5.2	15*	82	354	13	
9204230540	51.341	131.108	327/52/180	3.14 17	5.6	15*	50	327	3	
9308030719	51.157	130.745	355/60/194	1.22 18	6.0	15*	100	347	3	
9401030126	49.583	127.042	251/41/334	2.89 17	5.6	21	92	91	9	•
9506212024	50.919	130.747	161/90/175	1.51 17	5.4	15*	64	341	3	•
9610062013	48.965	128.208	46/86/8	2.21 18	6.2	15*	72	45	9	•
9610090712	49.581	129.977	332/72/184	5.22 17	5.8	15*	100	331	7	•
9702051929	51.543	131.474	350/75/200	7.36 16	5.2	15*	85	345	2	•
9709200709	50.754	130.523	347/63/189	7.63 16	5.2	15*	31	342	3	•
9806252251	50.085	130.269	328/90/180*	9.60 16	5.3	15*	68	328	5	•
9808301133	50.969	130.658	346/82/180	1.45 18	6.1	15*	83	346	3	•

Date: year month day hour minute. Lat, Lon: relocated latitude and longitude. Source information is taken from Dziewonski et al. (1994) and related sources. S/D/R: strike, dip and rake; *: constrained $M_{XZ} = M_{YZ} = 0$. M_O: seismic moment. M_W: moment magnitude. CD: centroid depth; *: constrained. DC: double couple percentage. SV: slip-vector azimuth. SO: source region. 1: Queen Charlotte Islands, 2: NW of TW seamounts, 3: TW seamounts to Dellwood knolls, 4: Dellwood knolls to Explorer rift, 5: Explorer rift, 6: Explorer deep, 7: north of western Sovanco, 8: eastern Sovanco, 9: Nootka transform, 10: inside Explorer plate, 11: Juan de Fuca ridge, 12: Juan de Fuca-North America subduction zone, 13 Pacific intra-plate. •: RMT exists (see Table 2.1).

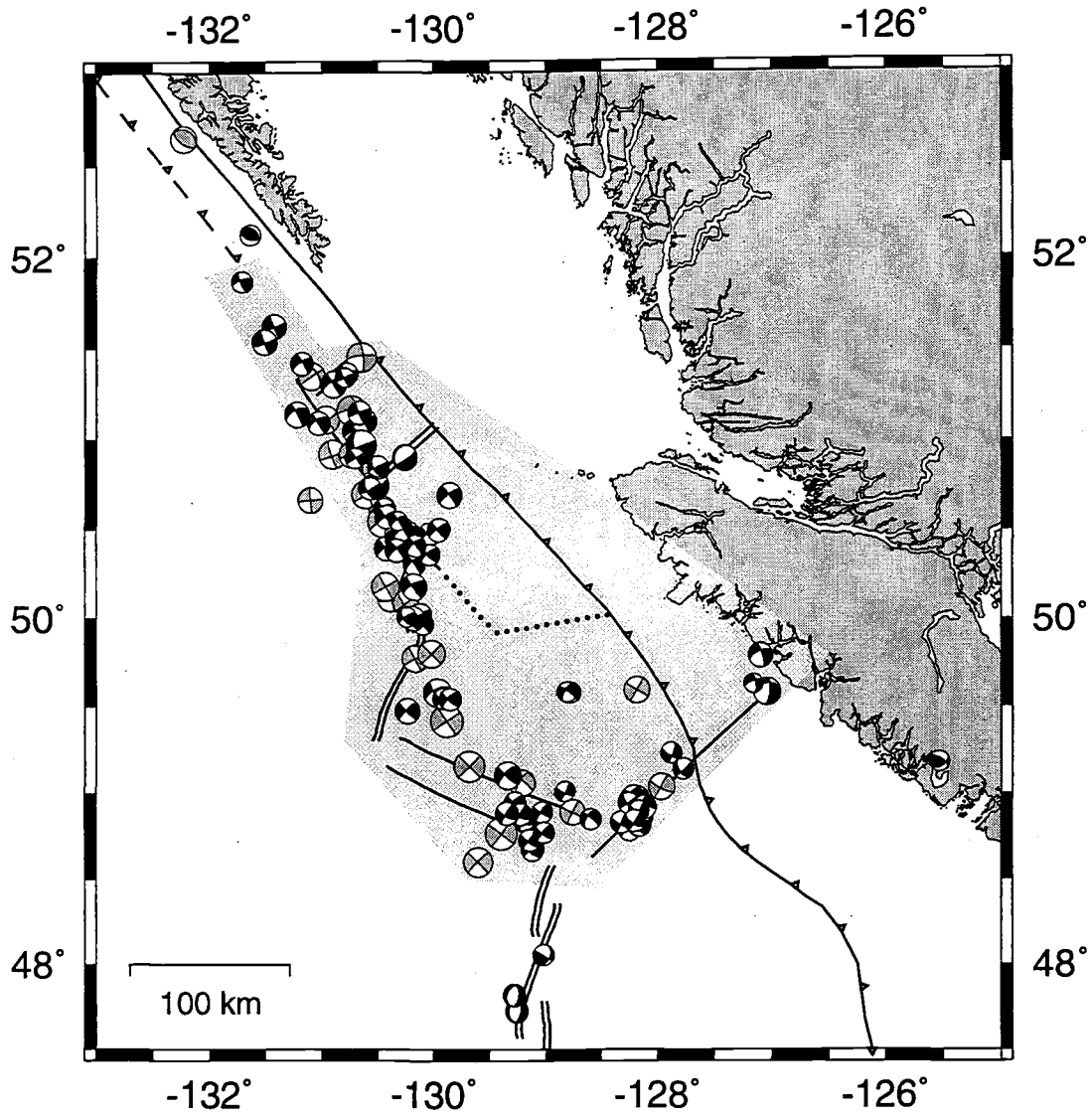

Figure 2.3. Map of fault plane solutions (lower-hemisphere projections, size proportional to Mw). Black: relocated regional moment tensor (RMT) solutions (epicenter uncertainties ≤12 km); dark gray: RMT solutions (relocation uncertainties >12 km) on their Pacific Geoscience Centre locations, except three Juan de Fuca ridge events located by NOAA; light gray: relocated Harvard centroid moment-tensor (CMT) solutions. All events are listed in Tables 2.1 and 2.2.

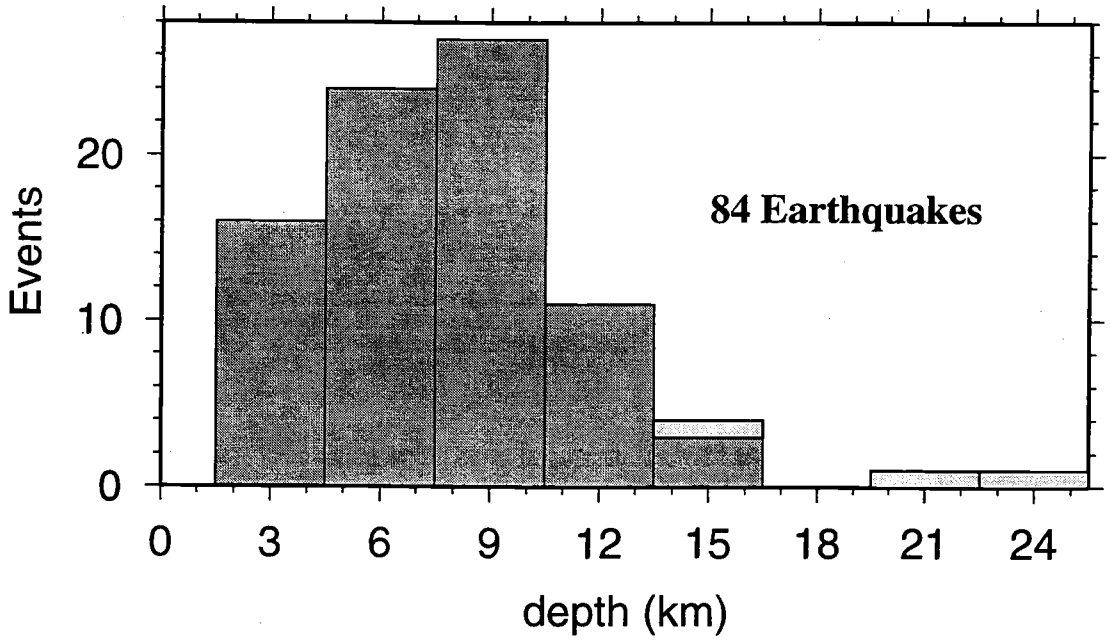

Figure 2.4. Earthquake centroid depths of the RMT solutions. The lightly shaded areas represent three events near Nootka Island where Juan de Fuca and presumably Explorer plate subduct beneath North America; deeper earthquakes in this region are thus expected. Not shown is a 60 km deep event beneath central Vancouver Island.

plane solutions by choosing the nodal plane as the fault plane that agrees best with local geology. For the strike-slip earthquakes in the Explorer region, slip vector azimuth uncertainties depend mainly on uncertainties in strike, which is the best resolved source parameter (±5°). The slip vector azimuths, with uncertainties of only about 5°, define the current plate motion directions tightly.

Figure 2.5 shows the distribution of slip vector azimuths along Explorer region's boundary with the Pacific plate (gray shaded area), their average (line *AVE*), and two predicted plate motion directions based on current models (lines *PAC-NAM* and *PAC-EXP*). If Explorer region were cut by a Pacific-North America transform fault (*Barr and Chase, 1974; Rohr and Furlong, 1995*), the slip vector azimuths would follow Pacific-North American relative motion (340° azimuth, line *PAC-NAM*). If Explorer region were moving in Riddihough's (*1984*) Explorer plate sense, the slip vector azimuths would follow Pacific-Explorer relative motion (310° azimuth, line *PAC-EXP*). However, most observations and their average (line *AVE*) point in a 325° direction which is incompatible with either plate model.

Splitting the Explorer-Pacific boundary in five segments shows that the slip vector azimuths (thin solid lines, Figure 2.6) rotate counter-clockwise from a north-northwest direction in the north to a northwest direction in the south. For each segment, the average slip vector azimuth (solid line) corresponds well with the observed fault trend (dashed line), but is incompatible with Pacific-North America motion (gray *PAC-NAM* line) or Riddihough's (*1984*) predicted Explorer-Pacific plate motion (gray *PAC-EXP* line). This figure will be discussed in more detail later in the text.

2.2.3 Relocations

Routine earthquake locations in the Explorer region (Figure 2.2) are widely scattered and often far from morphologic features usually associated with offshore plate boundaries. This observation was used to argue that the bathymetric features are inactive remnants, no longer representing active plate boundaries, and that the earthquakes define a new Pacific-North America transform plate boundary (*Barr and Chase, 1974; Rohr and Furlong, 1995*). However, ocean bottom seismometer studies and small-earthquake ($3 \leq M \leq 5$) relocations reveal narrowly distributed earthquakes closely following bathymetric features, indicating that routine land-based epicenter locations are systematically mislocated by tens

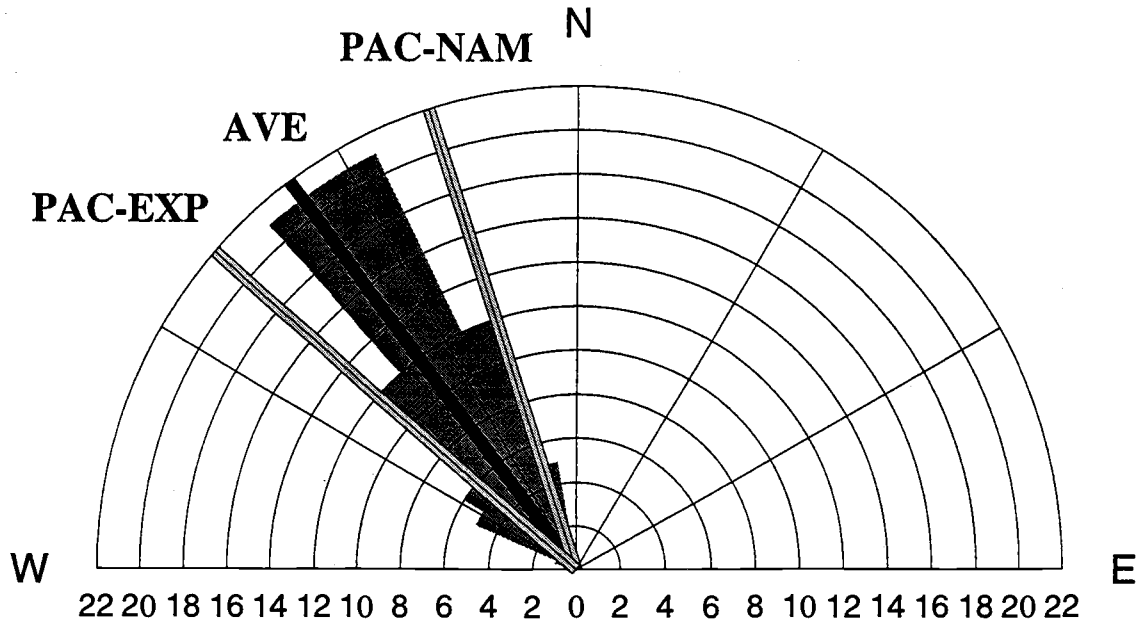

Figure 2.5. Earthquake slip vector azimuths along the Explorer-Pacific boundary (regions 2-8 in Tables 2.1 and 2.2). The observed azimuths (gray shaded area) are binned in 8° intervals. Semi-circles show the number of events per bin. The observed azimuths and their average of 323° (labeled AVE) are incompatible with Pacific-North America motion (340°, labeled PAC-NAM) and Riddihough's (*1984*) Pacific-Explorer motion (310°, labeled PAC-EXP).

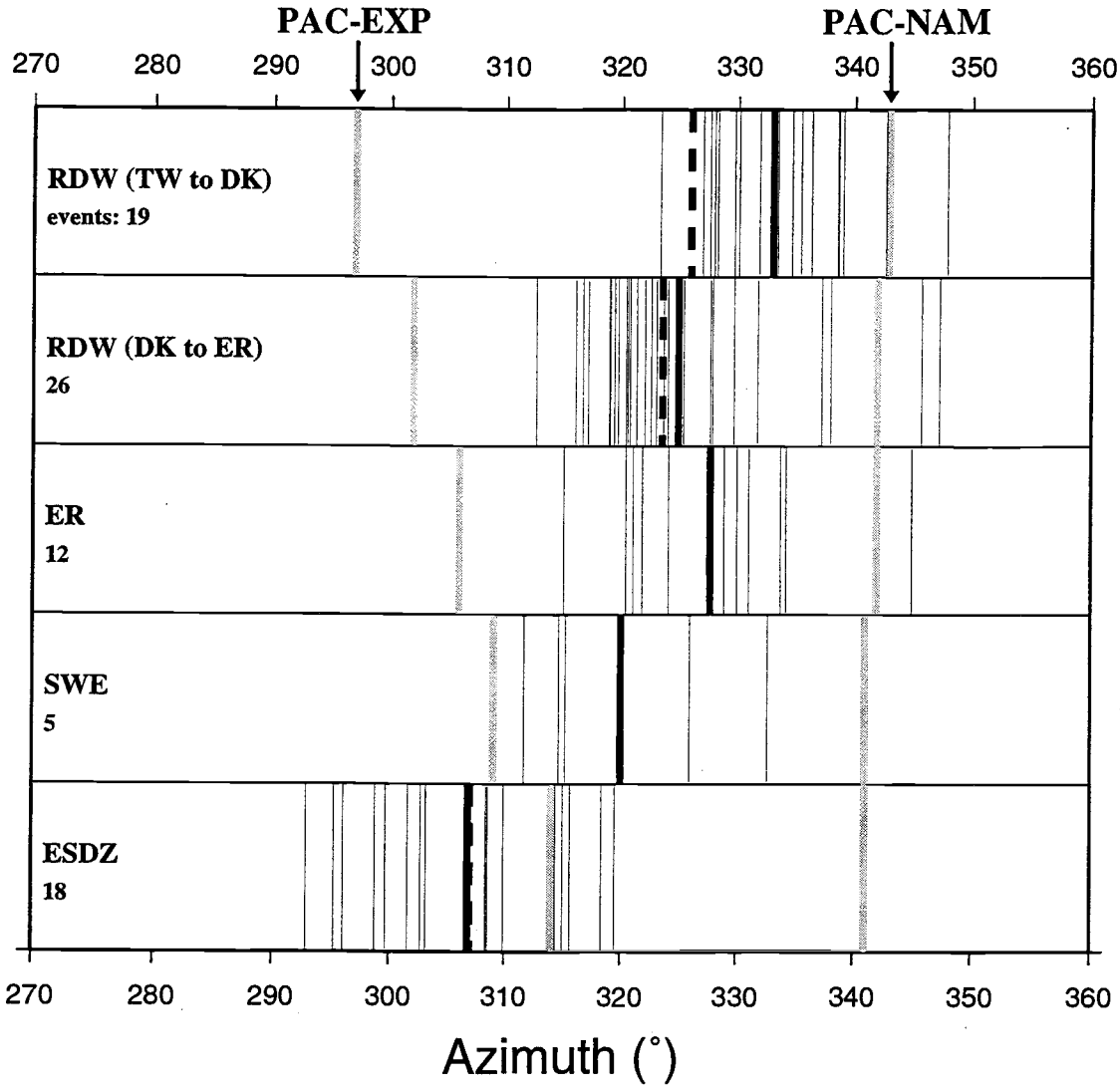

Figure 2.6. Slip vector azimuth distribution along five Explorer-Pacific segments. Panel 1: Revere-Dellwood-Wilson (RDW) fault from Tuzo Wilson (TW) seamounts to Dellwood Knolls (DK) (region 3 in Tables 2.1 and 2.2). Panel 2: RDW fault between DK and Explorer Rift (ER) (region 4). Panel 3: transform faults in ER section (region 5). Panel 4: Southwest Explorer transform fault(s) north of western Sovanco Fracture zone (SWE) (region 7). Panel 5: eastern Sovanco Fracture zone (ESDZ) (region 8). For each panel, thin solid lines are observed earthquake slip vector azimuths, and the thick solid line is their average; the dashed line shows the active fault trend (from bathymetry); the gray lines represent predicted Pacific-North America (PAC-NAM, from NUVEL-1 [*DeMets et al., 1990*]) and Riddihough's (*1984*) Pacific-Explorer (PAC-EXP) motion directions. Note the good correspondence between average slip vector azimuth and bathymetry for each panel, the discrepancy between observed azimuths, and both PAC-NAM and PAC-EXP predicted motion.

of kilometers to the northeast (*Hyndman and Rogers, 1981*; *Wahlström and Rogers, 1992*).

The locations of larger, tectonically more significant earthquakes-- a key to deciphering current plate boundaries-- had not been well determined. We thus relocated larger earthquakes in the Explorer region with the joint epicenter determination (JED) technique (*Douglas, 1967; Dewey, 1972*).

We simultaneously relocated 164 earthquakes using P-wave arrival time data from the International Seismological Centre (ISC), available from 1964 until 1987, and from the US Geological Survey since then. Only events with at least 30 teleseismic (event-station distance $18^\circ \leq \Delta \leq 110^\circ$) arrival time picks and events with a CMT or RMT solution (even if less than 30 picks were available) were included. The 30 P-wave pick criterion is essentially equivalent to relocating all $M > 5.0$ earthquakes. Because of the poor hypocenter depth resolution offered by teleseismic data, we fixed all depths to 10 km except the deeper 940103 event near Nootka Island, whose depth is well constrained by the Pacific Geoscience Centre (PGC) location and our RMT solution (Table 2.1).

To stabilize the JED inversion, we picked an independently well located earthquake, fixed its location, and relocated all other earthquakes relative to it. We chose the $M_W = 6.7$, 920406 earthquake on the Revere-Dellwood-Wilson fault because it was carefully located (*Cassidy and Rogers, 1995*) and has the most P arrival time picks of all events in our study. We tried other well located earthquakes as reference events (such as the 940103 earthquake near Nootka Island located by the PGC with local network data) and obtained very similar relocations.

The relocations (Figure 2.7), shown as open circles with thin lines pointing to the original epicenters, are on average about 25 km southwest of their original locations. This average difference is consistent with the reference event's epicenter (star, Figure 2.7) (*Cassidy and Rogers, 1995*) about 30 km southwest of its Preliminary Determination of Epicenters (PDE) location. Relocation moved the epicenters from inside the Explorer region towards the bathymetric features; more detailed inspection shows relocation also adjusted relative event locations, reducing the epicenter scatter.

The 113 well relocated epicenters, for which latitude and longitude uncertainties are less than 12 km at the 95% confidence level, reveal Explorer region's plate boundaries (Figure 2.8). We are confident in the overall location quality because seismicity and bathymetry correspond well. Particularly striking are the locations along Explorer Rift, which follow the bathymetry very closely. Also, PGC's earthquake locations close to Nootka Island (well constrained by local seismic stations on Vancouver Island) generally fall inside the confidence limits. Another indicator for good location quality comes from earthquakes near

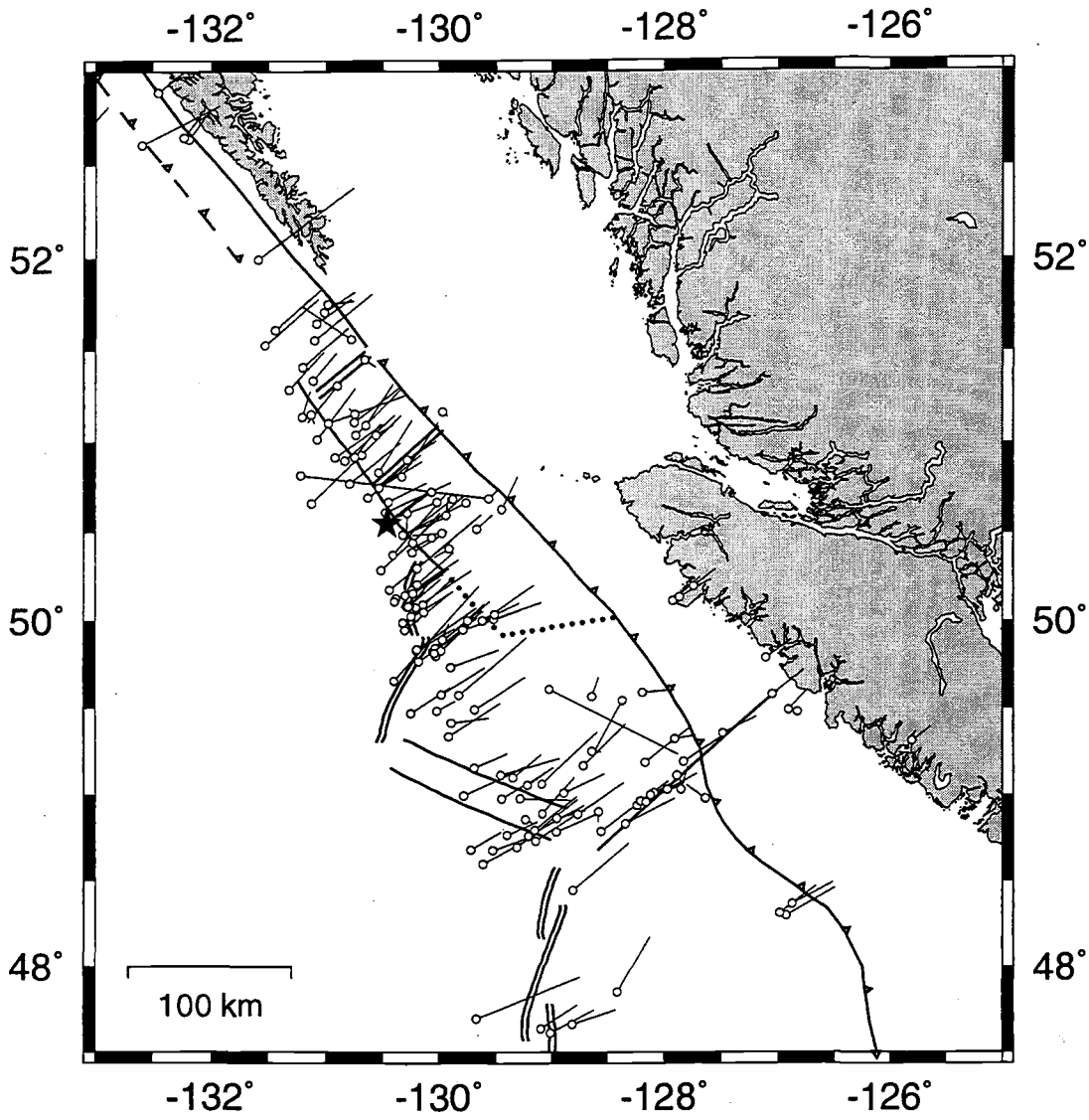

Figure 2.7. Relocation results. Open circles are relocated epicenters; the thin lines point to the original epicenters. Dark shaded star: reference event location (*Cassidy and Rogers, 1995*) with thick gray line pointing to its PDE location.

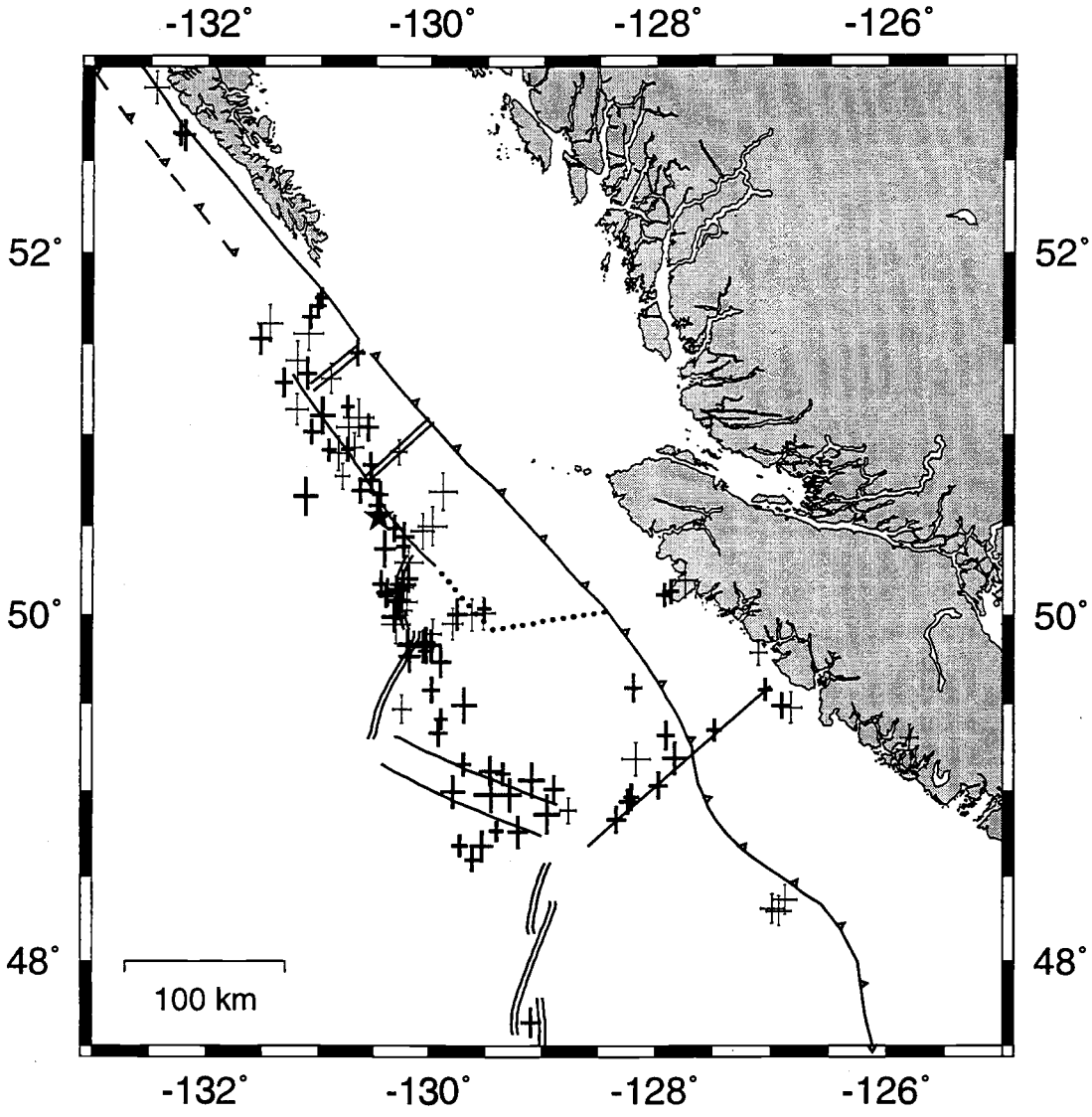

Figure 2.8. Uncertainty bars of 113 well-relocated earthquakes (events with latitude and longitude uncertainties ≤12 km at 95% confidence level). Thick bars mark $M \geq 5$ earthquakes. Dark shaded star: reference event location (*Cassidy and Rogers, 1995*).

Brooks peninsula. There, the relocations agree with locally recorded aftershock epicenters (*Spindler et al., 1997*). The remaining epicenter scatter in Figure 2.8 (along the northwest part of Revere-Dellwood-Wilson fault and in the eastern Sovanco fracture zone) and the deviation from bathymetric features (north of western Sovanco fracture zone) appear to be real features.

The relocations form a band roughly parallel to the Pacific-North America plate motion direction seemingly supporting the Pacific-North America transform hypothesis (*Barr and Chase, 1974; Rohr and Furlong, 1995*). However, the slip vector azimuths (Figure 2.6) are less northerly than the Pacific-North America motion direction. This suggests that several right-stepping transform faults, each parallel to the slip vector azimuths, are active with the overall seismicity apparently following a more northerly trend.

2.3 Discussion of Individual Segments

2.3.1 Queen Charlotte Transform Fault

The right-lateral Queen Charlotte transform fault forms the Pacific-North America plate boundary north of Explorer region. North of the Queen Charlotte Islands, the fault is parallel to the plate motion direction (NUVEL-1 [*DeMets et al., 1990*]), and motion is purely strike-slip (Figure 2.1). A counter-clockwise fault bend at the Queen Charlotte Islands (Figure 2.1) results in a 20° difference between fault trend and plate motion direction, requiring oblique Pacific-North America plate convergence along the southern Queen Charlotte fault.

Slip-partitioning into strike-slip motion along, and convergent motion perpendicular to, the southern Queen Charlotte fault has been suggested to account for the oblique plate motions (*Hyndman et al., 1981; Scheidhauer, 1997*). The Queen Charlotte fault, which runs close to the coast off Queen Charlotte Islands (Figure 2.8, also *Hyndman and Ellis, 1981; Bérube et al., 1989; Scheidhauer, 1997*), is separated by a 20-30 km wide terrace from the Pacific plate. This terrace is decoupled from either of the main plates: the Pacific plate subducts at the terrace's oceanward side and the terrace translates northwest relative to North America along Queen Charlotte fault (*Hyndman et al., 1981; Scheidhauer, 1997*). The three source mechanisms along the fault's southern part, two thrust and one strike-slip

(Figure 2.3), are consistent with slip-partitioning. Additional support for Pacific plate underthrusting comes from numerous morphological, seismic, and potential field data and flexural modeling (*Chase et al., 1975; Hyndman and Ellis, 1981; Hyndman et al., 1982; Riddihough, 1982; Yorath and Hyndman, 1983; Horn et al., 1984; Dehler and Clowes, 1988; Bérubé et al., 1989; Mackie et al., 1989; Sweeney and Seemann, 1991*). Relatively high seismicity on and east of Graham Island (*Bérubé et al., 1989; Bird and Rogers, 1996*) and compression in the Queen Charlotte basin (*Rohr and Dietrich, 1992*) indicate that some Pacific-North America deformation also occurs within the North American plate considerably east of the Queen Charlotte fault.

Relocations (Figure 2.9) and side-scan images (*Carbotte et al., 1989*) show that the Queen Charlotte fault terminates near the Tuzo Wilson seamounts.

2.3.2 Revere-Dellwood-Wilson Transform Fault

The seismically very active Revere-Dellwood-Wilson transform fault (Figure 2.9) forms the right-lateral boundary between the Pacific plate and Explorer region. The fault, visible on side-scan images from the Tuzo Wilson seamounts to Explorer Deep (*Carbotte et al., 1989; Davis and Currie, 1993*), is almost parallel to the southern Queen Charlotte fault and thus cannot accommodate the entire, more northerly oriented, Pacific-North America motion. The remaining convergent motion requires either slip-partitioning comparable to the setting along southern Queen Charlotte fault-- the fault is then a Queen Charlotte fault extension and forms the Pacific-North America boundary; or the Pacific and North American plates are separated by the Explorer plate-- the fault is then a Pacific-Explorer transform boundary and convergence occurs between the Explorer and North American plates. Compressional bathymetric features, similar to the terrace oceanward of southern Queen Charlotte fault, do not exist southwest of Revere-Dellwood-Wilson fault (*Carbotte et al., 1989*), thus favoring Explorer-North America convergence northeast of the fault.

Seismicity along Revere-Dellwood-Wilson fault extends from northwest of the Tuzo Wilson seamounts to its intersection with Explorer Rift (Figure 2.9). Strike-slip events northwest of the seamounts indicate the active fault, although not visible on side-scan images, extends past the seamounts. The scattered earthquake distribution between the seamounts and the Dellwood Knolls, also noted by Wahlström and Rogers (*1992*), indicates that several faults are active simultaneously. The slip vector azimuths (average:

Figure 2.9. Close-up of the Pacific-Explorer boundary. Plotted are fault plane solutions (gray scheme as in Figure 2.3) and well-relocated earthquake epicenters on top of bathymetry. Relocations labeled by solid triangles are pre-1964, historical earthquakes (see Appendix B). Solid lines mark plate boundaries inferred from bathymetry and side-scan data (Davis and Currie, 1993); dashed were inactive. QCF: Queen Charlotte fault, TW: Tuzo Wilson seamounts, RDW: Revere-Dellwood-Wilson fault, DK: Dellwood Knolls, PRR: Paul Revere ridge, ER: Explorer Rift, ED: Explorer Deep, SER: Southern Explorer ridge, ESM: Explorer seamount, SWE: Southwest Explorer fault(s), WSOV: western Sovanco Fracture zone, ESDZ: Eastern Sovanco Deformation Zone, HSC: Heck seamount chain, WV: active west valley of Juan de Fuca ridge, MV: inactive middle valley.

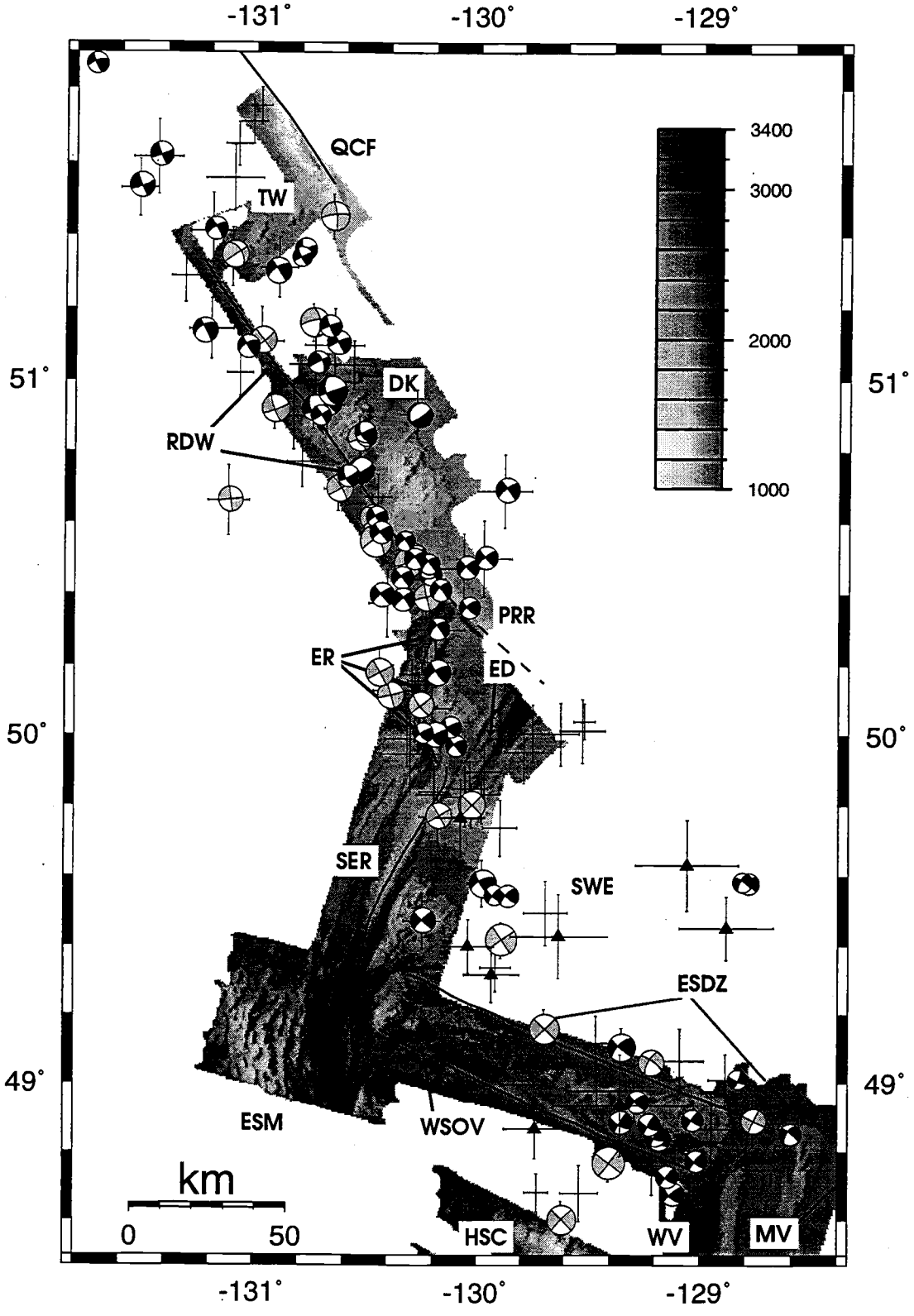
-131°
-130°
-129°
51°
50°
49°
QCF
TW
DK
RDW
PRR
ER
ED
SER
SWE
ESDZ
ESM
WSOV
HSC
WV
MV
3400
3000
2000
1000
km
0
50

332°, Figure 2.6) of the strike-slip events agree with the linear, 326°-trending Revere-Dellwood-Wilson fault trace (*Carbotte et al., 1989*), indicating that the active faults in this zone of scattered seismicity are roughly parallel to the Revere-Dellwood-Wilson fault. Seismicity tightly follows the Revere-Dellwood-Wilson fault along the southeast side of the Dellwood Knolls to the faults' intersection with Explorer Rift which is consistent with earlier results (*Hyndman and Rogers, 1981; Wahlström and Rogers, 1992; Cassidy and Rogers, 1995*). The source mechanisms, except for two normal faulting events, are strike-slip; and their slip vector azimuths (average: 325°, Figure 2.6) agree very well with the 323° fault trend (*Davis and Currie, 1993*). Seismicity stops abruptly at the faults' intersection with Explorer Rift (Figure 2.9; *Hyndman and Rogers, 1981; Wahlström and Rogers, 1992; Cassidy and Rogers, 1995*), suggesting the fault continuation, visible on side-scan data along the oceanward side of the Paul Revere Ridge to Explorer Deep (*Davis and Currie, 1993*), is inactive.

The slip vector azimuths from earthquakes along the Revere-Dellwood-Wilson fault and the fault's trend are inconsistent with Pacific-North America (about 342°, NUVEL-1) and Riddihough's (*1984*) Pacific-Explorer (about 300°) plate motion directions (Figure 2.6). Slip vector azimuths and fault trend, rather, define the current Explorer-Pacific relative plate motion direction.

The Tuzo Wilson seamounts and the Dellwood Knolls, both young volcanic fields, are considered to be active seafloor spreading centers (*Riddihough et al., 1980; Davis and Riddihough, 1982; Cousens et al., 1985; Carbotte et al., 1989*) or the result of pull-apart tectonism (*Allan et al., 1993; Rohr and Furlong, 1995*). Rohr and Furlong (*1995*) suggested pull-apart activity has migrated from the sediment-covered Dellwood Knolls (*Allan et al., 1993*) north-westward during the last 2 Ma and is now at the sediment-free, zero-radiometric age Tuzo Wilson seamounts (*Cousens et al., 1985; Carbotte et al., 1989; Allan et al., 1993*); in this process, Queen Charlotte fault retreated and Revere-Dellwood-Wilson fault lengthened to the northwest.

Our relocations indicate that seismic activity directly at the Tuzo Wilson seamounts and the Dellwood Knolls is low for moderate $M \geq 4$ earthquakes (Figure 2.9). Two normal faulting earthquakes near the Dellwood Knolls support active extension. Their location relative to each other, and whether they occurred within the Dellwood Knolls or on a small extensional jog of the Revere-Dellwood-Wilson fault, is not clear. Teleseismic relocation (Figure 2.9) places the second event more than 20 km southwest of the first, because P wave arrivals from stations to the northeast (mainly in Europe) are consistently late (0.5-1.5 s) for the second event relative to the first. The events, however, occurred less than 3 hours apart and have almost identical source mechanisms (Table 2.1) suggesting they may

have originated close to each other. This is supported by relative locations using regional arrival time data, which place the epicenters within a few kilometers of each other, and by inspection of seismograms from station BBB to the northeast of the epicenters (see Figure 2.2 for location), which do not show a 2 s S-P travel time difference between the two events as expected if the teleseismic locations were correct. We assume both events occurred next to each other. Their slip vector azimuths (325° and 331°), regardless of the actual locations, are consistent with motion parallel to the Revere-Dellwood-Wilson fault.

Scattered seismicity between the Tuzo Wilson seamounts and the Dellwood Knolls could probably be the result of recent or ongoing pull apart tectonism. A possible scenario is that the lengthening Revere-Dellwood-Wilson fault system tries to connect to the retreating Queen Charlotte fault by distributing transform motion along several parallel fault strands (slip vector azimuths are essentially Revere-Dellwood-Wilson fault parallel [Figure 2.6]). Most motion, though, is concentrated along the Revere-Dellwood-Wilson fault proper since only its fault trace is visible on side scan images (*Carbotte et al., 1989; Davis and Currie, 1993*).

Distributed seismicity between Revere-Dellwood-Wilson fault and Queen Charlotte fault extends past the Tuzo Wilson seamounts (Figure 2.9) indicating that pull-apart tectonism possibly continues to migrate to the northwest. A small volcanic field 30 km northwest of the seamounts (*Carbotte et al., 1989; Allan et al., 1993*), consistent with extension inside a pull-apart basin, and a continuation of Revere-Dellwood-Wilson fault past the seamounts (visible on seismic data for about 50 km [*Carbotte et al., 1989*]) support this interpretation.

Seismicity southeast of the Dellwood Knolls follows the Revere-Dellwood-Wilson fault tightly. This fault segment probably initiated about 2 Ma ago when spreading offshore Brooks peninsula ceased, and Dellwood Knolls' extension began (*Riddihough et al., 1980; Davis and Riddihough, 1982*). The segment is probably older and formed under different conditions than the segment northwest of the Dellwood Knolls; this could explain the difference in earthquake distribution.

2.3.3 Explorer Rift and Explorer Deep

Seismicity follows Explorer Rift's bathymetry closely (Figure 2.9), consistent with results of Wahlström and Rogers' (*1992*). Based on bathymetry, Botros and Johnson

(*1988*) suggested that Explorer Rift consists of three distinct parts: two short Explorer-Pacific spreading segments, almost perpendicular to the Revere-Dellwood-Wilson fault, and a pull-apart basin, connecting the segments with the Southern Explorer Ridge. Strike-slip source mechanisms imply the earthquakes occurred on transform faults connecting the spreading segments or bordering the pull-apart basin. Their slip vector azimuths (average: 328°, Figure 2.6), which agree with averages along Revere-Dellwood-Wilson fault, and the spreading segments' orientation indicate that Explorer Rift and Revere-Dellwood-Wilson fault are both part of the Pacific-Explorer plate boundary.

Several earthquakes (Figure 2.9) and fresh basalts (*Cousens et al., 1984; Michael et al., 1989*) inside Explorer Deep indicate that the former seafloor spreading center, abandoned only 0.3 Ma ago (*Botros and Johnson, 1988*), is not yet entirely dormant. The lack of source mechanisms, however, prohibits clearer tectonic interpretation.

The ridge jump rendered the segment of Revere-Dellwood-Wilson fault between Explorer Rift and Explorer Deep (which is still visible on side-scan images along the southwest side of Paul Revere ridge [*Davis and Currie, 1993*]) inactive. This segment is less northerly oriented than the remainder of Revere-Dellwood-Wilson fault northwest of Explorer Rift. Shifting spreading west to Explorer Rift, thus, stopped oblique motion, which probably had caused Paul Revere ridge uplift during the last 2 Ma (*Kulm et al., 1973*), and simplified Pacific-Explorer interactions.

2.3.4 Southwest Boundary of Explorer Region

Earthquake epicenters in Explorer region's southwest corner, consistent with Wahlström and Rogers (*1992*) results, are located east of Southern Explorer Ridge and north of western Sovanco Fracture zone (Figure 2.9). The source mechanisms are strike-slip (Figure 2.9). Their slip vector azimuths (average: 320°), incompatible with Pacific-North America (341°) and Riddihough's (*1984*) Pacific-Explorer (309°) motion, agree with the slip vector azimuths for events along Revere-Dellwood-Wilson fault and Explorer Rift, and with the Revere-Dellwood-Wilson fault trend (Figure 2.6).

Southern Explorer Ridge and western Sovanco Fracture zone-- plate boundaries according to Riddihough's (*1984*) Explorer plate model-- appear seismically inactive. To confirm that the lack of seismicity along western Sovanco Fracture zone is not an artifact of the relatively short 30-year observation period, we relocated large, older (1918-1963)

earthquakes (Appendix B), which potentially could have occurred in or near the corner region. We found that all well constrained historic earthquakes also occurred outside the corner region (Figure 2.9).

Seismicity and source mechanisms indicate a new Pacific-Explorer transform boundary cutting through Explorer region's southwest corner has formed. In this process, a triangular-shaped area, bordered by Southern Explorer Ridge (south of about 49.7°N), western Sovanco Fracture zone (west of about 129.8°), and the new transform fault(s), has transferred from the Explorer to the Pacific plate. Seismicity along the new boundary, which we refer to as Southwest Explorer transform boundary (Figure 2.9), is spread out indicating that several strike-slip faults could be active. The orientation of the fault(s) roughly parallel to the Revere-Dellwood-Wilson fault is constrained by the source mechanisms. Disrupted magnetic lineations east of Explorer ridge (*Botros and Johnson, 1988; Rohr and Furlong, 1995*), active seafloor and basement cutting faults inside the corner region (*Malacek and Clowes, 1978; Rohr and Furlong, 1996*), and a magma-starved southern end of Explorer ridge (*Michael et al., 1989*) are consistent with cessation of spreading along southern Explorer ridge, deformation along a new transform fault (or faults) and support "capture" of the corner by the Pacific plate.

2.3.5 Eastern Sovanco Fracture Zone

The epicenter distribution, slip vector azimuths and bathymetry along eastern Sovanco Fracture zone are distinct from other segments along the Explorer region-Pacific plate boundary. We refer to this area as the Eastern Sovanco Deformation Zone (ESDZ). Relocated earthquakes within ESDZ are broadly distributed (Figure 2.9; *Wahlström and Rogers, 1992*). The seismically active area includes an anomalous wide fault zone characterized by numerous rhomb-shaped fault bounded blocks (Figure 2.10; *Cowan et al., 1986; Davis and Currie, 1993*) and extends south to the Heck seamount chain. Detailed bathymetry (Figure 2.10) shows that the northwest trending nodal planes of the earthquake fault plane solutions are roughly parallel to the northwest trending fault scarps (307°), whereas the northeast trending fault scarps (55°) and nodal planes are not, suggesting the northwest trending scarps are primarily active. The slip vector azimuths (average: 308°, Figure 2.6) and fault trends are less northerly oriented than those along the Revere-

Figure 2.10. Detailed map of Eastern Sovanco Deformation Zone. Note uplifted faulted blocks. The orientations of the northwest trending bounding faults and earthquake nodal planes agree, whereas northeast trending scarps are more easterly oriented than the northeast trending nodal planes (fault plane solution gray scheme as in Figure 2.3, see Figure 2.9 for event location). Thus, the northwest trending faults are primarily active.

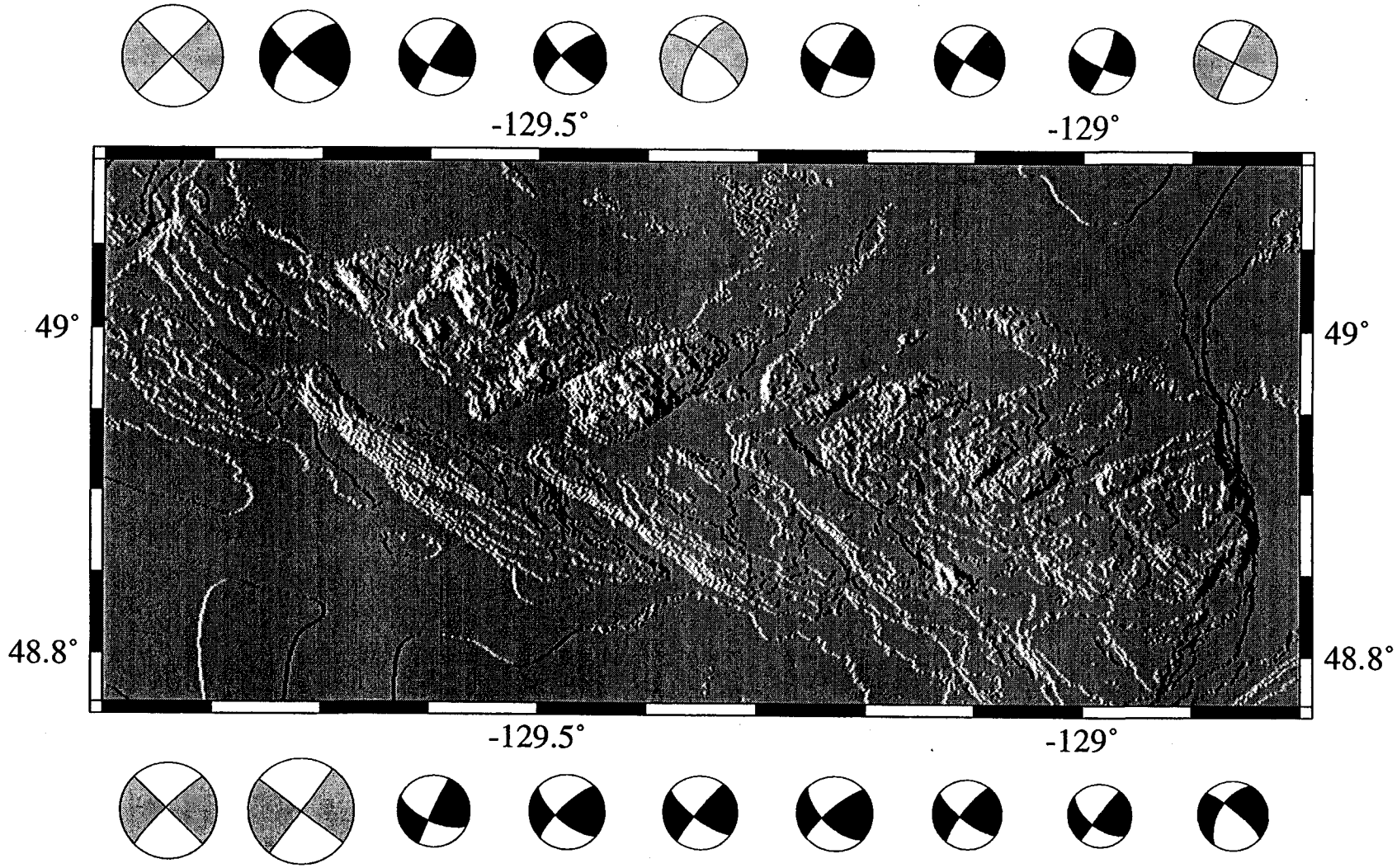
-129.5°
-129°
49°
49°
48.8°
48.8°
-129.5°
-129°

Dellwood-Wilson, Explorer Rift or Southwest Explorer segments (Figure 2.6) indicating that the ESDZ does not move in the same sense as the rest of Explorer plate.

Most earthquakes are relocated in the northern part of the ESDZ (north of about 48.8° N which is characterized by elevated fault bounded blocks). Several events, though, occurred close to the Heck seamount chain, indicating that distributed deformation extends at least south to 48.6° N. Detailed SeaBeam bathymetry is not available, but earlier work (*Barr and Chase, 1974; Davis and Lister, 1977*) shows the area between Heck seamount chain and the elevated blocks is filled with flat laying turbidite sediments. The striped magnetic anomaly pattern on the Pacific plate cannot be traced north of 48.5° N near the Sovanco Fracture zone (*Botros and Johnson, 1988; Wilson, 1993*). Wilson (*1993*) suggested this may be the result of disruption or overprinting of magnetization due to strong shearing in a former position of Sovanco Fracture zone between 48.5° N and 49° N. Earthquake activity suggests deformation is ongoing.

2.3.6 Nootka Fault Zone

The Nootka Fault zone, running from the northern tip of Juan de Fuca ridge to Nootka Island, forms Explorer region's southeast boundary with the Juan de Fuca plate. The narrow band of relocated epicenters (Figure 2.11) contrasts with a broader epicenter distribution reported by Wahlström and Rogers (*1992*). The left-lateral strike-slip source mechanisms (Figure 2.11) indicate transform motion, consistent with the small bathymetric relief across the fault (*Hyndman et al., 1979*).

Seismicity ends near Nootka Island; deeper earthquakes nearby (≥ 15 km, Figure 2.4; *Cassidy et al., 1988*) could reflect continuing left-lateral motion along Nootka fault underneath the North American continental shelf or deformation inside the overriding or subducting plates. The earthquake slip vector azimuths near Nootka Island are almost east-west trending, whereas slip vector azimuths along the southwest part of Nootka fault trend in a northeasterly direction (average azimuth: 37°). If the events had occurred along the same plate boundary (the active part of Nootka fault extends to Nootka Island), the Explorer-Juan de Fuca rotation pole would have to be located very close to, and to the southeast of, Nootka transform. This interpretation implies Nootka fault bends from a north-easterly direction near Juan de Fuca ridge to an east-west direction near Nootka Island. Our relocations, though relatively narrow and consistent with a linear, 50°-55°

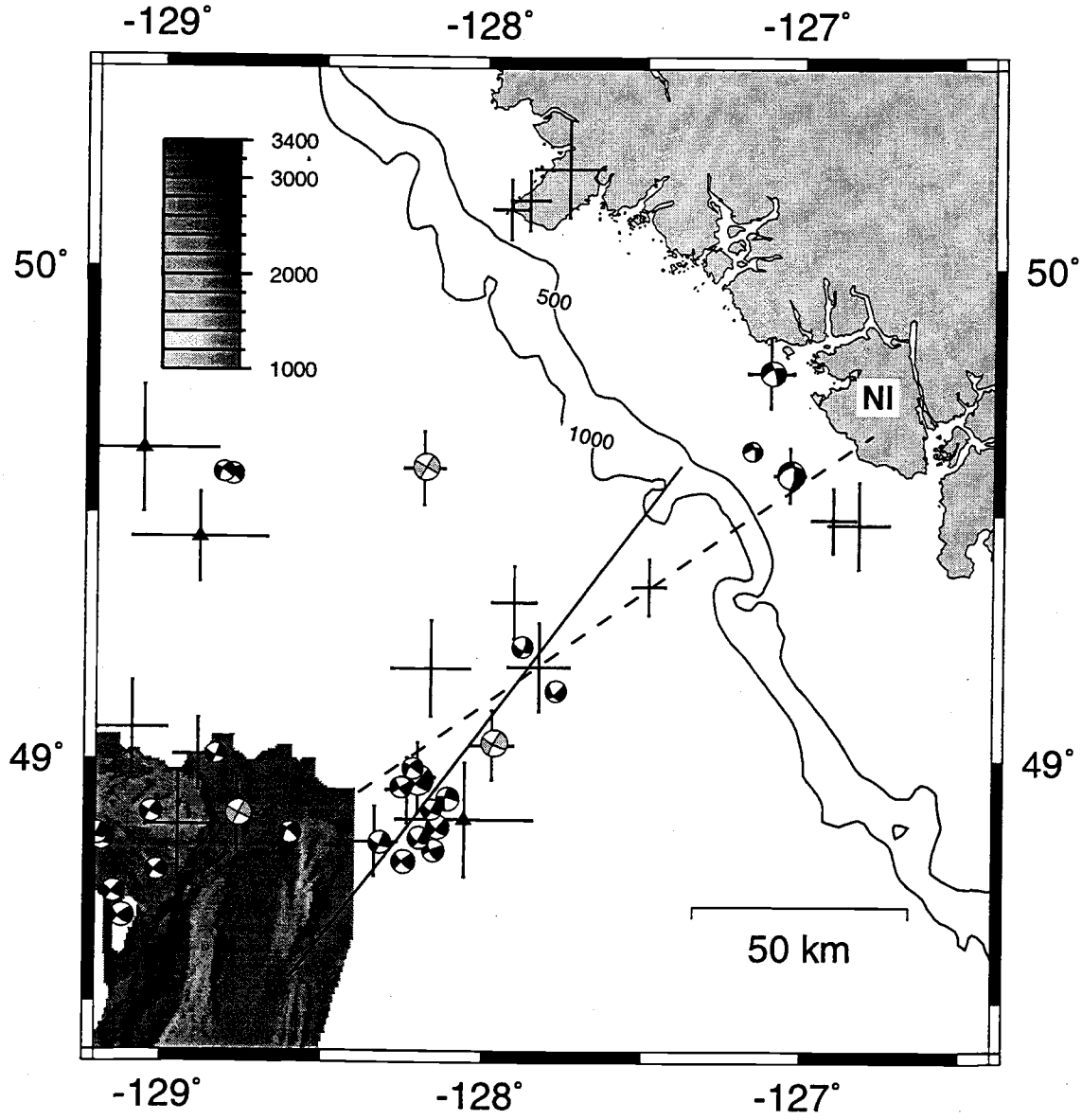

Figure 2.11. Close-up of the Juan de Fuca-Explorer boundary (Nootka fault). Plotted are fault plane solutions (gray scheme as in Figure 2.3) and well-relocated epicenters (triangles mark pre-1964, historical earthquakes, see Appendix B). High-resolution bathymetry is available only near Juan de Fuca ridge; the 500- and 1000 m contour lines (from low-resolution bathymetry) follow the base of the North American continental margin. Least-squares regression of all well-relocated epicenters from Juan de Fuca ridge to Nootka Island results in the dashed line, oriented at an azimuth of 55°. The solid line, which starts at a left-lateral offset of Juan de Fuca ridge and trends in the direction of the average slip vector azimuth (37°, excluding earthquakes beneath Nootka Island), is consistent with the epicenter locations southwest of the continental margin. NI: Nootka Island.

trending Nootka fault (Figure 2.11), do not exclude this possibility. Another possible interpretation is that the earthquakes near Nootka Island did not occur along Nootka fault. Hyndman et al. (*1979*) suggested that a left lateral offset of the ridge east of Juan de Fuca ridge's Middle Valley marks the southern intersection of a broad Nootka fault zone with the Juan de Fuca ridge. A line from this left lateral offset (Figure 2.11), which runs northeast in the direction of the average slip vector azimuth (37°, excluding the events near Nootka Island), encompasses most relocated epicenters along the southwest part of Nootka fault and intersects the coastline north of Nootka Island. A more northerly orientation of Nootka fault is consistent with the trend of the area having been affected by recent faulting (*Hyndman et al., 1979*). If Nootka fault, indeed, trends more northerly, then its active part appears to terminate near the North American continental shelf, and the earthquakes near Nootka Island result from deformation inside the overriding or subducting plates. Analysis of additional earthquakes along Nootka fault, particularly some events close to the North American continental shelf, is necessary to resolve this issue.

2.3.7 Northern Juan de Fuca Ridge

The only relocated earthquakes along northern Juan de Fuca ridge occurred close to the non-transform (*Karsten et al., 1986*) Cobb offset, which separates the ridge's Endeavor and Northern Symmetrical segments (Figure 2.8). Two normal faulting events on the southern Endeavor segment are consistent with active spreading; a strike-slip earthquake further north is probably associated with a step-over from the Endeavor to the West Valley spreading segment (Figure 2.3). South of the Cobb offset, Juan de Fuca ridge is essentially aseismic down to M = 2.3 (*Dziak and Fox, 1995*) with the notable exception of dike injections along the CoAxial segment 1993 (*Dziak et al., 1995*) and the Axial volcano 1998.

2.4 Instantaneous Pacific-Explorer Rotation Pole

We used earthquake slip vectors, which define the current Explorer plate motions relative to the surrounding plates, to determine the instantaneous Pacific-Explorer rotation pole, and we present estimates based on two different models. In the first, *Model A*, we used slip vector azimuths only from the Explorer-Pacific boundary (excluding the ESDZ), where most earthquakes occurred, to locate the Pacific-Explorer rotation pole, and applied an additional constraint to estimate the rotation rate. In the second, *Model B*, we added slip vector azimuths from events along Nootka fault; with slip vector azimuths from two plate boundaries, the location and rate of the Pacific-Explorer pole can be determined.

2.4.1 Pacific-Explorer Pole - Model A

Earthquake slip vector azimuths along the Revere-Dellwood-Wilson fault and the transform faults in the Explorer Rift and Southwest Explorer areas are similarly oriented; they agree with the bathymetric trends along the Revere-Dellwood-Wilson fault, and change systematically from a more northerly direction along the northwestern Revere-Dellwood-Wilson fault to a more northwesterly direction along the Southwest Explorer transform(s) (top four panels Figure 2.6). This suggests the segments are part of the same plate boundary defining the current Explorer-Pacific plate motion direction; the systematic change implies the Pacific-Explorer rotation pole is located northeast of Explorer region.

We used a grid search, minimizing the squared misfit between observed slip vector azimuths (regions 2-5 and 7, Tables 2.1 and 2.2) and predicted plate motion directions, to locate the instantaneous Pacific-Explorer rotation pole at 54.0° N and 120.0° W (Figure 2.12). The location uncertainty is elongated perpendicular to the plate boundary (Figure 2.12) because slip vector azimuths along the short plate boundary change only little. Pacific-Explorer motion directions predicted by the pole agree with the slip vector azimuths and bathymetric trends (top four panels Figure 2.13). Along the ESDZ (bottom panel Figure 2.13), the predicted motion direction, obtained only from the data shown in the top four panels, disagrees with the bathymetry and observed slip vector azimuths. Including ESDZ slip vector data to the grid search resulted in Pacific-Explorer poles whose predicted motion directions deviated from bathymetric trends and, overall, agreed less well with

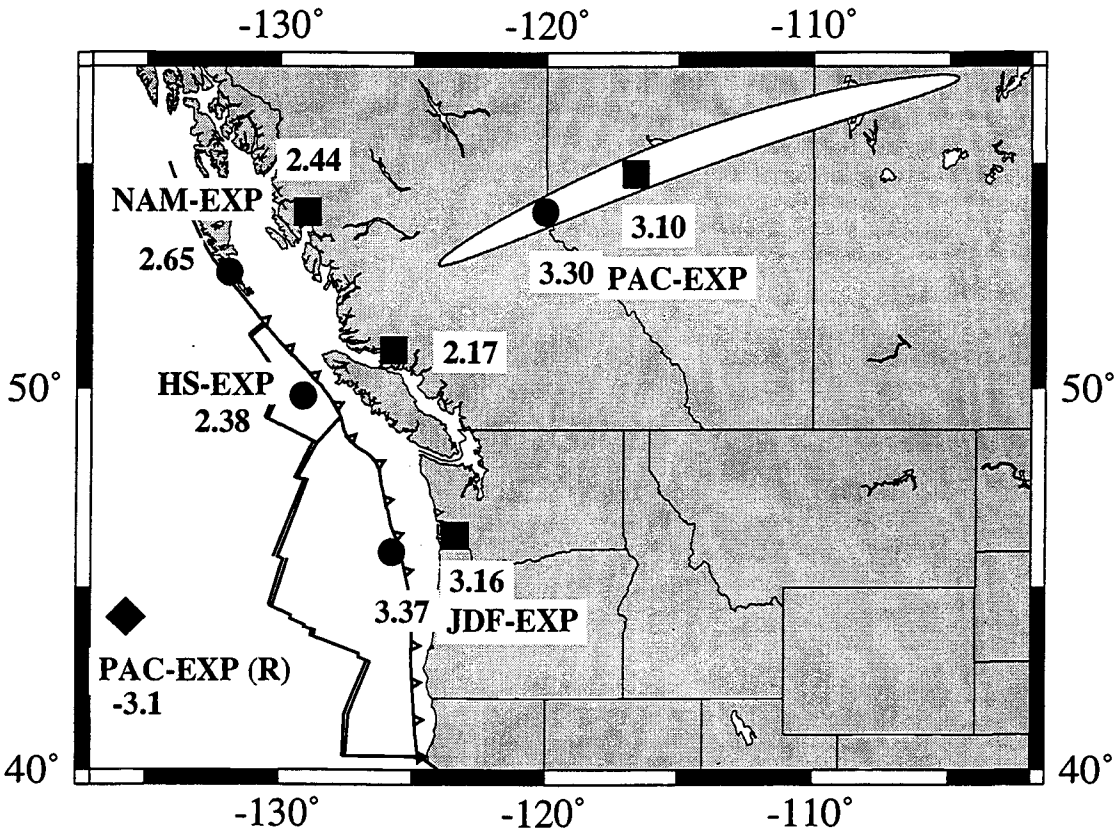

Figure 2.12. Explorer plate instantaneous rotation poles. Circles are Model A, squares are Model B poles, the diamond represents Riddihough's (*1984*) 0.5 Ma mean Pacific-Explorer pole. Numbers beneath poles are rotation rates in °/myr, positive if second plate moves counter clockwise relative to first. The ellipse surrounding Model A's Pacific-Explorer pole depicts the area where the mean misfit between observed and calculated slip vector directions differs by less than 5% from the best solution (mean misfit of 8.0°); the area for Model B's pole is similar. EXP: Explorer, PAC: Pacific, NAM: North America, JDF: Juan de Fuca, HS: Hot spot framework. See Table 2.3 for derivation of NAM-EXP, HS-EXP, and JDF-EXP poles.

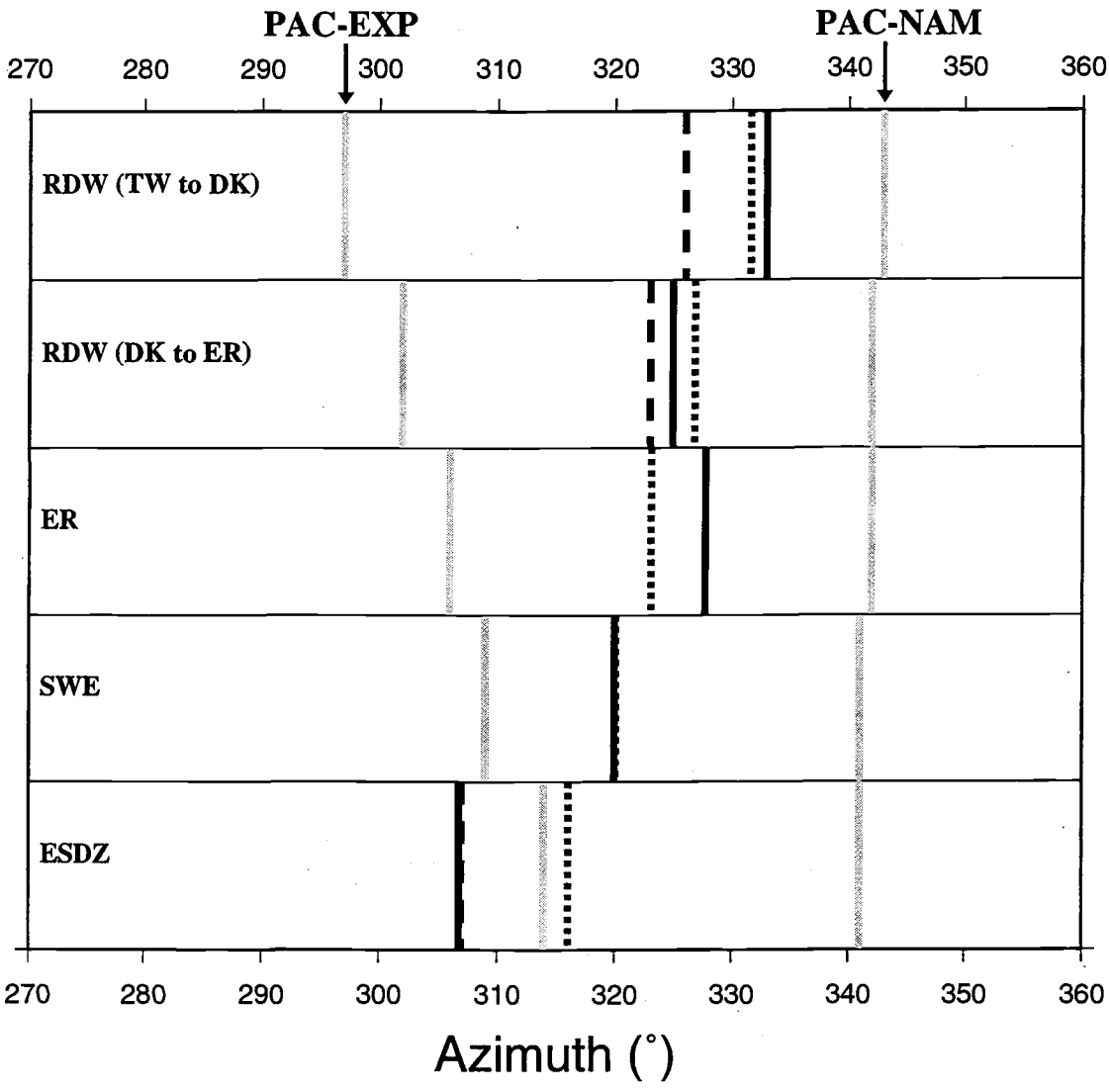

Figure 2.13. Pacific-Explorer motion directions (dotted) predicted by Model A's Pacific-Explorer rotation pole (Figure 2.12); Model B's predicted directions (not shown) are similar. Panels are the same as in Figure 2.6. For each panel, the solid line is the average observed slip vector azimuth; the dashed line shows the active fault trend, and the gray lines represent Pacific-North America (PAC-NAM, from NUVEL-1 [*DeMets et al., 1990*]) and Riddihough's (*1984*) Pacific-Explorer (PAC-EXP) motion directions. For the top four panels, note the good agreement between predicted motion direction and observations (average slip vector azimuth and bathymetry). For the ESDZ, note the large discrepancy between predicted motion direction and observations.

observed slip vector azimuths. This supports our assertion that the internally deforming ESDZ is not moving in the same sense as the rest of Explorer plate.

We estimated the Pacific-Explorer rotation rate by closing the velocity triangle at the Pacific-North America-Explorer triple junction (at the Tuzo Wilson seamounts near 51.5° N, 131.0° W), which is required for an internally consistent plate model. At the triple junction, North America moves 4.6 cm/yr to the south-southeast (azimuth: 164°; NUVEL-1A, [*DeMets et al., 1994*]) and Explorer plate moves, according to our pole location, to the southeast (azimuth: 155°) relative to the Pacific plate (Figure 2.14). An additional parameter (Explorer-Pacific motion rate, or Explorer-North America motion or motion direction) is needed to close the triangle. A less northerly orientation of the Pacific-Explorer motion relative to the Pacific-North America motion, well constrained by the slip vector azimuths, requires some convergence between the Explorer and North American plates. The lack of earthquakes along the Explorer-North America boundary (Figure 2.8) suggests that motion between the two plates is small; using that as a constraint, we closed the triangle by choosing Explorer-North America motion perpendicular to Explorer-Pacific motion (gray lines, Figure 2.14). This choice minimizes Explorer-North America motion at the triple junction (0.7 cm/yr). The Explorer-North America motion direction (azimuth of 65°) is not perpendicular to the North American margin (trend about 325°); the model, thus, predicts a small component of left-lateral Explorer-North America motion (0.1 cm/yr) besides the more prominent component of convergent motion (0.6 cm/yr). The choice also fixes the Pacific-Explorer motion rate at the triple junction to 4.5 cm/yr, which is equivalent to a Pacific-Explorer rotation rate of 3.3 °/my (Table 2.3). Requiring purely convergent Explorer-North America motion at the triple junction (azimuth: 55°, rate: 0.7 cm/yr), changes the Pacific-Explorer motion rate only slightly to 4.4 cm/yr (and the Pacific-Explorer rotation rate to 3.2°/my). Other choices of Explorer-North America motion also result in similar Pacific-Explorer rotation rate estimates; the estimate, for example, changes less than 20% if Explorer-North America motion at the triple junction is changed by 50% relative to our choice of 0.7 cm/yr (dashed gray lines, Figure 2.14), with right-lateral Explorer-North America motion reducing and left-lateral Explorer-North America motion increasing the Pacific-Explorer rotation rate estimate.

The North America-Explorer, Juan de Fuca-Explorer, and Hotspot-Explorer rotation poles (Table 2.3, Figure 2.12) are obtained by vector addition of the Pacific-Explorer pole with other published poles (*Wilson, 1993; DeMets et al., 1994; Gripp and Gordon, 1990*). According to Model A (gray arrows, Figure 2.15), Explorer-North America motion is predominantly convergent and the rate increases from about 0.7 cm/yr near the Tuzo Wilson seamounts (in a direction of 65°) to about 2.2 cm/yr off Nootka Island (azimuth:

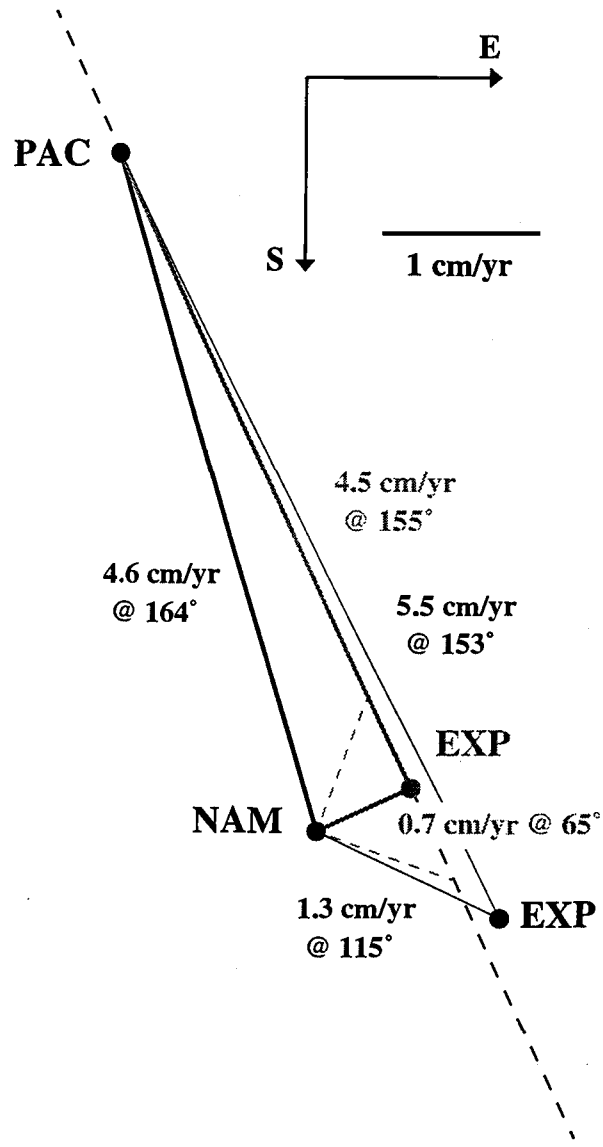

Figure 2.14. Velocity triangle at the Pacific-North America-Explorer (PAC-NAM-EXP) triple junction near the Tuzo Wilson seamounts. Model A. PAC-NAM motion (black line) (NUVEL-1A, [*DeMets et al., 1994*]) and PAC-EXP motion direction (black dashes) are defined. We close the triangle by minimizing EXP-NAM motion (0.7 cm/yr in a 65°-direction , gray line); the resulting EXP-PAC motion rate (4.5 cm/yr in a 155°-direction, gray line) is equivalent to a rotation rate of 3.3°/myr (for PAC-EXP pole at 54.0° N, 120.0° W, Figure 2.12, Table 2.3). A 50% deviation of EXP-NAM motion from minimum-motion assumption (gray dashes) changes the EXP-PAC motion rate by less than 20%. Model B. Rate (3.1°/myr) and location (54.8°N/116.6°W) of the PAC-EXP pole are determined simultaneously with slip vector data from the PAC-EXP and the Juan de Fuca-EXP boundaries. The model's predicted EXP-NAM (1.3 cm/yr in a 115°-direction) and EXP-PAC (5.5 cm/yr in a 153°-direction) motions are shown as thin solid lines.

Table 2.3. Instantaneous Rotation Poles of Explorer Plate.

Plate Pair	Lat (°N)	Lon (°W)	ω (°-Myr^{-1})	ω_x (°-Myr^{-1})	ω_y (°-Myr^{-1})	ω_z (°-Myr^{-1})	comment
Model A:							
PAC-EXP	53.99	120.04	3.30	-0.9701	-1.6775	2.6662	
JDF-EXP	45.92	125.76	3.37	-1.3694	-1.9016	2.4197	W'93
NAM-EXP	52.67	131.90	2.65	-1.0714	-1.1940	2.1037	N-1A
HSP-EXP	49.81	129.12	2.38	-0.9698	-1.1927	1.8199	HS2
Model B:							
PAC-EXP	54.80	-116.62	3.10	-0.8007	-1.5975	2.5332	
JDF-EXP	46.35	-123.38	3.16	-1.2000	-1.8216	2.2866	W'93
NAM-EXP	53.97	-129.00	2.44	-0.9020	-1.1140	1.9707	N-1A
HSP-EXP	50.90	-125.73	2.17	-0.8004	-1.1127	1.6869	HS2

PAC-EXP: Pacific-Explorer rotation pole derived in this study. Second (EXP) plate moves relative to first (PAC) plate, positive rotation rate ω indicates counter-clockwise rotation. ω_x, ω_y, ω_y, are cartesian coordinates of rotation vector. Plate abbreviations: EXP, Explorer; PAC, Pacific; JDF, Juan de Fuca; NAM, North America; HSP, hot spot reference frame. W'93: vector addition of PAC-EXP pole with PAC-JDF pole from Wilson (*1993*). N-1A: vector addition with NUVEL-1A PAC-NAM pole from DeMets et al. (*1994*). HS2: vector addition with PAC-HSP pole from Gripp and Gordon (*1990*).

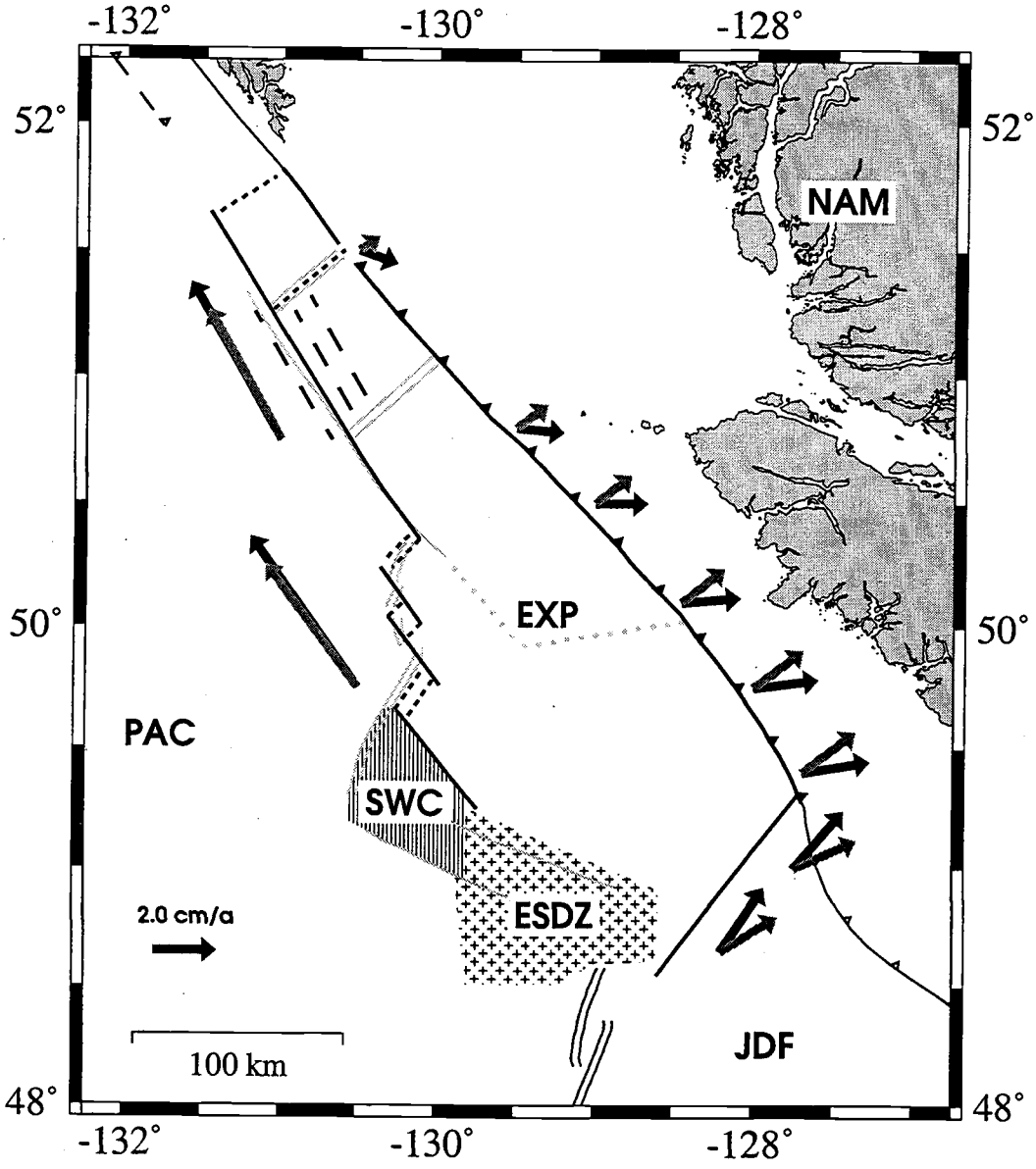

Figure 2.15. Predicted current Explorer plate motions (gray arrows are Model A's and black arrows are Model B's). Explorer plate's boundaries are shown in heavy black (transforms: solid lines, long dashes where inferred; subduction zone: barbed line; short dashes: spreading centers or extensional pull apart basins). We infer the extent of the Eastern Sovanco Deformation Zone (ESDZ) from the earthquake distribution (Figure 2.9). The Southwest Explorer corner (SWC) recently transferred from the Explorer to the Pacific plate; the SWC is bordered to the northeast by a (or several) Pacific-Explorer transform fault(s). Light gray lines show plate boundaries from Figure 2.1.

53°); right lateral Explorer-Pacific motion changes only little from the northwest part of Revere-Dellwood-Wilson fault (rate: 4.5 cm/yr, azimuth: 155°) to the Southwest Explorer transform(s) (rate: 4.9 cm/yr, azimuth: 140°), and left lateral motion along Nootka fault has a rate of about 2.4 cm/yr. The predicted motion directions along Nootka fault (from an azimuth of about 55° in the southwest to about 75° near Nootka Island), however, do not agree with the observed slip vector azimuths (average of 37° along the southwest part of the fault and about 80° near Nootka Island). In the next section, we included slip vector azimuths from the southwest part of Nootka fault to find a Pacific-Explorer rotation pole which is consistent with observations along the Pacific-Explorer and the Explorer-Juan de Fuca plate boundaries.

2.4.2 Pacific-Explorer Pole - Model B

For this model, we added slip vector azimuths from the short Nootka fault (region 9, Tables 2.1 and 2.2, excluding three events near Nootka Island which possibly did not occur on Nootka fault) to the grid search. With slip vector azimuths from two plate boundaries (Explorer-Pacific and Explorer-Juan de Fuca), and a known Pacific-Juan de Fuca rotation pole (we used the pole given by Wilson [*1993*]), the location and rate of the Pacific-Explorer rotation pole can be determined simultaneously.

We extended the grid search to include rotation rate as a parameter. For each trial Pacific-Explorer rotation pole, described by location and rate, we calculated an Explorer-Juan de Fuca rotation pole by vector addition of the trial Pacific-Explorer to Wilson's (*1993*) Pacific-Juan de Fuca rotation pole. A Pacific-Explorer pole at 54.8° N, 116.6° W rotating with a rate of 3.1°/my fits the observed slip vector azimuths along both plate boundaries best in a least-squares sense. The Pacific-Explorer pole location is mainly determined by observations from the Pacific-Explorer boundary, where we have about five times as many slip vectors compared to the Explorer-Juan de Fuca boundary. The pole's location uncertainty and the predicted Pacific-Explorer motion directions are similar to Model A (and thus not shown in Figures 2.12 and 2.13). For a given Pacific-Explorer pole location, the Explorer-Juan de Fuca slip vector azimuths constrain the Pacific-Explorer rotation rate tightly. For example at the best fitting Pacific-Explorer pole location, the rate changes only by ±0.2°/my for a misfit increase of 3%. The North America-, Juan de Fuca-, and Hotspot-Explorer rotation poles are listed in Table 2.3 and shown in Figure 2.12.

Model B (black arrows, Figure 2.15) predicts 5.5-6 cm/yr right-lateral Pacific-Explorer motion, oblique convergence between the Explorer and North American plates (with the rate increasing from about 1.3 cm/yr of predominantly left-lateral motion near the Tuzo Wilson seamounts to about 2.2 cm/yr of equal left-lateral and convergent motion offshore Nootka Island), and about 2.5 cm/yr left-lateral motion along Nootka fault. The predicted Explorer-Juan de Fuca relative motion trend (azimuth 35°-40°) agrees well with the slip vector azimuths along Nootka fault. The main differences compared to Model A are (Figures 2.14 and 2.15): Pacific-Explorer motion rate is faster; Explorer-North America motion, though similar in rate along most of the plate boundary, has a strong left-lateral component and is much more oblique, and Explorer-Juan de Fuca motion is more northerly oriented, which is required by the Nootka slip vector azimuths used to derive Model B.

2.4.3 Seismic Slip Rate Estimates

We determined seismic slip rate estimates for six segments-- Revere-Dellwood-Wilson, Explorer Rift, Explorer Deep, Southwest Explorer boundary, ESDZ, and Nootka fault-- to estimate how much of the predicted plate motions are taken up seismically. The seismic slip rate estimates are based on 80 years of seismicity and include corrections for location and magnitude bias (Appendix C). The estimates, probably good within a factor of 2, are consistent with Hyndman and Weichert's (*1983*) rates and are listed in Table 2.5.

The seismic rate estimates are not useful in distinguishing between the plate models (Model A or B) because of the large seismic slip rate uncertainties and the unknown and probably (from segment-to-segment) varying ratio of seismic-to-aseismic energy release. The seismic rates, however, show that a relatively large percentage of predicted Pacific-Explorer plate motion (Model A: 4.5 cm/yr; Model B: 6.0 cm/yr) is released seismically along the Revere-Dellwood-Wilson (seismic rate: 3.4 cm/yr) and Southwest Explorer (2.4 cm/yr) transform segments with larger earthquakes ($M \geq 5.5$) accounting for more than 95% of the rates. Along Explorer Rift segment, the seismic rate is small (0.6 cm/yr), and larger earthquakes contribute less (66%); this suggests transforms are short, and pull-apart extension and spreading primarily occur aseismically. Along the ESDZ, the seismic rate (2.0 cm/yr, assuming motion along one fault) and the contribution of large events (92%) are similar in size to the Revere-Dellwood-Wilson and Southwest Explorer transform segments.

The predicted rate along Nootka fault is about 2.5 cm/yr for both plate models (Model A and B). The seismic rate estimate is 1.5 cm/yr if Nootka fault extends to Nootka Island. The estimate, however, is almost entirely dominated by one $M_S = 7.2$ earthquake beneath Nootka Island that possibly occurred above the transform fault within North American crust (*Cassidy et al., 1988*); without the large event, the rate reduces to 0.3 cm/yr. We suggested earlier that earthquakes near Nootka Island might not be related to Nootka fault; the fault's seismogenic part possibly ends at its intersection with the continental margin. The seismic rate for this scenario is 0.4 cm/yr. The preferred lower estimates (0.3-0.4 cm/yr) indicate that earthquakes along Nootka fault contribute less to the plate motions than along the Pacific-Explorer transform segments, or alternatively, seismicity along Nootka fault has been unusually low during the last 80 years.

2.4.4 Explorer-North America Motion

Both plate models presented predict convergent motion between the Explorer and North American plates which increases from less than 1 cm/yr near the Tuzo Wilson seamounts to about 2 cm/yr near Nootka Island (Figure 2.15). Their common boundary, with the exception of a few events relocated near Brooks peninsula, lacks earthquakes (Figure 2.8; Wahlström and Rogers [*1992*]). Lack of seismicity along a convergent margin, however, is not entirely unusual; the Juan de Fuca-North America "Cascadia subduction zone", for example, also behaves essentially aseismically.

The relocated earthquakes near Brooks peninsula probably ruptured within the overriding North American crust; their source mechanisms show left-lateral strike slip motion along shallow north-dipping, east-west oriented faults (*Spindler et al., 1997*). Spindler et al. (*1997*) suggested the events' northeast-directed pressure axes, roughly parallel to Explorer-North America motion direction predicted by our Model A and by Riddihough's (*1984*) plate model, indicate plate coupling. An interpretation consistent with east-west oriented plate motions predicted by our Model B is that east-west trending faults take up all or part of the Explorer-North America motions; this also implies plate coupling, since the events occurred within North American crust.

Interestingly, the earthquake source mechanisms near Nootka Island are more like the mechanisms of the Brooks peninsula earthquakes than the mechanisms along Nootka fault (closer to Juan de Fuca ridge). This observation supports our earlier speculation that the

Nootka Island events might represent Explorer-North America rather than Explorer-Juan de Fuca interaction. Plate coupling between the Explorer and North American plates might thus extend from Brooks peninsula along the entire southwest part of the Explorer-North America plate boundary to Nootka Island (we lack earthquake data to infer northwest of Brooks peninsula). A GPS-site on Vancouver Island north of Brooks peninsula moves very slowly (2.8±1.4 mm/yr) to the northwest (azimuth: about 300°) relative to stable North America (*Dragert and Hyndman, 1995*), indicating that coupling probably terminates west of the GPS-site and closer to the coast of Vancouver Island. This would limit the width of the locked and transition zones for a subduction thrust to about 50 km (from the deformation front to Vancouver Island) which is an important parameter in terms of earthquake hazard assessment.

Evidence (in addition to the scant earthquake data) supports active Explorer-North America convergence. The margin morphology changes significantly offshore Brooks peninsula, possibly the result of a long-lived ridge-transform-trench triple junction offshore Brooks peninsula (*Riddihough, 1977; Lewis et al., 1997*). Southeast of the peninsula, the continental margin is broad and deformed (*Tiffin et al., 1972; Chase et al., 1975; Davis and Hyndman, 1989*); oceanic basement dips landward (*Davis and Hyndman, 1989; Clowes et al., 1997*), and receiver function analysis, heat flow and gravity data reveal a subducting slab beneath Vancouver Island (*Cassidy et al., 1998; Lewis et al., 1997*).

Northwest of Brooks peninsula, convergent motion probably began less than 2 Ma ago when spreading jumped from offshore Brooks peninsula to the Dellwood Knolls (*Riddihough et al., 1980; Davis and Riddihough, 1984*). The recent onset and small rate (< 1.5 cm/yr, according to our plate models) limit overall convergence to less than 30 km, explaining the lack of a subducted slab beneath northern Vancouver Island (*Cassidy et al., 1998*). The margin's narrow, steep morphology (*Tiffin et al., 1972; Chase et al., 1975*) is probably a remnant of long-lived transform motion (*Lewis et al., 1997*). Evidence for convergence is found only in the Pleistocene Winona basin (the part of Winona Block southeast of the Dellwood Knolls, Figure 2.1) which is characterized by actively deforming, northwest striking compressional folds and ridges (*Srivastava et al., 1971; Chase et al., 1975; Davis and Riddihough, 1982*). Progressively increasing sediment deformation from northwest to southeast inside the basin (*Srivastava et al., 1971; Riddihough et al., 1980; Davis and Riddihough, 1982*) is consistent with our plate models which predict a northwest to southeast increase in Explorer-North America motion (Figure 2.15). Seismic data and gravity modeling along a line from Winona basin to southern Queen Charlotte basin (*Yuan et al., 1992*) are consistent with active subduction.

Northwest of the Dellwood Knolls, slow convergence (< 1 cm/yr, according to our plate models) probably started less than 1 Ma ago (*Carbotte et al., 1989; Allan et al., 1993*); the small expected cumulative motion (<10 km) explains lack of convergent features. Gravity modeling consistent with subduction, along a line which starts between the Tuzo Wilson seamounts and the Dellwood Knolls and runs northeast, is inconclusive, since existing seismic refraction data do not constrain the model (*Spence and Long, 1995*).

2.4.5 General Remarks

The uncertainties involved in the determination of the Pacific-Explorer rotation poles are large compared to the differences between the models. Small variations of the slip vector azimuths along the relatively short Pacific-Explorer boundary result in a Pacific-Explorer pole location which is ill-determined in a direction perpendicular to the plate boundary [Figure 2.12]. Other uncertainties arise from assuming the Explorer-North America motion in Model A, and from the choice of what constitutes the Explorer-Juan de Fuca boundary in Model B. With the available data, it is more useful to look at the similarities between the models, which probably represent stable and well resolved general features of the present-day Explorer plate motions. These features are (Figure 2.15): northwest oriented, right-lateral Pacific-Explorer motion parallel to the Revere-Dellwood-Wilson fault trend; northeast oriented, left-lateral Explorer-Juan de Fuca motion, and convergent Explorer-North America motion, which increases from northwest to southeast along the plate boundary. The predicted plate motion rate along the Pacific-Explorer boundary (about 4-6 cm/yr) is faster than along the Explorer-Juan de Fuca (about 2-3 cm/yr) and the Explorer-North America (< 2 cm/yr) boundary; this is consistent with the earthquake distribution (Figure 2.2) and the seismic slip rate estimates (Table 2.5).

2.5 Discussion

Our earthquake relocations and source mechanisms provide important constraints for the current plate boundaries and plate motions in the Explorer region. One of the most

exciting results involves the transfer of Explorer plate material to the Pacific plate in the southwest corner of Explorer region. Following a discussion of the main results, we present a model of recent plate motions (last 2+ Ma) consistent with (and resulting in) the current plate configuration; the model considers crustal transfer as a result of changes in Explorer plate motions.

The plate motion direction along Explorer region's boundary with the Pacific plate, defined by earthquake slip vector azimuths and the Revere-Dellwood-Wilson fault trend, is well constrained (Figure 2.5). The motion direction is incompatible with the more northerly Pacific-North America motion, and thus requires an independently moving Explorer plate. Plate models that postulate a Pacific-North America transform fault cutting through a now-tectonically inactive Explorer plate (*Barr and Chase, 1974; Rohr and Furlong, 1995*) are incorrect. Furthermore, the current Pacific-Explorer motion direction is more northerly than predicted by Riddihough (*1984*); this implies either the magnetic anomaly orientations generated at the short Explorer ridge spreading segment (used by Riddihough [*1984*] to determine plate motions) define current motions inaccurately, or Explorer plate motions changed recently during the current magnetic polarity chron (the Brunhes normal chron which began about 0.7 Ma ago).

The relocations and source mechanisms also suggest the existence of three distinct areas in Explorer region (Figure 2.15). First, the independently moving Explorer plate which occupies almost the entire Explorer region including the Winona block. The similarity of earthquake slip vector azimuths (along the Revere-Dellwood-Wilson, Explorer Rift, and Southwest Explorer transform segments, Figure 2.6), which indicates the segments are part of the same boundary with the Pacific plate, as well as the absence of seismicity along a Winona-Explorer boundary (dotted line, Figure 2.8) suggest only one plate-- Explorer plate-- exists. Second, the Eastern Sovanco Deformation Zone (ESDZ), which is a broad zone of distributed seismicity in Explorer region's southeast corner (Figure 2.9). A difference in slip vector azimuths compared to the segments to the northwest (Figure 2.6) indicates that the ESDZ is not moving coherently with the remainder of Explorer plate; we suggest internal deformation within the ESDZ accommodates Pacific-Explorer relative motions. And third, the Southwest Corner (SWC) of Explorer region which is tectonically inactive (Figure 2.9). We suggest the SWC transferred recently from the Explorer to the Pacific plate; the active Pacific-Explorer plate boundary is now formed by the transform(s) along the northeast boundary of the SWC.

The Pacific-Explorer plate boundary consists of several right-stepping transform faults separated by small pull-apart basins or short spreading centers along the Explorer Rift and central Explorer ridge (Figure 2.15). Seismicity (for $M \geq 4$ earthquakes) is primarily

associated with the transform segments, whereas spreading centers and pull-aparts appear almost aseismic (Figure 2.9). The transform segments from northwest to southeast are: the Revere-Dellwood-Wilson fault, whose active part runs from northwest of the Tuzo Wilson seamounts to the faults' intersection with Explorer Rift; several short transforms connecting spreading centers and pull-aparts along Explorer Rift; the Southwest Explorer transform boundary (consisting of one or several en-echelon faults), and transform faults in the ESDZ. It is important to recognize that relocated seismicity (Figure 2.8), which appears to outline a broad linear plate boundary (from the north tip of Juan-de-Fuca ridge to Queen Charlotte fault following a north-northwest trend close to the Pacific-North America plate motion direction), does not describe the actual plate boundary configuration properly; the trend is more northerly than (and thus inconsistent with) the slip vector azimuths (Figure 2.6). The combination of earthquake locations and slip vector azimuths (roughly) defines the faults' location and requires that several right-stepping transform faults form the Pacific-Explorer plate boundary (Figure 2.15). The postulated plate boundary follows bathymetric features closely along the Revere-Dellwood-Wilson fault, the Explorer Rift segment and most of the ESDZ; thus, bathymetry, seismicity and current tectonics are closely related in the Explorer region.

The slip vector azimuths and Revere-Dellwood-Wilson fault trend define only Pacific-Explorer relative motion direction; they do not constrain the rate. We used two approaches to estimate the current Pacific-Explorer rotation pole (location and rate). In the first, Pacific-Explorer slip vector azimuths define the location; and assuming the Explorer-North America motion, we estimated the Pacific-Explorer motion rate. In the second, we added slip vector azimuths from Nootka fault and simultaneously determined rate and location of the Pacific-Explorer pole. The resulting Pacific-Explorer rotation pole estimates are quite similar (Figure 2.12, Table 2.3), which implies that general features of Explorer plate motions are well constrained despite the large uncertainties involved in both approaches. These general features (northwest oriented, right-lateral Pacific-Explorer motion following the Revere-Dellwood-Wilson fault trend; northeast oriented, left-lateral Explorer-Juan de Fuca motion, and convergent Explorer-North America motion) follow directly from the slip vector azimuths and the Explorer-North America plate boundary orientation. Of particular importance are the well constrained Pacific-Explorer plate motion direction (325° average along the plate boundary, Figure 2.13) and the Pacific-Explorer pole location northeast of Explorer region. Both are inconsistent with Riddihough's (*1984*) model for recent Explorer plate motions which predicts a Pacific-Explorer pole southwest of Explorer region (Figure 2.12) and a less northerly oriented Pacific-Explorer motion (Figure 2.13). Our

predicted present-day Explorer plate motions, however, are basically that suggested for the Winona block (*Davis and Riddihough, 1982*).

According to Davis and Riddihough (*1982*), Winona block is an independent plate in the northwest part of Explorer region (Figure 2.1) which formed about 1-2 Ma ago and moves independently of Explorer plate. The slip vector azimuths along the Pacific plate boundary (Figure 2.6), however, vary smoothly from northwest (Revere-Dellwood-Wilson fault, the Winona-Pacific boundary according to Davis and Riddihough [1982]) to southeast (Southwest Explorer boundary, which is part of the Explorer-Pacific boundary), indicating that motions relative to the Pacific plate can be explained by one plate. We also did not relocate any earthquakes along the postulated Explorer-Winona plate boundary (Figure 2.7). Our single "Explorer plate" (Figure 2.15) encompasses both Explorer plate and Winona block, and, as mentioned, its present-day motions are essentially that predicted for Winona block (*Davis and Riddihough, 1982*). Consequently, either the two plates merged, or there never existed another independent plate besides the Explorer plate. Plate merger during the last several hundred thousand years (during the Brunhes anomaly) is possible. It is also possible, though, to explain existing data with only one plate. We favor this simpler explanation, which requires that Explorer plate motions changed to "Winona motions" when spreading jumped from offshore Brooks peninsula to the Dellwood Knolls (1-2 Ma ago [*Riddihough et al., 1980; Davis and Riddihough, 1982*]); since then, Pacific-Explorer motion direction has been defined by the Revere-Dellwood-Wilson fault trend.

Explorer plate motions tied to the Revere-Dellwood-Wilson fault trend and a Pacific-Explorer pole northeast of Explorer region for approximately the last 2 Ma, however, contradict Riddihough's (*1984*) model. The Pacific-Explorer pole, according to Riddihough (*1984*), remained southwest of Explorer region since independent Explorer plate motion began about 4 Ma ago; the predicted Pacific-Explorer motion directions are incompatible with the Revere-Dellwood-Wilson fault trend, and predicted Explorer-North America convergence increases from southeast (near Nootka Island) to northwest (near Brooks peninsula), which is inconsistent with the observed northwest-to-southeast increase in sediment deformation in Winona basin (*Srivastava et al., 1971; Riddihough et al., 1980; Davis and Riddihough, 1982*). Riddihough's (*1984*) poles, then, require an independent Winona block.

Riddihough (*1984*) derived the Pacific-Explorer poles from magnetic anomaly data generated at Explorer ridge. Since along-ridge spreading rate variations are not available from the short ridge, Riddihough (*1984*) had to use fanning of magnetic anomalies (i. e. magnetic anomaly azimuths differ on both sides of a ridge systematically with age) to infer

a pole location southwest of Explorer region. Inspection of his data (Figure 3 in [*Riddihough, 1977*]) shows fanning during the last 2 Ma was small. Considering uncertainties in azimuth determination along the short ridge, we suggest Riddihough's (*1984*) Pacific-Explorer pole locations younger than 2 Ma, actually, are not well resolved. Another possible explanation for the discrepancy between Riddihough's (*1984*) predicted plate motions and "Winona motion" of Explorer plate during the last 2 Ma is that the magnetic anomaly record may lag behind changes in plate motion (a plate motion change may not necessarily reorient an existing spreading ridge [*Wilson et al., 1984*]). Wilson et al. (*1984*) showed for the magnetic anomalies generated at Juan de Fuca ridge, that ridge reorientation required by changes in plate motion can be modeled by propagating ridges; thus ridge segments oriented in the "old" motion sense may be active until being replaced by a propagator (oriented properly relative to the new plate motions), possibly long after the new plate motions initiated. Yet another possibility is that Explorer plate motions changed only during the Brunhes magnetic anomaly (during the last 0.7 Ma). This would reconcile our current plate motions with Riddihough's (*1984*), but would require independent Winona block motions.

2.5.1 Tectonic Model of Explorer Plate (from 2+ Ma BP to now)

Models for the tectonic evolution of Explorer plate and Winona block have been presented in a number of publications (*Barr and Chase, 1974; Riddihough, 1977, 1984; Riddihough et al., 1980; Davis and Riddihough, 1982; Botros and Johnson, 1988; Lister, 1989*). The current Explorer plate motions and the current aerial extent of Explorer plate deduced in our study (Figure 2.15) require several adjustments to these models. In particular, our results require that Explorer plate encompasses Winona block, and that current Explorer plate motions are essentially that suggested for the Winona block (*Davis and Riddihough, 1982*). We sketch a simple model (Figure 2.16) based on the earlier publications which satisfies our results, and at the same time minimizes the number of plates involved and the number of significant changes in plate configurations. The model, which does not require an independent Winona block, consists of two stages of Explorer plate motions (roughly from 4 Ma to 2 Ma, and from 2 Ma to now), and involves one additional change in the plate boundary configuration (which probably occurred several hundred thousand years ago). We want to stress, however, that we cannot rule out

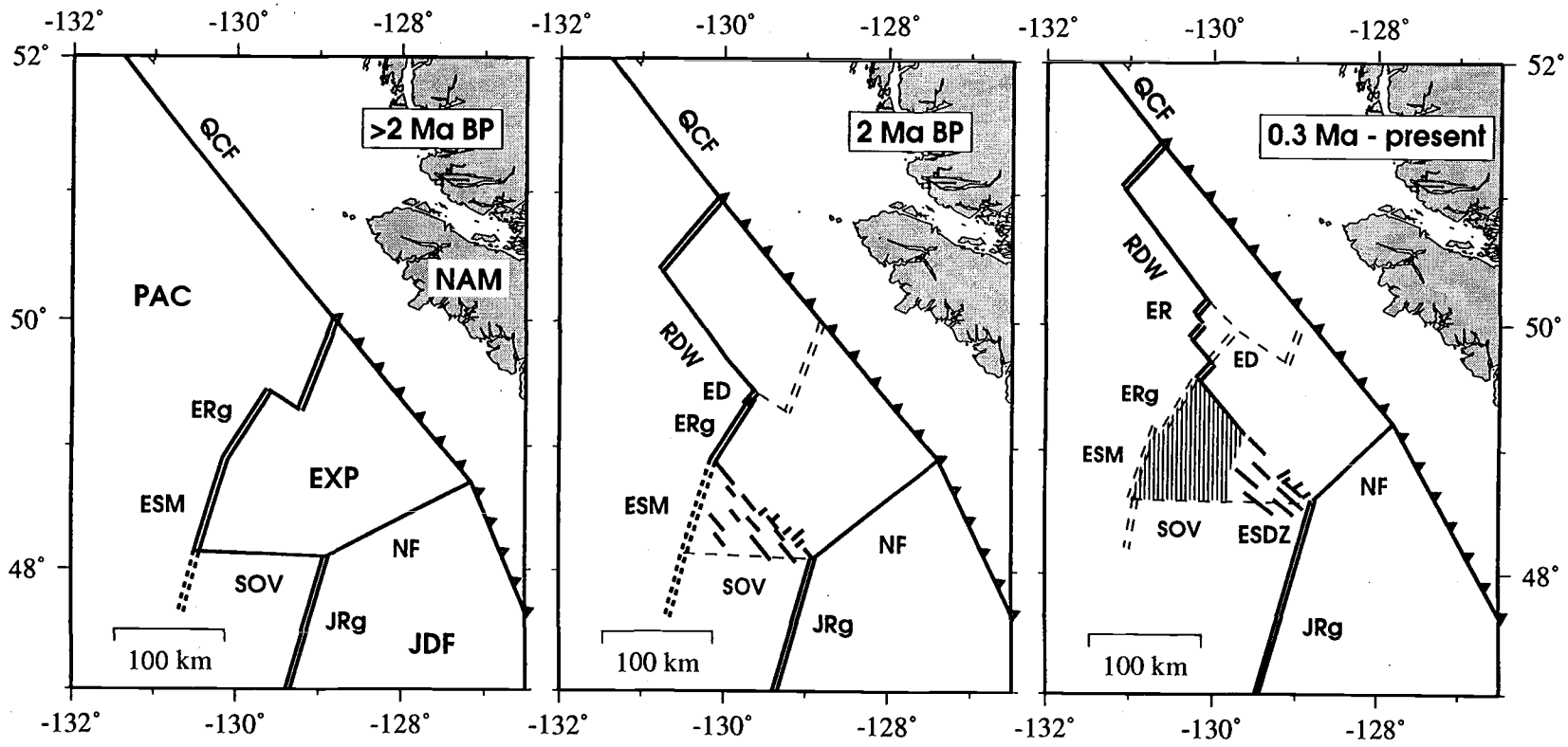

Figure 2.16. Schematic plate tectonic reconstruction of Explorer region during the last 2+ Ma. Note the transfer of a crustal block (hatched) from the Explorer to the Pacific plate. Active plate boundaries (and faults in areas of distributed deformation) are drawn in bold (short dashes were extension/spreading probably occurred at less than the Explorer-Pacific motion rate or was short-lived); inactive boundaries are shown as thin, long dashes. Single lines: transform faults; double lines: spreading centers; barbed lines: subduction zones with barbs in down-going plate direction. QCF: Queen Charlotte fault; RDW: Revere-Dellwood-Wilson fault; ED: Explorer Deep; ER: Explorer Rift; ERg: Explorer Ridge; ESM: Explorer seamount; SOV: Sovanco Fracture zone; ESDZ: Eastern Sovanco Deformation zone; JRg: Juan de Fuca ridge; NF: Nootka fault.

independent Winona block motion followed by a subsequent merger of Winona block with Explorer plate.

2.5.1.1 Before 2 Ma BP

Independent Explorer plate motion began at least about 4 Ma ago when the spreading directions along the Explorer and Juan de Fuca ridges started to differ (*Riddihough, 1984; Botros and Johnson, 1988*). From about 4 Ma to 2 Ma ago, the Explorer plate motions are that described by Riddihough (*1984*). The Pacific-Explorer-North America triple junction is located offshore Brooks peninsula (*Riddihough, 1977; Lewis et al., 1997*), and a short left-lateral transform fault connects the northern ridge segment offshore Brooks peninsula with Explorer ridge, which migrates to the northwest due to asymmetric spreading (more material accretes to Explorer than to Pacific side) lengthening the transform (*Riddihough et al., 1980; Davis and Riddihough, 1982*). Explorer ridge's extent to the south is not quite clear. Botros and Johnson (*1988*) modeled the magnetic anomaly sequence generated at Explorer Seamount, which suggests the seamount was an active part of the Explorer ridge system at least until magnetic anomaly chron 2A (about 2.6 Ma ago) and became inactive before chron 2 (about 1.9 Ma ago). Deformed magnetic anomalies on the Pacific plate in the vicinity of Juan de Fuca ridge as far south as 48° N (current latitude) require that extension associated with Explorer ridge occurred even south of Explorer Seamount (*Wilson, 1993*); the amount of extension is small (about 5 km, which is equivalent to less than 0.2 Ma of extension at the current Juan de Fuca ridge half-spreading rate of 3 cm/yr), and its timing is not well constrained (younger than chron 2, possibly even more recent than chron 1 -- about 0.7 Ma). In our simple model, we place Sovanco Fracture zone at the south end of Explorer Seamount and ignore extension further south; the fracture zone is a (roughly) east-west trending transform fault connecting Explorer Seamount with Juan de Fuca ridge.

Bathymetric ridges at Explorer Seamount trend in a 17° direction, which is almost parallel to the Juan de Fuca ridge orientation (azimuth of about 20° for the last 4 Ma [*Riddihough, 1984; Botros and Johnson, 1988*]). Spreading perpendicular to those ridges would imply that the Explorer Seamount segment of Explorer ridge did not reorient (to a trend of about 30°) when Explorer plate split from Juan de Fuca plate, but remained active in the Juan de Fuca motion sense, possibly, for another 2 Ma. This is consistent with

Wilson et al. (*1984*), who suggested that pre-existing spreading ridges may not rotate to a new motion direction when plate motions change.

A roughly east-west trending Sovanco Fracture zone follows from the estimated locations of the southern terminus of Explorer seamount and the north tip of Juan de Fuca ridge. A northwest-southeast orientation (azimuth of about 300°) of the fracture zone, in compliance with Riddihough's (1984) Explorer-Pacific plate motion direction, appears unlikely, even if we consider errors in the ridge-tip locations. The fracture zone initiated about 7-8 Ma ago (*Barr and Chase, 1974; Riddihough, 1977, 1984; Botros and Johnson, 1988*) as an east-west oriented spreading center offset (parallel to the Juan de Fuca ridge spreading direction at the time), and it seems possible that the fracture zone remained roughly east-west oriented (±20°) throughout most of its existence (until 2 Ma). As pointed out by Riddihough (*1977*), a clockwise difference in spreading direction relative to the fracture zone trend implies compression along Sovanco Fracture zone.

2.5.1.2 About 2 Ma BP

Uplift of Paul Revere ridge, subsidence of Winona basin and compression of basin sediments begin near the Pliocene-Pleistocene boundary (slightly less than 2 Ma ago) (*Kulm et al., 1973; Davis and Riddihough, 1982*), and spreading at the Explorer Seamount segment of Explorer ridge stops sometimes between chron 2A (ends about 2.6 Ma ago) and chron 2 (about 1.8 Ma ago) (*Botros and Johnson, 1988*). We suggest these changes at the north and south end of Explorer plate occurred (almost) simultaneously as a response to changes of Explorer plate motion, roughly 2 Ma ago. Since then, Explorer plate motions are that described in this study.

Winona basin subsidence and Paul Revere ridge uplift are probably the result of a jump of the spreading center from offshore Brooks peninsula to the Dellwood Knolls; the timing (2 Ma ago) is roughly consistent with Riddihough et al. (*1980*). Although Riddihough et al. (*1980*) preferred a more recent onset of Dellwood Knoll activity (based on the generally positive magnetic anomaly near the knolls, suggested to be chron 1-- < 0.7 Ma), they could not exclude a 1.5 Ma-or-older age of the knolls (based on modeling of magnetic anomalies and on the thickness of manganese encrustation). A new transform fault, the Revere-Dellwood fault, connects the Dellwood Knolls with the north tip of Explorer ridge. And Winona basin (bordered by the Dellwood Knolls, the Revere-Dellwood fault, the now-

inactive spreading center offshore Brooks peninsula and the continental margin) has switched from the Pacific to the Explorer plate. We suggest the fault's orientation (roughly 325°) has defined the Explorer-Pacific plate motion direction for the last 2 Ma.

The postulated new plate motion trend is significantly more northerly than the east-west oriented Sovanco Fracture zone; this possibly inhibits further east-west motion and requires a clockwise reorientation of Sovanco Fracture zone (described similarly by Botros and Johnson [*1988*]). The Explorer Seamount ridge segment becomes disconnected from the remainder of Explorer ridge during reorientation, and spreading at the seamount stops before chron 2 (about 1.8 Ma ago). Explorer Seamount and the area immediately to the east possibly transferred from the Explorer to the Pacific plate due to the reorientation.

The mechanism for the "clockwise rotation of Sovanco Fracture zone" is not clear. We have difficulties envisioning a single strike-slip fault rotating through unbroken oceanic crust. Supported by current bathymetry, particularly along eastern Sovanco Fracture zone, it appears more likely that short strike-slip faults formed which were distributed over a wide area and were oriented properly with respect to the new plate motion direction. Simultaneous seismic activity on sets of parallel strike-slip faults is well documented in many continental settings (e.g., *Nur et al., 1989*) and has been proposed to account for the elevated rhomb-shaped blocks in the Sovanco Fracture zone (*Cowan et al., 1986*). Bathymetry and earthquake source mechanisms along eastern Sovanco Fracture zone (Figure 2.10) indicate the northwest trending right-lateral faults are primarily active. Simple geometric considerations show that slip on sets of right-lateral faults results in counter-clockwise rotation of blocks and their bounding faults (*Nur et al., 1989*). The difference between the predicted current Explorer-Pacific motion direction (about 320°) and the observed fault trends and slip vector azimuths (about 305°) is consistent with counter-clockwise rotation. Distributed deformation inside a broad shear zone, although currently confined to the ESDZ, appears to be a likely mechanism for the reorientation of Sovanco Fracture zone which could-- in the form of slip along multiple faults, and associated fault and block rotations-- account for the distorted magnetic anomalies north of 48.5° N.

We lack a compelling argument as to why the ridge jumped to the Dellwood Knolls. Davis and Riddihough (*1982*) suggested that the Pacific plate broke along a structural weakness (the inactive fracture zone part of the left-lateral fault which offset spreading off Brooks peninsula from Explorer ridge) when bending stresses due to oblique underthrusting of the Pacific plate beneath North America (Pacific-North America motion is more northerly than the trend of the continental margin) exceeded a breaking threshold. The ensuing Revere-Dellwood fault, however, trends more northerly (about 325°) than the inactive fracture zone (about 300°-310°).

2.5.1 3 About 0.3 Ma BP to now

Based on the width of the magnetic anomalies at the northern end of Explorer ridge, Botros and Johnson (*1988*) suggested that spreading shifted about 0.3 Ma ago 40 km to the northwest from Explorer Deep to Explorer Rift. The Revere-Dellwood fault segment between Explorer Deep and Explorer Rift, which was less northerly oriented than the fault segment northwest of Explorer Rift and had caused (part of) Paul Revere ridge uplift, became inactive.

As suggested by Rohr and Furlong (*1995*), the Revere-Dellwood fault probably lengthened to the northwest past the Dellwood Knolls towards the Tuzo Wilson seamounts (the fault, then, becomes "Revere-Dellwood-Wilson fault"), while the Queen Charlotte fault retreated. This is required if spreading shifted from the Dellwood Knolls to the Tuzo Wilson seamounts during the last 2 Ma. The Explorer-Pacific plate motion rate is about 4.5-6.0 cm/yr (according to our plate models), which accounts for a distance of 45-60 km between the knolls and seamounts. The actual distance between the two, however, is about 80 km, which implies asymmetric spreading with more material accreting to the east (Explorer plate) than the west (Pacific plate) (30% to 90% asymmetry; following Wilson et al. [*1984*], 30% asymmetry means one plate spreads at 1.3 times the expected half spreading rate, and the other at 0.7 times that rate). Recent (during Brunhes magnetic anomaly, < 0.7 Ma) volcanism at the knolls indicates that migration of spreading from the Dellwood Knolls to the Tuzo Wilson seamounts was not a smooth process. Either spreading stayed close to the Dellwood Knolls until sometimes during the Brunhes anomaly and then jumped to the Tuzo Wilson seamounts, or the area northwest of the Dellwood Knolls developed into a zone of distributed deformation during the last 2 Ma with possibly synchronous volcanism at several places (a pull-apart basin). Earthquake relocations and mechanisms (Figure 2.9), indicating that several strike-slip faults are active, are consistent with the second interpretation.

We suggest the Southwest Explorer (SWE) boundary also developed recently (perhaps during the last several hundred thousand years). The SWE boundary is parallel to the Explorer-Pacific plate motion direction and, based on the earthquake distribution (Figure 2.9), possibly consists of several transform faults. The new boundary caused the transfer of a triangular shaped area bordered by the SWE, southern Explorer ridge and western

Sovanco Fracture zone from the Explorer to the Pacific plate. The continuity of Explorer ridge (see Figure 3 in Michael et al. [*1989*] or Figure 4 in Davis and Currie [*1993*]) and the continuity of the Brunhes magnetic anomaly along the ridge south to about 49.2° N (*Botros and Johnson, 1988*) requires that the transfer must have occurred recently (transferred ridge segments move with the Explorer-Pacific half-spreading rate-- about 2-3 cm/yr or 20-30 km/Ma-- relative to the active ridge segment). A possible jump of Explorer ridge 5-10 km to the east during the Brunhes anomaly (*Botros and Johnson, 1988; Michael et al., 1989*) and the possibility of subcrustal, lateral magma flow from the northern (active) part of Explorer ridge to the southern, distal end (*Michael et al., 1989*) could mask some of the offset. Alternatively, the SWE boundary is just developing, and no offset between the active and the (inactive) transferred ridge segments is expected yet. The new SWE plate boundary is based on relocating 80 years of larger earthquakes, which is too short to rule out any tectonic activity inside the transferred crustal block; however, larger earthquakes during these 80 years consistently occurred close to the SWE, suggesting the SWE is currently the primary plate boundary.

The transform(s) along the SWE cover(s) only the western half of the Explorer-Pacific plate boundary between Explorer ridge and Juan de Fuca ridge; the eastern part undergoes distributed deformation inside the ESDZ. A still developing SWE, which initiated close to the Explorer ridge and lengthens towards the southeast, could possibly cut through the ESDZ in the future, simplifying the boundary between the ridges. The resulting Explorer-Pacific boundary would then consist of two longer transform segments (Revere-Dellwood-Wilson and Southwest Explorer) and a step-over characterized by short ridge and transform segments near Explorer Rift. As an entity, the transform boundary would look similar to the Pacific-North America transform model proposed by Rohr and Furlong (*1995*), although fault orientation requires an independent Explorer plate.

2.5.1.4 The Southwest Corner Region - Capture of a Microplate Fragment

One of the most interesting results stemming from our research is the proposed transfer of a large piece of Explorer plate material to the Pacific plate in the southwest corner of the Explorer region. Based on seismicity (which outlines the current location of the Explorer-Pacific plate boundary) and the extent of distorted magnetic anomalies and Explorer Seamount (which probably outline the plate boundary location about 2 Ma ago), the area

"captured" by the Pacific plate during the last 2 Ma extends roughly from 48.5° N to 49.7° N and from 130.7° W to 129.7° W. Magnetic anomalies inside the area are distorted (see Figure 4 in Botros and Johnson [*1988*]); and later recognition of capture would mainly depend on identifying the preserved former Explorer-Pacific ridge (Explorer Seamount and south part of Explorer ridge) which is part of, and moves with, the Pacific plate.

We proposed that the material transfer is the result of a clockwise rotation of Explorer plate motions (relative to the Pacific plate) which required a similar shift in the orientation of the Pacific-Explorer plate boundary; the material transfer did not affect independent Explorer plate motions. The currently unfolding process involving the Explorer microplate indicates that capture of a microplate fragment is not necessarily synonymous with cessation of independent microplate motion as has been suggested for microplate remnants preserved offshore California and Baja California (*Atwater, 1989; Lonsdale, 1991; Stock and Lee, 1994; Nicholson et al., 1994; Bohannon and Parsons, 1995*). Explorer plate might exist for another couple million years without further fragmentation or changing of its plate motions (until completely subducting beneath North America), while the transferred plate fragment is long since part of the Pacific plate. Studies of microplate remnants offshore California and Baja California have to rely solely on the plate remnants which attached to the Pacific plate; whether those remnants are entire microplates (microplate capture represents cessation of independent microplate motion) or just microplate fragments (fragment capture and independent microplate motion are not directly related) is difficult to resolve, but possibly affects the plate motion history along parts of the west coast of North America (e.g., the onset of Pacific-North America transform motion at a certain latitude, and the effects of capture on the tectonic development along the western part of the North American plate).

2.5.2 Future of the Explorer Plate

This study would not be complete without speculating on the future of Explorer plate. Plate motions in the Explorer region changed significantly during the last 5 Ma. Before the break-up of Explorer plate from Juan de Fuca plate about 4 Ma ago, the Juan de Fuca plate subducted at a rate of >5 cm/yr beneath North America and moved easterly (azimuth of 105° at 50° N, 130° W) relative to the Pacific plate (*Riddihough, 1984*). After the plate break-up, and until about 2 Ma ago, Explorer plate subducted beneath North America at a

slower rate (average of about 3-4 cm/yr), and motion relative to the Pacific plate shifted clockwise (average azimuth of about 120°) (*Riddihough, 1984*). According to our model, the current Explorer-North America convergence rate is about 1-2 cm/yr, and Explorer plate moves in a south-easterly direction (azimuth of 145°) relative to the Pacific plate (Figure 2.15). Overall, Explorer-Pacific motion shifted about 40° clockwise and became more like Pacific-North America motion (which trends in a 160° direction according to NUVEL-1 [*DeMets et al., 1990*]), and Explorer-North America motion slowed considerably.

A similar slow-down of motion relative to North America has been reported for the Monterey and Arguello microplate remnants now preserved in the Pacific plate offshore California (*Stock and Lee, 1994*). These microplates, which fragmented off the north tip of the southward retreating Cocos plate, supposedly moved independently for only a few Ma before their motion relative to North America ceased (*Stock and Lee, 1994*). Yet, their remnants are now part of the Pacific plate (*Atwater, 1989; Lonsdale, 1991; Stock and Lee, 1994*). Stock and Lee (*1994*) speculated that obliquely compressional Pacific-North America motion across the microplate-Pacific transform boundary could have sheared off the microplate at the continental margin and sutured it to the Pacific plate. Nicholson et al. (*1994*), on the other hand, suggested that Monterey-Pacific spreading simply stopped, causing the microplate to adopt the Pacific plate motions.

Obviously, the reasons and mechanisms for cessation of independent microplate motion are not well understood. We do not attempt a thorough analysis of this problem, which is beyond the scope of this paper, but a brief look at the main driving and retarding forces of plate motions-- "slab pull", "ridge push", and frictional and viscous resistance-- (e.g., *Forsyth and Uyeda, 1975; Turcotte and Schubert, 1982*) suggests that a reduction of slab-pull forces may impede subduction of young, more buoyant oceanic crust. Explorer plate consists entirely of young (< 10 Ma) oceanic material, and a subducting slab has been imaged only south of Brooks peninsula, but not between the peninsula and the Tuzo Wilson seamounts (*Cassidy et al., 1998*); slab-pull forces are probably small (compared to established subduction of old lithosphere along a long trench). Another aspect suggested by Riddihough (*1984*) is that self-driving forces of smaller plates may be overcome by the influence of larger, adjacent plates. It seems possible, then, that Explorer plate might cease to subduct beneath North America in the future (microplate capture).

Figure 2.17 shows four scenarios for Explorer plate's future; all lead to the plate's demise within a few million years. In the simplest case (Figure 2.17 a), current plate motions persist until Explorer plate is completely subducted beneath North America in about 7 Ma. The Pacific-North America plate boundary would extend along the continental margin all the way to Nootka transform, thus lengthening Queen Charlotte fault. The new

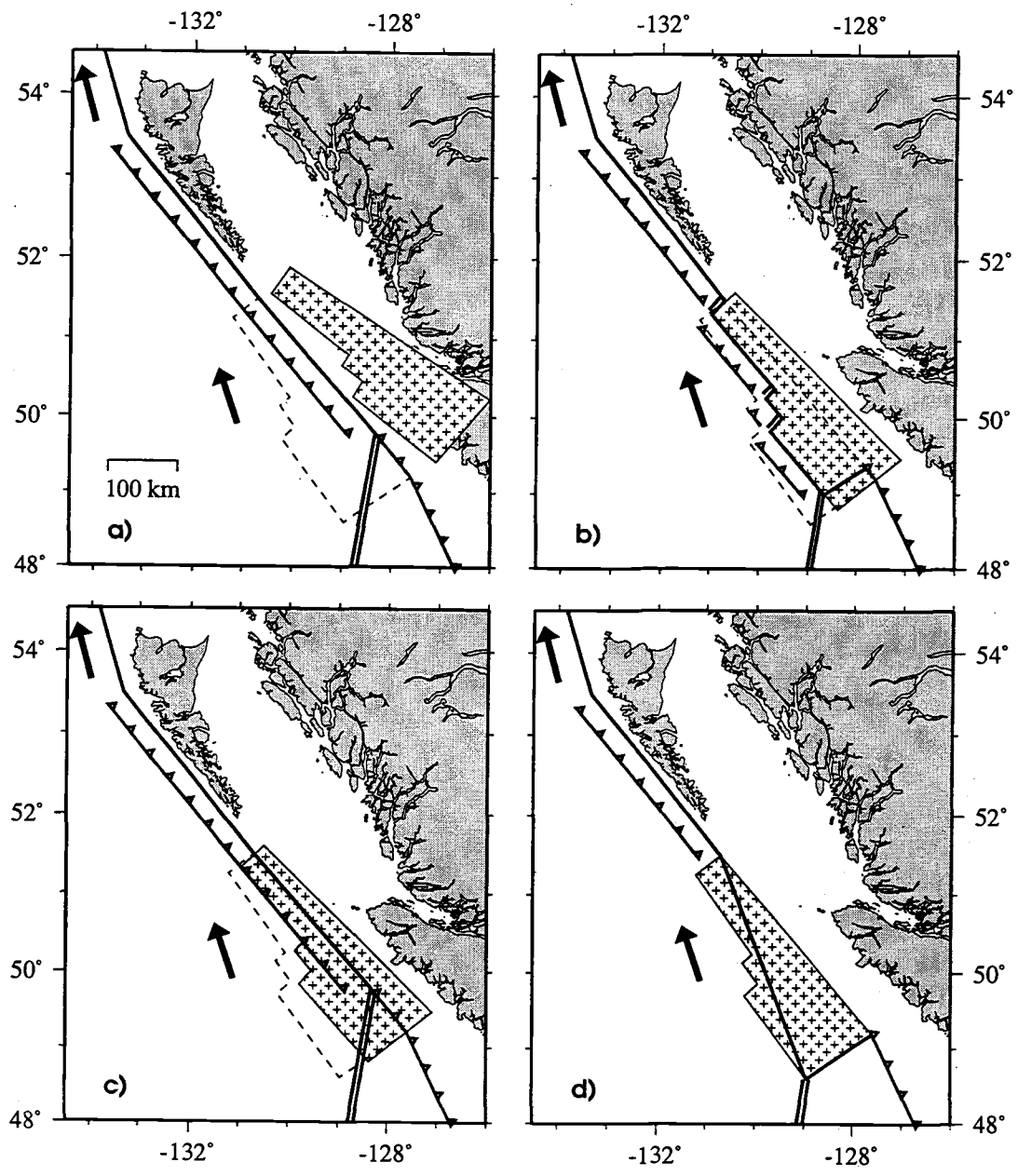

Figure 2.17. Possible scenarios for future evolution of Explorer plate. See text for details. Arrows: Pacific-North America motion direction; solid lines: transform; double lines: spreading segment or pull apart; barbed lines: subduction with barbs in downgoing plate direction; dashes: outline of current Explorer plate. All locations are relative to a fixed North American plate. For simplicity, Explorer-Pacific spreading (or extension) is not considered. a) Explorer plate (stippled) subducts beneath North America. b) Explorer plate captured by North American plate. c) Explorer plate captured by Pacific plate. d) (Defunct) Explorer plate bisected by a Pacific-North America transform identical to Barr and Chase's (*1974*) and Rohr and Furlong's (*1995*) model.

boundary segment would be obliquely oriented to the Pacific-North America motion direction (solid arrows, Figure 2.17), requiring either oblique convergence, intra-plate deformation, or slip-partitioning (depicted in Figure 2.17 a) as observed along the existing southern Queen Charlotte fault. The new plate configuration with a Pacific-North America-Juan de Fuca triple junction offshore Nootka Island would look remarkably similar to the set-up before Explorer plate fragmented from Juan de Fuca plate (e.g., *Riddihough, 1977*).

If Explorer-North America motion stops before subduction is completed, then Explorer plate's remainder could become part of North America (Figure 2.17 b). Capture by North America moves the Pacific-North America boundary to the (former) Explorer-Pacific boundary. The difference in boundary orientation (325°) and Pacific-North America motion direction (340°) implies oblique convergence. This scenario requiring ocean-ocean convergence is unlikely because of buoyancy considerations.

In Figure 2.17 c, Explorer plate remnants become part of the Pacific plate like the Monterey and Arguello microplates described by Stock and Lee (*1994*). Explorer-North America motion stops before subduction is completed; ensuing transpressional Pacific-North America motion across the former Explorer-Pacific transform couples Explorer plate's remnant to the Pacific plate and eventually shears the remnant off North America at the continental margin, which will become the new Pacific-North America boundary. The resulting plate configuration would be identical to case a.

All three above cases imply a long (> 500 km) transpressional Pacific-North America plate boundary. A simple transform fault bisecting Explorer plate and running from Queen Charlotte fault's south tip to the north tip of Juan de Fuca ridge (the tectonic model of Barr and Chase [*1974*] and Rohr and Furlong [*1995*]) could completely accommodate the Pacific-North America plate motions (Figure 2.17 d). Though this scenario requires the initiation of a new transform fault cutting through oceanic crust, we think that the simplicity of the resulting plate motions makes it a possible candidate for Explorer plate's future.

2.6 Concluding Remarks

A very interesting result of our study is the suggested transfer of an Explorer plate fragment to the Pacific plate at a time when the Explorer plate is moving independently. Current independent Explorer plate motion is well constrained by earthquake source mechanisms along the Explorer-Pacific plate boundary (Explorer plate motions-- rates and

directions besides the Explorer-Pacific direction-- are currently not very well resolved; improvements, using earthquake data, require a better understanding of the extent of Nootka fault). The transfer of the plate fragment is based on relocations of larger earthquakes which occurred during the last 80 years, a very short time span in tectonic terms; but we think the consistency of our relocations indicates that the current plate boundary is north of western Sovanco Fracture zone.

Tectonic models developed to explain preserved microplate fragments offshore California and Baja California assumed that the capture of the fragments implied capture of an entire plate and, thus, cessation of independent microplate motion. In comparison, our result indicates that plate fragments can transfer from a microplate to a surrounding bigger plate, while the microplate remains tectonically independent. Analysis of previous and current plate motions suggests that the transfer is the result of changes in the relative motions of the Explorer plate, which are possibly related to the difficulties the young, buoyant Explorer crustal material has subducting beneath North America. The plate motion changes created a space problem along the Explorer-Pacific plate boundary; we speculate that the microplate is weaker and more easily deformable, and, thus, responded by fragmenting.

We speculate further, that capture of crustal material probably occurs on all scales-- from small fragments to entire microplates. The example of the captured Explorer plate fragment, then, represents just one of many possible scenarios with the details of the material transfer determined by the geometries and relative motions of the plates involved.

2.7 Appendices

2.7.1 Appendix A - Waveform Fits

In this appendix, we present examples of waveform fits and source parameter uncertainty estimates from regional moment-tensor analysis for five earthquakes (for all a RMT and a CMT solution exist). Double-couple orientations (strike/dip/rake) follow the convention of Aki and Richards (*1980*). Centroid depths are given relative to the seafloor.

2.7.1.1 January 3, 1994, offshore Nootka Island (Figure 2.18)

The January 3, 1994 earthquake near Nootka Island was our first RMT solution in the Explorer region. The event pre-dates installation of near-by stations PHC, OZB, and CBB on Vancouver Island (Figure 2.2). We use 28 seismograms from 10 stations to obtain the source parameters in the low-frequency 0.016-0.033 Hz pass-band. The match between synthetic and observed waveforms is very good. The azimuthal-dependent amplitude variations tightly constrain the source mechanism (254/40/332), which is almost identical to the CMT solution (251/41/334).

The event's source parameters are well resolved. Uncertainties in strike, dip, and rake were estimated by observing the variance increase relative to the best fit model (lower right of Figure 2.18). Assuming a northward dipping fault and a 20 km centroid depth, we find strike and dip are more tightly constrained than rake. A 5% variance increase results in uncertainty estimates of about ±5° for strike and dip, and ±10° for rake. A more rigorous statistical *t-test* (*Huang et al., 1986*), applied to all RMT solutions in the Explorer region, revealed that a 5% variance increase is commonly equivalent to a 75% to 90% confidence level. The well resolved centroid depth of 20 km (lower left of Figure 2.18) is consistent with the CMT estimate of 21 km and the Pacific Geoscience Centre's hypocenter depth of 22 km. A 5% variance increase results in a centroid depth uncertainty of about ±6 km. The fault plane solution is stable over a wide depth-range. The seismic moment at the best-fit depth (2.83×10^{17} Nm, $M_w = 5.6$) is almost identical to the CMT estimate (2.89×10^{17} Nm).

2.7.1.2 June 21, 1995, Revere-Dellwood-Wilson Transform (Figure 2.19)

The June 21, 1995 earthquake on the northwest part of the Revere-Dellwood-Wilson transform illustrates source parameter retrieval when data from only a few stations are available. The event pre-dates installation of near-by stations PHC, OZB, CBB, and MOBC (Figure 2.2), and four of the five available stations are more than 500 km from the epicenter. We thus inverted the 15 seismograms in the low-frequency 0.016-0.033 Hz

Figure 2.18. Upper part: Observed (solid) and synthetic (dashed) seismograms for the best-fit model in the 30- to 60-sec period passband for the January 3, 1994 earthquake. Z, R, and T are vertical, radial, and transverse components. All seismogram amplitudes are normalized to an epicentral distance of 100 km assuming cylindrical geometrical spreading. The stations are listed in azimuthal order; numbers beneath station codes are event-station azimuth and distance. The triangles on the fault plane solution (lower hemisphere projection) depict the station coverage. Lower left: Residual variance reduction versus centroid depth. Numbers beneath the fault plane solutions are seismic moment (in 1017 Nm) and percent double couple of moment-tensor solution. Lower right: Residual variance reduction versus deviation from best-fitting double couple mechanism for 20 km centroid depth and northward dipping fault. The dashed line represents a 5% variance increase relative to best-fit double couple.

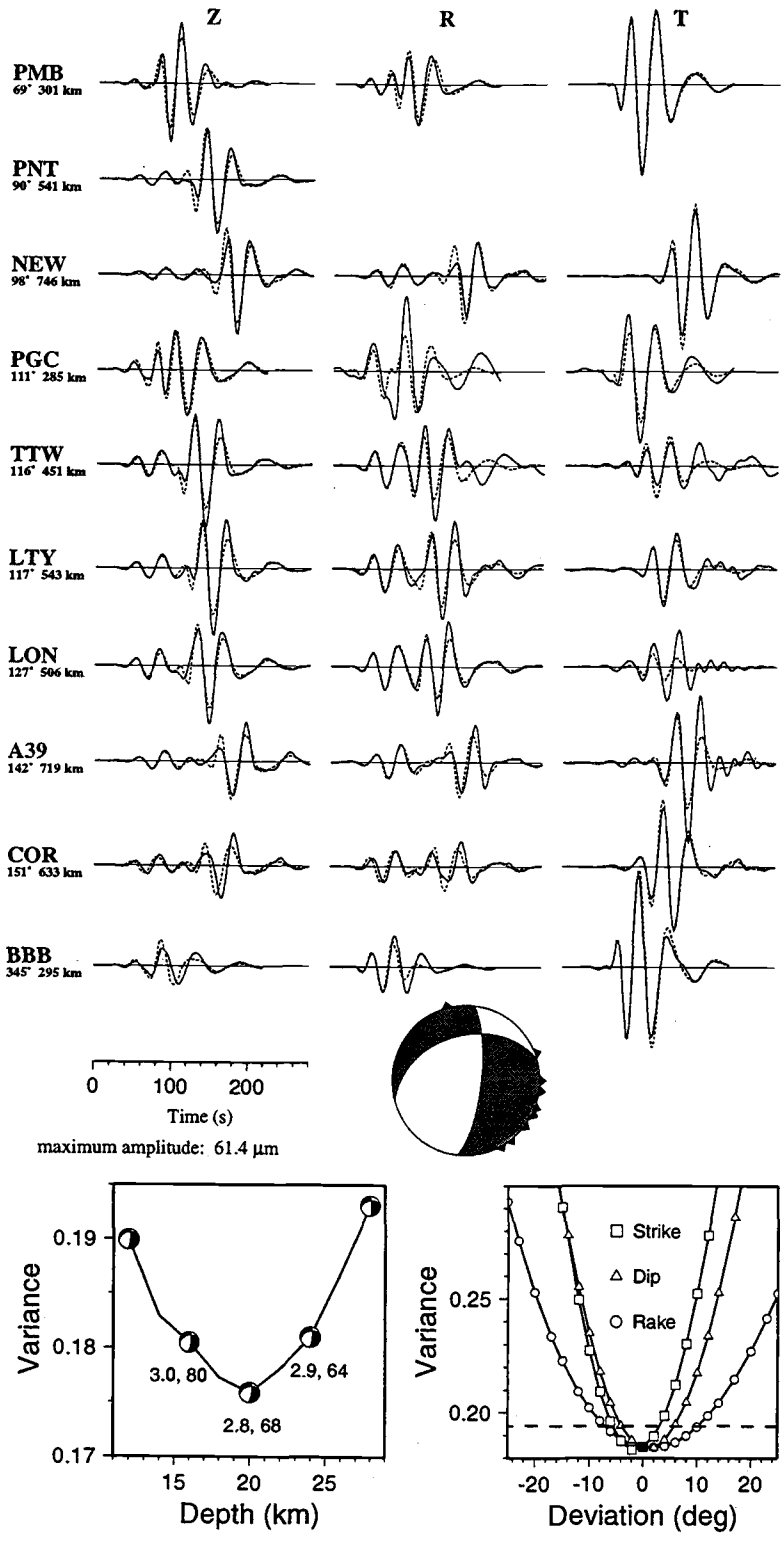
Z
R
T
PMB
69° 301 km
PNT
90° 541 km
NEW
98° 746 km
PGC
111° 285 km
TTW
116° 451 km
LTY
117° 543 km
LON
127° 506 km
A39
142° 719 km
COR
151° 633 km
BBB
345° 295 km
0
100
200
Time (s)
maximum amplitude: 61.4 μm
Variance
0.19
0.18
0.17
3.0, 80
2.9, 64
2.8, 68
15
20
25
Depth (km)
Strike
Dip
Rake
Variance
0.25
0.20
-20
-10
0
10
20
Deviation (deg)

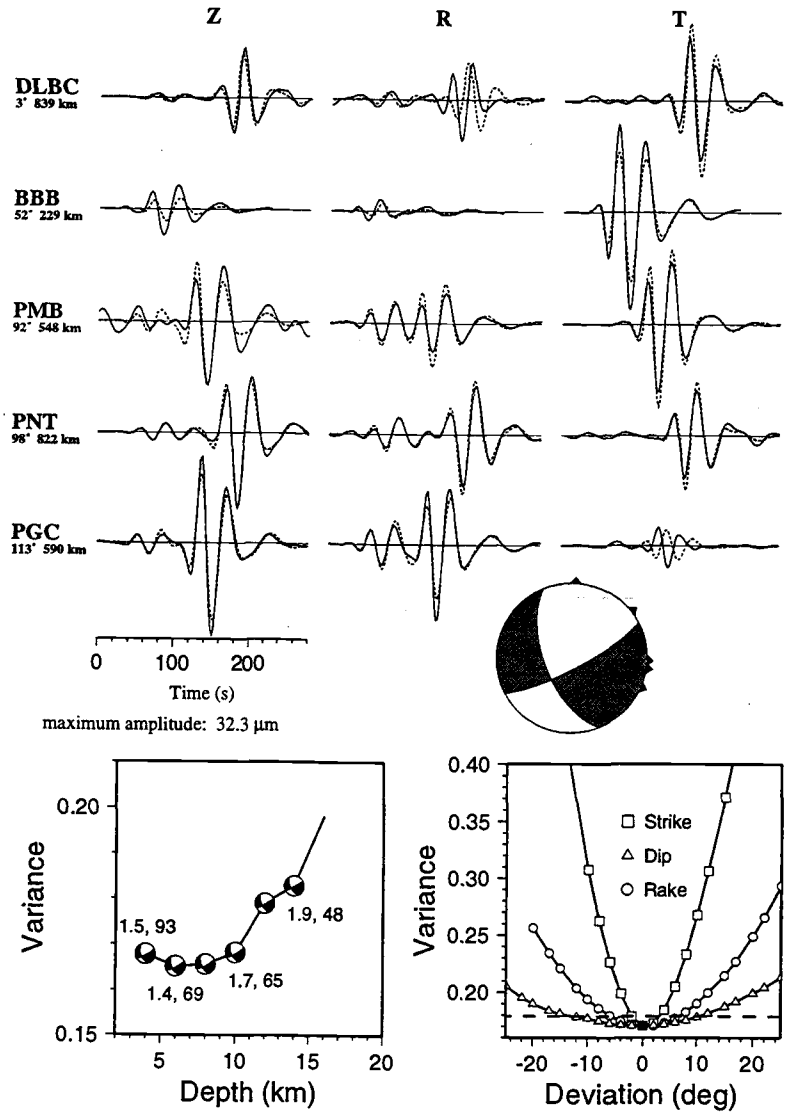

Figure 2.19. Waveform fit in the 30- to 60-sec period passband for the June 21, 1995 earthquake, and variance versus centroid depth and deviation from best double couple mechanism. See Figure 2.18 for further details.

pass-band. The synthetics generally match the observed waveforms well, except for the wave shape of the low-amplitude (nodal) transverse component at station PGC. The strong azimuthal-dependent amplitude variations constrain the mechanism (158/61/193), and the fault plane solution agrees with the CMT solution (161/90/175).

The earthquake was shallow (best-fit centroid depth of 6 km). The variance reduction plot shows a broad minimum between 4-12 km, due to the low frequencies used for inversion. The fault plane solution is stable over a wide-depth range, and the seismic moment (1.45×10^{17} Nm, $M_w = 5.4$) agrees well with the CMT estimate (1.51×10^{17} Nm). Assuming a northwest trending fault plane and 6 km centroid depth, the bounds for a 5% variance increase are ±2°, ±15°, and ±5° for strike, dip, and rake, respectively. For the earthquakes in our study, strike is generally very well resolved-- even when seismograms from only a few stations are available.

2.7.1.3 October 6, 1996, Nootka Transform (Figure 2.20)

The Nootka transform earthquake of 20:13 UTC, October 6, 1996 was the largest event ($M_o = 2.40 \times 10^{18}$ Nm, $M_w = 6.2$) in the Explorer region during the last 4 years. The waveform fit in the 0.01-0.05 Hz pass-band is generally good; the strike-slip mechanism (41/86/335) agrees with the CMT solution (46/86/8). The shallow centroid depth of 4 km is well resolved. Assuming a northeast trending fault plane and a centroid depth of 4 km, the bounds for a 5% variance increase are ±3°, +5° to -10°, and ±15° for strike, dip, and rake, respectively.

2.7.1.4 October 9, 1996, Southwest Explorer Transform Boundary (Figure 2.21)

The strike-slip source mechanism (147/75/153) for the 07:12 UTC, October 9, 1996 event ($M_o = 5.77 \times 10^{17}$ Nm, $M_w = 5.8$) on a transform fault north of western Sovanco Fracture zone agrees with the CMT solution of 332/72/184. The waveform fit in the 0.01-0.04 Hz pass-band is generally good. The 6 km, shallow centroid depth is well resolved.

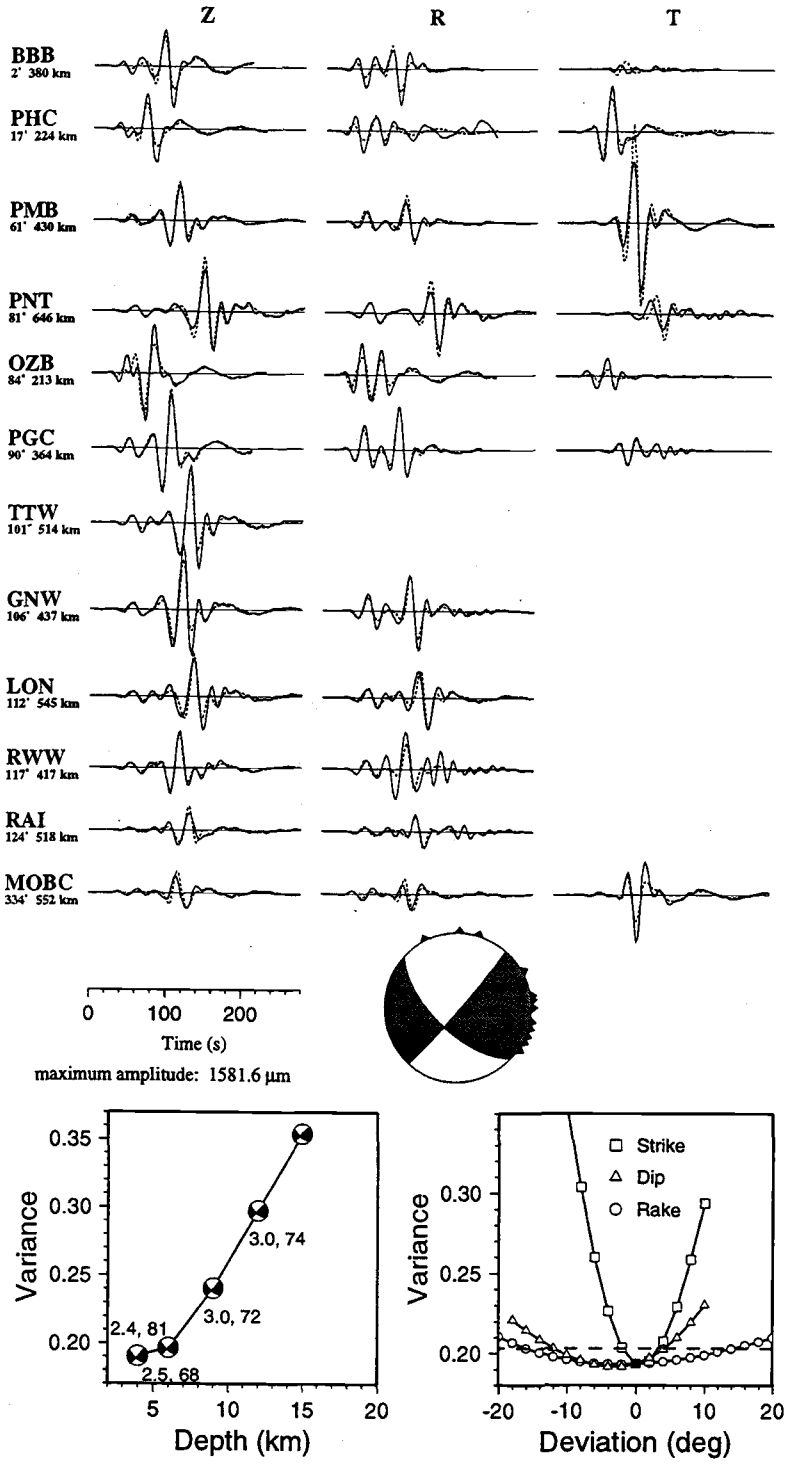

Figure 2.20. Waveform fit in the 20- to 100-sec period passband for the 20:13 UTC, October 6, 1996 earthquake, and variance versus centroid depth and deviation from best double couple mechanism. See Figure 2.18 for further details.

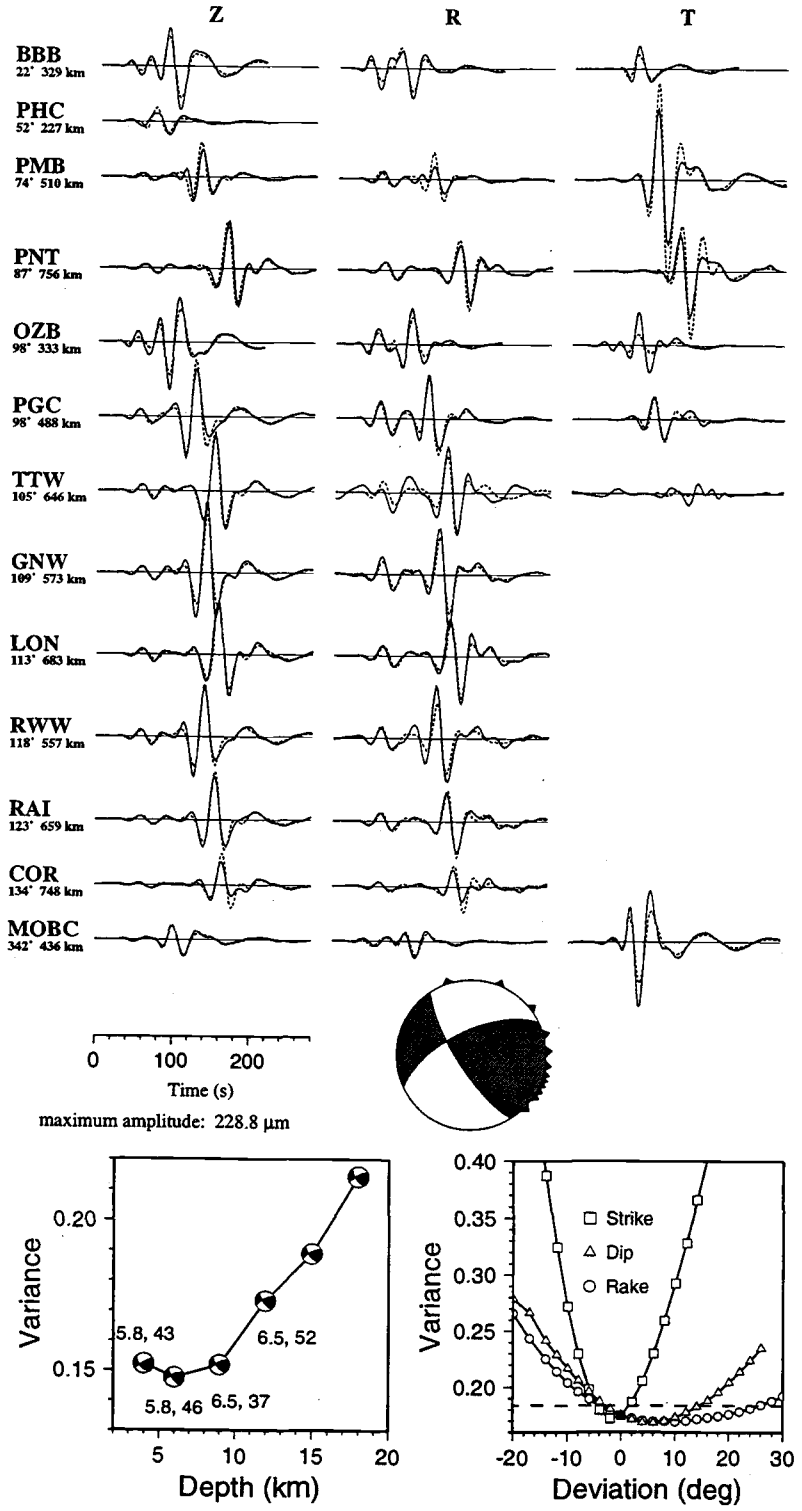

Figure 2.21. Waveform fit in the 25- to 100-sec period passband for the 07:12 UTC, October 9, 1996 earthquake, and variance versus centroid depth and deviation from best double couple mechanism. See Figure 2.18 for further details.

For a northwest trending fault and 6 km centroid depth, the bounds for a 5% variance increase are ±4°, +15° to -5°, and +25° to -5° for strike, dip, and rake, respectively.

2.7.1.5 September 20, 1997, Revere-Dellwood-Wilson Transform (Figure 2.22)

The normal faulting mechanism (61/79/284) for the 07:09 UTC, September 20, 1997 earthquake (M_o = 1.37 x 10^{16} Nm, M_w = 5.4) on the Revere-Dellwood-Wilson transform appears to disagree from the strike-slip CMT solution (347/63/189). The CMT solution, however, was fixed to a centroid depth of 15 km. Our solution, for a 15 km centroid depth, becomes more strike-slip and starts to approach the CMT solution (see fault plane solutions in lower left inset of Figure 2.22). Our shallow centroid depth of 4 km is well resolved, and the discrepancy between RMT and CMT solution is partly explained by the fixed CMT depth. In addition, the event is relatively small for CMT analysis. The unusually large CLVD component (less than 4% of the about 15000 existing CMT's have a higher CLVD) and the large relative moment-tensor error (for definition see *Davis and Frohlich, 1995*)-- only about 20% of all CMT's have a larger relative error-- indicate that the CMT solution is not well constrained.

The slip vector azimuth estimate, important for tectonic interpretation, is not much affected by the discrepancy between the fault plane solutions. Assuming a westward-dipping fault plane, the RMT slip vector azimuth is 331°, whereas the CMT estimate is 342°.

2.7.2 Appendix B - Relocation of pre-1964 Earthquakes

In this appendix, we relocate large older earthquakes which could have occurred in or near Explorer region's southwest corner.

We selected all M ≥ 6 earthquakes that occurred from 1918 to 1963-- the time span covered by the International Seismological Summary (ISS) arrival time data-- and were listed by the ISS, the Canadian Earth Physics Branch (EPB), or the Gutenberg and Richter (*1954*) catalogs to have occurred in the Explorer region south of 50° N and west of 129.5°

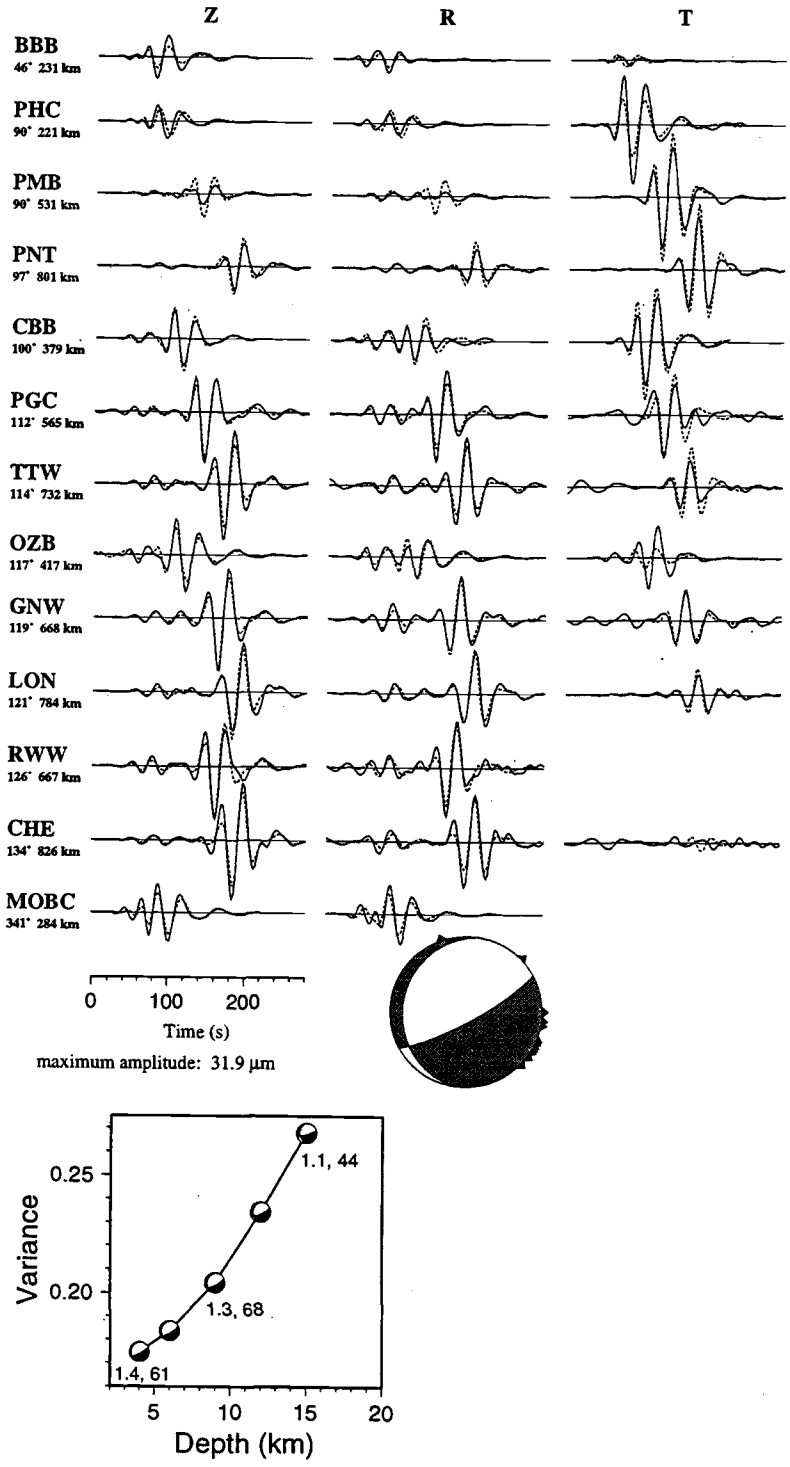

Figure 2.22. Waveform fit in the 25- to 50-sec period passband for the 07:09 UTC, September 20, 1997 earthquake, and variance versus centroid depth. See Figure 2.18 for further details.

W. The teleseismic ($\Delta \geq 16°$) P wave arrival time data set is rather sparse. We thus relocated the historic earthquakes relative to the post-1963 events shown in Figure 2.7 with the JED technique. Holding the locations and origin-times of the more recent, generally better recorded events fixed essentially froze the station correction terms; this stabilized the relocation of the historic events. Earthquake depths were fixed to 10 km. Table 2.4 lists the relocated epicenters shown in Figure 2.9.

For the events investigated which occurred during 1941, only stations in the United States and Canada reported arrival time data. This severely restricts the azimuthal coverage thus degrading the location quality. For the October 1, 1941 event, we added regional picks to the teleseismic arrival time data to improve the azimuthal coverage; this helped to constrain the event's longitude (Figure 2.9 and Table 2.4). We could not reliably relocate the November 6, 1941 earthquake listed in the EPB catalog as a M = 6 event at 49.35° N and 129.83° W. Most arrival times come from California stations southeast of Explorer region, which cover only a narrow azimuthal sector, and a single pick from the College/Alaska station to the northwest very strongly affects the location estimate. With the College pick the epicenter is at about 49° N/130° W and without at 48° N/125° W. Because of the sensitivity of this event's location to a single arrival time pick, we decided not to include this event.

2.7.3 Appendix C - Seismic Slip Rate Estimates

In this appendix, we compare seismic slip rates for several segments along Explorer region's plate boundaries with predicted plate motion rates to determine if earthquakes contribute significantly to the plate motions.

Seismic slip rate of a fault is its cumulative seismic moment divided by area, rigidity, and time window. We assumed a rigidity of 3.5×10^{10} N/m^2 and an uniformly 10 km wide seismogenic layer based on the RMT centroid-depth distribution (Figure 2.4). Segment lengths listed in Table 2.5 were estimated from bathymetry and seismicity (Figures 2.7-2.9).

We added magnitude estimates from the ISC, PDE, EPB, and the Decade of North American Geophysics (DNAG) catalogs covering the last 80 years to the moment-tensors for the cumulative seismic moments. The catalogs provide only magnitude estimates which we converted to seismic moment using a moment-magnitude relationship (*Hanks and*

Table 2.4. Pre-1964 Earthquake Relocations in Explorer Region's Southwest Corner.

Date	Mag	Lat (°N)	Lon (°W)	NA	AzGp (°)
3509232212	6.2 PAS	49.45	128.89	22	210
3901031718	5.6 PAS	49.43	129.63	10	190
3902080539	6.5 EPB	48.88	128.06	9	194
3907180326	6.5 EPB	48.87	129.73	36	188
4110011949*	6.0 EPB	48.94	129.35	16	284
4206091106	5.7 EPB	49.63	129.06	9	194
4607180606	6.5 EPB	49.40	130.04	35	158
4607180716	6.5 EPB	49.32	129.93	29	158
6206021226	5.8 EPB	49.77	130.07	30	149

Date: year month day hour minute. Mag: magnitude and source; PAS: Pasadena, EPB: Earth Physics Branch, Canadian Geological Survey, Ottawa. Lat, Lon: relocated latitude and longitude. NA: number of arrival time picks used in relocation; AzGp: maximum azimuthal gap between two stations. *: relocated using regional and teleseismic P wave arrival time data; all other events: teleseismic data only.

Table 2.5. Seismic Slip Rates vs. Plate Motion Rates.

Segment	Length (10^3 m)	EV (#)	LEV (#)	$\Sigma(M_o)$ (10^{18} Nm)	LCO (%)	RATE (mm/yr)	Model A (mm/yr)	Model B (mm/yr)	R (mm/yr)	WIL (mm/yr)
RDW	150	202	30	141.5	97	34	46	56	44	
ER	50	67	13	8.4	67	6	47	57	42	
SWE	70	49	14	49.8	96	25	48	58	40	
ED	?	45	3	7.1	70	?				
ESDZ	80	107	20	37.9	90	17	49	59	39	
NOO	150	62	9	64.0	96	15	24	25	29	45
	150	61	8	13.9	83	3	24	25	29	45
	100	47	5	11.8	83	4	24	25	29	45

We assumed an uniform seismogenic width of 10 km, a rigidity of 3.5×10^{10} N/m^2, and 80 years of data coverage for each segment. Segment: RDW Revere-Dellwood-Wilson transform, ER Explorer Rift, SWE Southwest Explorer transform boundary, ED Explorer Deep, ESDZ Eastern Sovanco Deformation Zone, NOO Nootka transform. Length: estimated segment length. EV: number of events. LEV: number of $M \geq 5.5$ events. $\Sigma(M_o)$: cumulative seismic moment. LCO: contribution of $M \geq 5.5$ events to cumulative seismic moment. RATE: seismic slip rate estimate. Model A, Model B, R, WIL: plate model rate estimates, Model A, Model B: this study, R: Riddihough (*1984*), WIL: Wilson (*1993*). See text for explanation for NOO segment.

Kanamori, 1979). We first applied the relationship to events with a RMT or CMT solution to compare the moment magnitudes (M_W) with the body (m_b) and surface (M_S) wave magnitude estimates (Figure 2.23). For our data set, we found that an events' m_b is systematically smaller (on average by 0.46 magnitude units) than its M_W, and that M_S and M_W are equivalent only for $M_S \geq 5.8$. We thus added 0.46 magnitude units to m_b before applying the moment-magnitude relationship to the smaller catalog events ($M < 5.8$) and only converted larger events ($M \geq 5.8$) directly.

We considered six segments: Revere-Dellwood-Wilson, Explorer Rift, Explorer Deep, north of western Sovanco, ESDZ, and Nootka. Assigning relocated events (Figure 2.7) was straight forward. For other events, we removed the average bias found from relocation (15 km south, 22 km west) before assigning events to a segment (Figure 2.24). The large number of $M \geq 4$ events-- 520-- de-emphasizes questionable assignments. The sizes of the selection boxes are appropriate considering location errors for old events are significant.

The resulting slip rate estimates (Table 2.5) agree well with Hyndman and Weichert's (*1983*) results and imply that a large percentage of the predicted plate motions (Table 2.5) are accommodated seismically. Considering the effects introduced by erroneous assessments of fault area, rigidity and cumulative seismic moment (catalog completeness, segment assignment, magnitude-moment conversion, moment vs. moment-tensor summation), we suggest our seismic slip rates are good within a factor of two, and random errors outweigh systematic errors greatly.

Three seismic slip rate estimates are listed for Nootka transform. The first and second assume the active fault extends beneath the North American margin to Nootka Island. The first estimate (1.5 cm/yr) is almost entirely dominated by one $M_S = 7.2$ earthquake beneath Nootka Island which probably occurred above the transform in North American crust (*Cassidy et al., 1988*); excluding that event results in the second estimate (0.3 cm/yr). The third estimate (0.4 cm/yr) assumes the active Nootka fault ends near the continental margin (dashed boundaries Figure 2.24) which is consistent with our Model B plate motion model.

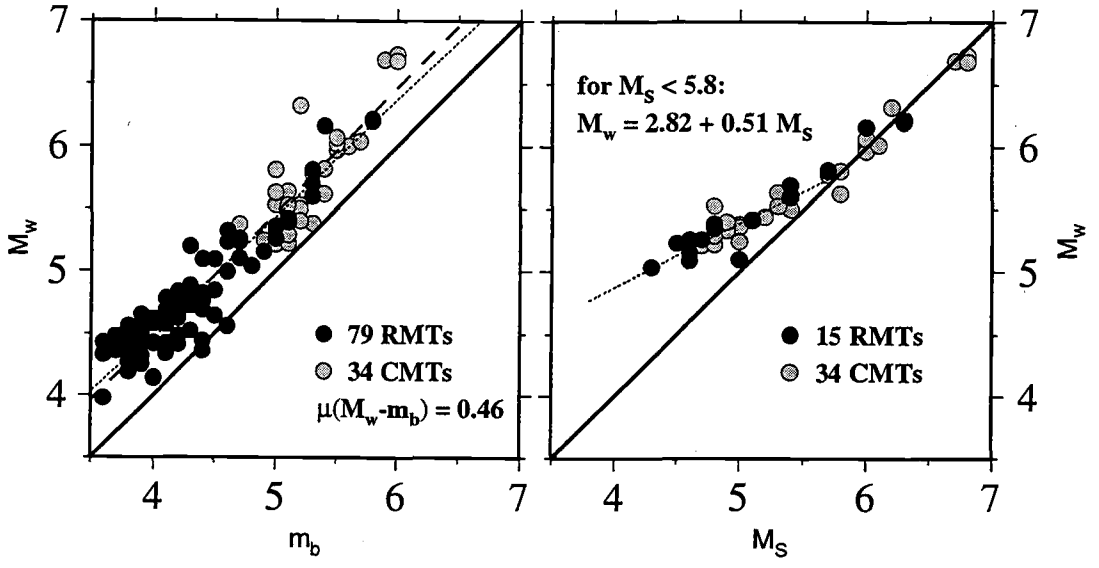

Figure 2.23. Left: moment-magnitude (M_W) vs. body wave magnitude (m_b). Right: M_W vs. surface wave magnitude (M_S). Black circles: regional moment-tensor solutions (RMT), gray circles: Harvard centroid moment-tensor solutions (CMT). For one-to-one correspondence between the magnitude scales, all circles would fall on the diagonal (solid black line). M_W-vs.-m_b: On average M_W is 0.46 units bigger than m_b (long dashes); the least squares fit (short dashes) is only insignificantly different from the average difference (i.e., slope close to 1). M_W-vs.-M_S: For $M_S \geq 5.8$, M_W and MS are equivalent; for $M_S < 5.8$ (and $M_S > 4.2$), linear regression results in $M_W = 2.82 + 0.51 \times M_S$ (short dashes).

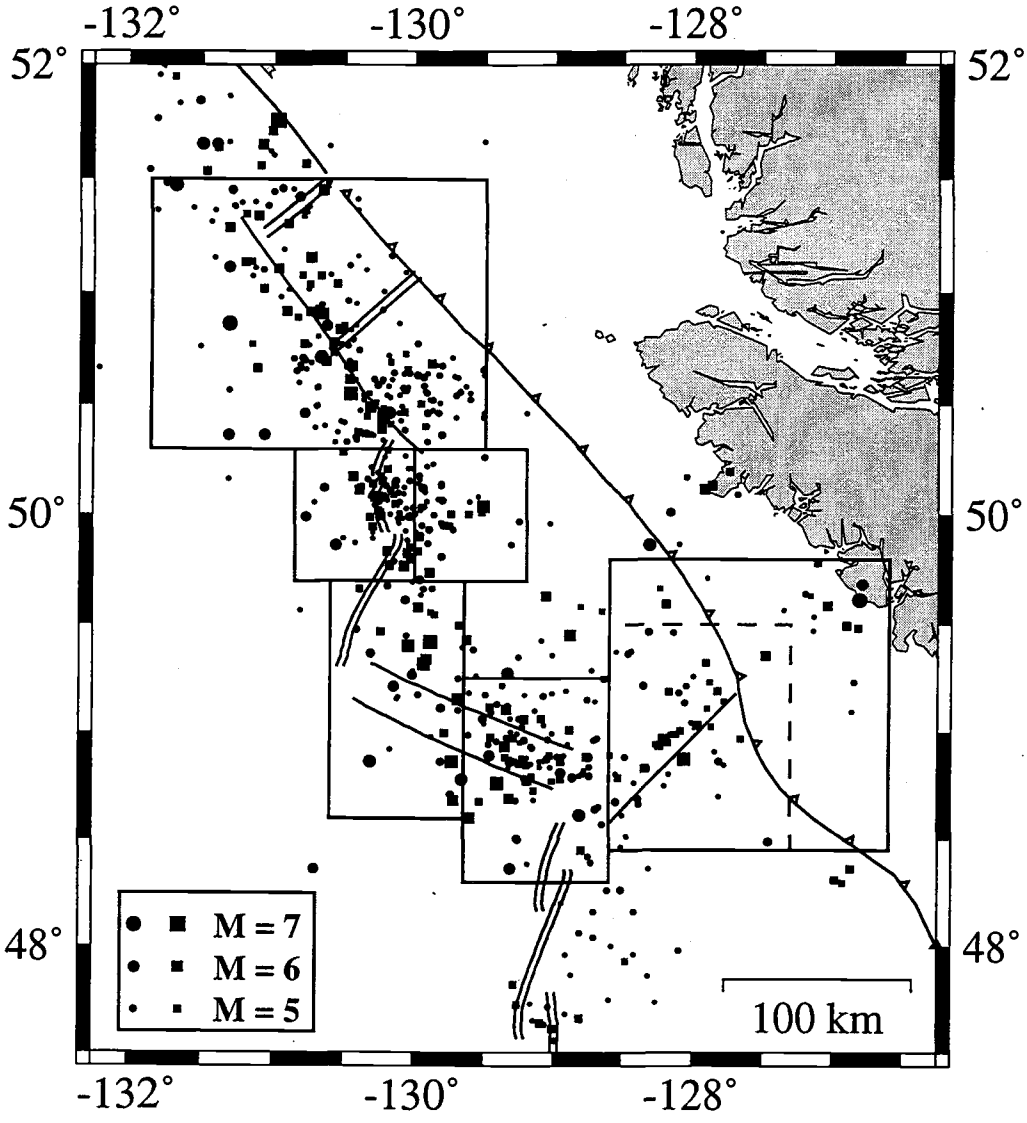

Figure 2.24. Magnitude ≥ 4.0 earthquakes in Explorer region (1912-1997) used for seismic slip rate estimates (from ISC, PDE, EPB, and DNAG catalogs, CMT and RMT solutions). Events are plotted on their relocated epicenter (squares). For not-relocated events (circles), we moved the epicenters by the average relocation bias (15 km to south, 22 km to west). We divided the Explorer plate boundary in six segments (Table 2.5) and assigned all events inside a box to that segment (see text for Nootka fault boxes).

3. SEISMOTECTONICS OF THE BLANCO TRANSFORM FAULT ZONE

3.1 Introduction

The recent establishment of a broadband seismograph network along the coast of the Pacific Northwest and the availability of data from Navy's offshore SOSUS (Sound Surveillance System) hydrophone arrays for earthquake studies provided the framework for long-term monitoring of the seismicity along the entire Blanco Transform Fault Zone (BTFZ). Previously, detailed, long-term seismotectonic studies of oceanic transform fault systems had been impossible due to the remoteness of those features. Thus, earlier studies roughly fall into two categories. In the first, researchers relied on teleseismic data (recorded several thousand kilometers away from the earthquake epicenters), mainly to determine the source mechanisms and the seismicity distribution (e.g., *Bergman and Solomon, 1988; 1992; Engeln et al., 1986; Wolfe et al., 1993; Goff et al., 1987; Kanamori and Stewart, 1976*) of the relatively infrequent larger earthquakes, while the second category involves short-term deployments of ocean bottom seismometers and analysis primarily of micro-earthquakes (e.g., *Tréhu and Solomon, 1983; Wilcock et al., 1990*). In this chapter, we present the results of the first five years of monitoring the BTFZ, which already present a more comprehensive and detailed picture of the seismic activity and deformation style of an oceanic transform fault system than ever before.

The BTFZ is a 350 km long transform fault zone which forms the Pacific-Juan de Fuca plate boundary connecting the Gorda and the Juan de Fuca ridge (Figure 3.1) in the northeast Pacific ocean. Based on high-resolution SeaBeam bathymetry, Embley and Wilson (*1992*) divided the BTFZ into five transform fault segments which are separated by deep basins. A 150 km-long, continuous transform segment follows Blanco Ridge which is the dominant feature in the eastern part of the BTFZ (*Ibach, 1981; Embley and Wilson, 1992; Dziak et al., submitted to Mar. Geophys. Res.*). Embley and Wilson (*1992*) suggested four additional, shorter transform segments: one at the east end of the BTFZ running from Gorda Ridge to Gorda Depression, and three segments along the western part of the BTFZ connecting the Cascadia, Surveyor, and East Blanco depressions with Juan de Fuca ridge. A lineation, which runs from Cascadia Depression for about 150 km to the northwest and forms the south side of Parks Plateau, has been interpreted as a formerly

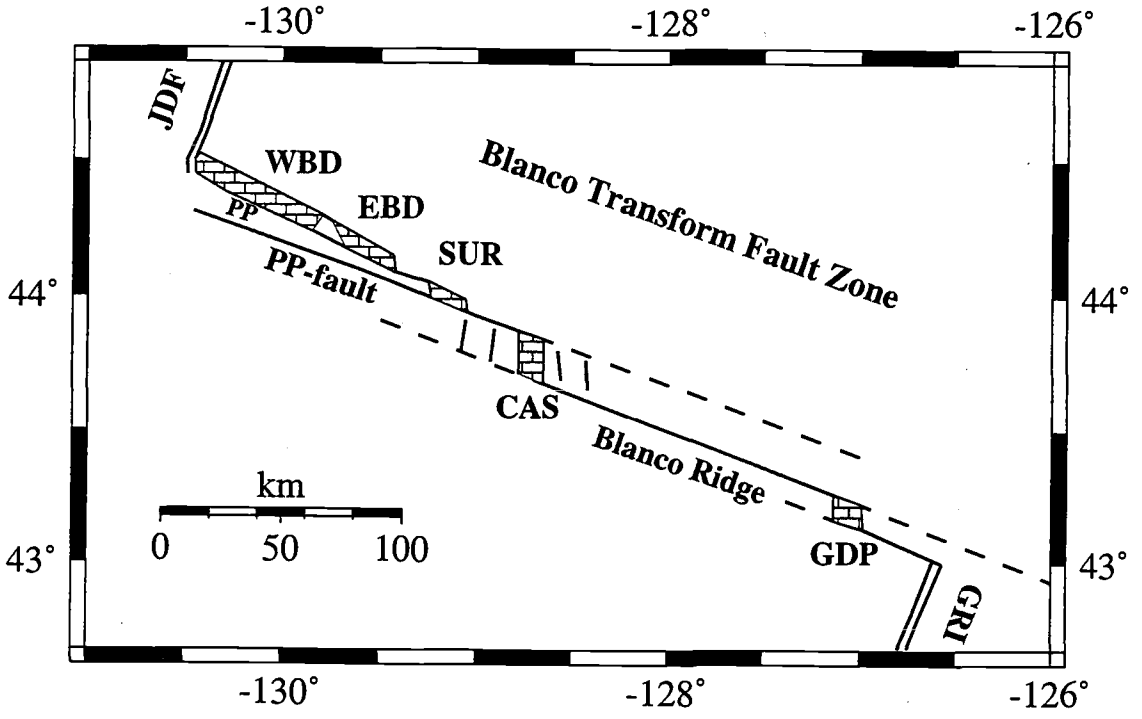

Figure 3.1. Schematic map of the Blanco Transform Fault Zone following the interpretation of Embley and Wilson (*1992*). Solid, northwest trending lines are active transform faults, dashed lines are inactive fault traces, the basins are stippled, and north trending solid lines near CAS are normal fault scarps. Juan de Fuca (JDF) and Gorda (GRI) ridges are shown as double lines. GDP, CAS, SUR, EBD, and WBD are the Gorda, Cascadia, Surveyor, East Blanco, and West Blanco depressions, PP refers to Parks Plateau.

(*Embley and Wilson, 1992; Dauteuil, 1995*) or currently active transform fault (*Delaney et al., 1981*). Micro-earthquake activity has been reported (*Johnson and Jones, 1978*) inside the largest basin-- Cascadia Depression in the central part of the BTFZ-- with tectonic subsidence of 1.8 cm/yr over the last 6600 years inferred by Griggs and Kulm (*1973*). Basement doming in the basin's center inferred from seismic reflection data led DeCharon (*1989*) and Embley and Wilson (*1992*) to suggest ongoing seafloor spreading. The smaller basins along the BTFZ, however, were interpreted to be oceanic analogs to pull-apart structures along divergent continental wrench-fault systems (*Embley and Wilson, 1992*). The BTFZ is seismically very active (e.g., *Tobin and Sykes, 1968; Bolt et al., 1968; Chandra, 1974; Dziak et al. 1991*), but a detailed seismotectonic study has been impossible due to the lack of precise earthquake locations and earthquake source mechanisms.

The broadband seismograph array (Figure 1.1), deployed over the last several years, consists of more than twenty digital three-component broadband high-dynamic range seismic stations that are distributed along coastal northern California, Oregon, Washington, and British Columbia and provide data of unprecedented quality. We have routinely determined source parameters of small to moderate sized ($M \geq 4.0$) earthquakes by modeling the regional waveforms since 1994, when the station distribution became sufficient for analysis. In addition to our regional moment-tensors solutions, we also include the Harvard centroid moment-tensor solutions (*Dziewonski et al., 1994*, and references therein) available for larger earthquakes since 1976; both methods use robust waveform matching techniques providing reliable earthquake source parameters.

Land based earthquake locations fall consistently to the northeast of the transform fault zone defined by the bathymetry (*Dziak et al., 1991*). We thus relocated all larger earthquakes using teleseismic arrival time data. These relocations also provide a comparison with the locations based on SOSUS, whose performance for earthquake studies has not yet been fully independently checked.

The SOSUS hydrophone arrays, operated by the US. Navy, are designed to record long-range acoustic signals for military purposes. Several arrays are located in the northeast Pacific, though their exact placement is a secret. Researchers at the National Oceanic and Atmospheric Agency laboratory in Newport/OR, headed by C. Fox and R. Dziak began utilizing these arrays in 1991 to locate earthquakes in the Juan de Fuca region. The very slow, well-known propagation speed of acoustic signals (T-phase) in the water column permits very precise location of the acoustic signal's source (*Fox et al., 1995*)-- comparable in quality to earthquake locations within a local land-network; additionally, the efficient propagation of the acoustic signals allows detection of earthquakes of much smaller magnitude than is possible by conventional means (*Fox et al., 1994*).

With the improved data set, we can address outstanding questions of regional and global significance. For example: how do the earthquake locations and source mechanisms compare with segmentation of the BTFZ inferred from SeaBeam bathymetry (*Embley and Wilson, 1992*)? Unusual source mechanisms in the vicinity of oceanic transform faults have been attributed to compressional jogs or extensional offsets (*Wolfe et al., 1993*); are the inferred pull-apart basins (*Embley and Wilson, 1992*) seismically active, and are their source mechanisms consistent with extension? What is the depth extent of faulting; how do the centroid depths along the BTFZ compare with depths along other oceanic transform faults determined from short-term micro-earthquake studies (e.g., *Reichle et al., 1976; Tréhu and Solomon, 1983; Wilcock et al., 1990*)? A good agreement between cumulative seismic slip rates and plate motion rates has been reported for several oceanic transform faults-- e.g., for the Gibbs fracture zone (*Kanamori and Stewart, 1976*), for the Romanche and Jan Mayen transform faults (*Brune, 1968*), for the Romanche, Bullard, and Conrad transform faults (*Stewart and Okal, 1981*), and for the transform faults in the Gulf of California (*Reichle et al., 1976; Goff et al., 1987*); in contrast, seismic slip along the Eltanin fracture zone accounted for less than ten percent of the predicted plate motion rate from 1920-1981 (*Stewart and Okal, 1983*). Contradicting results exist for the BTFZ (*Hyndman and Weichert, 1983; Dziak et al., 1991*); we reexamine the cumulative seismic slip rate along the BTFZ, and, using the improved locations, also map the seismic slip distribution along the length of the BTFZ.

3.2 Data and Methods

3.2.1 Earthquake Moment Tensors

We use complete three-component regional seismograms recorded by the broadband seismograph network located in the Pacific Northwest of the US and British Columbia (Figure 1.1) to determine the earthquake source parameters (seismic moment-tensor, centroid depth, seismic moment, and source time history). The regional moment tensor (RMT) method is described in Chapter 2, and for a more detailed description we refer to

Nábelek and Xia (*1995*). For calculating synthetic seismograms (*Bouchon, 1982*), we used an oceanic crustal model (Table 3.1).

The actual frequency band used for inversion depends on earthquake size and signal-to-noise ratio. In most cases we use the 0.02-0.05 Hz band; for larger events with better low-period signal-to-noise ratio, we change the high-pass to 0.01 Hz. Three-component data are used whenever possible; however, noisy traces are discarded. On average, 25-30 waveforms from more than a dozen stations are used for the inversion.

Routine analysis began in January 1994 and since then, we have determined the source parameters of more than 120 earthquakes distributed along the entire length of the fault zone. Strike-slip source mechanisms dominate, but we also found normal faulting events which were generally located in or near one of the deep basins. These mechanisms are listed in Table 3.2. Based on more detailed investigations of parameter uncertainties (chapter 2 of this thesis; *Braunmiller et al., 1995a*), we estimate average uncertainties in strike, dip, and rake of ±5°, ±15°, and ±20°. Source mechanisms are discussed in chapter 3.4.

The earthquakes range in size from moment magnitude M_W 3.8 to 6.5; the size distribution (Figure 3.2 top) indicates that our catalog is complete down to about M_W = 4.4-4.5. The frequency-size distribution (Figure 3.2 middle) shows the number of earthquakes N greater or equal to M_W versus M_W. The slope b of the distribution describes the relative rate of occurrence between small and large events. In the magnitude range where the catalog is complete, b is about 1, which is consistent with global averages (e.g., *Scholz, 1990*). Not included in the linear regression are data points associated with the larger events ($M_W > 5.4$), since their occurrence rate is not well constrained by the short, five year time-span covered by the analysis.

The centroid depth distribution of the earthquakes (Figure 3.2 bottom) indicates that most events occurred at shallow depths (4 and 6 km). Considering the uncertainties in the centroid depths of about ±3 km-- estimated by observing the variance increase relative to the best-fit depth-- it is quite possible that all earthquakes occurred within the oceanic crust (assuming estimates for the average oceanic crustal thickness of 6 km [*Chen, 1992*] are applicable to the BTFZ.) We cannot, however, exclude activity in the uppermost mantle (< 12-15km depth) entirely. Almost all analyzed events are relatively small; centroid and hypocenter depths are, therefore, roughly equivalent. The depth distribution implies that the seismogenic zone along the BTFZ is probably less than 10 km wide. Further discussion on the depth distribution is covered in chapter 3.4.1.

In addition to our RMT solutions, we used the source parameter estimates from the 28 Harvard centroid moment-tensor (CMT) solutions available for the BTFZ since 1976

Table 3.1. Crustal layer parameters used for calculation of synthetic seismograms.

Thickness (km)	v_p (km/s)	v_s (km/s)	Density (g/cm^3)
1.50	4.20	2.07	2.55
1.80	6.00	3.02	2.75
3.70	6.90	3.48	3.00
half-space	8.10	4.33	3.35

Table 3.2. Regional Moment-Tensor Solutions.

Date	Lat (°N)	Lon (°W)	LS	S/D/R (°)	M_W	CD (km)	DC (%)	CO
9002121344	43.934	-128.976	R	165/52/-107	5.63	6	82	6
9208210102	43.797	-128.457	R	198/26/-61	5.54	6	98	12
9211172037	43.733	-128.647	R	226/42/-43	5.20	6	60	13
9305092216	43.524	-128.254	R	301/84/-131	5.20	6	83	18
9401190116	43.437	-127.806	R	299/68/-153	5.74	9	65	29
9402282151	44.319	-130.112	N	124/78/-176	5.42	6	94	32
9402282153	44.434	-130.025	R	294/79/-17	5.70	4	98	33
9405111254	44.324	-130.101	N	288/62/-144	4.72	6	62	16
9406140204	43.580	-128.237	N	296/70/-140	4.82	6	55	18
9406300730	43.537	-128.314	N	294/83/-133	4.77	6	56	24
9407131752	43.266	-127.044	R	307/85/-124	4.99	6	84	19
9407222244	43.121	-127.040	N	304/69/-144	4.16	6	99	7
9408121126	43.832	-128.695	N	282/58/178	4.01	9	26	9
9410251559	44.150	-129.655	N	300/73/-147	5.05	9	71	21
9410270438	43.025	-126.248	N	303/81/-146	4.53	6	52	12
9410271745	43.427	-127.549	R	295/75/-158	6.48	9	73	63
9410282002	43.798	-128.489	J	1/65/-97	4.44	6	93	21
9410300223	43.306	-127.234	N	299/73/-144	4.70	9	100	20
9410302054	43.486	-128.072	N	304/76/-142	4.37	6	51	10
9411022048	43.550	-128.018	N	298/87/-124	4.97	4	85	19
9411060404	43.288	-127.174	N	301/76/-143	4.78	6	84	20
9411071502	43.294	-127.143	N	303/85/-137	4.38	9	74	12
9411222123	43.406	-127.553	N	297/75/-162	5.00	6	71	19
9412210742	44.400	-129.900	J	299/81/-133	4.52	6	70	13
9502221019	43.079	-126.651	J	302/76/-150	4.28	6	70	20
9503280343	43.233	-127.077	N	304/61/-150	4.04	6	86	15
9504221423	44.147	-129.657	N	294/73/-145	4.62	6	80	24
9505040618	43.022	-126.701	N	339/62/-91	4.16	6	65	12
9505122350	43.392	-127.442	N	301/71/-159	4.14	6	91	10
9505130603	43.389	-127.442	N	117/88/141	4.73	6	20	21
9506092136	43.941	-129.224	J	290/83/-163	4.56	6	75	24
9507090616	44.466	-130.377	N	129/79/148	4.69	6*	16	30
9507090618	44.526	-130.308	N	126/70/170	4.55	6*	82	29
9508030541	43.160	-126.782	N	117/58/-176	4.24	6	17	25
9508142132	44.049	-128.720	R	5/63/-81	4.69	6	90	22
9508151057	43.852	-128.888	N	331/65/-105	4.21	6	98	19
9508260541	43.437	-127.558	J	112/88/151	4.10	4	25	26
9509020941	43.812	-128.693	N	12/62/-96	4.61	9	61	26
9509231826	44.309	-130.041	N	291/49/-161	4.10	4	52	14
9509250758	43.828	-128.906	N	19/64/-90	5.00	9	66	36
9509250801	43.899	-128.834	N	14/62/-88	4.50	9	52	23
9509251909	43.760	-128.532	R	11/63/-91	4.83	9	56	26
9509260139	43.209	-127.277	R	295/84/-155	5.35	6	69	42
9510070827	43.924	-129.260	R	350/60/-97	4.96	6	74	33
9510070857	44.034	-129.191	N	350/63/-94	4.35	6	62	21
9510071058	43.982	-129.043	N	353/66/-89	5.09	6	100	23
9510081803	44.014	-129.127	N	346/62/-91	4.42	6	61	16
9510150649	43.633	-128.552	N	299/70/-165	3.79	6*	73	8
9510191500	43.292	-127.257	N	291/80/-173	4.28	4	50	21
9511160114	44.302	-129.815	J	289/76/-156	4.65	6	91	33
9511230040	44.153	-129.616	J	120/66/-171	4.51	6	15	30
9512051503	43.423	-127.634	J	108/75/170	4.31	4	41	29
9512130715	43.422	-127.606	J	295/73/-174	4.58	6	49	18
9512240251	43.132	-126.941	N	297/83/-136	4.55	4	99	27

Table 3.2. Continued.

Date	Lat (°N)	Lon (°W)	LS	S/D/R (°)	M_W	CD (km)	DC (%)	CO
9601090737	43.139	-126.497	R	296/85/-160	5.22	4	61	35
9601170216	43.877	-128.452	J	9/58/-98	4.79	9	56	29
9601170758	43.836	-128.769	J	291/56/-162	4.75	6	50	30
9601170825	43.890	-128.762	J	293/55/-162	5.12	6	24	31
9602060532	43.598	-128.388	N	301/72/-162	4.14	4	67	20
9602060540	42.688	-126.761	N	26/56/-74	4.55	6	64	26
9602082132	44.041	-129.315	N	283/88/-172	4.14	6*	56	16
9602200052	43.355	-126.731	R	296/72/-153	5.26	4	99	43
9602200121	43.275	-127.107	N	111/89/173	4.44	6	54	25
9603152241	42.914	-126.675	N	26/50/-81	3.93	6	85	26
9603281141	43.213	-127.040	J	283/77/-167	4.34	4	30	7
9604090748	43.948	-129.148	N	295/68/-161	4.57	6	99	37
9604151229	43.456	-127.652	R	110/85/149	5.41	4	63	55
9604291139	44.326	-129.882	J	296/58/-156	4.31	6	91	32
9605030029	44.373	-130.154	N	115/72/-145	4.10	4	99	18
9605181914	43.336	-127.434	N	109/82/171	4.50	4	58	29
9605220302	43.923	-129.242	J	106/88/168	4.26	6	61	29
9607172236	43.161	-127.055	N	341/50/-89	4.23	6	76	24
9607281500	43.038	-126.842	J	116/86/160	4.25	6	35	26
9608260711	43.816	-128.434	J	16/64/-89	4.91	9	75	38
9610012209	43.924	-129.062	N	352/49/-86	4.53	6	100	37
9610030725	43.964	-129.022	N	346/56/-91	4.50	12	59	31
9610031000	43.941	-128.972	N	343/62/-93	4.99	9	94	37
9610031009	43.931	-129.128	R	342/60/-95	5.32	9	99	47
9610161250	43.344	-127.596	N	302/61/-157	4.37	6	71	28
9610161307	43.337	-127.580	N	300/68/-151	4.15	9	82	25
9611040012	43.974	-129.162	N	290/73/-148	4.45	4	61	32
9611042254	43.503	-127.355	R	298/73/-157	5.47	6	83	41
9611080551	44.347	-130.205	N	295/78/-153	4.64	4	58	31
9611080555	44.329	-130.210	N	295/75/-140	4.71	4	72	31
9611192220	43.139	-126.912	N	193/33/-60	4.47	6	42	20
9611241822	43.179	-126.969	N	181/42/-54	4.43	6	23	20
9612080348	43.843	-129.573	R	289/89/-163	5.27	4	77	61
9612080542	43.938	-129.402	R	285/89/-150	4.93	4	76	39
9701131632	43.561	-128.233	N	291/76/-147	4.49	4	71	32
9702201103	43.287	-127.398	N	294/81/-153	4.51	6	93	24
9703231641	43.354	-127.361	R	298/82/-141	4.71	4	70	31
9704121641	43.129	-126.717	N	119/86/166	4.81	6	38	29
9704170944	44.412	-130.445	N	335/57/-91	4.25	12	68	23
9704171417	44.329	-129.922	N	290/81/-142	4.79	4	78	45
9705271531	43.198	-127.307	N	116/59/-176	4.28	6	72	28
9705282303	43.356	-127.511	N	295/88/-162	4.51	4	68	37
9706092120	43.863	-128.671	N	306/54/-127	4.11	6	69	24
9707071325	43.425	-127.532	R	109/76/-175	5.18	4	74	57
9707101848	44.180	-129.417	R	118/77/176	4.79	6	39	26
9707110203	44.205	-129.273	R	116/83/177	5.42	4	63	53
9707111752	44.083	-129.495	N	296/72/-123	4.57	4	82	24
9710010628	43.138	-127.205	N	318/76/162	4.31	6	80	33
9710050142	43.206	-127.114	N	299/74/-158	4.06	6	64	12
9710111543	44.272	-130.075	N	289/79/175	4.70	4	73	46
9710111554	44.228	-129.928	R	110/88/-180	5.47	4	62	50
9710190409	43.324	-127.404	J	292/73/-166	4.48	9	75	32
9710220234	44.277	-129.872	J	294/54/-167	4.09	4	79	20
9712030943	43.287	-127.784	N	290/84/-174	4.38	4	80	26

Table 3.2. Continued.

Date	Lat (°N)	Lon (°W)	LS	S/D/R (°)	M_W	CD (km)	DC (%)	CO
9801041833	43.958	-128.641	N	6/65/-93	4.79	9	96	33
9801061114	44.306	-129.987	N	291/55/-169	4.07	6	81	21
9801080329	42.851	-126.582	N	35/66/-66	4.51	9	65	15
9801190038	44.019	-129.285	N	289/75/-165	4.17	4	85	13
9801262325	44.043	-129.273	N	295/89/-144	4.82	4	64	41
9803230228	43.357	-127.057	R	113/89/173	5.25	6	64	56
9803261224	43.317	-127.589	N	295/67/-159	4.53	9	57	35
9804030842	43.093	-126.770	N	117/75/174	4.41	6	38	23
9804200648	44.045	-129.350	N	286/78/-154	4.14	6	81	27
9804211838	44.181	-129.698	N	291/72/-157	4.41	4	51	29
9806050604	43.221	-127.579	N	291/68/-158	4.15	6	65	28
9806060708	42.960	-126.794	N	296/79/-175	4.27	6	30	23
9806251112	43.228	-127.355	N	118/78/-154	4.03	6	13	26
9807141613	43.984	-129.307	N	290/59/-158	4.19	4	64	24
9808020751	42.947	-126.517	N	119/79/-149	4.00	6	68	20
9808250034	43.189	-127.230	N	299/68/-153	4.15	4	79	17
9809061234	43.317	-127.584	N	298/67/-155	4.70	9	83	34

Date: year month day hour minute. Lat, Lon: latitude and longitude. LS: location source; R: relocated, N: NOAA-PMEL, J: at OSU using regional P and S arrivals. S/D/R: strike, dip, and rake. M_W: moment magnitude. CD: centroid depth. DC: double couple percentage. DC = (1-2ε)x100[%], ε = |smallest|/|largest| moment-tensor eigenvalue. CO: number of components (vertical, radial, transverse) used.

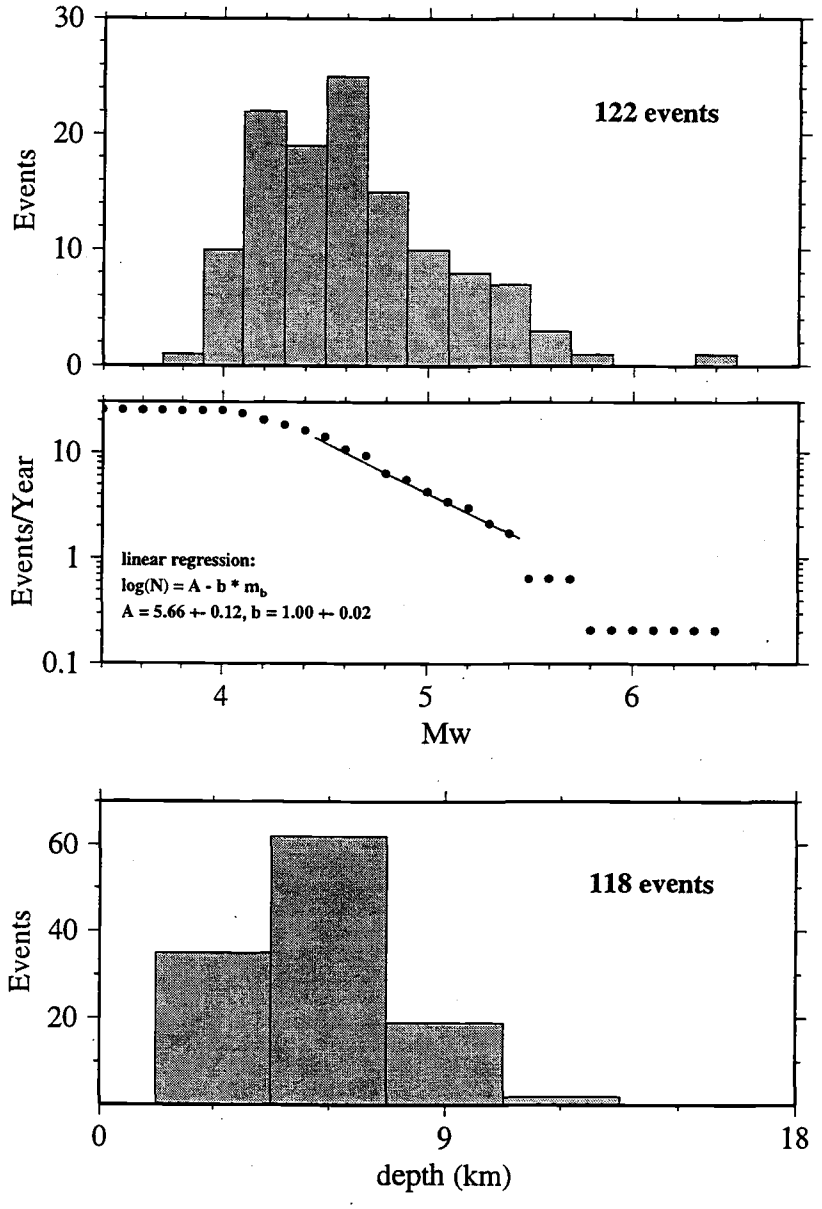

Figure 3.2. Size and depth distribution of the analyzed earthquakes. Top: Histogram of event magnitudes. Middle: Number of earthquakes per year N greater or equal moment magnitude M_W vs. M_W. Linear regression analysis was applied in the magnitude range covered by the solid line. Bottom: Histogram of event centroid depths. Only earthquakes with resolved centroid depth are shown.

(Table 3.3). For eleven recent, larger earthquakes, both RMT and CMT solutions exist, and in most cases they agree very well with each other.

A comparison of the M_W estimates with the body (m_b) and surface wave (M_S) magnitudes provided by the International Seismological Centre (ISC) and the National Earthquake Information Center (NEIC) shows a significant discrepancy (Figure 3.3). The scatter in the M_W-m_b-plot is large, and linear regression does not provide a significantly better fit to the data points than the simple average M_W-m_b-difference (0.51 magnitude units, long dashes in Figure 3.3). M_S also underestimates M_W; linear regression yields a $M_W = 2.12 + 0.68\ M_S$ relation. The small M_S estimates ($M_S < 4$), however, are dubious (since M_S is determined from 20 second period surface waves recorded at teleseismic distances); for larger earthquakes ($M \approx 6$), the M_W-M_S-difference is small. A m_b-M_S-discrepancy, comparable in size to the 0.5 M_W-m_b-difference presented here, has been suggested for earthquakes along oceanic transform faults (*Stewart and Okal, 1981*).

3.2.2 Earthquake Relocations

Routine earthquake locations along the BTFZ are scattered and biased to the northeast of the bathymetric features which define the plate boundary (Figure 3.4 top). We thus relocated larger earthquakes with the joint epicenter determination (JED) technique (*Douglas, 1967; Dewey, 1972*) to better understand how these larger, tectonically more significant earthquakes are distributed. The main advantage of the JED technique over single event earthquake locations is the greatly improved resolution of the relative locations between events. These precise relative locations allow us to check the consistency of the SOSUS based locations.

We simultaneously relocated 144 earthquakes that occurred from 1964 to 1998, using data from the ISC available for the time span 1964-1995 and from the US Geological Survey since then. Only events with at least 20 teleseismic (event-station distance $18° \leq \Delta \leq 100°$) P-wave arrival time picks were included. Because of poor depth resolution offered by teleseismic data, all hypocenter depths were constrained to 10 km.

To stabilize the inversion, we relocated all earthquakes relative to the $M_W = 6.5$ 850313 event because it has the most P-wave picks in our data set, and it is located close to Blanco Ridge. The ISC locations of this event and of the three other largest events in the ISC-catalog are close to Blanco Ridge and south of the main epicenter cluster (between 127.5°

Table 3.3. Harvard Centroid Moment-Tensor Solutions.

Date	Lat (°N)	Lon (°W)	S/D/R (°)	M_W	CD (km)	DC (%)
7707281522	43.977	-129.225	306/75/-167	5.78	15*	75
8003301349	43.308	-127.251	120/86/156	5.57	15*	86
8111031347	43.358	-127.828	297/90/180*	6.44	10.1	87
8111221137	43.547	-127.232	115/87/-178	5.86	15*	94
8211131544	44.124	-129.643	287/90/180*	5.68	15*	84
8503131934	43.404	-127.669	297/72/-172	6.46	10.0	86
8601300715	43.352	-127.548	295/90/180*	5.26	15*	92
8610052157	43.330	-127.353	295/81/-170	5.63	15*	91
8706270601	43.321	-127.300	294/76/-173	5.40	15*	87
8710170812	43.240	-126.738	298/12/180	5.42	15*	96
8712071748	43.293	-127.345	115/84/-168	5.18	15*	98
8810231348	43.996	-129.863	294/90/180*	5.51	15*	67
8901111223	44.394	-129.765	332/43/-81	5.07	15*	19
8905161221	43.403	-127.753	295/76/-168	5.58	15*	75
9001161257	43.599	-127.112	117/82/-177	5.59	15*	98
9001171205	43.452	-127.545	118/83/165	5.68	15*	96
9002121344	43.934	-128.976	150/90/-180*	5.47	15*	56
9208841427	43.510	-127.141	116/80/-178	5.66	15*	82
9208210102	43.797	-128.457	214/28/-55	5.42	15*	15
9402282152	44.434	-130.025	299/78/-169	5.62	15*	97
9410271745	43.427	-127.549	296/88/-175	6.33	15*	97
9604151229	43.456	-127.652	113/74/179	5.37	15*	74
9610031009	43.931	-129.128	181/20/-78	5.36	15*	85
9611042254	43.503	-127.355	295/76/-169	5.45	15*	74
9612080348	43.843	-129.573	295/90/-180*	5.16	15*	64
9707110203	44.205	-129.273	301/81/-172	5.40	15*	89
9710111554	44.228	-129.928	298/82/-167	5.42	15*	90
9803230228	43.357	-127.057	293/84/162	5.24	15*	84

Date: year month day hour minute. Lat., Lon.: relocated latitude and longitude. Source information is taken from Dziewonski et al. (*1994*) and related sources. S/D/R: strike, dip, and rake; *: constrained $M_{XZ} = M_{YZ} = 0$. M_W: moment magnitude. CD: centroid depth; *: constrained. DC: double couple percentage.

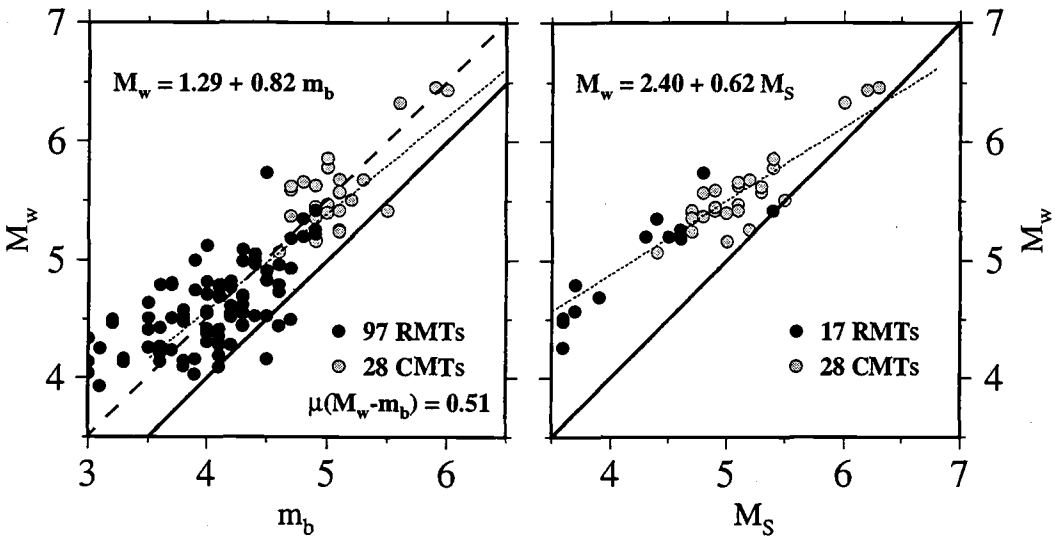

Figure 3.3. Left: Moment-magnitude (M_W) vs. body wave magnitude (m_b). Right: M_W vs. surface wave magnitude (M_S). Black circles: regional moment-tensor solutions (RMT), gray circles: Harvard centroid moment-tensors (CMT). For a one-to-one correspondence between the magnitudes, all circles would fall on the diagonal (solid line). M_W-vs.-m_b: On average M_W is 0.51 units bigger than m_b (long dashes); the least squares fit (short dashes)-- $M_W = 1.29 + 0.82\ m_b$ for (for $m_b \geq 3.5$ events) does not fit significantly better than the average M_W-m_b-difference. M_W-vs.-M_S: linear regression yields $M_W = 2.40 + 0.62\ M_S$.

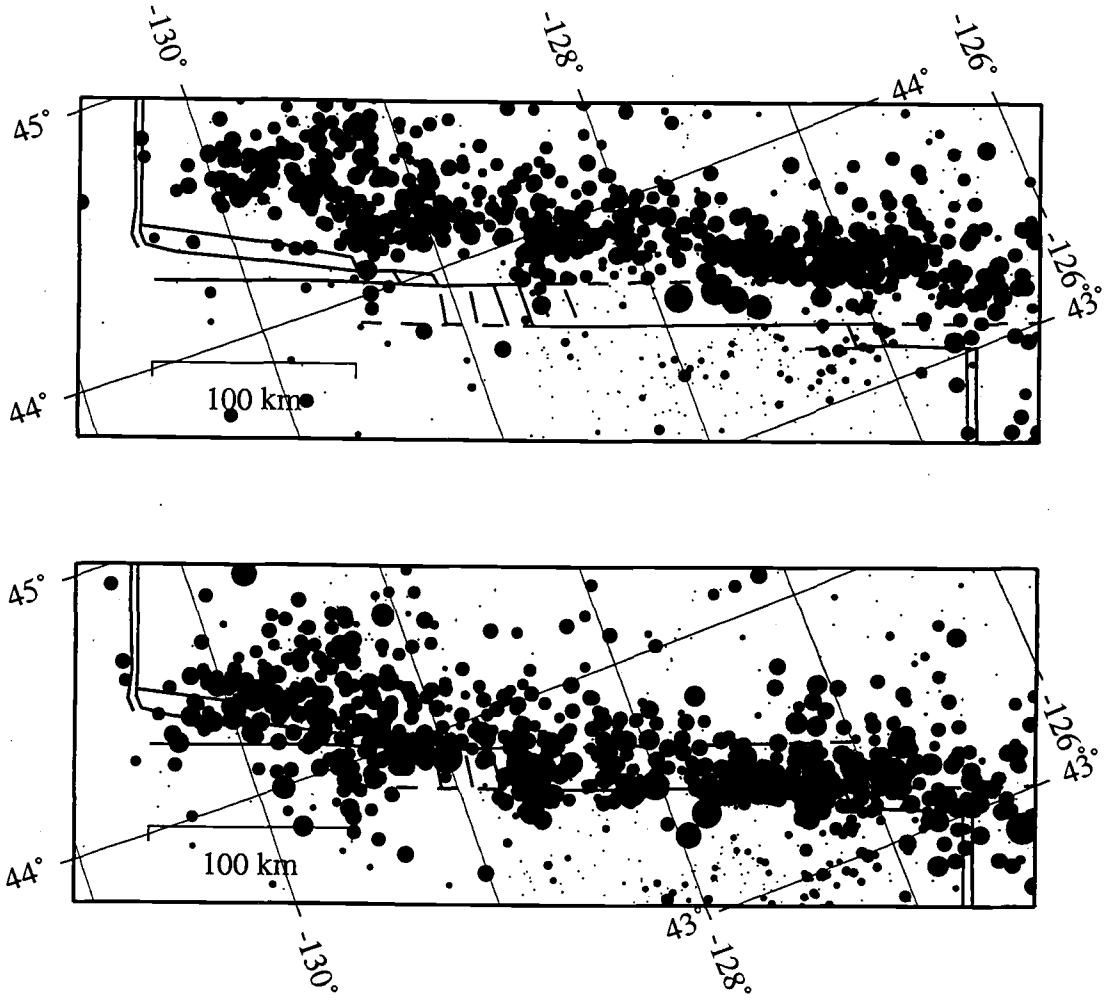

Figure 3.4. Top: Earthquake epicenter distribution in the vicinity of the BTFZ determined by ISC (1964-1995) and PDE (1996-08/1998). The epicenters are shifted to the northeast of the BTFZ. Bottom: Epicenter distribution after relocation. JED-relocated epicenters are plotted on their relocated epicenters; we applied the average shift found from the relocation (including the translation of the cluster due to shifting the reference event onto Blanco Ridge) to all other earthquakes. This corrected distribution correlates better with the BTFZ.

W and 128° W, Figure 3.4 top); it appears they are better located in an absolute sense than the smaller earthquakes, probably due to a better, more even azimuthal distribution, and a larger number of arrival time picks.

The JED fixed the relative locations of the entire earthquake cluster. We then translated the entire cluster such that the reference event's epicenter fell onto a point on Blanco Ridge; this assumes the reference event actually occurred on Blanco Ridge, which appears likely considering the event had a strike-slip mechanism and the transform fault runs along Blanco Ridge (*Dziak et al., manuscript submitted to Mar. Geophys. Res.*). We translated the reference event onto the point on Blanco Ridge (43.404° N, 127.669°) which was closest to the reference event's ISC-location (about 12 km distant, in a southerly-- 200° azimuth-- direction). Relocations shown in all subsequent Figures are relative to this "translated" 850313 epicenter.

Figure 3.5 shows the relocation result; open circles are the relocated epicenters with thin lines pointing to their original locations. The events shifted on average about 30-40 km south-southwest of their original locations. Only part of this shift can be attributed to the overall translation of the cluster; the remainder consists of the relative shifts due to relocation. Translation of the reference event (marked by a star in Figure 3.5) is shown as a thick gray line.

Translation of the 850313 event onto Blanco Ridge (and with it the entire relocated cluster of earthquakes) is not unique, but the distribution of the relocated epicenters is consistent with bathymetry (Figure 3.5): they are bounded to the east and west by the Gorda and Juan de Fuca ridges, and relocated events near Cascadia Depression have normal faulting mechanisms (see chapter 3.4.1.2). This supports our translation of the event cluster; however, translating the cluster further by about ± 10-15 km along the BTFZ and about ± 5-10 km perpendicular to the BTFZ is possible without significantly degrading the match between epicenter distribution and bathymetry.

We also tried a range of different events and groups of events (by fixing the locations of several events simultaneously) as reference event(s). We found the JED-determined relative locations are very well constrained (±3-5 km), independent of choice of reference event(s). The absolute location of the entire event cluster, of course, depends strongly on the choice of reference event(s). Fixing the location of an event with only few arrival time picks, or fixing event groups whose relative locations are inconsistent with their arrival time data set, mainly increased the uncertainty estimates for the relocations.

In the following discussions, we consider only well relocated epicenters (for which latitude and longitude uncertainties are less than 12 km at the 95% confidence limit). The larger uncertainties associated with the other events indicate inconsistencies in their arrival

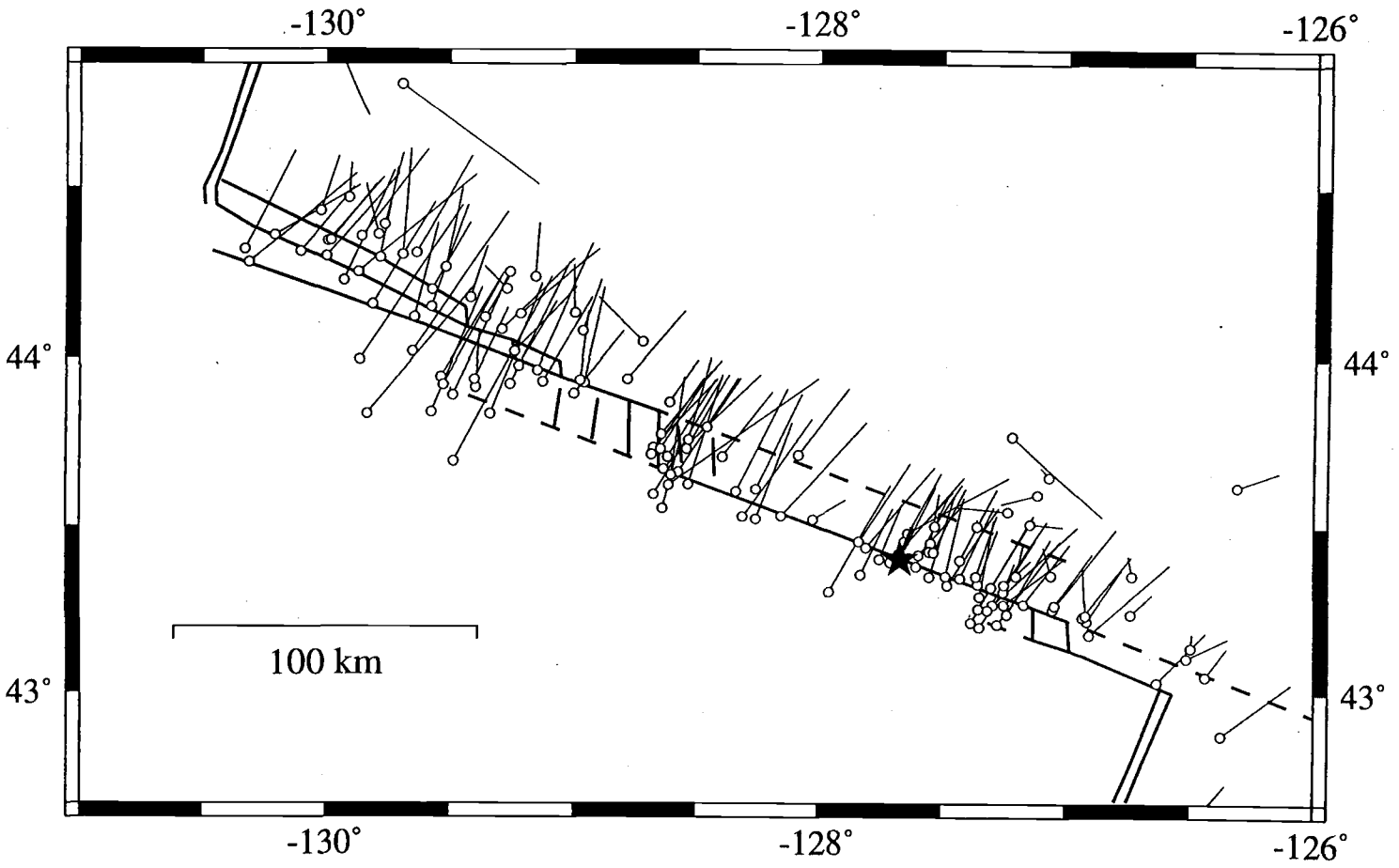

Figure 3.5. Relocation results. Open circles are relocated epicenters; the thin lines point to the original epicenters. The reference event's location on Blanco Ridge is marked by a shaded star; the thick gray line points to its ISC location.

time data set; many of these events shifted by a large amount during relocation and/or shifted in a direction significantly different from the direction the entire cluster shifted (which is to the south-southwest). Removing these events decreases the scatter in the relocated epicenters (see section 3.4.1.1).

3.3 Comparison between JED and SOSUS Locations

Offshore earthquake locations are often of low quality due to the distance to and the one-sided distribution of the land seismic stations; the earthquake epicenters shown in Figure 3.4 (top) illustrate this for the BTFZ. SOSUS locations, however, appear to be of a quality comparable to earthquake locations within a dense land seismic network: Fox et al. (*1995*) compared the SOSUS based locations of five explosions on the Juan de Fuca ridge with their actual location and found an average location difference of less than ±2 km. Detecting earthquake swarms along the Juan de Fuca ridge and the western BTFZ that were not recorded by land seismic networks (*Dziak et al., 1995; 1996*) is an example of the usefulness of the SOSUS array data for studies of oceanic ridge-transform systems. Rapid response efforts in both cases (*Embley et al., 1995; Dziak et al., 1996*) found anomalies in the water column and on the ocean floor near the swarm sides which suggest that SOSUS's earthquake locations are accurate.

The relationship between earthquake epicenters and the mechanism for T-phase generation (*Tolstoy and Ewing, 1950; Biot, 1952; Johnson et al., 1967*), however, is not as fully understood. Our relocations provide an independent check for the consistency of the SOSUS based earthquake locations, and to a lesser degree, on the absolute locations. Of the relocated earthquakes, 24 have been located with SOSUS data (R. Dziak, pers. comm.). Ideally-- if both data sets are internally consistent-- we expect that a simple translation of one data set would result in coinciding locations (i.e., the relative locations of both data sets are the same). This is not the case (Figure 3.6). The relocations, shown as open circles with thin lines pointing to the SOSUS locations (solid squares), are on average about 25 km away from the SOSUS locations, while the direction from the SOSUS locations to the relocated epicenters varies considerably. In most cases, the SOSUS location falls outside the earthquake relocation's 95% confidence ellipsoid. Near Blanco Ridge, most of the shift is along ridge, and relocated epicenters are predominantly west of the SOSUS locations. In the western part of the BTFZ, relocated epicenters are mainly east

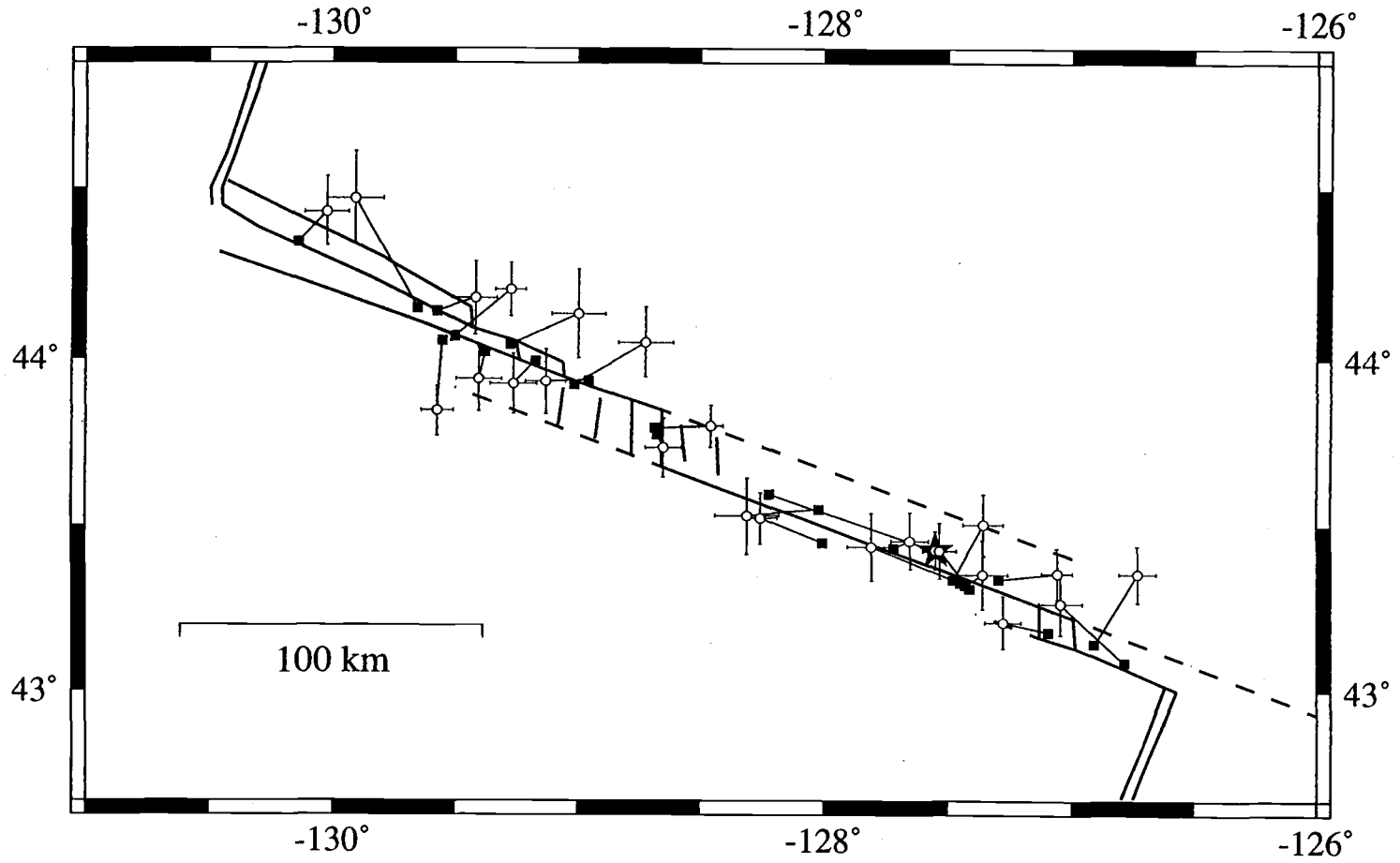

Figure 3.6. Comparison of JED and SOSUS locations. Open circles are relocated epicenters; thin lines connect to the SOSUS based locations (solid squares). Most SOSUS locations are outside the 95% confidence limits (solid bars) of the relocations. The shaded star marks the location of the 941027 earthquake, which is about 70 km southeast of the event's SOSUS location.

of the SOSUS locations and scatter over a wider region than the SOSUS locations which closely follow bathymetric features. This close relation could indicate the location precision; another interpretation, however, is that more T-phase energy is transmitted into the water column in areas of rough/steep bathymetry.

The most severe location difference, marked by a star, was found for the 941027 earthquake-- the largest event ($M_W = 6.5$) along the BTFZ during the last two decades. The epicenter is JED-relocated along the central-to-eastern part of Blanco Ridge, while the SOSUS based location is about 70 km to the northwest along the western part of Blanco Ridge. We speculate that a long rupture duration of about 25 seconds (inferred from the RMT-analysis' source time function, empirical Green's functions analysis [*Braunmiller et al., 1995b*], and a 10 second centroid-time shift of the CMT-solution [*Dziewonski et al., 1995*]) caused a long ringing signal in the hydrophone data which hampered a good location.

The uncertainties and limitations intrinsic in teleseismic relocations do not allow a more detailed discussion of potential SOSUS location uncertainties or errors. A more detailed study involving ocean bottom seismometer, ocean bottom hydrophones, and/or close-by hydrophones (which record crustal phases necessary for hypocenter depth resolution in addition to the T-phases generally recorded by the long-range SOSUS arrays) would be necessary to investigate fully the SOSUS location capabilities.

3.4 Results - Seismotectonics and Fault Zone Segmentation

3.4.1 General Results

3.4.1.1 Overview of Relocation Results

This section presents a brief overview of the seismicity along the BTFZ; a detailed description of seismicity and source mechanisms is presented in chapter 3.4.2 *Discussion of Fault Zone Segments*. The 123 well relocated epicenters, for which latitude and

longitude uncertainties are less than 12 km at the 95% confidence level, are shown in Figure 3.7. The uncertainty bars of the larger ($M \geq 5$) and generally better-constrained epicenters are in bold.

Activity along the BTFZ terminates near its intersection with the Gorda Ridge (Figure 3.7). Few events were relocated between the ridge and Gorda Depression, and since we relocated only larger events, this implies that earthquakes along the easternmost part of the BTFZ are small. The eastern part of Blanco Ridge transform (from about 127.1° W to 127.8° W) is seismically very active, and the earthquakes follow the ridge relatively closely. Several events north of Blanco Ridge (at about 43.5° N, 127.25° W) indicate possible activity on a second fault strand. Few earthquakes occurred along the western part of Blanco Ridge (west of 127.8° W), while many epicenters are close to or fall inside Cascadia Depression.

West of Cascadia Depression, the distribution of the relocated earthquakes is more scattered than along the eastern part of the BTFZ (Figure 3.7). We ran several additional inversions during which we relocated only earthquakes along the western part of the BTFZ to investigate if the wider epicenter scatter is artificial, introduced by the dominance of arrival time picks associated with events near Blanco Ridge. The events' distribution was unaffected. Morphologically, this part of the BTFZ is also more complicated (*Embley and Wilson, 1992*), and different plate boundary locations have been suggested near the BTFZ-Juan de Fuca ridge intersection: along the north wall of West Blanco Depression (*Embley and Wilson, 1992; Juteau et al., 1995*), along the south wall (*Embley and Wilson, 1992*), and running obliquely through West Blanco Depression (*Dauteuil, 1995*). Our relocations indicate that west of Surveyor Depression several fault strands are active simultaneously. Several earthquakes south of the West and East Blanco Depressions suggest the lineament along the southern margin of Parks Plateau is possibly seismically active; this is incompatible with submersible dive reports of sedimented volcanic flows across the lineament (*Juteau et al., 1995*).

3.4.1.2 Overview of Moment-Tensor Results

Separating strike-slip and normal faulting source mechanisms (Figure 3.8) shows that the deformation style along the BTFZ varies systematically. The majority of earthquakes along the BTFZ have strike-slip source mechanisms (Figure 3.8 bottom). The eastern part

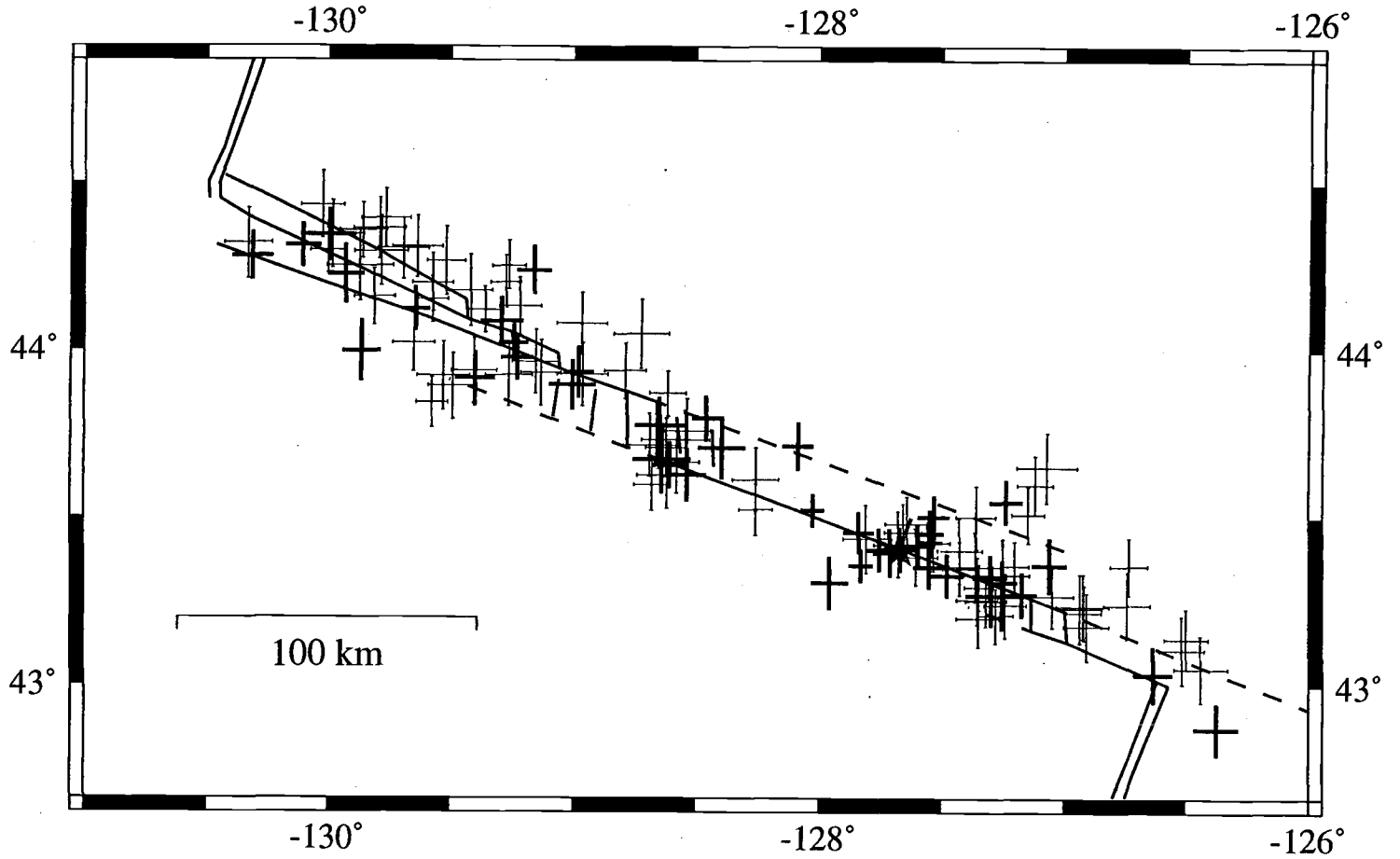

Figure 3.7. Uncertainty bars for 123 well-relocated epicenters (events with latitude and longitude uncertainties ≤12 km at 95% confidence level). Thick bars mark M ≥ 5 earthquakes, and the shaded star shows the reference event's location.

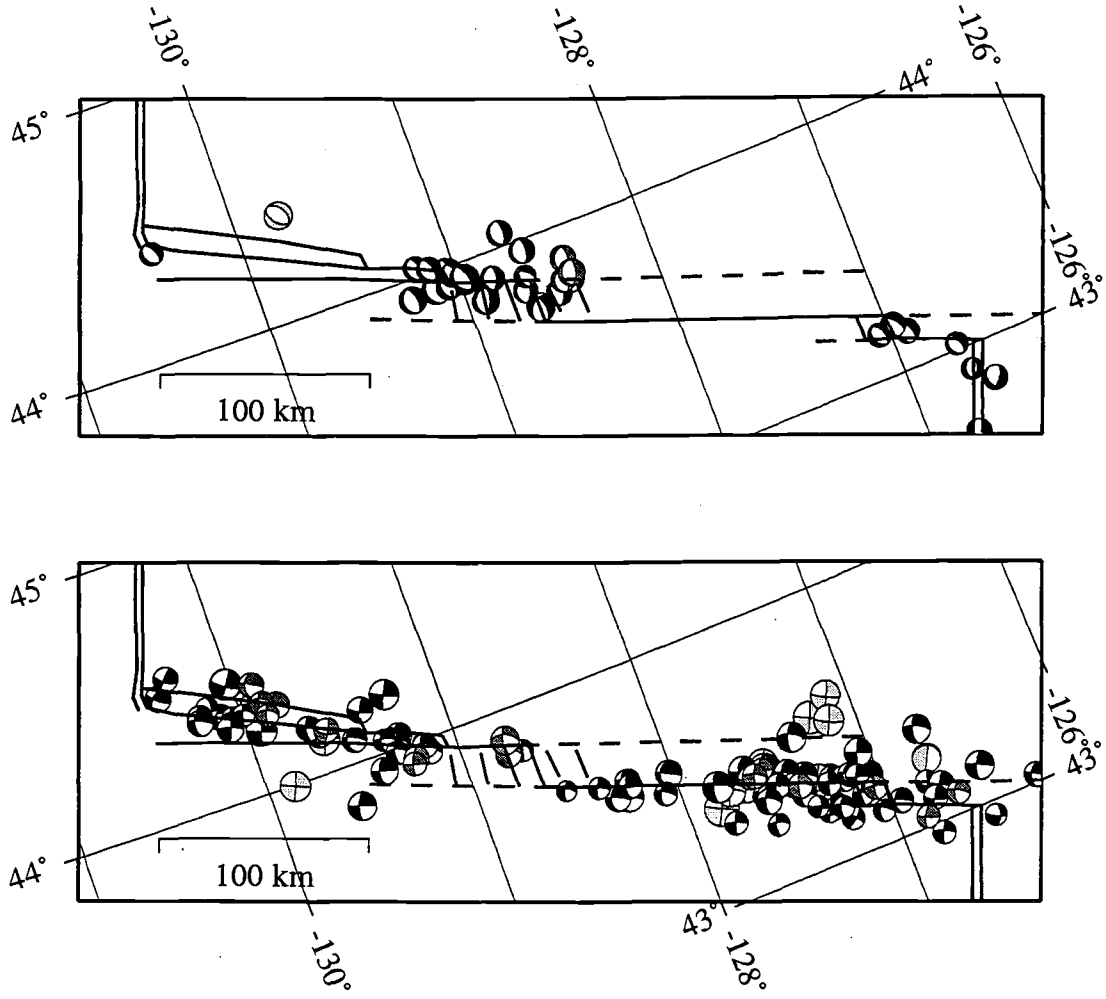

Figure 3.8. Map of the fault plane solutions (lower-hemisphere projections, size proportional to M_w). Top: normal faulting earthquakes; bottom: strike-slip earthquakes. Black: relocated RMT solutions (epicenter uncertainty ≤12 km); dark gray: RMT solutions on SOSUS based NOAA-PMEL locations; medium gray: RMT solutions on locations determined with regional P and S arrival time data for events where SOSUS data were not available; light gray: relocated CMT solutions. All events are listed in Tables 3.2 and 3.3.

of Blanco Ridge (127° W to 128° W) appears seismically to be the most prolific; the epicenters of the three largest (M_W 6.4-6.5) earthquakes are along this part of the BTFZ. In comparison, relatively few strike-slip earthquakes occurred along the western part of Blanco Ridge (west of 128° W). Strike-slip earthquakes along Gorda Depression, possibly along its northern and southern walls, continue to Gorda Ridge with the northern wall a continuation of Blanco Ridge. One mechanism east of the BTFZ-Gorda ridge intersection indicates that the fracture zone is not entirely seismically inactive. Four relatively large (M_W 5.5-5.9) earthquakes north of Blanco Ridge (at about 127.25° W) indicate a second active fault strand. Only three strike-slip mechanisms were found between the Cascadia and Surveyor depressions, an area dominated by normal faulting activity. Along the western part of the BTFZ (from west of about 129.2° to the BTFZ-Juan de Fuca ridge intersection), strike-slip mechanisms dominate, with the largest earthquake ($M_W = 5.8$) being significantly smaller than those along the Blanco Ridge.

Most normal faulting earthquakes (Figure 3.8 top) cluster in a broad area from about 128.5° W to 129.25° W which includes Cascadia Depression, its flanking back-tilted fault blocks and Surveyor Depression. Additionally, normal faulting earthquakes are found along the northern Gorda ridge, inside Gorda Depression, at the south tip of Juan de Fuca ridge, and possibly near or inside the East Blanco Depression (the sole CMT solution just northwest of the East Blanco Depression has one of the highest uncertainties in the moment-tensor components and one of the highest non double-couple source components of the 15000+ earthquake Harvard-CMT catalog; the mechanism may thus be poorly determined). No other normal faulting event was located inside Eastern Blanco Depression; microearthquake and hydrothermal activity (*Dziak et al., 1996*) indicate the depression is tectonically active, but earthquake size (at least during the last five years covered by RMT analysis) is confined to small events ($M_W < 4$).

3.4.1.3 Slip Vectors and T-axes

Slip vector azimuths of strike slip earthquakes. The slip vector azimuths of the strike-slip earthquakes are consistent along the length of the BTFZ (Figure 3.9 bottom); their average orientation (291°, Figure 3.8 bottom) agrees very well with the predicted Pacific-Juan de Fuca plate motion direction (290°, *Wilson, 1993*). Detailed inspection shows the azimuths change systematically along the BTFZ (Figure 3.10): the median azimuth is 286°

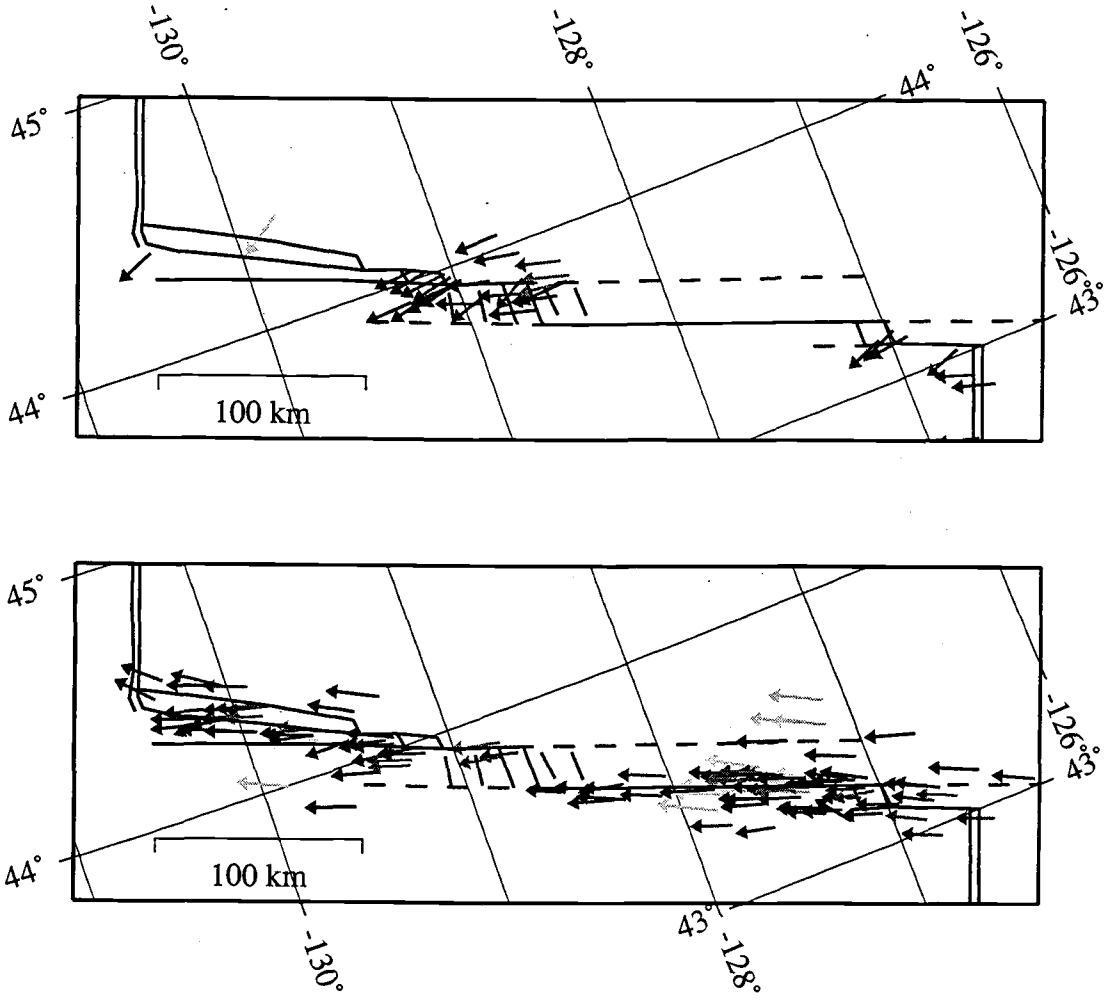

Figure 3.9. Top: Map of T-axis orientations of the normal faulting events. Bottom: Map of slip vector azimuths of the strike slip earthquakes. Gray scheme as in Figure 3.8.

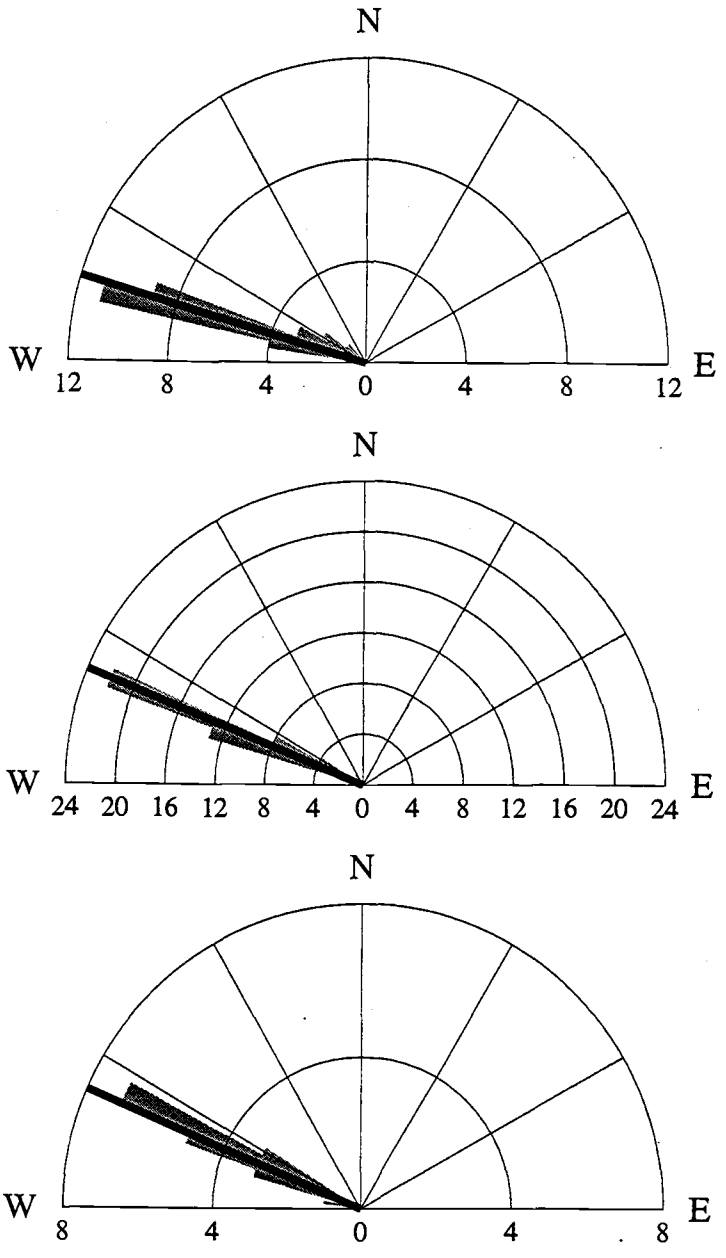

Figure 3.10. Slip vector azimuths of the strike slip earthquakes divided in three groups. Top: events west of 129° W; center: between 127.1°-128.6° W; bottom: east of 127° W. The observed azimuths (gray shaded area) are binned in 4° intervals, semi-circles show the number of events per bin. Note the narrow distribution of the slip vector azimuths in each group. The median slip vector azimuth (solid black line) rotates clockwise from west to east (top to bottom).

west of 129° W, 292° along Blanco Ridge, and 293° east of 127.1° W. The rotation and magnitude compare very well with the predicted changes in plate motion direction along the BTFZ (288° at the BTFZ-Juan de Fuca ridge-, and 292° at the BTFZ-Gorda ridge-intersection, *Wilson, 1993*). Resolving such small variations attests to the high overall quality of the RMT and CMT source mechanisms. For the RMT solutions, the strike of the northwest trending nodal planes (and thus of the slip vector azimuths) is very well constrained due to the station distribution (i.e., the nodal plane runs through the network). Current models for the Pacific-Juan de Fuca plate motions are based solely on magnetic anomaly data (e.g., *Riddihough, 1984; Wilson, 1993*); the precise estimates of the slip vector azimuths along the BTFZ define the relative plate motion direction and thus provide new constraints for updating these models.

Slip vector plunges of strike slip earthquakes. The plunge of the slip vector of a pure strike slip earthquake is zero (i.e., the motion is purely lateral). RMT solutions, however, in addition to the lateral motion (Figure 3.11 bottom), show a strong, Juan-de-Fuca plate-down component relative to the Pacific plate. The dip-slip component could be real, indicating a significant amount of vertical motion, or artificial, caused by the one-sided station distribution and an inadequate velocity-depth model for synthetic seismogram calculation. Based on the observation that the largest plunges are observed for older (pre-1995) and smaller events for which less data were available, we suggest the effect is mainly artificial. This is supported by the small plunges of the CMT solutions (Figure 3.11 bottom); they do, however, have a small, consistent Juan-de-Fuca plate-down component. A plot of the slip vector plunges (Figure 3.11 top) shows little variation between the eastern and western parts of the BTFZ; with the current data set we cannot resolve the presence of suggested differential plate subsidence on either side of the transform (*Fox and Gallo, 1984*). An interesting observation is that the largest plunges along Blanco Ridge are observed near the transform fault's intersection with the bathymetrically deeper, extensional Cascadia and Gorda depressions. The larger plunges could imply Juan de Fuca plate moves down relative to the Pacific plate near the basins; at present, this is speculative.

T-axis orientations. The T-axis orientations of the normal faulting earthquakes fall into two groups (Figure 3.9 top). The first, which consists of earthquakes at the north tip of Gorda ridge and events near Cascadia depression (east of 129° W), has T-axis orientations of about 275°-290°, roughly parallel to the plate motion direction. The second group--comprised of events in the Gorda Depression, the western part (west of 129°) of the normal faulting cluster near Surveyor Depression, and the two western most normal faulting

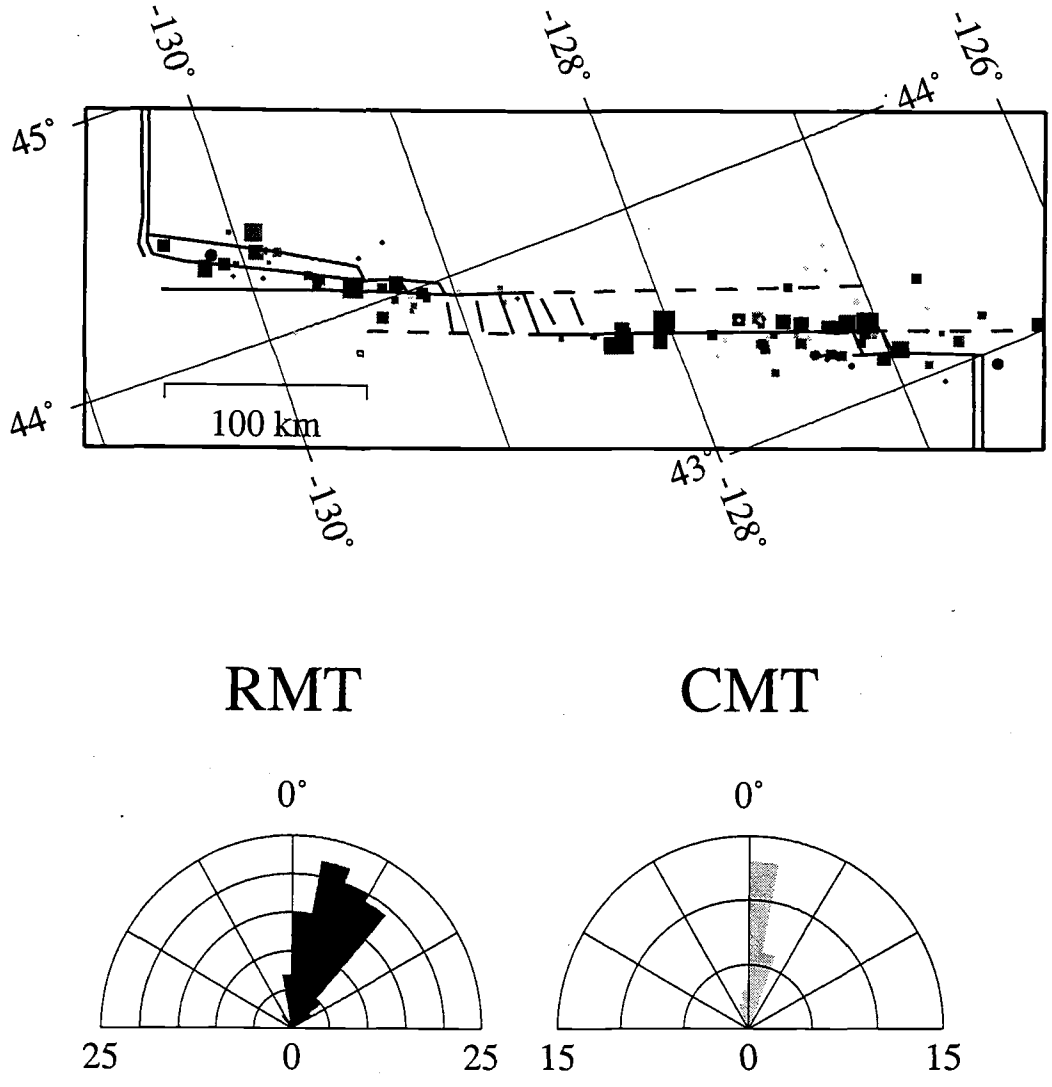

Figure 3.11. Top: Map of the slip vector plunges of the strike slip earthquakes (gray scheme as in Figure 3.8). Squares denote a Juan de Fuca plate-down component relative to the Pacific plate during strike slip faulting, circles an up component. Size of the symbols is proportional to plunge angle emphasizing large plunges. Bottom: left side shows plunge angles for RMT solutions, right for CMT solutions. Events with a Juan de Fuca plate-down component plot to the right of the center line in the rose diagrams. The plunges are binned in 10° intervals.

events-- has T-axis orientations of 245°-270°, which is oblique to the plate motion directions and to the orientation of the transform faults bordering the normal faulting region. The T-axis (and fault) orientations, though, agree with the trend of oblique bathymetric features observed in the Surveyor and Gorda Depressions (*Embley and Wilson, 1992*). Distributed extension oblique to the orientation of bordering transform fault segments is commonly observed in pull-apart basins (*Mann et al., 1983; Christie-Blick and Biddle, 1985*).

The T-axis orientations of the second group and of the strike-slip earthquakes are consistent with each other, while the T-axes of the first group are rotated clockwise by roughly 45°. (T-axis directions for the strike-slip earthquakes are predicted to be at a 45°-angle to the nodal planes, which have an average trend of about 200° and 290°, respectively; see Figure 3.8 for the nodal planes.) In other words, the same stress field can cause the strike-slip earthquakes and the normal faulting events in the second group, but not the events in the first group. Explaining the fault mechanisms with one common stress field requires that one set occur on faults with low resolved shear stress; with our data set alone, we cannot distinguish which fault set is weak. The Juan de Fuca intra-plate stress field is not known precisely; the earthquake fault plane solutions along the plate boundary itself do not constrain the stress field (*McKenzie, 1969*), and intra-plate earthquakes occur infrequently. Spence (*1989*) suggested pervasive north-south compression inside the Juan de Fuca plate and the adjoining North American plate, while Wang et al. (*1997*), based on left-lateral strike-slip faults which cut the accretionary prism (*Goldfinger et al., 1992*), suggested the principal compressive stress axis σ_1 rotates from north-south inside the Gorda plate to a northeast-southwest direction offshore Oregon. In both cases, the transform faults along the BTFZ are at a high angle to the σ_1 directions-- which would imply they are weak. That oceanic transform faults are weak had previously been suggested based on the observed orthogonality of ridge-transform boundaries (*Lachenbruch and Thompson, 1972; Froidevaux, 1973*), and earthquake fault plane solutions supporting the concept of weak oceanic transforms were presented for the Kane (*Wilcock et al., 1990*) and the Mendocino (*Wang et al., 1997*) transform faults. Only a better understanding of the Juan de Fuca intra-plate stress field can answer the question if the BTFZ transform faults are weak.

3.4.1.4 Centroid Depth Distribution

The centroid-depth distribution (Figure 3.2 bottom) of the RMT solutions indicated that the seismogenic zone width along the BTFZ is less than 10 km wide. A cross-sectional view (Figure 3.12 bottom) along the length of the BTFZ shows that centroid depths change systematically. Most events along the western part of the BTFZ (west of Surveyor Depression) and in the eastern part (near Gorda Depression) fall in the 4-6 km depth range; along Blanco Ridge, events deeper than 6 km are restricted to the eastern part.

The region between the Surveyor and Cascadia Depressions is dominated by normal faulting earthquakes in the 6-9 km depth range and is devoid of shallow activity. Cascadia Depression is inferred to be a short spreading center (*DeCharon, 1989; Embley and Wilson, 1992*); deeper sources, however, are difficult to reconcile with active spreading. A possible explanation is that the excitation functions-- the building blocks for the synthetic seismograms-- are biased systematically as to preclude 4 km-shallow depths for normal faulting earthquakes. We can roughly test this explanation by examining centroid depths of analyzed normal faulting earthquakes along the near-by Gorda Ridge (the ridge segment at the eastern terminus of the BTFZ). Centroid depths along Gorda Ridge (Figure 3.13) include several 4 km-shallow events near the central part of the ridge. We conclude that the lack of shallow activity and the presence of deeper events near Cascadia Depression are real. The centroid depths, however, do not preclude active spreading. A microearthquake study at the northern Gorda Ridge found hypocenter depths mainly in the 0-11 km depth range (*Solano, 1985*). Short-term ocean bottom seismometer deployments at the Mid-Atlantic Ridge near the Kane (*Toomey et al., 1985; 1988*) and Oceanographer transform faults (*Cessaro and Hussong, 1986*) show focal depths mainly at 5-8 km depth. The depth range of coseismic faulting inferred from centroid depths of larger mid-ocean ridge earthquakes (*Huang et al. 1986; Jemsek et al., 1986; Huang and Solomon, 1987; 1988*) is about 2-10 km.

The inferred width of the seismogenic zone (<10 km) is roughly consistent with results from short term microearthquakes studies of transform fault zones. Wilcock et al. (*1990*) found focal depths of up to 9 km for the Kane Transform fault; Prothero and Reid (*1982*) located earthquakes between 4-9 km depth along the Rivera fracture zone; Reichle et al. (*1976*) reported hypocenter depths between 3-5 km for transforms in the Gulf of California, and Tréhu and Solomon (*1983*) determined focal depths mainly from 0-4 km depth along the Orozco Fault zone. The earthquake depths determined by the short-term deployments (about two weeks) may not necessarily represent good estimates for the long

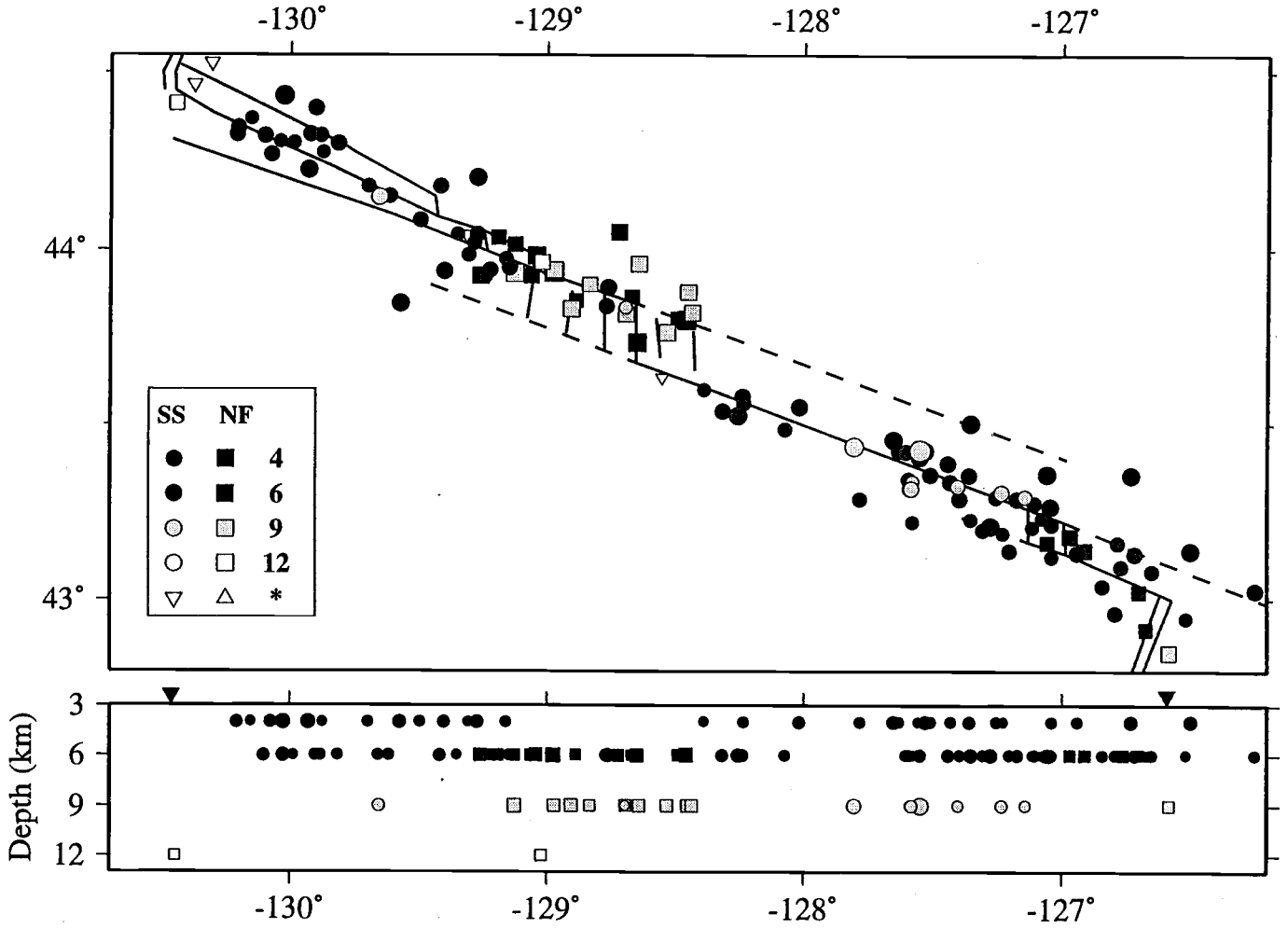

Figure 3.12. Top: centroid depth distribution of the RMT solutions along the BTFZ. SS: strike slip earthquakes; NF: normal faulting earthquakes; *: centroid depth not resolved. Bottom: cross section of the centroid depths.

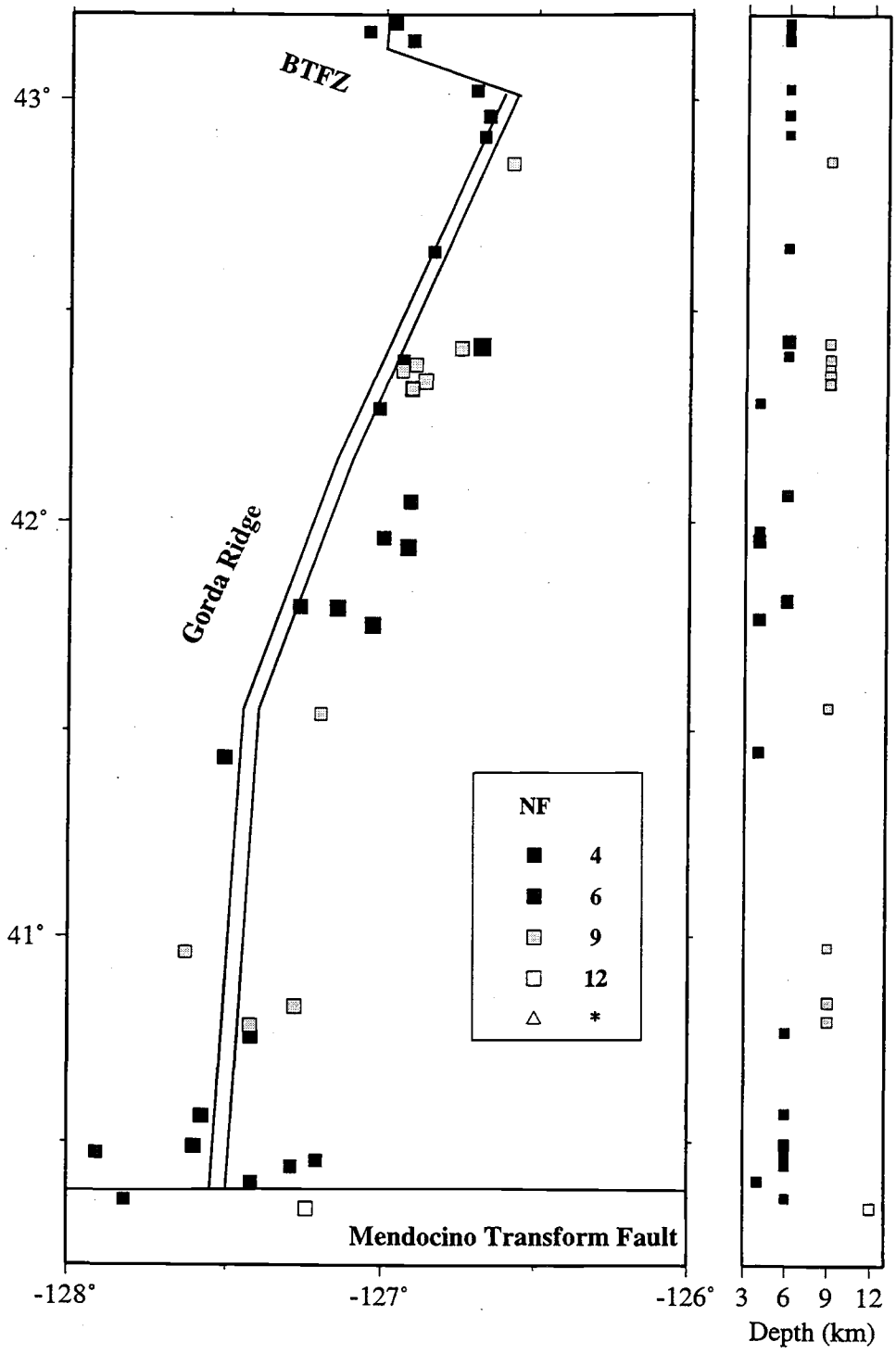

Figure 3.13. Left: centroid depth distribution of normal faulting (NF) earthquakes along Gorda Ridge. Right: cross section of the centroid depths.

term distribution of the hypocenter depths. In contrast, our estimates are the result of the first long-term (five years) monitoring of an entire transform fault zone. Centroid depths near the ridge-transform intersection appear to shallow slightly; Wilcock et al. (*1990*) found a similar result. Shallowing is consistent with thermal models (e.g., *Chen, 1988*) which predict elevated isotherms near the intersection that should lead to a decrease in the width of the seismogenic zone. Tréhu and Solomon (*1983*), however, found the deepest events near the intersection.

3.4.2 Discussion of Fault Zone Segments

Based on the variation of the deformation style along the length of the BTFZ (Figures 3.8), we divide the BTFZ into four segments: Gorda Depression, Blanco Ridge, Cascadia and Surveyor Depressions, and West Blanco. These segments are not fault segments, but rather represent areas of similar deformation; each of the four areas probably consists of several active faults and fault segments. This proposed division of the BTFZ, based solely on seismic data, correlates very well with segmentation deduced from bathymetry (*Embley and Wilson, 1992*).

3.4.2.1 Gorda Depression Segment

This easternmost segment of the BTFZ (Figure 3.14) consists of a basin immediately north and west of the Gorda ridge-BTFZ intersection (at about 43.0° N, 126.6° W), the deep Gorda Depression-- centered at about 127.1° W-- and transform faults which bound the basin and depression to the north and south. Our few relocations cannot distinguish between activity along the northern or southern fault. Based on morphology, Embley and Wilson (*1992*) suggested that the southern transform fault forms the plate boundary from Gorda ridge to Gorda Depression. This is consistent with the normal faulting earthquakes occurring only inside the Gorda Depression (with the exception of one event located near the inside corner between the Gorda ridge and the eastern BTFZ transform segment) and implies that strike-slip activity right-steps at the depression. However, the northern

Figure 3.14. Close up of the eastern part of the BTFZ. Plotted are fault plane solutions (gray scheme as in Figure 3.8) and well-relocated earthquake epicenters on top of bathymetry. Solid and dashed lines mark inferred (*Embley and Wilson, 1992*) locations of active and inactive faults, respectively.

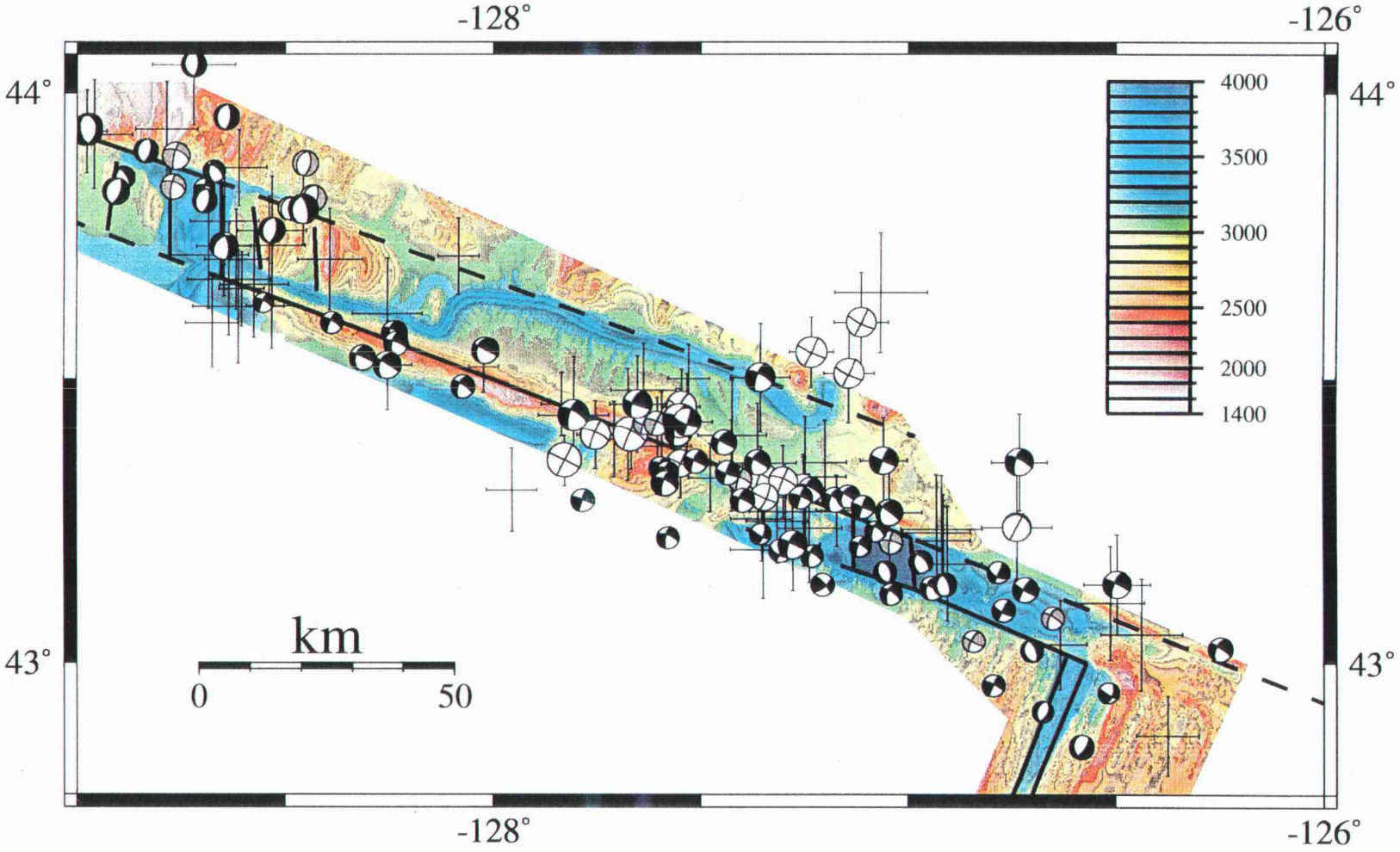
-128°
-126°
44°
43°
4000
3500
3000
2500
2000
1400
km
0
50

bounding scarp may also be active east of Gorda Depression. A single SOSUS-located strike-slip mechanism east of the ridge-transform intersections falls on the continuation of this scarp and indicates deformation in the fracture zone. Several strike-slip earthquakes on the southern transform (between 127.2°-127.4° W) indicate that the bathymetric trough extending from the southwest corner of the depression to the west is an active fault.

Based on the seismicity, we suggest that two parallel fault strands are active along the entire eastern part of the BTFZ, while normal faulting earthquakes (with $M_W \geq 4$) are confined to the deepest part, Gorda depression. This implies (distributed ?) extensional deformation must occur inside the bathymetric deep between Gorda Depression and Gorda Ridge. The overall rhomb-shaped geometry of the eastern BTFZ is similar to mature pull-apart basins described by Mann et al. (*1983*).

3.4.2.2 Blanco Ridge Segment

A transform fault along the narrow Blanco Ridge forms the Pacific-Juan de Fuca plate boundary running from the north side of Gorda Depression to the south side of the Cascadia Depression. All fault plane solutions are strike-slip (Figure 3.8), and their median slip vector azimuth of 292° (Figure 3.10) is consistent with the predicted plate motion direction (291°, *Wilson, 1993*). Relocated epicenters follow Blanco Ridge relatively narrowly, and the only $M \geq 6$ earthquakes along the entire BTFZ (from 1964-1998) occurred along the Blanco Ridge segment.

The Blanco Ridge is a prominent, transform-parallel ridge. Seismicity follows Blanco Ridge from the ridge-transform intersection (near 126.5° W) to Cascadia Depression (about 128.7° W); Blanco Ridge, however, extends further south-eastward to about 126° W (*Embley and Wilson, 1992*). The origin of transform parallel ridges is unknown; several possibilities mainly involving serpentinite intrusions, volcanism due to extension, and dip-slip faulting-- due to changes in spreading direction which cause extension or compression across the fault-- have been presented to explain their origin (*Thompson and Melson, 1972; Bonatti, 1976; 1978*). Ibach (*1981*), based on single channel seismic reflection data, suggested that Blanco Ridge is the result of transform normal compression, while Embley and Wilson (*1992*) and Dziak et al. (submitted to Mar. Geophys. Res.) suggested that extensive shearing allowed water to penetrate into deeper parts of the crust which caused serpentinite diapirism. The fault plane solutions along the length of Blanco Ridge are

strike-slip; we find no evidence for current compression across the fault zone suggesting that Ibach's (*1981*) interpretation is incorrect. Petrologic samples retrieved during three submersible dives in the central part of Blanco Ridge (near 127.5° - 128° W) include lower crustal-derived gabbros indicating uplift, however, no serpentinite samples were found possibly reflecting a sampling problem (Dziak et al., submitted to Mar. Geophys. Res.).

The earthquake relocations (Figure 3.14) and the ad-hoc shifted locations (Figure 3.4 lower part) show a large number of earthquakes between Gorda Depression and about 127.9° W, further west, seismicity drops markedly. The epicenters of the three largest RMT and CMT earthquakes are all located in the region of Blanco Ridge (between 127.5°-127.9° W; a $m_b = 6.1$ earthquake which occurred in 1968 is located at 128° W) where Gorda Ridge-parallel abyssal hill topography on the Pacific plate is apparently uplifted and merges with Blanco Ridge (*Embley and Wilson, 1992*). We suggest this intersection area divides the Blanco Ridge segment into two main parts. Nucleation of large earthquakes near fault zone complexities has been observed for many earthquakes (*King and Nábelek, 1985*).

SOSUS located aftershocks of the 941027 $M_w = 6.5$ earthquake, which was relocated near 127.55° W, form a band from 127.8° W to the west tip of Blanco Ridge at about 128.7° W (Dziak et al., submitted to Mar. Geophys. Res.). If these locations are correct, main shock rupture may have been unilateral towards northwest along a fault at the western part of Blanco Ridge. This is supported by preliminary teleseismic body wave analysis using the method of Nábelek (*1984*) which shows an improved fit for a northwest propagating rupture model over a point source solution and a southeast directed rupture. Deeper (9 km) centroid depths from RMT analysis (Figure 3.4) are restricted to the eastern part of Blanco Ridge; propagation of large earthquakes' ruptures into the western part of Blanco Ridge segment could explain that difference.

Four strike-slip earthquakes north of Blanco Ridge at about 127.25° W roughly align with a linear bathymetric feature that forms the north wall of Cascadia Depression and runs further northwest where the lineament forms the south boundary of Parks Plateau (Figures 3.1 and 3.14). Their presence implies that the fault strand is active east of Cascadia Depression. This is supported by relocated epicenters of two additional earthquakes, one near 126.75° W-- with a strike-slip mechanism-- and another near 128.1° W. Clustering of the events near 127.25° W possibly reflects fault complexity. The absence of more events along this fault segment east of Cascadia Depression is puzzling, but may be explained by very small slip rates and long recurrence intervals.

3.4.2.3 Cascadia and Surveyor Segments

All earthquake fault plane solutions in the Cascadia and Surveyor segments have normal faulting mechanisms (Figure 3.15)-- except for three strike slip events which possibly occurred on a short transform fault segment at the north wall of Cascadia Depression. The T-axis orientations of the normal faulting events (Figure 3.9) differ between the events associated with Cascadia Depression and Surveyor Depression, the change approximately occurs near 129° W (Figures 3.9 and 3.15).

Normal faulting events east of 129° are associated with Cascadia Depression and the inward-facing back-tilted normal fault blocks which border the depression on either side. The T-axis orientations (275° to 290°) agree with the trend of the normal faults (275° to 280°), which is slightly non-orthogonal (about 10°) to the orientation of the ridges bounding the fault blocks (Blanco Ridge transform is the southern bounding fault). The scarp which bounds the fault blocks to the north continues from Cascadia Depression linearly to the northwest, becoming the southern scarp of the Parks Plateau (*Embley and Wilson, 1992*). About a dozen well-relocated earthquake epicenters near the eastern boundary of the depression imply that stronger, presumably normal faulting, earthquakes occur frequently in or near Cascadia Depression; this is different from the other basins.

Is Cascadia Depression a short spreading center? Acoustically opaque zones within at least 500 m of sediment fill inside the basin were interpreted as igneous intrusions (*DeCharon, 1989; Embley and Wilson, 1992*); the inner valley floor is subsiding at a rate of 1.8 cm/yr over the last 6600 years (*Griggs and Kulm, 1973*), and the basin undergoes extension at a rate comparable to the Pacific-Juan de Fuca plate motion rate over the past 12000 years (*DeCharon, 1989*). Following the non-steady state model of rift valley development (*Kappel and Ryan, 1986*), DeCharon (*1989*) suggested that the lack of extrusives and the high subsidence rate can be explained by an episode of tectonic extension (vs. an episode of volcanism). The earthquake data-- relatively deep centroids (see chapter 3.4.1.2) and the similarity of the Cascadia Depression and Gorda Ridge earthquake source mechanisms (Figures 3.9 and 3.14)-- are consistent with that model.

Normal faulting events west of 129° W are located in close proximity to the Surveyor Depression and have T-axis orientations which are rotated to 245° - 270°. Their T-axis orientations are consistent with the structural lineaments within the basin.

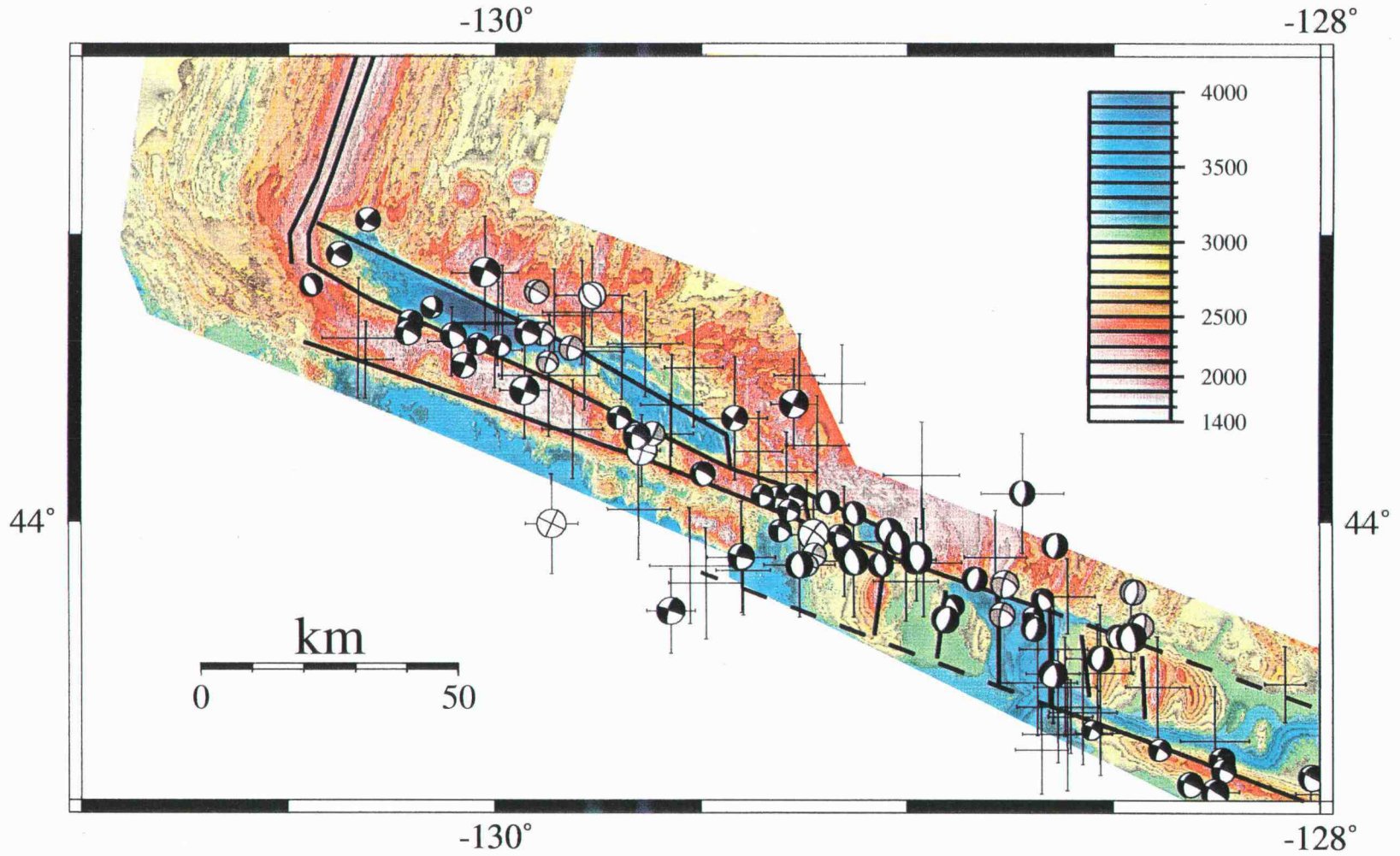

Figure 3.15. Close up of the western part of the BTFZ. See Figure 3.14 for legend.

3.4.2.4. West Blanco Segment

West of about 129.2° W, strike-slip earthquake mechanisms dominate again (Figure 3.15). Only two normal faulting source mechanisms were determined in this western part: one dubious CMT solution (see earlier discussion of the event) located near the boundary between East and West Blanco Depression, and one small event near the southern tip of Juan de Fuca ridge. Its northwest-southeast oriented nodal planes agree well with the orientation of the seafloor bathymetry which bends towards the transform fault zone. All other fault plane solutions are strike-slip.

Relocated epicenters along the West Blanco Segment are more widely distributed than along the other three segments suggesting that several fault strands comprise the Pacific-Juan de Fuca plate boundary. Owing to the complex morphology of this segment, several different plate boundary locations have been presented which cover the entire width of the seismically active area: the north wall of West Blanco Depression which trends in a 292° - 295° direction (*Embley and Wilson, 1992; Juteau et al., 1995*), the south wall of West Blanco Depression (*Embley and Wilson, 1992*) which also trends in a 292° - 295° direction, a fault cutting in a 287°- to 288°-direction obliquely through the West Blanco Depression (*Dauteuil, 1995*), and the linear fault scarp at the south boundary of the Parks Plateau which trends in a 290° direction (*Delaney et al., 1981*). All proposed fault strands are closely spaced such that, given the location uncertainties, most earthquakes could have occurred on more than one, and the difference in fault orientation is only on the order of the slip vector azimuth uncertainties (probably around ±5°). This precludes a unique interpretation. The earthquake distribution, however, is inconsistent with activity along only one transform fault, and slip vector azimuths outline three distinct groups, each with internally consistent relative motion directions.

Based on the locations and slip vector azimuths (Figure 3.16), we suggest that actually three strands are active. First, the northern active fault strand probably runs along the north wall of West Blanco Depression. The slip vector azimuths of several earthquakes (290°-300°) are roughly consistent with the trend of the wall (about 295°). Submersible dives on the central part of the north wall revealed several outcrops with striated fault planes, interpreted to represent active transform fault activity (*Juteau et al., 1995*). Second, a transform fault, which runs from the northeast corner of West Blanco Depression obliquely through the depression to the ridge tip near 44.4° N and 130.4° W, is seismically active. The fault trends in a 287°- to 288°-direction and is a prominent feature in processed

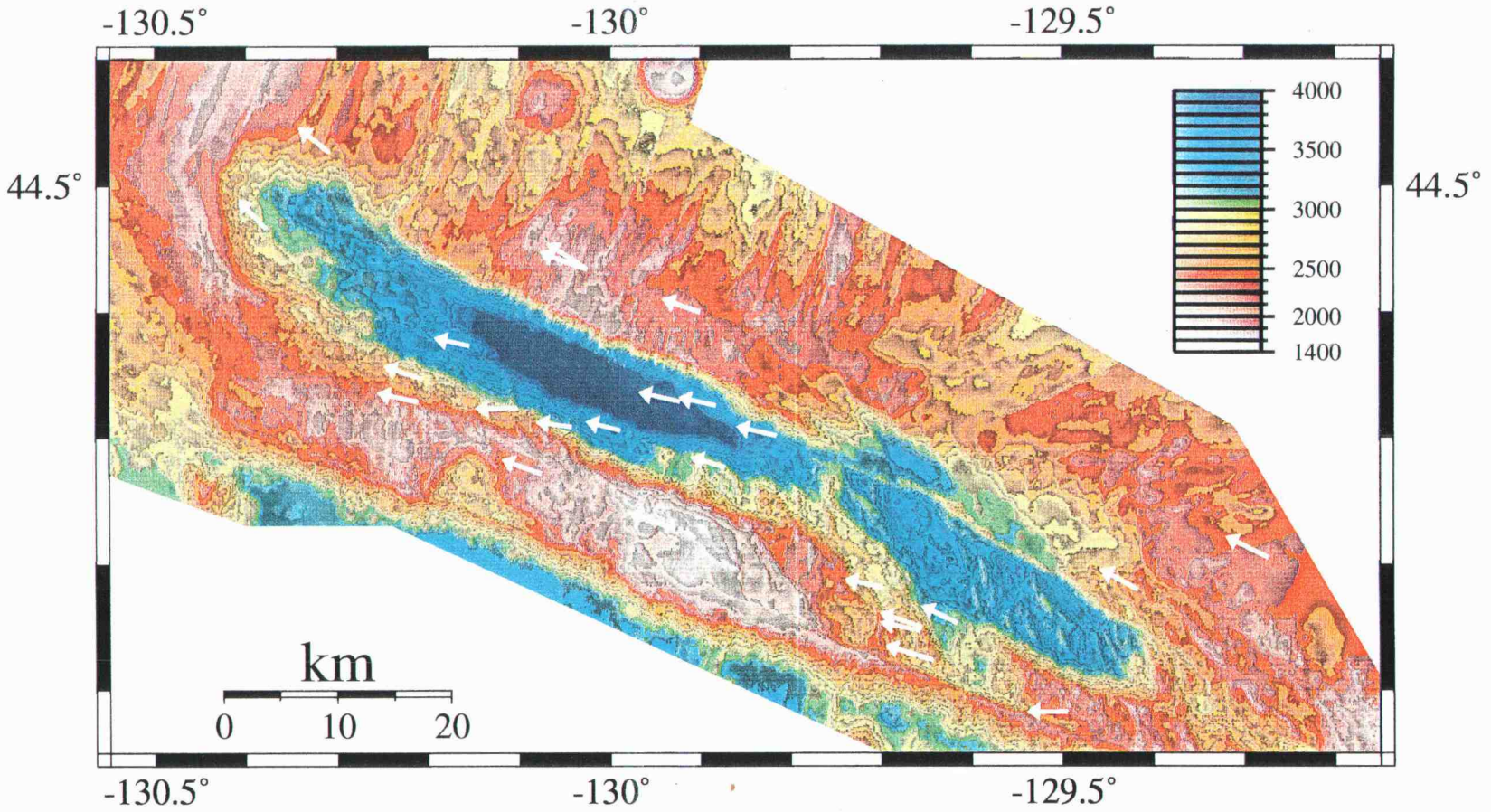

Figure 3.16. Close up of the BTFZ-Juan de Fuca ridge-transform intersection. The deep basins are East Blanco Depression and West Blanco Depression (WBD), the bathymetric high south of WBD is the Parks Plateau. White arrows are slip vector azimuths with the tails at the epicenters.

SeaBeam bathymetry maps (*Dauteuil, 1995*). An epicenter band which runs through West Blanco Depression and whose mechanisms have a median slip vector azimuth of 283° possibly occurred along that fault. The third, southern most active fault strand either follows the south wall of West Blanco Depression or runs along the south side of Parks Plateau (or both are active). We favor activity along the south wall of West Blanco Depression, since the wall terminates near the ridge tip and since the lineament along the south side of Parks Plateau is covered by sedimented volcanic flows (*Juteau et al., 1995*). The slip vectors of the two western-most strike slip events trend in a 310° and 316° direction suggesting that very close to the ridge-transform intersection short transform fault segments exist which are rotated towards the ridge axis. Activity along the north wall of West Blanco Depression and along the obliquely trending transform fault, which cuts through West Blanco Depression, requires right-stepping (of part) of the plate boundary motion, a possible locus where this might occur is the East Blanco Depression.

The three-stranded model proposed for the West Blanco Segment pushes the interpretation of our earthquake locations and source mechanisms to the limit. Earthquake epicenter uncertainties of less than ±3-4 km are required to define the currently active faults along the West Blanco Segment. Considering the reported inconsistencies (chapter 3.3) in the SOSUS data, only a study using ocean bottom seismic instruments appears capable to resolve this issue.

3.5 Seismic Slip Rate Distribution

3.5.1 Seismic Slip Rate Estimates from Observed Earthquakes

We sum the seismic moments of all earthquakes along the BTFZ which occurred during 1964-08/1998, using the ISC and PDE catalogs as our data sources. In addition to comparing the seismic slip rate estimate with the predicted plate motion rate (5.6 cm/yr, *Wilson 1993*), we present a map of the slip distribution along the length of the BTFZ. The map is constructed by projecting the earthquakes onto the BTFZ using the relocation results and employing empirical relations to estimate rupture length and slip from an earthquake's seismic moment. Previously, cumulative seismic moment estimates were used to determine

average seismic slip rates along entire transform faults (e.g., *Brune, 1968*). With this new approach we were able to identify areas of high and low slip along the BTFZ, providing an estimate of fault zone segmentation along an oceanic transform fault from seismicity data.

Mapping the seismic slip distribution consists of three simple steps. We have direct knowledge of the location (from relocation) and seismic moment (from RMTs and CMTs) for only a small subset of events. For all other earthquakes we need to estimate their location or seismic moment or both.

From relocation, we know the average epicenter shift (21 km to the south and 14 km to the west). Shifting all non-relocated events by that amount centers the seismicity around the BTFZ (Figure 3.4 bottom). Then we projected all epicenters-- relocated and ad-hoc shifted epicenters-- onto a line running from 43.0° N, 126.6° W to 44.45° N, 130.4° W-- a straight-line approximation to the actual BTFZ geometry. The coordinates represent the intersection of Gorda ridge with the south wall bordering Gorda Depression and of Juan de Fuca ridge with West Blanco Depression, respectively. Only events less than 50 km from the line were considered to exclude intra-plate and Gorda ridge earthquakes.

The next step involves converting body wave magnitudes to seismic moment (for events with no RMT or CMT solution). We use the relation given by Hanks and Kanamori (*1979*), but based on the observed discrepancy between M_w and m_b (Figure 3.3), we add the average M_w-m_b difference of $\Delta m = 0.5$ magnitude units to the m_b values before converting to seismic moment M_0.

$$M_w = m_b + \Delta m = \frac{2}{3} \cdot \log M_0 - 10.7 \qquad (3.1)$$

The error introduced to the seismic moment estimates by an incorrect assumption of Δm is: $10^{(\Delta m_{true} - \Delta m)}$. For $(\Delta m_{true} - \Delta m) = 0.1$; the true moment is thus underestimated by about 40%. For most larger events in our data set a CMT solution exists. Thus the magnitude-moment conversion is mainly applied to the numerous observed smaller events.

The final step is to distribute the seismic moment along the length of the fault zone. We use a very simple parameterization that assumes the slip is evenly distributed over a rectangle; the seismic moment is then related to the fault length **L** and slip **u** by:

$$M_0 = \mu \cdot W \cdot L \cdot u \qquad (3.2)$$

The bold symbols are to emphasize **L**, **u**, and **W**. They are not vectors. We used a rigidity of $\mu = 3.5 \times 10^{10}$ Nm, consistent with our velocity-depth model (Table 3.1), and a width of the seismogenic zone **W** = 7 km, consistent with the centroid depth distribution

(Figure 3.2 bottom). For large earthquakes, Scholz (*1982*) inferred that the slip **u** increases linearly with the fault length **L**; for interplate strike-slip earthquakes he gives the empirical relation $\mathbf{u} = 1.25 \times 10^{-5}\ \mathbf{L}$. Thus, M_0 is proportional to $\mathbf{L}^2$ (and $\mathbf{u}^2$). We centered the rectangle at the events' projected location on the fault zone; slip is thus equally distributed on both sides of that point and the rupture mimics a bilateral rupture. This parameterization is certainly not accurate; however, it provides a means to plot the seismic moments of all events in a simple, coherent fashion. For smaller events, a rupture width of 7 km is unrealistic and a circular crack model is a better description of the rupture area. The crack radius reaches 3.5 km only for $M_w = 5.6$ (assuming a stress drop of 3 MPa, a global average proposed by Kanamori and Anderson [*1975*]); for smaller earthquakes our parameterization thus underestimates the fault length **L** (and slip **u**) by distributing the slip equally over a narrow strip **L** of large width **W**. We summed the seismic moments in 1 km increments along the fault; thus, the bias is insignificant within the slip maps's resolution.

Figure 3.17 shows the resulting slip-rate distribution along the BTFZ during 1964-08/1998 (34.7 years). The distribution varies tremendously, indicating that the fault zone consists of several segments. All large earthquakes (shown as stars-- $M_w > 6.0$-- and open circle-- $m_b > 6.0$) occurred along the Blanco Ridge segment of the BTFZ (185 km - 290 km in Figure 3.17) and their contributions dominate the entire distribution. The average seismic slip rate (4.5 cm/yr) along the Blanco Ridge segment accounts almost completely for the predicted plate motion rate (5.6 cm/yr, horizontal line in Figure 3.17). Figure 3.18 shows the slip rate distribution under the assumption that the $M_w = 6.5$ 941027 earthquake ruptured unilaterally to the northwest (see discussion in chapter 3.4.2.2). The average seismic slip rate west of Blanco Ridge (0 km - 185 km) is 1.1 cm/yr, and from Blanco Ridge to the BTFZ-Gorda ridge intersection (290 km - 360 km) the average is 0.9 cm/yr; these estimates represent only 15% to 20% of the expected plate motion rate. The average rate for the Cascadia and Surveyor segment of 1.1 cm/yr implied lateral motion (strike slip) during earthquakes; we observed mainly normal faulting earthquakes (Figure 3.8), assuming a 45°-average fault dip the rate reduces to 0.8 cm/yr. The slip rate averaged over the entire length of the BTFZ is 2 cm/yr. This rate, however, does not describe the actual slip rate for any segment, which illustrates that averaging over the entire length of transform faults is a gross oversimplification.

Hyndman and Weichert (*1983*) suggested that seismicity from 1899-1983 accounts for the entire plate motion along the BTFZ, which is more than twice our "average" estimate. They used a seismic zone width of 4 km, which-- based on the centroid depth distribution (Figure 3.12)-- underestimates the true width by about a factor of 2. After correcting for that bias, their estimate decreases to about 2.5 - 3 cm/yr which compares well with our rate.

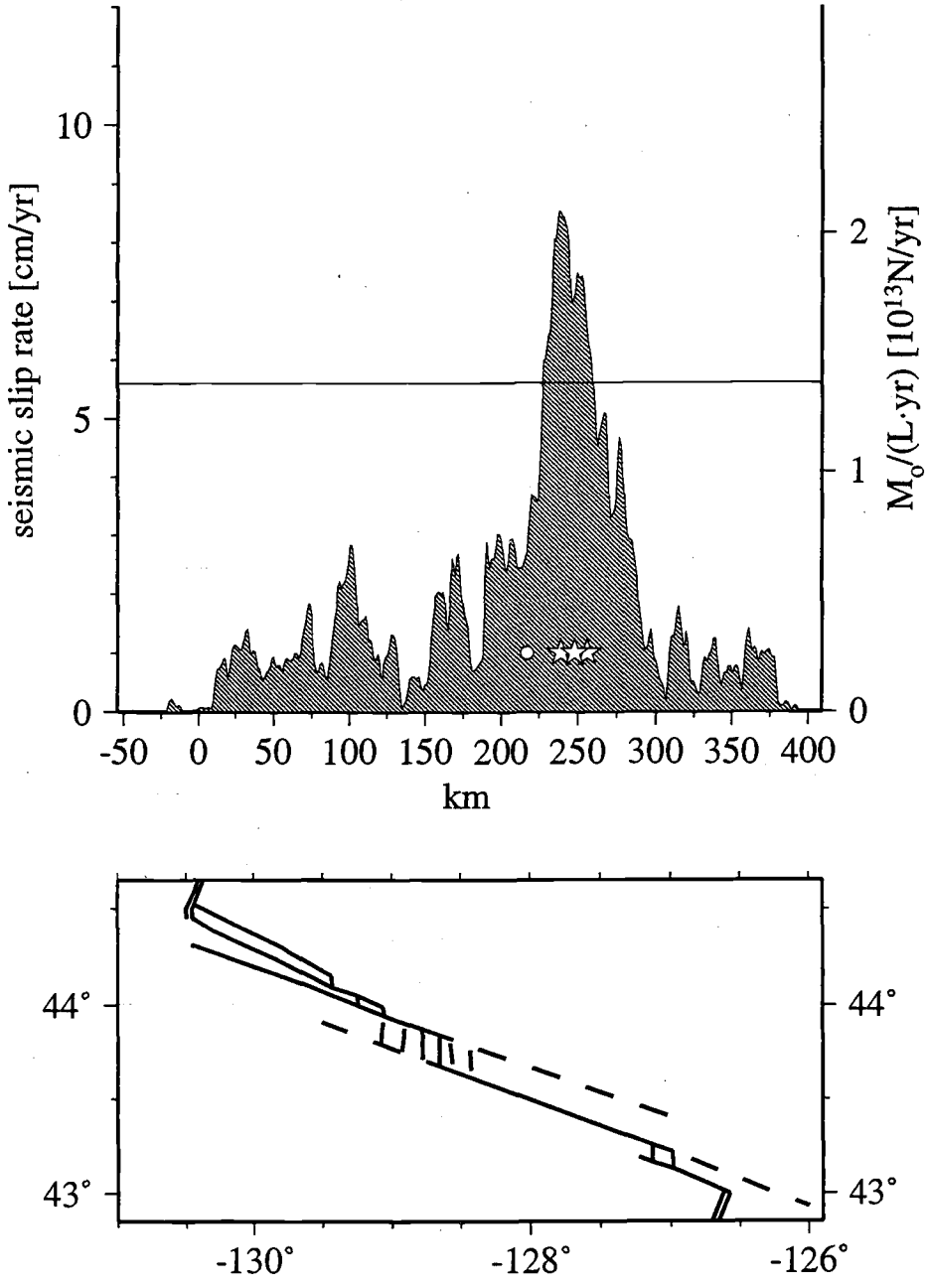

Figure 3.17. Top: seismic slip rate distribution along the BTFZ. The x-axis is relative to 44.45° N, 130.4° W (approximately the BTFZ-Juan de Fuca ridge intersection). The horizontal line at slip rate 5.6 cm/yr corresponds to the expected plate motion rate (*Wilson, 1993*). Stars mark show the location of three $M_w \geq 6$ earthquakes, and the circle denotes the location of one $m_b = 6.1$ earthquake (which occurred in 1968 pre-dating CMT analysis). The earthquake data cover a time span from 1964-08/1998. See text for details. Bottom: overview map of the BTFZ.

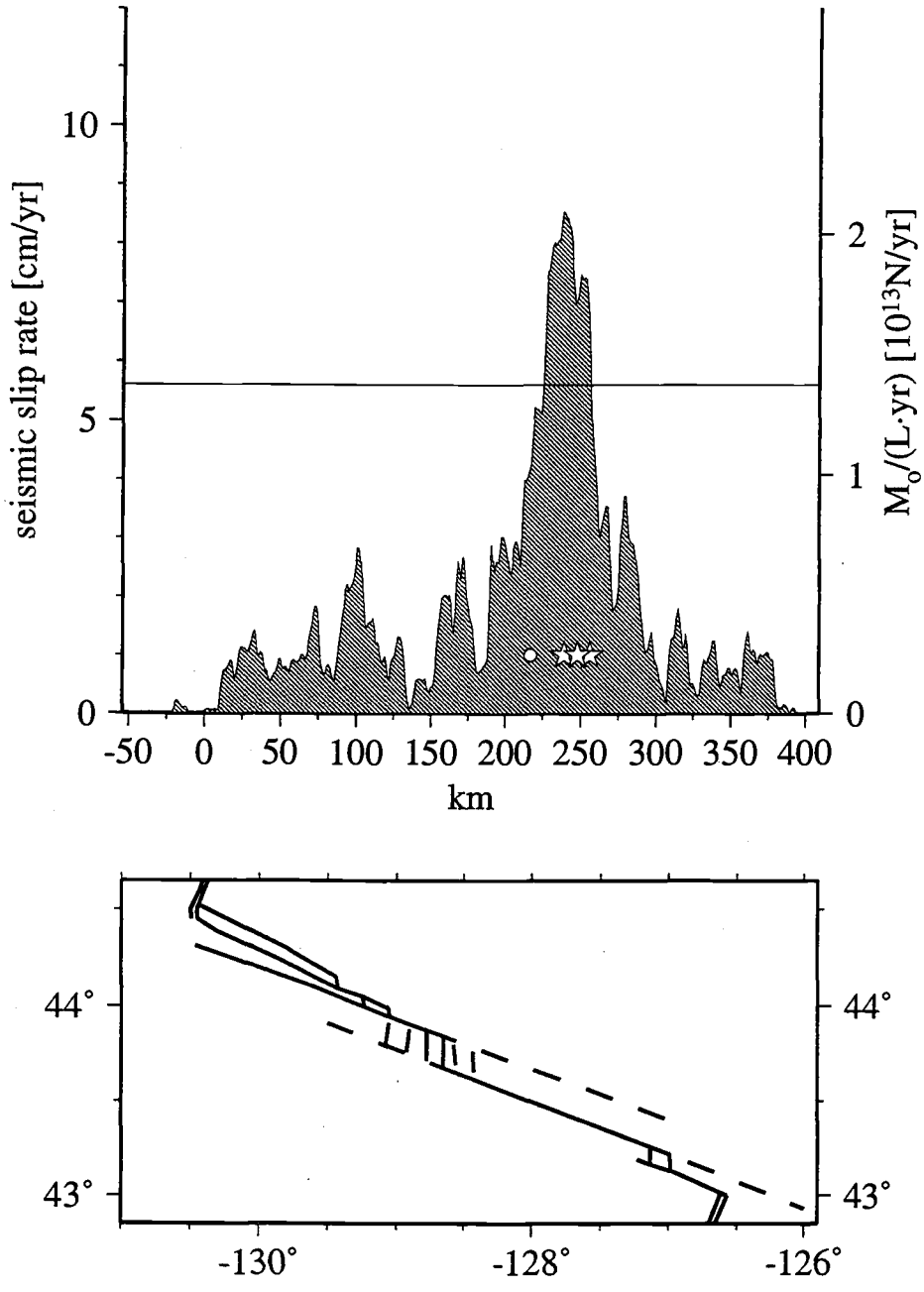

Figure 3.18. Seismic slip rate distribution assuming unilateral rupture to the northwest during the 941027 earthquake. Otherwise as in Figure 3.17.

Dziak et al. (*1991*) divided the BTFZ in two parts at Cascadia Depression and determined slip rate estimates from 1963-1988 for each. They used, however, an incorrect formula in Anderson (*1979*) (see discussion below); their corrected and recalculated slip rate estimates for the northwest and southeast part of the BTFZ are 0.7 cm/yr, and 1.9 cm/yr, respectively, which are about 50% lower than ours.

The influence of seismogenic zone width **W** on the slip rate distribution is illustrated in Figure 3.19. The solid line shows the distribution presented in Figure 3.17 (**W** = 7 km); the long dashes are for **W** = 5 km, and the short dashes for **W** = 10 km, which are probably lower and upper bounds for **W** based on the centroid depth distribution (Figure 3.12). The main effect of decreasing **W** from 10 km to 5 km is to increase the seismic slip rate and to broaden the slip distribution (since $\mathbf{L} \sim \mathbf{u} \sim \mathbf{W}^{-0.5}$). This effect actually is even more pronounced, since a decrease in **W** also decreases the rigidity μ averaged over **W** (rigidity increases with depth in the lithosphere).

Figure 3.20 shows how varying the slip-length ratio **u/L** affects the slip rate distribution. The solid line shows the distribution presented in Figure 3.17 ($\mathbf{C} = \mathbf{u/L} = 1.25 \times 10^{-5}$); the long dashes are for a ratio of $\mathbf{C_1} = 0.5\ \mathbf{C}$, and the short dashes for $\mathbf{C_2} = 2\ \mathbf{C}$. The slip distribution is only affected near the large earthquakes (Blanco Ridge), everywhere else the changes are minimal. In regions dominated by smaller earthquakes increasing **L** and decreasing **u** cancel between two neighboring earthquakes, the overall distribution does not change. In regions dominated by larger events, the shape and width of the side-lobes (the transition area from the large-earthquakes to the small-earthquakes) of the slip distribution are most strongly affected, since neighboring large earthquakes do not exist to compensate for the changes in **L** and **u**. This effect is most pronounced near 175-200 km; for $\mathbf{C_2}$, the slip rate drops drastically near 200 km creating an area of very low slip between 175-200 km, while for $\mathbf{C_1}$, no such gap exists.

Figure 3.21 shows the slip distribution of the RMT and CMT events separated in strike-slip (hatched) and normal faulting earthquakes (solid). Strike-slip earthquakes dominate the moment release along the western most part of the BTFZ (0-115 km), along Blanco Ridge, and along Gorda Depression, while normal faulting earthquakes dominate in the Surveyor-Cascadia-Depression area (115-185 km).

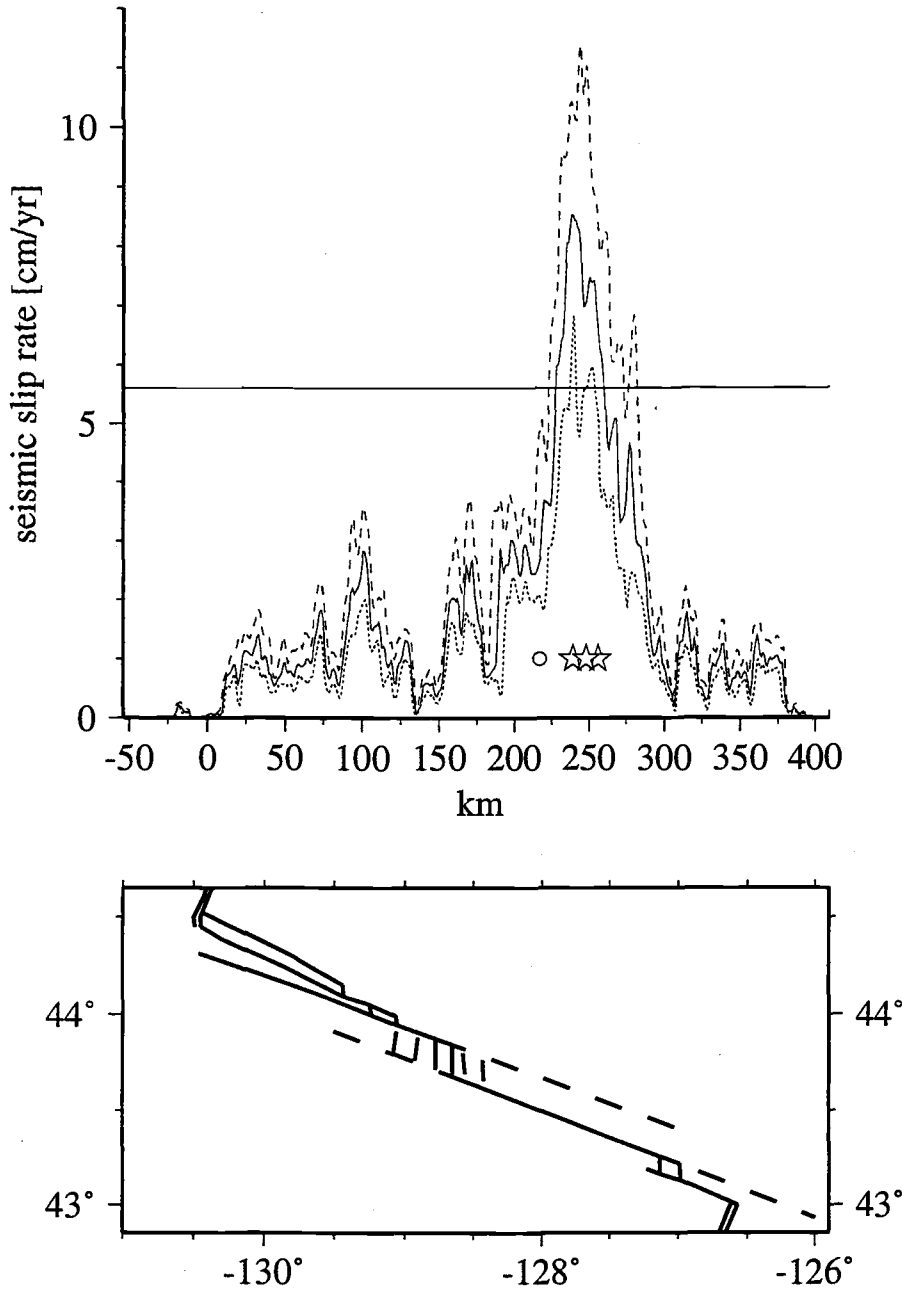

Figure 3.19. Seismic slip rate as a function of seismogenic zone width W. Solid line shows the slip rate estimate from Figure 3.17 (W = 7 km), the long dashes for W = 5 km, and the short dashes for W = 10 km.

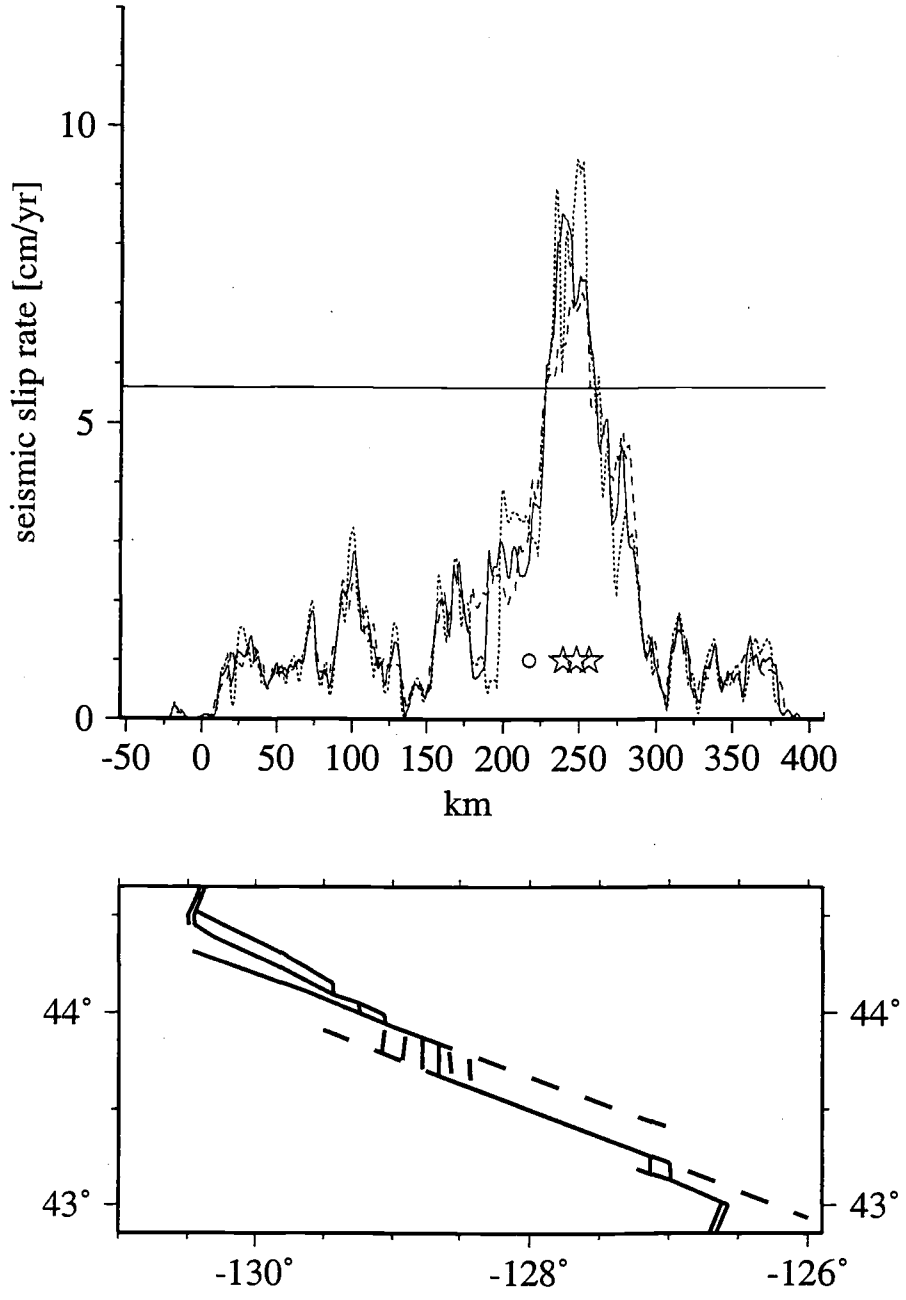

Figure 3.20. Seismic slip rate as a function of slip/rupture-length during earthquake faulting. The solid line represents the estimate shown in Figure 3.17 ($C = 1.25 \times 10^{-5}$); the long dashes are for a ratio of $C_1 = 0.5$ C, and the short dashes are for $C_2 = 2$ C.

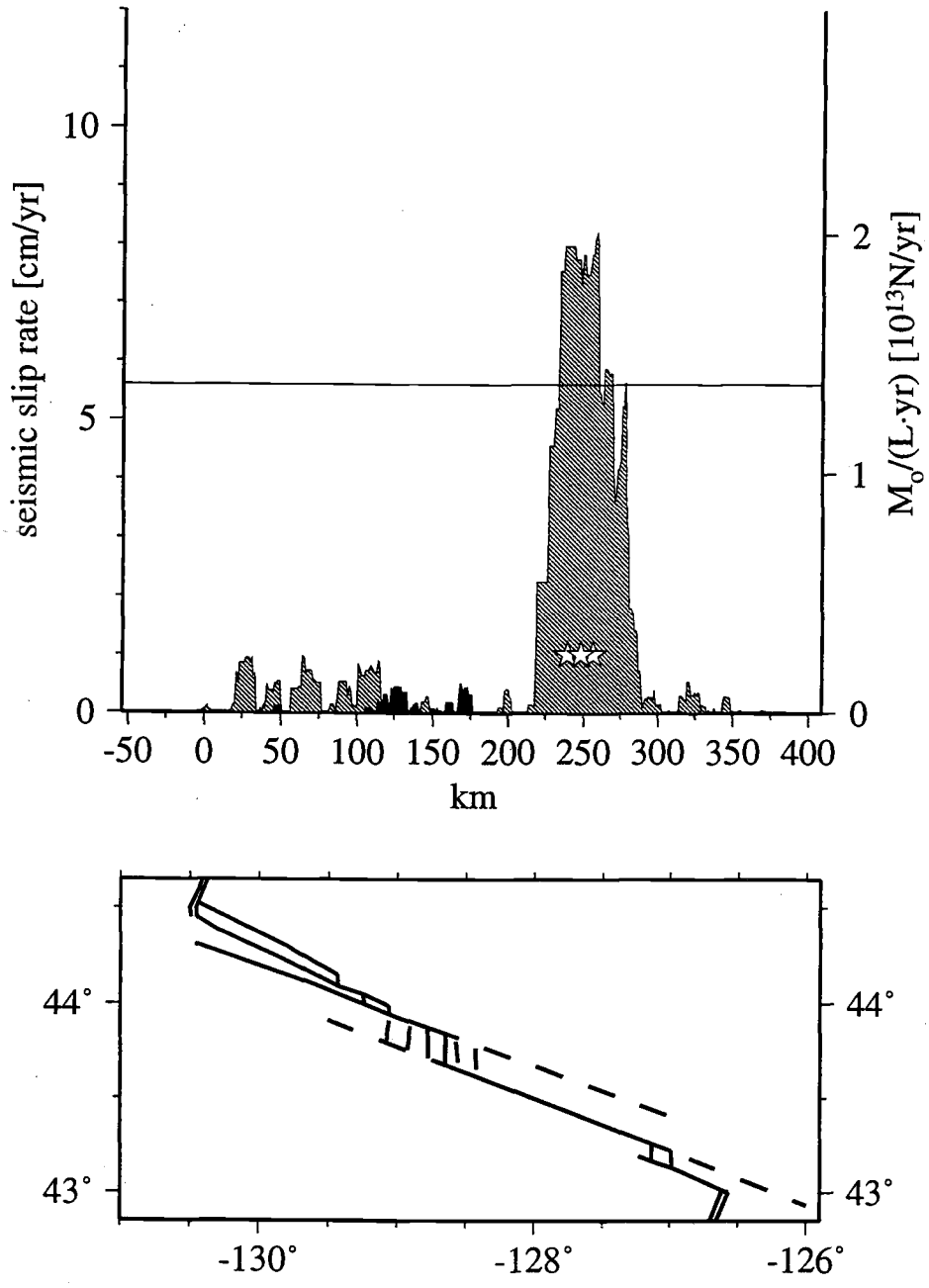

Figure 3.21. Seismic slip rate distribution from the RMT and CMT solutions. The time span covered is 1977-08/1998, however, before RMT analysis, only larger events ($M_w \geq 5$) are included. The stippled areas represent strike-slip faulting, while the solid areas represent normal faulting.

3.5.2 Seismic Slip Rate Estimates from Frequency-Magnitude Curves

In the previous section, we estimated the slip rates from the magnitudes and seismic moments of the observed earthquakes. However, many earthquakes, particularly the smaller ones are not detected or no magnitude was determined (for the BTFZ, ISC and PDE catalogs are probably complete only to about m_b = 4.3-4.4, see Figure 3.22). The observed self-similarity of earthquakes, however, provides a way to estimate how many earthquakes of a certain size occur per time interval. This allows an estimate of the seismic slip rate which takes all earthquakes (observed and unobserved) into account. The derivation below follows Molnar (*1979*). The frequency-magnitude relationship (*Gutenberg and Richter, 1954*)

$$\log N = a - b \cdot M \qquad (3.3)$$

describes the number of earthquakes N with magnitude greater/equal to M. Figure 3.22 shows the frequency magnitude curves for the four segments of the BTFZ.

Combining the frequency-magnitude relation with the moment-magnitude relation (e.g., *Thatcher and Hanks, 1973; Hanks and Kanamori, 1979*)

$$\log M_0 = c \cdot M + d \qquad (3.4)$$

(with c = 1.5 and d = 16.05 in Hanks and Kanamori [*1979*]), yields

$$\log N(M_0) = a + \frac{b \cdot d}{c} - \frac{b}{c} \cdot \log M_0 \qquad (3.5)$$

where $N(M_0)$ is the number of events with seismic moment greater/equal M_0. Re-writing gives

$$N(M_0) = \alpha \cdot M_0^{-\beta} \qquad (3.6)$$

where

$$\alpha = 10^{(a + b \cdot d \div c)} \text{ and } \beta = b / c$$

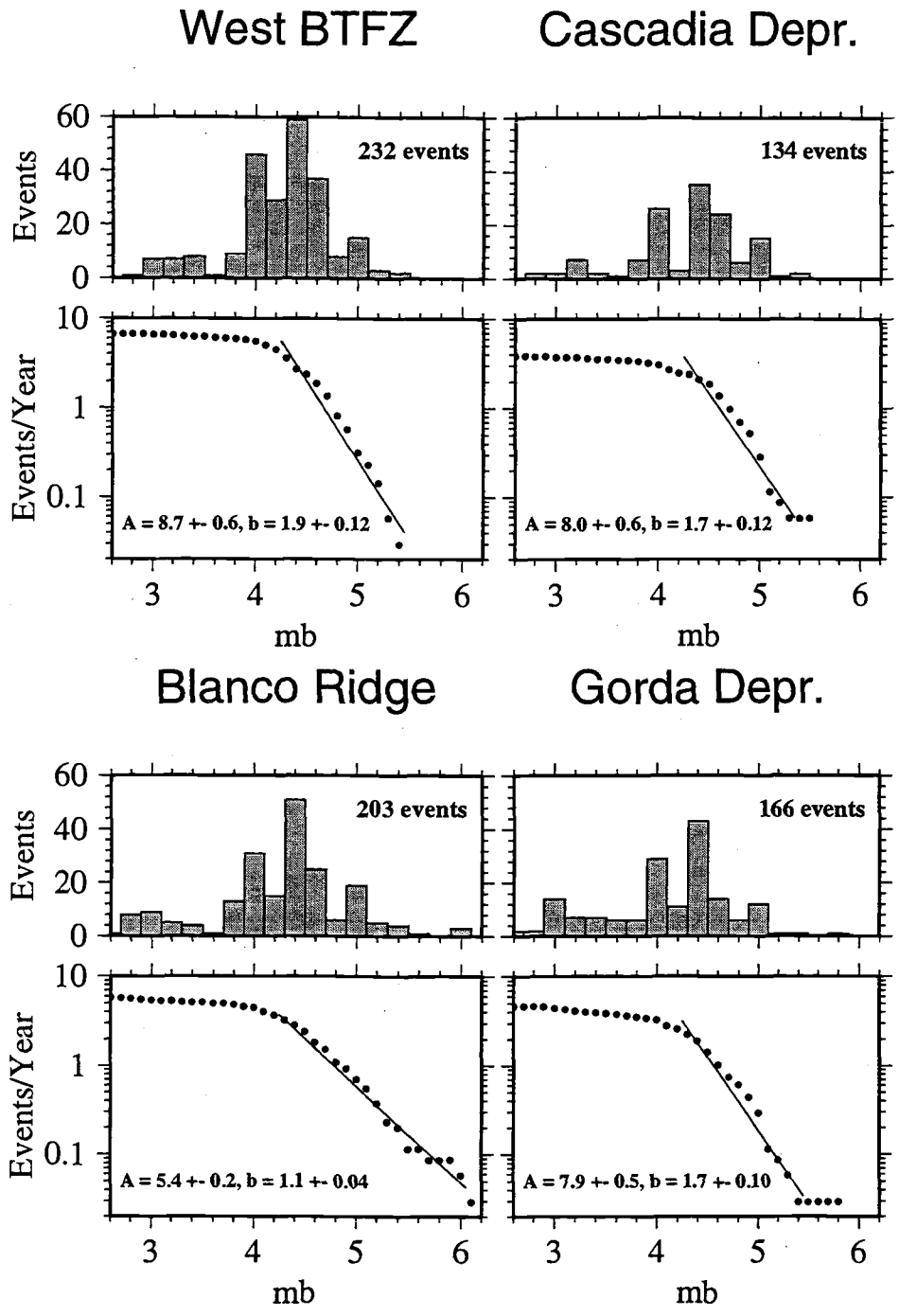

Figure 3.22. Frequency-magnitude relation along four segments of the BTFZ. Each of the four panels shows a histogram of the event magnitudes (top) and the corresponding frequency-magnitude relation (bottom). Linear regression analysis was applied in the magnitude range covered by the solid lines. See text for details.

The cumulative seismic moment rate can be obtained by integrating the product of the density distribution $n(M_0) = - dN/dM_0$ and M_0. Molnar (1979) suggested to truncate $N(M_0)$-vs.-M_0 at a maximum seismic moment M_0^{max} based on the observation that earthquake size is limited. The integration yields

$$\sum (M_0) = \alpha \div (1 - \beta) \cdot (M_0^{max})^{(1-\beta)} \qquad (3.7)$$

where $\sum (M_0)$ equals the cumulative seismic moment rate. Anderson (*1979*) integrated over $N(M_0)$ instead of $n(M_0)$ (and made a mistake in the integration itself). Similar derivations for $\sum (M_0)$ have been presented (e.g., *Weichert, 1980; Anderson and Luco, 1983*), the main difference in the results is caused by truncating $N(M_0)$ or $n(M_0)$ at a maximum magnitude. Anderson and Luco (*1983*) showed that Molnar's (*1979*) estimate is larger because $N(M_0)$-truncation implies that more events close to M_0^{max} "occur" than for $n(M_0)$-truncation.

From equation (3.7) it is obvious that the cumulative seismic moment rate becomes infinite, if $\beta \geq 1$ (or-- for $c = 1.5$-- if $b \geq 1.5$): the smallest events contribute more to the cumulative seismic moment than the largest events. For most parts of the world b is near 1, and the largest events dominate the seismic moment release rate (e.g., *Scholz, 1990*). Infinite cumulative seismic moments are physically not plausible. Aki (*1987*) determined the frequency-magnitude relationship for a group of smaller earthquakes in southern California. He found fewer smaller events than expected from extrapolating the frequency-magnitude relationship from large to small events, this departure from self-similarity occurred near magnitude 3. If this is true, then smaller earthquakes ($M < 3$) contribute only insignificantly to the cumulative seismic moment rates even if b, determined from the larger earthquakes, is larger than 1.5.

Gorda Depression Segment. Contributions from strike-slip earthquakes dominate the moment-release rate (Figure 3.21). The estimated slip rate (0.9 cm/yr) accounts for only about 15% of the Pacific-Juan de Fuca plate motion rate. The shallow centroid depths (4-6 km, Figure 3.12) allow a slight reduction of the seismogenic zone width **W**, however, this would only slightly increase the slip rate. Either most of the slip occurs aseismic or many smaller events, not reported in the ISC and PDE catalogs contribute significantly to the total seismic moment release. The lower right of Figure 3.22 shows the frequency-magnitude curve for the Gorda Depression segment. The least-squares fit to the magnitude-frequency relationship has a large slope $b = 1.7$; from equation (3.7) this would imply an infinite seismic slip rate which is not observed. Extrapolating the number of expected earthquakes

from the frequency-magnitude relation to smaller events and adding contributions from these "virtual" events to the observed seismic slip rate (Figure 3.23) shows that seismicity could account for the entire plate motion; earthquakes with $m_b \geq 2.4$ account for the full plate motion rate if the predicted recurrence rate (b-value) applies to the smaller events. It appears highly unlikely that no earthquakes smaller than $m_b = 2.4$ occur, which suggests the true recurrence rate for small earthquakes deviates from the frequency-magnitude relationship determined from the larger, $m_b \geq 4.3$ earthquakes as had been proposed by Aki (*1987*).

Blanco Ridge Segment . The seismic slip rate along the Blanco Ridge segment (4.5 cm/yr) accounts for almost the entire plate motion rate (5.6 cm/yr). The straight-line fit to the frequency-magnitude relation (lower left Figure 3.22) has a slope b = 1.1, which is much lower than along the other three segments. The smaller b-value implies that larger earthquakes dominate the moment release rate. Extrapolating the frequency-magnitude relation to smaller events and summing over their "virtual" contribution, thus, adds little to the cumulative seismic moment estimate (Figure 3.23). Most deformation occurs during large earthquakes. Fox et al. (*1994*) located about 300 earthquakes during one year along the Gorda and Blanco Ridge segments; we find, extrapolating the frequency magnitude relationship for both segments to smaller magnitudes, that 300 earthquakes/year correspond to a SOSUS detection threshold of $m_b = 3.3$ (with a range from 2.8 to 3.7). A short hydrophone deployment recorded micro-earthquakes at the south side of Blanco Ridge (*Johnson and Jones, 1978*). Thus smaller earthquakes do occur along the Blanco Ridge segment, however, probably not as frequent as along other segments.

Cascadia and Surveyor Segments. Observed seismicity accounts for only about 20% of the predicted plate motions (Figure 3.8). The b-value of 1.7 of the frequency-magnitude relation (Figure 3.22) indicates that small events possibly contribute significantly to the cumulative seismic moment release rate. Adding the contributions from the smaller events shows that all $m_b \geq 2.8$ earthquakes could account for the full plate motion rate (Figure 3.23). If all earthquakes occur on dipping fault planes (we assume 45°-dipping normal faults) the full rate is reached by summing contributions from all $m_b \geq 2.3$ earthquakes.

West Blanco Segment. The observed seismic slip rate along the West Blanco Depression accounts for only about 20% of the plate motion rate. The centroid depths are shallow, thus the seismogenic width may actually be slightly less than 7 km; however, a small change of about 1-2 km in width affects the seismic rate estimate only slightly. We

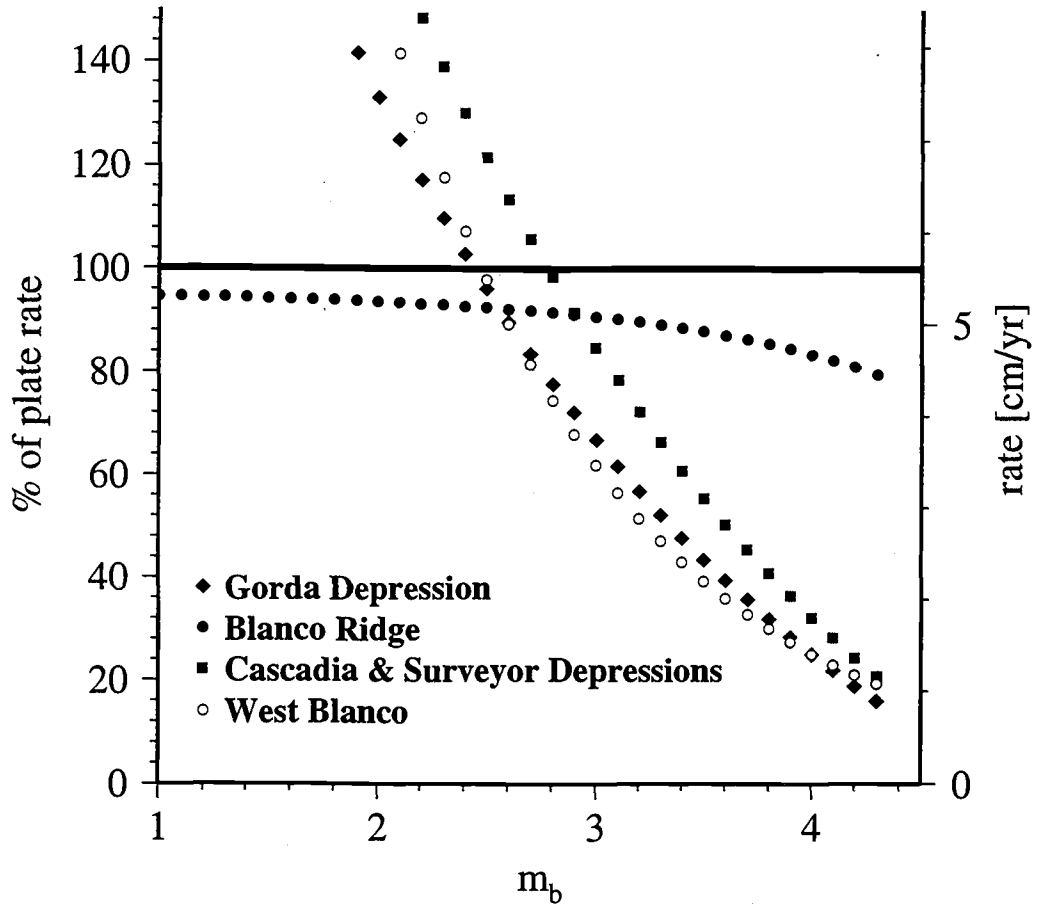

Figure 3.23. Slip rate estimates from extrapolating frequency-magnitude relationship. Percentage (relative to full plate motion rate of 5.6 cm/yr-- heavy horizontal line) and absolute amount of the seismic slip rate are shown for four segments: Gorda Depression, Blanco Ridge, Cascadia and Surveyor Depressions, and West Blanco segment. The rates at $m_b = 4.3$ are averages for each segment determined from observed seismicity (Figure 3.17) assumed to be complete for $m_b \geq 4.3$. For smaller m_b's, seismic slip rates are obtained from extrapolation of the frequency-magnitude relation (equation 3.3 with a and b given in Figure 3.22) and application of the moment-magnitude relation (equation 3.1). When including smaller earthquakes, the seismic slip rate increase exponentially for $b > 1.5$ (Gorda Depression, Cascadia and Surveyor Depressions, and West Blanco segment); for $b < 1.5$ (Blanco Ridge), the rate is dominated by contributions from large earthquakes.

fit the frequency-magnitude relation (upper left corner, Figure 3.22) with a slope of b = 1.9, the largest value for any of the four segments. The large b-value implies that small (not recorded) earthquakes affect the seismic slip rate estimate significantly, summing all "virtual" $m_b \geq 2.4$ earthquakes results in a seismic slip rate estimate that accounts for the entire plate motion rate (Figure 3.23). Thus slip along the West Blanco Segment may entirely be seismic. Inspection of the earthquake catalogs (ISC and PDE) indicates that many swarm like sequences, without a dominant "main" event but with many similarly sized smaller earthquakes, occur along the West Blanco segment. However, lack of catalog completeness (catalogs are complete only down to about $m_b = 4.3$-4.4, see magnitude-event histograms in Figure 3.22) makes a more thorough investigation impossible. SOSUS based locations could provide the necessary data: Fox et al (*1994*) located about 640 earthquakes during a one year time span from the Cascadia-Surveyor and the West Blanco Segments, extending our frequency-magnitude relation for the two segments to 640 earthquakes suggests the SOSUS-detection threshold is $m_b = 3.3$ (with a possible range from 2.7 to 3.8).

Including smaller earthquakes to the cumulative seismic moment (seismic slip rate) estimates suggests that seismicity could account for the full plate motion rate along the entire BTFZ. The slopes (b-values) of the frequency-magnitude relation are not well determined (Figure 3.22) possibly reflecting catalog incompleteness and inaccuracies in determination of m_b. However, the difference between the Blanco Ridge segment and the other segments is well resolved; the difference implies that moment release along Blanco Ridge mainly occurs during large earthquakes, while smaller earthquakes contribute most to the seismic moment release along the other segments.

3.6 Concluding Remarks

The newly available regional broadband seismic data allowed the most detailed, long-term monitoring effort of an oceanic transform fault system to date. With the new data we were able to determine source mechanisms of more than 120 earthquakes distributed along the entire length of the BTFZ. The faulting style inferred from the source mechanisms agrees well with the morphology, with normal faulting earthquakes occurring inside the Gorda, Cascadia, and Surveyor depressions and strike-slip earthquakes occurring along the

easternmost part of the BTFZ, along Blanco Ridge, and along the tectonically more complex western part of the BTFZ.

We suggest that two strike-slip faults border the entire, bathymetrically deep eastern part of the BTFZ from Gorda Ridge to (and including) Gorda Depression; this entire part is a mature pull-apart basin.

The largest (strike-slip) earthquakes nucleated in the central part of Blanco Ridge where unusually shallow abyssal hill topography merges with the Blanco Ridge. This fault zone complexity divides the Blanco Ridge transform into two fault segments. The eastern part is seismically very active, while only few earthquakes occurred in the western part. The difference is possibly due to large earthquakes rupturing into the western segment.

The horizontal principal stress axes for earthquakes near Cascadia Depression are rotated relative to the axes of other earthquake source mechanisms along the BTFZ. The axes orientations are consistent with the spreading direction at the Gorda and Juan de Fuca ridges; this may indicate active seafloor spreading at Cascadia Depression.

Seismic activity along the western part of the BTFZ is distributed over several fault strands. Larger earthquakes accommodate only a small portion of the expected plate motions, but the large observed b-value suggests smaller earthquakes could account for the remainder. Deformation probably occurs seismically along many small fault segments.

The seismic slip rate distribution along the BTFZ indicates that the seismic behavior along a transform fault zone can differ significantly from segment to segment. We expect, that application of our simple procedure for estimating the slip rate distribution could be a very useful tool to investigate segmentation of oceanic transform faults. A reliable estimate based on our procedure requires precise earthquake locations and a relatively complete earthquake catalog over the duration of at least one full seismic cycle.

Comparing the teleseismically relocated epicenters indicates some inconsistencies in the SOSUS based earthquake locations. More precise absolute locations with close range instrumentation are necessary to fully evaluate SOSUS' performance for earthquake studies.

4. LOCATION AND SOURCE PARAMETERS OF OFFSHORE PETROLIA, CALIFORNIA EARTHQUAKE

4.1 Introduction

The Mendocino triple junction is an area of intense seismic activity (e.g., *Castillo and Ellsworth, 1993; Smith et al., 1993; Schwartz, 1995*). However, the one-sided seismic station distribution results in large uncertainty and possible systematic bias in earthquake locations, hampering tectonic interpretations of this complicated plate boundary.

During the 1994 Mendocino triple junction experiment (*Tréhu et al., 1995*), an $m_b = 4.7$ earthquake on 19 June located offshore Petrolia (Figure 4.1) was well recorded by nine ocean bottom hydrophones (OBH) and seismometers (OBS). The good azimuthal station coverage of the combined land and offshore recordings allows precise location of the earthquake, which may be useful as a master event for relocation of other events in the vicinity. The moment-tensor estimate from regional waveforms is presented to complete the analysis and to independently check the hypocentral depth estimate.

4.2 Locating the Earthquake

The inset in Figure 4.1 shows the OBH/OBS and land seismic station distribution around the epicenter. Table 4.1 gives the OBH/OBS sites in the immediate vicinity, including one within a few kilometers of the epicenter, had been retrieved only hours before the event. The seismograms recorded by the OBH/OBS are shown in Figure 4.2. The arrival times from land stations were taken from the Northern California Earthquake Data Center. We used HYPOINVERSE (*Klein, 1978*) to locate the earthquake.

The offshore data, 90 to 120 km from the epicenter, consist of P_n arrivals, which are insensitive to hypocentral depth. Hypocentral depth control comes mainly from close land stations (P_g arrivals) to the north- and southeast of the epicenter.

To illustrate the improved resolution of the hypocentral parameters using the combined onshore-offshore data set, we first performed inversions using only the land data. To

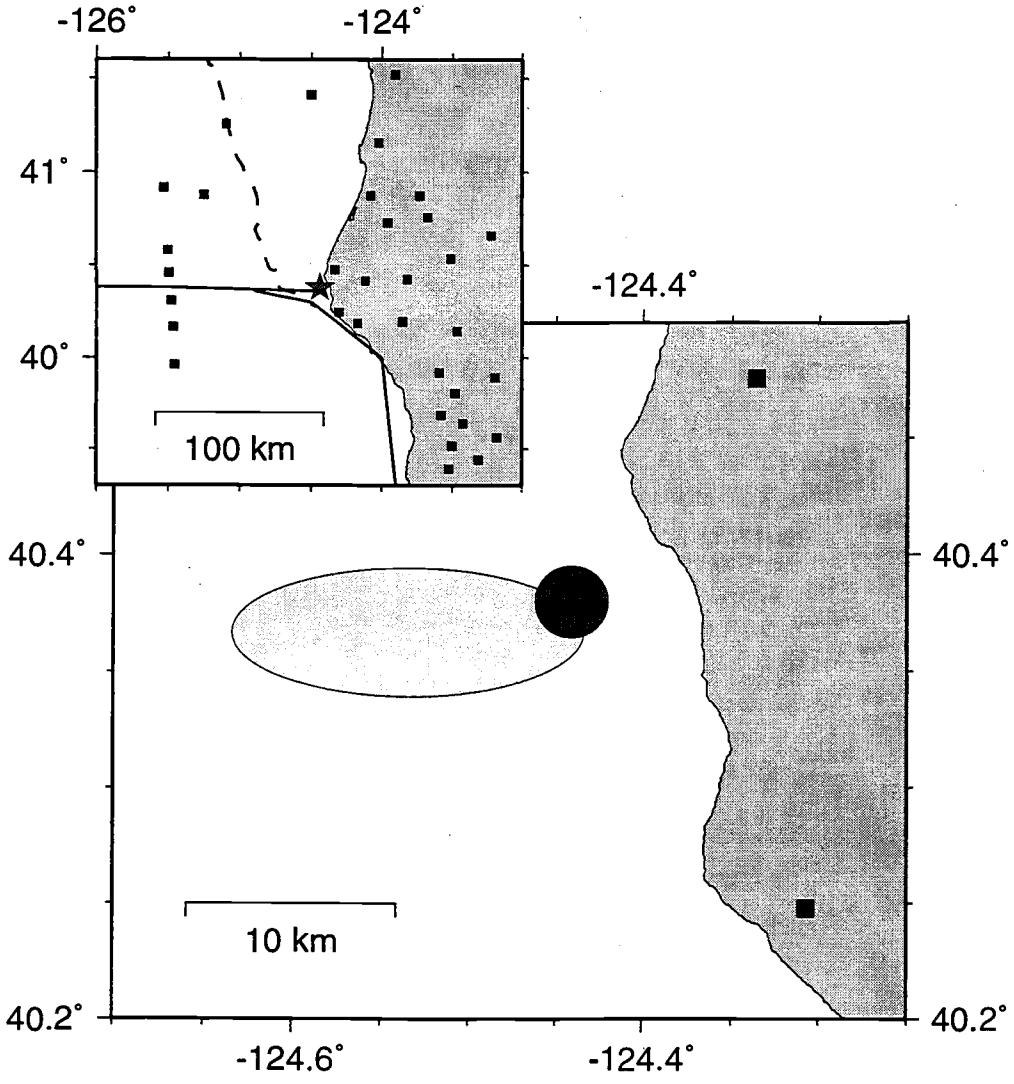

Figure 4.1. Inset, regional map. Squares denote OBH/OBSs and land seismic stations used for earthquake location. Star shows final epicenter (for oceanic mantle velocity [v_{om}] of 7.9 km/sec). Solid lines sketch Mendocino and San Andreas transform faults' location of triple junction as well as seaward continuation of San Andreas fault are not known precisely. Dashed line shows deformation front. Main figure, close-up of epicentral region. Light-shaded ellipse depicts an area of possible locations when only land data are used. Dark-shaded ellipse shows possible area of locations when OBH/OBS data are included (for v_{om} = 7.9 km/sec).

Table 4.1. OBH/OBS Locations and *P* Arrival Times.

OBH/OBS	Latitude (°)	Longitude (°)	Water Depth (m)	*P* Arrival (sec)
OBH16	41.413	-124.501	345	50.12
OBH23	41.258	-125.096	3100	48.45
OBH22	40.918	-125.533	3075	47.95
OBH21	40.881	-125.254	2990	45.60
OBSC1	40.583	-125.503	2893	46.11
OBH17	40.459	-125.496	2810	45.90
OBH18	40.306	-125.483	1890	45.97
OBSC3	40.166	-125.470	2375	46.31
OBH24	39.963	-125.455	2950	47.01

P arrival time is measured from 940619 10:39 UTC.

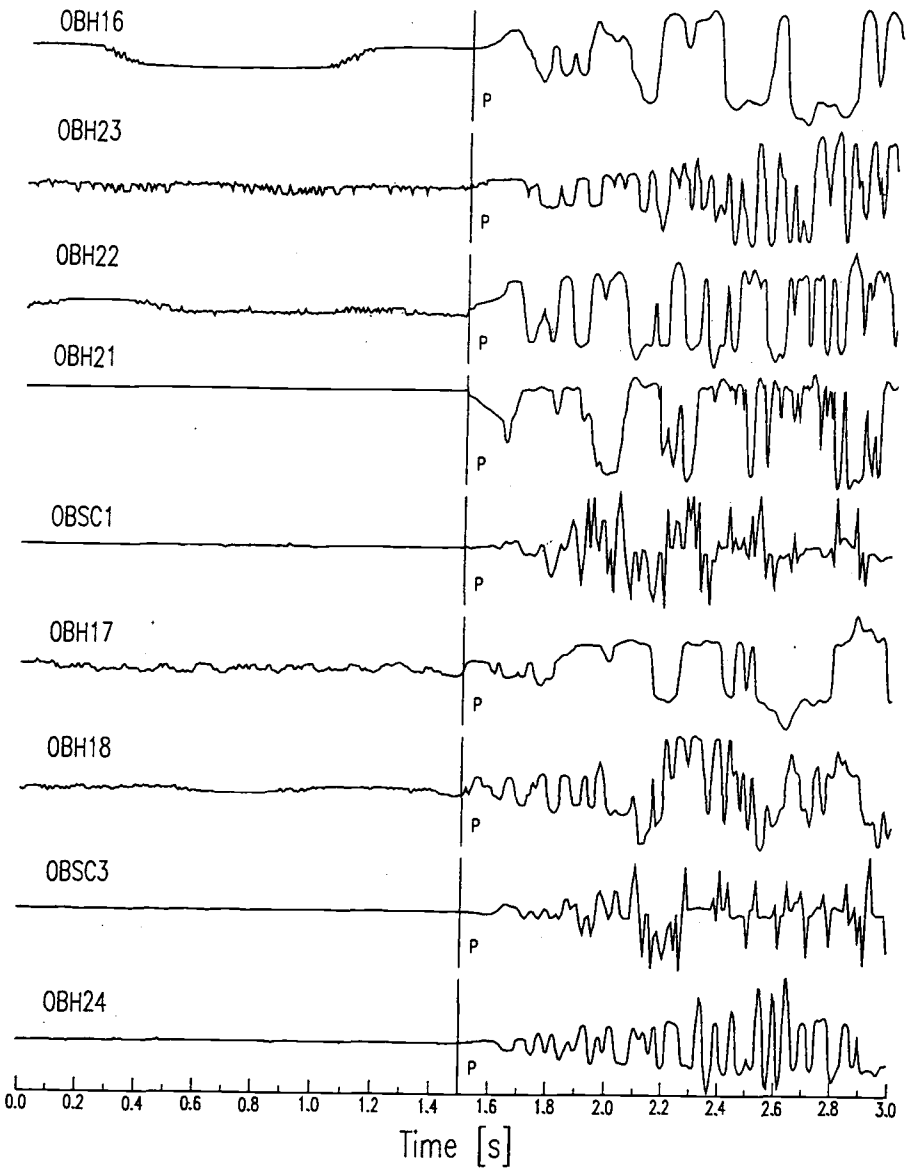

Figure 4.2. Unfiltered OBH/OBS data used in this study centered on the *P* pick (Table 4.1 gives pick times). *P* arrivals were read from enlarged traces; reading uncertainties are generally less than 0.1 sec. On all instruments, the recording system sees to have been saturated shortly after the *P* onset, distorting the waveforms.

investigate how location estimates are affected by the choice of velocity models and inversion parameters, we used five different velocity models (A through E in Figure 4.3) and varied the inversion parameters for each velocity model. Next we used the combined data set, applied offshore velocity models (Figure 4.3) to the OBH/OBS data, and inverted for the hypocenter for each of the five land velocity models.

The light-shaded ellipse in Figure 4.1 illustrated the influence of velocity structure, inversion parameters, and station corrections on the earthquake location when only land data are used. The ellipse represents a combination of locations from many HYPOINVERSE runs using different velocity models, varying inversion parameters, and adding/removing station corrections (where available). The epicenter's latitude is well constrained by the land data; however, the lack of data from the west causes the epicenter's longitude to be strongly influenced by the choice of inversion parameters and velocity model.

Closer examination of the results indicates that the uncertainty is due primarily to the choice of inversion parameters, particularly "distance weighting" and "residual weighting." Uncertainly in the velocity model is a secondary effect. For a given set of inversion parameters, the locations obtained from the velocity models are generally within 3 km in longitude and within less than 2 km in latitude from their common centroid. For a given velocity model, however, changing the inversion parameters strongly affects longitude, with possible shifts on the order of 10 km. Origin time primarily trades off with longitude; epicenter locations closest to the coast have predicted origin times up to 1.5 seconds later than for westernmost locations.

Hypocenter depth is affected by both the velocity model and inversion parameters, though the large majority of combinations tested did yield depths between 18 and 21 km. The average nominal 2σ uncertainties for individual locations ($\pm$0.8 sec, $\pm$2.1 km, $\pm$6.6 km, and $\pm$2.5 km for origin time, latitude, longitude, and hypocenter depth, respectively) underscore the lack of longitudinal control when only land stations are used.

The dark-shaded ellipse in Figure 4.1 shows the epicentral uncertainty when the OBH/OBS data are included. The greatly improved azimuthal station coverage provided by the combined land and OBH/OBS data se constrains the longitude and, furthermore, decreases the epicenter's dependence on the choice of (land) velocity structure. The inversion parameters for the combined data se were chosen such that all OBH/OBS data have significant weight, i.e., the "distance weighting" included stations up to 150-km epicentral distance. For an oceanic upper-mantle velocity (v_{om}) of 7.9 km/sec, we obtain average hypocenter parameters of 10:39:33.2 UTC for origin time, 40.376° N latitude, 124.441° W longitude, and a depth of 18.8 km. The locations obtained from the different

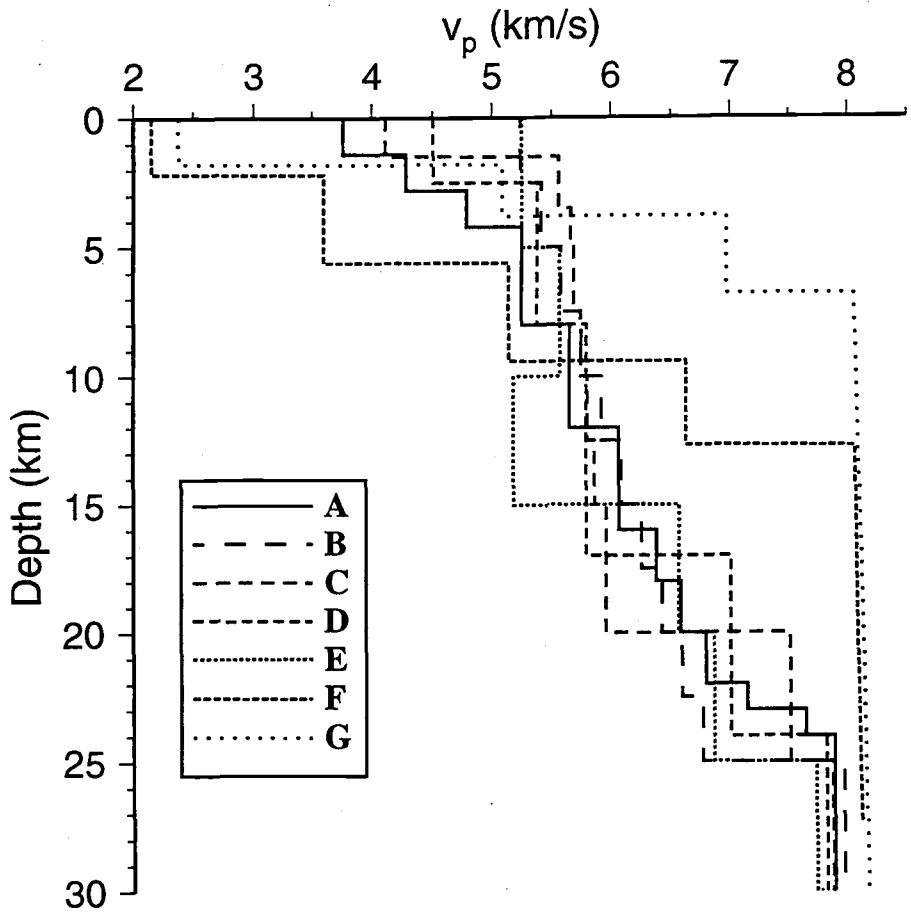

Figure 4.3. Velocity models used for locating the earthquake. For land stations: A, Northern California Seismic Network model (*Oppenheimer personal comm.*); B, University of California at Berkeley model (UCB seismic station report): C, Castillo and Ellsworth (*1993*); D, Humboldt Bay model (*Smith et al., 1993*); E, Verdonck and Zandt (*1993*). For offshore stations: F, oceanic shelf model applied to OBH16; G, oceanic shelf model applied all other OBH/OBS s. Models A, B, F, and G were originally linear velocity gradient models, which we approximated by discrete homogeneous layers.

land velocity models are generally within 0.1 sec in origin time, within less than 1 km in latitude and longitude, and within less than 2 km in depth from the average location. The average nominal 2σ uncertainties for individual locations using the combined land and OBH/OBS data set decreases to ±0.2 sec in origin time, ±1.9 km in latitude, ±1.4 km in longitude, and ±2.5 km in depth, primarily improving the longitudinal control. Varying the oceanic upper-mantle velocity between 7.7 and 8.1 km/sec affects the epicenter's longitude only slightly: for 7.7 km/sec, the epicenter moves about 2 km farther offshore compared with 8.1 km/sec, while the origin-time becomes earlier by about 0.3 sec (Table 4.2).

4.3 Regional Moment-Tensor Inversion

Modeling of complete three-component waveforms recorded at regional distances is used to estimate the seismic moment-tensor and to provide an independent constraint on the earthquake's depth. The method is described in Nábelek and Xia (*1995*) and Braunmiller *et al.* (*1995a*). We used the Northern California Seismic Network crustal model (*Oppenheimer, personal comm.*) (Figure 4.3) with a Poisson's ratio of 0.27 for calculating synthetic discrete wavenumber seismograms (*Bouchon, 1982*).

Using only stations at epicentral distances closer than 350 km (DBO, ARC, YBH, WDC, MIN, ORV, and BKS) and inverting in the 20- to 70-sec period band, we find a best-fitting centroid depth of 21 km, we obtain a strike of 220°, dip of 81°, and rake of 38°. The waveform fit is shown in Figure 4.5. The large-amplitude variations (e.g., very nodal vertical and radial component at YBH, and nodal transverse component at WDC and MIN) constrain the predominantly strike-slip mechanism well. The mechanism is quite stable (Figure 4.4) with a slightly increasing strike-slip component with depth. The north-south-trending *P* axis is typical for events with the Gorda plate (e.g., *Velasco et al., 1994*).

4.4 Discussion and Conclusions

Accuracy of earthquake locations offshore northern California is hampered by one-sided station distribution. When using only arrival-time data recorded onshore, as is

Table 4.2. Location estimates of the 940619 earthquake.

	Origin Time (h:m:s)	Latitude (°)	Longitude (°)	Depth (km)
V_{om} 7.9	10:39:33.2	40.376	-124.441	18.8
V_{om} 7.7	10:39:33.0	40.377	-124.455	18.7
V_{om} 8.1	10:39:33.3	40.376	-124.428	18.8
PDE	10:39:32.8	40.354	-124.457	19.0

Given are three locations with velocity of oceanic upper mantle (v_{om}) varying from 7.7 to 8.1 km/sec. Each location represents the average of several inversions with varying crustal models for the land stations. As a reference, the USGS location (Preliminary Determination of Epicenters bulletin) is given.

Number of stations with weight ≥0.1 was 29, azimuthal gap was ~100°, distance to closest station was ~15 km.

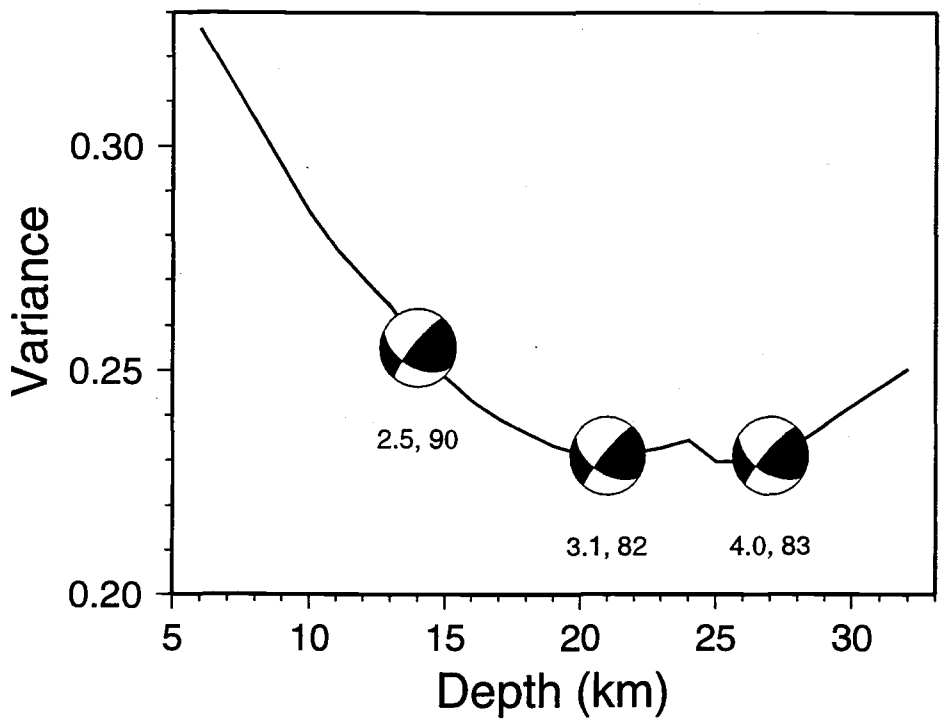

Figure 4.4. Residual variance reduction versus centroid depth for regional waveform inversion. Numbers beneath fault place solutions are seismic moment (in 10^{16} N-m) and percent double couple of moment-tensor solution. At best depth of 21 km, we obtain 220°, 81° , and 38° for strike, dip, and rake, respectively.

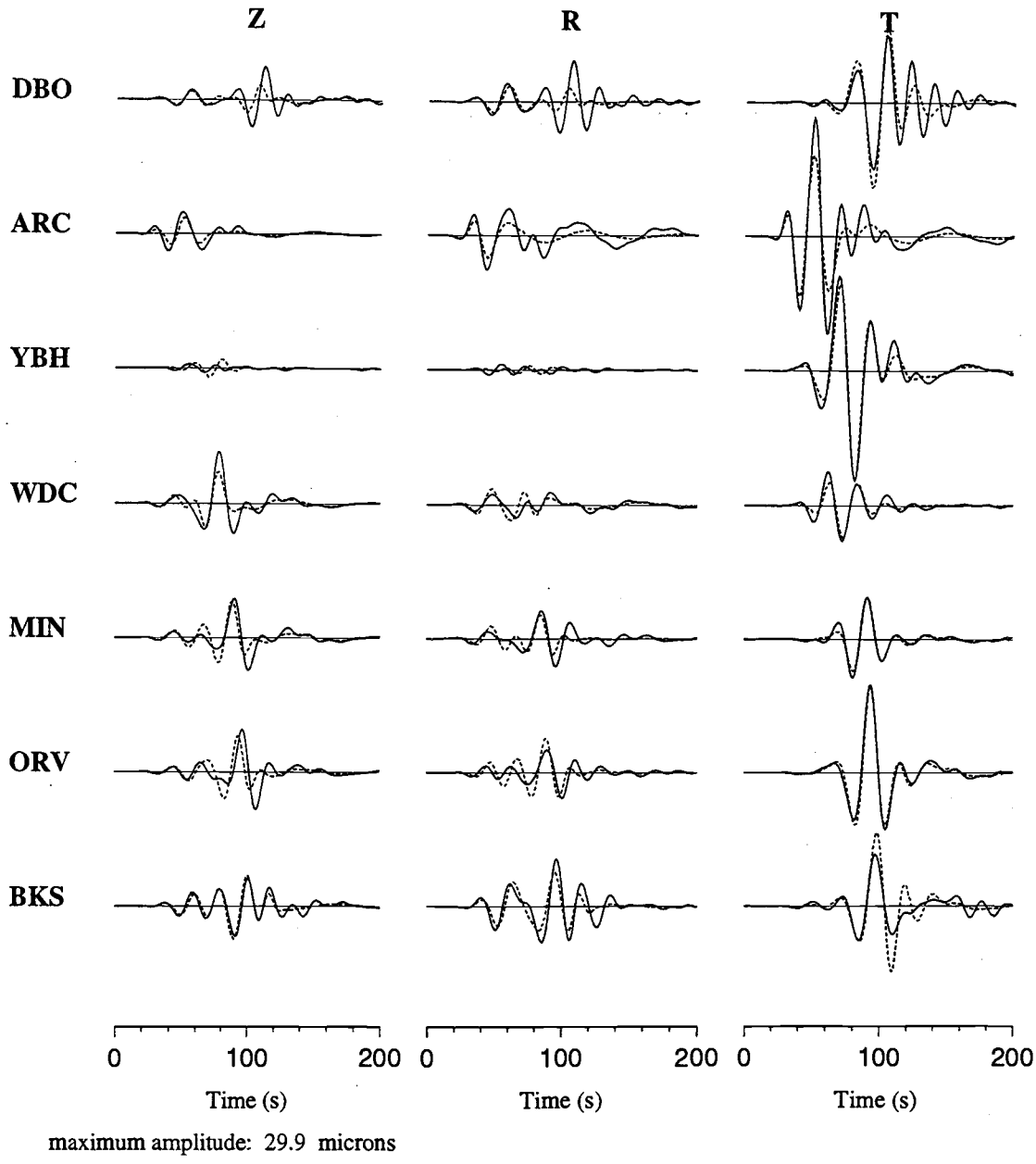

Figure 4.5. Waveform fit in the 20-70-sec period passband for the best-fit model. Solid lines are observed seismograms; dashed lines are synthetic seismograms; Z, R, and T indicate vertical, radial, and transverse component, respectively. All seismogram amplitudes are normalized to an epicentral distance of 100 km assuming cylindrical geometrical spreading.

generally the case, we found that the estimated longitude is strongly influenced by the choice of inversion parameters ("distance weighting" and "residual weighting") and to a lesser degree by the velocity model.

The combined land and OBH/OBS data set, because of its improved azimuthal coverage, yields an earthquake epicenter location (Figure 4.1) that is essentially independent of the assumed velocity model on land and of the exact inversion parameter choice, as long as offshore data have significant weight. The relatively homogeneous, simple travel path to the OBH/OBS (mainly within the uppermost oceanic mantle) allows the use of simple oceanic velocity models. In this study, we varied the oceanic upper-mantle velocity v_{om}) between 7.7 and 8.1 km/sec, and found only a small effect on longitude (Table 4.2). Moreover, as the constraint on v_{om} improves as a result of ongoing studies, the uncertainty will decrease further.

The OBH/OBS data do not directly ass information on the hypocenter depth; however, by constraining the longitude more tightly, the trade-off between longitude, origin time, and depth is also reduced. We consistently obtain a hypocentral depth between 18 km [*Castillo and Ellsworth (1993) and Smith et al., (1993) models]* and 20 km [*Verdonck and Zandt (1994) model*]. This depth is consistent with the depth (19 to 27 km) obtained from regional waveform inversion (Figure 4.4). The regional moment-tensor inversion also showed that the event was a strike-slip earthquake with north-south-trending *P* axis, as is typical for Gorda plate earthquakes.

This study underscored the importance of OBH/OBS data for high-quality earthquake locations in the seismically very active (e.g., *Castillo and Ellsworth, 1993; Smith et al., 1993*) Mendocino triple junction region. The precise location of the 1994 Petrolia earthquake may be useful a master event for relocating other events, improving tectonic interpretations of the area. Furthermore, OBH/OBS deployments lasting several months, which are now possible, could help to map the seismicity in detail and improve and constrain existing velocity models, inversion parameter, and station corrections for the land network.

5. CONCLUSIONS

In this thesis, we present the first detailed, long-term seismotectonic studies of oceanic ridge-transform systems. The proximity of the Juan de Fuca plate to a network of broadband seismic stations in western North America provides a unique synergy of interesting tectonic targets, high seismicity, and recording capabilities. Our main tools are earthquake source parameters, determined by robust waveform modeling techniques, and precise earthquake locations, determined by joint epicenter relocation. Regional broadband data are used to invert for the source moment tensors of the frequent, moderate-sized ($M \geq 4$) earthquakes; this analysis began 1994. We include Harvard centroid moment-tensors available since 1976 for larger ($M \geq 5$) earthquakes.

Two studies comprise the main part of this thesis. In the first, we determine the current tectonics of Explorer region offshore western Canada. Earthquake slip vector azimuths along the Pacific-Explorer boundary require an independent Explorer plate. We determine its rotation pole and provide a tectonic model for the plate's history over the last 2 Ma. Plate motion changes caused distributed deformation in the plate's southeast corner and caused a small piece in the southwest corner to transfer to the Pacific plate. Capture of the plate fragment indicates that preserved fragments not necessary represent entire microplates.

In the second study, we investigate seismicity and source parameters along the Blanco Transform Fault Zone (BTFZ). The deformation style-- strike slip and normal faulting-- correlates well with observed changes in BTFZ's morphology. We infer that Blanco Ridge probably consists of two fault segments, that several parallel faults are active along BTFZ's west part, and that Cascadia Depression possibly is a short spreading center. The slip distribution along the BTFZ is highly variable, although seismicity could account for the full plate motion rate along the entire BTFZ.

The final part is a short study where we locate an earthquake in the tectonically active Mendocino triple junction region offshore northern California using land and offshore data. The precise location may be useful as a master event for relocating other earthquakes.

Bibliography

Aki, K., Magnitude-frequency relation for small earthquakes: A clue to the origin of *f-max* of large earthquakes, *J. Geophys. Res.*, 92, 1349-1355, 1984.

Aki, K., and P. G. Richards, *Quantitative Seismology: Theory and Methods, vol. 1*, W. H. Freeman, New York, 1980.

Allan, J. F., R. L. Chase, B. Cousens, P. J. Michael, M. P. Gorton, and S. D. Scott, The Tuzo Wilson volcanic field, NE Pacific: Alkaline volcanism at a complex, diffuse, transform-trench-ridge triple junction, *J. Geophys. Res.*, 98, 22367-22387, 1993.

Anderson, J. G., Estimating the seismicity from geological structure for seismic-risk studies, *Bull. Seis. Soc. Am.*, 69, 135-158, 1979.

Anderson, J. G., and J. E. Luco, Consequences of slip rate constraints on earthquake occurrence relations, *Bull. Seis. Soc. Am.*, 73, 471-496, 1983.

Atwater, T., Plate tectonic history of the northeast Pacific and western North America, *in: The geology of North America, vol. N; The eastern Pacific Ocean and Hawaii*, eds. E. L. Winterer, D. M. Hussong, and R. E. Decker, pp. 21-72, Geological Society of America, Boulder, CO, 1989.

Barr, S. M., and R. L. Chase, Geology of the northern end of the Juan de Fuca Ridge and sea-floor spreading, *Can. J. Earth Sci.*, 11, 1384-1406, 1974.

Bergman, E. A., and S. C. Solomon, Transform fault earthquakes in the north Atlantic: source mechanisms and depth of faulting, *J. Geophys. Res.*, 93, 9027-9057, 1988.

Bérubé, J., G. C. Rogers, R. M. Ellis, and E. O. Hasselgren, A microseismicity study of the Queen Charlotte Islands region, *Can. J. Earth Sci.*, 26, 2556-2566, 1989.

Biot, M. A., The interaction of Rayleigh and Stoneley waves in the ocean bottom, *Bull. Seis. Soc. Am., 42*, 81-93, 1952.

Bird, A. L., and G. C. Rogers, Earthquakes in the Queen Charlotte Islands region (abstract), *Trans. Am. Geophys. Union*, 77 , F522, 1996.

Bohannon, R. G., and T. Parsons, Tectonic implications of post-30 Ma Pacific and North America relative plate motions, *Geol. Soc. Am. Bull.*, 107, 937-959, 1995.

Bolt, B. A., C. Lomnitz, and T. V. McEvilly, Seismological evidence on the tectonics of central and northern California and the Mendocino escarpment, *Bull. Seis. Soc. Am., 58*, 1735-1767, 1968.

Bonatti, E., Vertical tectonism in oceanic fracture zones, *Earth Planet. Sci. Lett., 37*, 369-379, 1978.

Bonatti, E., Serpentinite protrusions in the oceanic crust, *Earth Planet. Sci. Lett., 32*, 107-113, 1976.

Botros, M., and H. P. Johnson, Tectonic evolution of the Explorer - northern Juan de Fuca region from 8 Ma to the present, *J. Geophys. Res.*, 93, 10421-10437, 1988.

Bouchon, M., The complete synthesis of seismic crustal phases at regional distances, *J. Geophys. Res.*, 87, 1735-1741, 1982.

Braunmiller, J., J. L. Nábelek, B. Leitner, and A. Qamar, The 1993 Klamath Falls, Oregon, earthquake sequence: source mechanisms from regional data, *Geophys. Res. Lett.*, 22, 105-108, 1995a.

Braunmiller, J., J. L. Nábelek, and B. Leitner, Seismic monitoring of the Juan de Fuca plate with regional boadband data (abstract), *Trans. Am. Geophys. Union*, 76, F381, 1995b.

Brune, J. N., Seismic moment, seismicity, and rate of slip along major fault zones, *J. Geophys. Res.*, 73, 777-784, 1968.

Carbotte, S. M., J. M. Dixon, E. Farrar, E. E. Davis, and R. P. Riddihough, Geological and geophysical characteristics of the Tuzo Wilson seamounts: implications for the plate geometry in the vicinity of the Pacific-North America-Explorer triple junction, *Can. J. Earth Sci.*, 26, 2365-2384, 1989.

Cassidy, J. F., R. M. Ellis, C. Karavas, and G. C. Rogers, The northern limit of the subducted Juan de Fuca plate system, submitted to J. Geophys. Res., 1998.

Cassidy, J. F., and G. C. Rogers, The rupture process and aftershock distribution of the 6 April 1992 M_S 6.8 earthquake, offshore British Columbia, *Bull. Seis. Soc. Am.*, 85, 716-735, 1995.

Cassidy, J. F., R. M. Ellis, and G. C. Rogers, The 1918 and 1957 Vancouver Island earthquakes, *Bull. Seis. Soc. Am.*, 78, 617-635, 1988.

Castillo, D. A., and W. L. Ellsworth, Seismotectonics of the San Andreas fault system between Point Arena and Cape Mendocino in northern California: implications for the development and evolution of a young transform, *J. Geophys. Res.*, 98, 6543-6560, 1993.

Chandra, U., Seismicity, earthquake mechansims, and tectonics along the western coast of North America, from 42° N to 61° N, *Bull. Seis. Soc. Am.*, 64, 1529-1549, 1974.

Chase, R. L., D. L. Tiffin, and J. W. Murray, The western Canadian continental margin, *in: Canada's continental margins and offshore petroleum exploration*, eds. C. J. Yorath, E. R. Parker, and D. J. Glass, Can. Soc. Petr. Geol., Memoir 4, pp. 701-721, 1975.

Chen, Y. J., Oceanic crustal thickness versus spreading rate, *Geophys. Res. Lett.*, 19, 753-756, 1992.

Chen, Y., Thermal model of oceanic transform faults, *J. Geophys. Res.*, 93, 8839-8851, 1988.

Christie-Blick, N., and K. T. Biddle, Deformation and basin formation along strike-slip faults, *in: Strike-slip deformation, basin formation and sedimentation*, eds. K. T.

Biddle, and N. Christie-Blick, spec. pub. Society of Economic Paleontologists and Mineralogists, Tulsa, v. 37, pp. 1-34, 1985.

Clowes, R. M., D. J. Baird, and S. A. Dehler, Crustal structure of the Cascadia subduction zone, southwestern British Columbia, from potential field and seismic studies, *Can. J. Earth Sci.*, 34, 317-336, 1997.

Cousens, B. L., R. L. Chase, and J. G. Schilling, Geochemistry and origin of volcanic rocks from Tuzo Wilson and Bowie seamounts, northeast Pacific Ocean, *Can. J. Earth Sci.*, 22, 1609-1617, 1985.

Cousens, B. L., R. L. Chase, and J. G. Schilling, Basalt geochemistry of the Explorer Ridge area, northeast Pacific Ocean, *Can. J. Earth Sci.*, 21, 157-170, 1984.

Cowan, D. S., M. Botros, and H. P. Johnson, Bookshelf tectonics: rotated crustal blocks within the Sovanco fracture zone, *Geophys. Res. Lett.*, 13, 995-998, 1986.

Cox, A., and D. Engebretson, Change in motion of the Pacific plate at 5 Myr BP, *Nature*, 313, 472-474, 1985.

Dauteuil, O., Fault pattern from SeaBeam processing: the western part of the Blanco fracture zone (NE Pacific), *Mar. Geophys. Res.*, 17, 17-35, 1995.

Davis, E. E., and R. G. Currie, Geophysical observations of the northern Juan de Fuca ridge system: lessons in seafloor spreading, *Can. J. Earth Sci.*, 30, 278-300, 1993.

Davis, E. E., and R. D. Hyndman, The structure and tectonic history of the northern Cascadia subduction zone: recent accretion and deformation, *Geol. Soc. Am. Bull.*, 101, 1465-1480, 1989.

Davis, E. E. and R. P. Riddihough, The Winona Basin: structure and tectonics, *Can. J. Earth Sci.*, 19, 767-788, 1982.

Davis, E. E., and C. R. B. Lister, Tectonic structures on the Juan de Fuca ridge, *Geol. Soc. Am. Bull.*, 88, 346-363, 1977.

Davis, S. D., and C. Frohlich, A comparison of moment tensor solutions in the Harvard CMT and USGS catalogs (abstract), *Trans. Am. Geophys. Union*, 76, F381, 1995.

DeCharon, A. V., Structure and tectonics of Cascadia segment, central Blanco transform fault zone, *M.Sc. Thesis, Oregon State University, Corvallis, Oregon*, pp. 73, 1989.

Dehler, S. A., and R. M. Clowes, The Queen Charlotte Islands refraction project. Part I. The Queen Charlotte fault zone, *Can. J. Earth Sci.*, 25, 1857-1870, 1988.

Delaney, J. R., H. P. Johnson, and J. L. Karsten, The Juan de Fuca ridge-hot spot-propagating rift system: new tectonic, geochemical, and magnetic data, *J. Geophys. Res.*, 86, 11747-11-750, 1981.

DeMets, C., R. G. Gordon, D. F. Argus, and S. Stein, Effect of recent revision to the geomagnetic reversal time scale on estimates of current plate motions, *Geophys. Res. Lett.*, 21, 2191-2194, 1994.

DeMets, C., R. G. Gordon, D. F. Argus, and S. Stein, Current plate motions, *Geophys. J. Int.*, 101, 425-478, 1990.

Dewey, J. W., Seismicity and tectonics of western Venezuela, *Bull. Seis. Soc. Am.*, 62, 1711-1752, 1972.

Douglas, A., Joint epicentre determination, *Nature*, 215, 47-48, 1967.

Dragert, H., and R. D. Hyndman, Continuous GPS monitoring of elastic strain in the northern Cascadia subduction zone, *Geophys. Res. Lett.*, 22, 755-758, 1995.

Dziak, R. P., C. G. Fox, R. W. Embley, J. E. Lupton, G. C. Johnson, W. W. Chadwick, and R. A. Koski, Detection of and response to a probable volcanogenic T-wave event swarm on the western Blanco Transform Fault Zone, *Geophys. Res. Lett.*, 23, 873-876, 1996.

Dziak, R. P., C. G. Fox, and A. E. Schreiner, The June-July 1993 seismo-acoustic event at CoAxial segment, Juan de Fuca ridge: evidence for a lateral dike injection, *Geophys. Res. Lett.*, 22, 135-138, 1995.

Dziak, R. P., and C. G. Fox, Juan de Fuca ridge T-wave earthquakes August 1991 to present: volcanic and tectonic implications (abstract), *Trans. Am. Geophys. Union*, 76, F410, 1995.

Dziak, R. P., C. G. Fox, and R. W. Embley, Relationship between the seismicity and geologic structure of the Blanco Transform Fault Zone, *Mar. Geophys. Res.*, 13, 203-208, 1991.

Dziewonski, A. M., G. Ekström, and M. P. Salganik, Centroid-moment tensor solutions for October-December, 1993, *Phys. Earth Planet. Interiors*, 85, 215-225, 1994.

Embley, R. W., W. W. Chadwick, I. R. Jonasson, D. A. Butterfield, and E. T. Baker, Initial results of the rapid response to the 1993 CoAxial event: relationships between hydrothermal and volcanic processes, *Geophys. Res. Lett.*, 22, 143-146, 1995.

Embley, R. W., and D. S. Wilson, Morphology of the Blanco Transform Fault Zone - NE Pacific: implications for its tectonic evolution, *Mar. Geophys. Res.*, 14, 25-45, 1992.

Engebretson, D. C., A. Cox, and R. G. Gordon, *Relative motions between oceanic and continental plates in the Pacific Basin*, Geol. Soc. Am. Spec. Pap. 206, pp. 59, 1985.

Engeln, J. F., D. A. Wiens, and S. Stein, Mechanisms and depths of Atlantic transform earthquakes, *J. Geophys. Res.*, 91, 548-577, 1986.

Forsyth, D., and S. Uyeda, On the relative importance of the driving forces of plate motion, *Geophys. J. R. astr. Soc.*, 43, 163-200, 1975.

Fox, C. G., W. E. Radford, R. P. Dziak, T-K. Lau, H. Matsumoto, and A. E. Schreiner, Acousitc detection of a seafloor spreading episode on the Juan de Fuca ridge using military hydrophone arrays, *Geophys. Res. Lett*, 22, 131-134, 1995.

Fox, C. G., R. P. Dziak, H. Matsumoto, and A. E. Schreiner, Potential for monitoring low-level seismicity on the Juan de Fuca ridge using military hydrophone arrays, *Marine Technology Society Journal*, 27, 22-30, 1994.

Fox, P. J., D. G. Gallo, Tectonic model for ridge-transform-ridge plate boundries: Implications for the structure of oceanic lithosphere, *Tectonophysics*, 104, 205-243, 1984.

Froidevaux, C., Energy dissipation and geometric structure at spreading plate boundaries, *Earth Planet. Sci. Lett.*, 20, 419-424, 1973.

Goff, J. A., E. A. Bergman, and S. C. Solomon, Earthquake source mechanisms and transform fault tectonics in the Gulf of California, *J. Geophys. Res.*, 92, 10485-10510, 1987.

Goldfinger, C. L., D. Kulm, R. S. Yeats, B. Appelgate, M. MacKay, and G. F. Moore, Transverse structural trends along the Oregon convergent Margin: Implications for Cascadia earthquake potential and crust rotations, *Geology*, 20, 141-144, 1992.

Griggs, G. B., and L. D. Kulm, Origin and development of Cascadia deep-sea channel, *J. Geophys. Res.*, 9, 6325-6339, 1973.

Gripp, A. E., and R. G. Gordon, Current plate velocities relative to the hotspots incorporating the NUVEL-1 global plate motion model, *Geophys. Res. Lett.*, 17, 1109-1112, 1990.

Gutenberg, B., and C. F. Richter, *Seismicity of the Earth and associated phenomena*, 2nd ed., Princeton University Press, 1954.

Hanks, T. C., and H. Kanamori, A moment magnitude scale, *J. Geophys. Res.*, 84, 2348-2350, 1979.

Horn, J. R., R. M. Clowes, R. M. Ellis, and D. N. Bird, The seismic structure across an active oceanic/continental transform fault zone, *J. Geophys. Res.*, 89, 3107-3120, 1984.

Huang P. Y., S. C. Solomon, Centroid depths of mid-ocean ridge earthquakes: Dependence on spreading rate, *J. Geophys. Res.*, 93, 13,445-13,447, 1988.

Huang P. Y., S. C. Solomon, Centroid depths of mid-ocean ridge earthquakes in the Indian Ocean, Gulf of Aden, and Red Sea, *J. Geophys. Res.*, 92, 1361-1382, 1987.

Huang P. Y., S. C. Solomon, E. A. Bergman, and J. L. Nábelek, Focal depths and mechanisms of Mid-Atlantic ridge earthquakes from body wave inversion, *J. Geophys. Res.*, 91, 579-598, 1986.

Hyndman, R. D., and D. H. Weichert, Seismicity and rates of relative motion on the plate boundaries of western North America, *Geophys. J. R. astr. Soc.*, 73, 59-82, 1983.

Hyndman, R. D., T. J. Lewis, J. A. Wright, M. Burgess, D. S. Chapman, and M. Yamano, Queen Charlotte fault zone: heat flow measurements, *Can. J. Earth Sci.*, 19, 1657-1669, 1982.

Hyndman, R. D., and R. M. Ellis, Queen Charlotte fault zone: microearthquakes from a temporary array of land stations and ocean bottom seismographs, *Can. J. Earth Sci.*, 18, 776-788, 1981.

Hyndman, R. D., and G. C. Rogers, Seismicity surveys with ocean bottom seismographs off western Canada, *J. Geophys. Res.*, 86, 3867-3880, 1981.

Hyndman, R. D., R. P. Riddihough, and R. Herzer, The Nootka fault zone - A new plate boundary off western Canada, *Geophys. J. R. astr. Soc.*, 58, 667-683, 1979.

Hyndman, R. D., G. C. Rogers, M. N. Bone, C. R. B. Lister, U. S. Wade, D. L. Barrett, E. E. Davis, T. Lewis, S. Lynch, and D. Seemann, Geophysical measurements in the region of the Explorer ridge offshore western Canada, *Can. J. Earth Sci.*, 15, 1508-1525, 1978.

Ibach, D. H., The Sturcture and tectonics of the Blanco Fracture Zone *M. Sc. Thesis, Oregon State University, Corvallis, Oregon*, pp. 60, 1981.

Jemsek, J. P., E. A. Bergman, J. L. Nábelek, and S. C. Solomon, Focal depths and machanisms of large earthquakes on the Arctic mid-ocean ridge system., *J. Geophys. Res.*, 91, 13,993-14,005, 1986.

Johnson, R. H., R. A. Norris, and F. K. Duennebier, Abysally generated T-phases, *Hawaii Inst. Geophys. Rep., HIG-67-1*, 1967.

Johnson, S. H., and P. R. Jones, Microearthquakes located on the Blanco fracture zone with sonobuoy arrays, *J. Geophys. Res.*, 83, 255-261, 1978.

Juteau, T., D. Bideau, O. Dauteuil, G. Manach, D. D. Naidoo, P. Nehlig, H. Ondreas, M. A. Tivey, K. X. Whipple, and J. R. Delaney, A submersible study in the Western Blanco Fracture Zone, N. E. Pacific: structure and evolution during the last 1.6 Ma, *Mar. Geophys. Res.*, 17, 399-430, 1995.

Kanamori, H., and G. S. Stewart, Mode of strain release along the Gibbs fracture zone, Mid-Atlantic ridge, *Phys. Earth Planet. Inter.*, 11, 312-332, 1976.

Kanamori, H., and D. L. Anderson, Theoretical basis of some empirical relations in seismology, *Bull. Seis. Soc. Am.*, 65, 1073-1095, 1975.

Kappel, E. S., and W. B. F. Ryan, Volcanic episodicity and a non-steady state rift valley along northeast Pacific spreading centers: Evidence from SeaMARC I, *J. Geophys. Res.*, 91, 13,925-13,940, 1986.

Karsten, J. L., S. R. Hammond, E. E. Davis, and R. G. Currie, Detailed geomorphology and neotectonics of the Endeavor segment, Juan de Fuca ridge: new results from SeaBeam swath mapping, *Geol. Soc. Am. Bull.*, 97, 213-221, 1986.

King, G. C. P., and J. L. Nábelek, The role of bends in faults in the initiation and termination of earthquake rupture, *Science*, 228, 984-987, 1985.

Klein, F. W., *Hypocenter Location Program HYPOINVERSE, U.S. Geol. Sur. Open-File Rept. 78-694*, pp. 113, 1978.

Kulm, L. D., R. von Huene, J. R. Duncan, J. C. Ingle, S. A. Kling, L. F. Musich, D. J. W. Piper, R. M. Pratt, H.-J. Schrader, O. Weser, and S. W. Wise, Jr., Site 177, *Initial Reports of the Deep Sea Drilling Project*, Volume 18, pp. 233-285, 1973.

Lachenbruch, A. H., and G. A. Thompson, Oceanic ridges and transform faults: Their intersection angles and resistance to plate motion, *Earth Planet. Sci. Lett.*, 15, 116-122, 1972.

Lewis, T. J., C. Lowe, and T. S. Hamilton, The continental signature of a ridge-trench-transform triple junction: northern Vancouver Island, *J. Geophys. Res.*, 102, 7767-7781, 1997.

Lister, C. R. B., Plate tectonics at an awkward junction: rules for the evolution of Sovanco Ridge area, NE Pacific, *Geophys. J.*, 96, 191-201, 1989.

Lonsdale, P., Structural patterns of the Pacific floor offshore of Peninsular California, *in: Gulf and Peninsular Province of the Californias*, eds. Dauphin, J. P., and B. R. T. Simoneit, Amer. Ass. Petr. Geol. Memoir 47, pp. 87-143, 1991.

Mackie, D. J., R. M. Clowes, S. A. Dehler, R. M. Ellis, and L. P. Morel-À-L'Huissier, The Queen Charlotte Islands refraction project. Part II. Structural model for transition from Pacific to North America plate, *Can. J. Earth Sci.*, 26, 1713-1725, 1989.

Malacek, S. J., and R. M. Clowes, Crustal structure near Explorer Ridge from a marine deep seismic sounding survey, *J. Geophys. Res.*, 83, 5899-5912, 1978.

Mann P., M. R. Hempton, D. C. Bradley, and K Burke, Development of pull-apart basins, *J. Geol.*, 91, 529-554, 1983.

McKenzie, D. P., The relation between fault plane solutions for earthquakes and the directions of the principal stresses, *Bull. Seis. Soc. Am.*, 59, 591-601, 1969.

McManus, D. A., M. L. Holmes, B. Carson, and S. M. Barr, Late Quaternary tectonics, northern end of Juan de Fuca ridge, *Mar. Geol.*, 12, 141-162, 1972.

Michael, P. J., R. L. Chase, and J. F. Allan, Petrologic and geologic variations along southern Explorer Ridge, northeast Pacific Ocean, *J. Geophys. Res.*, 94, 13895-13918, 1989.

Molnar, P., Earthquake recurrence intervals and plate tectonics, *Bull. Seis. Soc. Am.*, 69, 115-133, 1979.

Nábelek J. L., Determination of earthquake source parameters from inversion of body waves, *Ph.D. thesis, Mass. Inst. of Tech.*, 1984.

Nábelek J., and G. Xia, Moment-tensor analysis using regional data: application to the 25 March, 1993, Scotts Mills, Oregon earthquake, *Geophys. Res. Lett.*, 22, 13-16, 1995.

Nicholson, C., C. C. Sorlien, T. Atwater, J. C. Crowell, and B. P. Luyendyk, Microplate capture, rotation of the western Transverse Ranges, and initiation of the San Andreas transform as a low-angle fault system, *Geology*, 22, 491-495, 1994.

Nur, A., H. Ron, and O. Scotti, Kinematics and mechanics of tectonic block rotations, in: *Slow deformation and transmission of stress in the Earth*, eds. S. C. Cohen, and P. Vanicek, Amer. Geophys. Un., Geophys. Monograph 49, pp. 31-46, 1989.

Prothero, W. A., and I. D. Reid, Microearthquakes on the East Pacific Rise at 21°N and the Rivera Fracture Zone, *J. Geophys. Res.*, 87, 8509-8518, 1982.

Reichle, M. S., G. F. Sharman, and J. N. Brune, Sonobuoy and teleseismic study of Gulf of California transform fault earthquake sequences, *Bull. Seis. Soc. Am.*, 66, 1623-1640, 1976.

Riddihough, R. P., Recent movements of the Juan de Fuca plate system, *J. Geophys. Res.*, 89, 6980-6994, 1984.

Riddihough, R. P., Contemporary movements and tectonics on Canada's west coast; a discussion, *Tectonophysics*, 86, 319-341, 1982.

Riddihough, R. P., Gorda plate motions from magnetic anomaly analysis, *Earth Planet. Sci. Lett.*, 51, 163-170, 1980.

Riddihough, R. P., A model for recent plate interactions off Canada's west coast, *Can. J. Earth Sci.*, 14, 384-396, 1977.

Riddihough, R. P., R. G. Currie, and R. D. Hyndman, The Dellwood Knolls and their role in triple junction tectonics off northern Vancouver Island, *Can. J. Earth Sci.*, 17, 577-593, 1980.

Rohr, K. M. M., and K. P. Furlong, Images of the initiation of a transform plate boundary, the Explorer transform zone (abstract), *Trans. Am. Geophys. Union*, 77, F655, 1996.

Rohr, K. M. M., and K. P. Furlong, Ephemeral plate tectonics at the Queen Charlotte triple junction, *Geology*, 23, 1035-1038, 1995.

Rohr, K. M. M., and J. R. Dietrich, Strike slip tectonics and development of the Tertiary Queen Charlotte Basin, offshore western Canada: evidence from seismic reflection data, *Basin Research*, 4, 1-19, 1992.

Scheidhauer, M., Crustal structure of the Queen Charlotte transform fault zone from multichannel seismic reflection and gravity data, *M. Sc. Thesis, Oregon State University, Corvallis, Oregon*, pp. 184, 1997.

Scholz, C. H., *The Mechanics of Earthquakes and Faulting*, Cambridge University Press, Cambridge, 1990.

Scholz, C. H., Scaling relations for strong ground motions in large earthquakes, *Bull. Seis. Soc. Am.*, 72, 1-14,1982.

Schwartz, S. Y., Source parameters of aftershocks of the 1991 Costa Rica and 1992 Cape Mendocino, California, earthquakes from inversion of local amplitude ratios and broadband waveforms, *Bull. Seis. Soc. Am.*, 85, 1560-1575, 1995.

Smith, S. W., J. S. Knapp, and R. C. McPherson, Seismicity of the Gorda plate, structure of the continental margin, and an eastward jump of the Mendocino triple junction, *J. Geophys. Res.*, 98, 8153-8171, 1993.

Solano, A. E., Crustal structure and seismicity of the Gorda Ridge, *Ph. D. Thesis, Oregon State University, Corvallis, Oregon*, pp. 185, 1985.

Spence, G. D., and D. T. Long, Transition from oceanic to continental crust structure: seismic and gravity models at the Queen Charlotte transform margin, *Can. J. Earth Sci.*, 32, 699-717, 1995.

Spence, W., Stress origins and Earthquake potentials in Cascadia, *J. Geophys. Res.*, 94, 3076-3088, 1989.

Spindler, C., G. C. Rogers, and J. F. Cassidy, The 1978 Brooks peninsula, Vancouver Island, earthquakes, *Bull. Seis. Soc. Am.*, 87, 1011-1023, 1997.

Srivastava, S. P., D. L. Barrett, C. E. Keen, K. S. Manchester, K. G. Shih, D. L. Tiffin, R. L. Chase, A. G. Thomlinson, E. E. Davis, and C. R. B. Lister, Preliminary analysis of geophysical measurements north of Juan de Fuca ridge, *Can. J. Earth Sci.*, 8, 1265-1281, 1971.

Stewart, L. M., and E. A. Okal, Seismicity and aseismic slip along the Eltanin Fracture Zone, *J. Geophys. Res.*, 88, 495-507, 1983.

Stewart, L. M., and E. A. Okal, Do all transform faults exhibit m_b-M_S disparity? (abstract), *EOS,Ttrans. AGU*, 62, 1031-1032, 1981.

Stock, J. M., and J. Lee, Do microplates in subduction zones leave a geologic record? *Tectonics*, 13, 1472-1487, 1994.

Stock, J. M., and P. Molnar, Uncertainties and implications of the Cretaceous and Tertiary position of North America relative to Farallon, Kula, and Pacific plates, *Tectonics*, 6, 1339-1384, 1988.

Sweeney, J. F., and D. A. Seemann, Crustal density structure of Queen Charlotte Islands and Hecate Strait, British Columbia, *in: Evolution and hydrocarbon potential of the Queen Charlotte Basin, British Columbia*, ed. G. Woodsworth, Geological Society of Canada, paper 90-10, pp. 89-96, 1991.

Thatcher, W., and T. Hanks, Source parameters of southern California earthquakes *J. Geophys. Res.*, 78, 8547-8576, 1973.

Thompson, G., and W. G. Melson, The petrology of oceanic crust across fracture zones in the Atlantic Ocean: Evidence for a new kind of seafloor spreading, *J. Geol.*, 80, 526-538, 1972.

Tiffin, D. L., B. E. B. Cameron, and J. W. Murray, Tectonics and depositional history of the continental margin off Vancouver Island, British Columbia, *Can. J. Earth Sci.*, 9, 280-296, 1972.

Tobin, D. G., and L. R. Sykes, Seismicity and tectonics of the Northeast Pacific ocean, *J. Geophys. Res.*, 73, 3821-3845, 1968.

Tolstoy, I., and M. Ewing, The T-Phase of shallow focus earthquakes, *Bull. Seis. Soc. Am.*, 84, 735-750, 1994.

Toomey, D. R., S. C. Solomon, G. M. Purdy, and M. H. Murray, Microearthquakes beneath the Median Valley of the Mid-Atlantic Ridge near 23°N: Tomography and Techtonics, *J. Geophys. Res.*, 93, 9093-9112, 1988.

Toomey, D. R., S. C. Solomon, G. M. Purdy, and M. H. Murray, Microearthquakes beneath the Median Valley of the Mid-Atlantic Ridge near 23°N: Hypocenters and focal mechanisms, *J. Geophys. Res.*, 90, 5443-5458, 1985.

Tréhu, A. M., and the Mendocino Working Group, Pulling the rug out from under California: seismic images of the Mendocino triple junction region, *EOS*, 76, 369-381, 1995.

Tréhu, A. M., and S. C. Solomon, Earthquakes in the Orozco transform zone: seismicity, source mechanisms, and tectonics, *J. Geophys. Res.*, 88, 8203-8225, 1983.

Turcotte, D. L., and G. Schubert, *Geodynamics: Applications of Continuum Physics to Geological Problems*, John Wiley & Sons, New York, 1982.

Velasco, A. A., C. J. Ammon, and T. Lay, Recent large earthquakes near Cape Mendocino and in the Gorda plate: broadband source time functions, fault orientations and rupture complexities, *J. Geophys. Res.*, 99, 711-728, 1994.

Verdonck, D., and G. Zandt, Three-dimensional crustal structure of the Mendocino triple junction region from local earthquake travel times, *J. Geophys. Res.*, 99, 23843-23858, 1994.

Wahlström, R., and G. C. Rogers, Relocation of earthquakes west of Vancouver Island, British Columbia, 1965-1983, *Can. J. Earth Sci.*, 29, 953-961, 1992.

Wang, K., H Jiangheng, and E. E. Davis, Transform push, oblique subduction resistance, and intraplate stress of the Juan de Fuca plate, *J. Geophys. Res.*, 102, 661-674, 1997.

Wessel, P., and W. H. F. Smith, New version of the generic mapping tools released, *Trans. Am. Geophys. Union*, 76, 329, 1995.

Wilcock, W. S. D., G. M. Purdy, and S. C. Solomon, Microearthquake evidence for extension across the Kane transform fault, *J. Geophys. Res.*, 95, 15439-15462, 1990.

Wilson, D. S., Confidence intervals for motion and deformation of the Juan de Fuca plate, *J. Geophys. Res.*, 98, 16053-16071, 1993.

Wilson, D. S., Deformation of the so-called Gorda plate, *J. Geophys. Res.*, 94, 3065-3075, 1989.

Wilson, D. S., A kinematic model for the Gorda deformation zone as a diffuse southern boundary of the Juan de Fuca plate, *J. Geophys. Res.*, 91, 10259-10269, 1986.

Wilson, D. S., R. N. Hey, and C. Nishimura, Propagation as a mechanism of reorientation of the Juan de Fuca ridge, *J. Geophys. Res.*, 89, 9215-9225, 1984.

Wolfe, C. J., E. A. Bergman, and S. C. Solomon, Oceanic transform earthquakes with unusual mechanisms and locations: relation to fault geometry and state of stress in the adjacent lithosphere, *J. Geophys. Res.*, 98, 16187-16211, 1993.

Yorath, C. J., and R. D. Hyndman, Subsidence and thermal history of Queen Charlotte Basin, *Can. J. Earth Sci.*, 20, 135-159, 1983.

Yuan, T., G. D. Spence, and R. D. Hyndman, Structure beneath Queen Charlotte Sound from seismic-refraction and gravity interpretation, *Can. J. Earth Sci.*, 29, 1509-1529, 1992.